MEDICAL AND INDUSTRIAL APPLICATIONS OF MICROFLUIDIC-BASED CELL/TISSUE CULTURE AND ORGANS-ON-A-CHIP: ADVANCES IN ORGANS-ON-A-CHIP AND ORGANOIDS TECHNOLOGIES

EDITED BY: Qasem Ramadan, Massimo Alberti, Martin Dufva and
Yi-Chung Tung

PUBLISHED IN: Frontiers in Bioengineering and Biotechnology

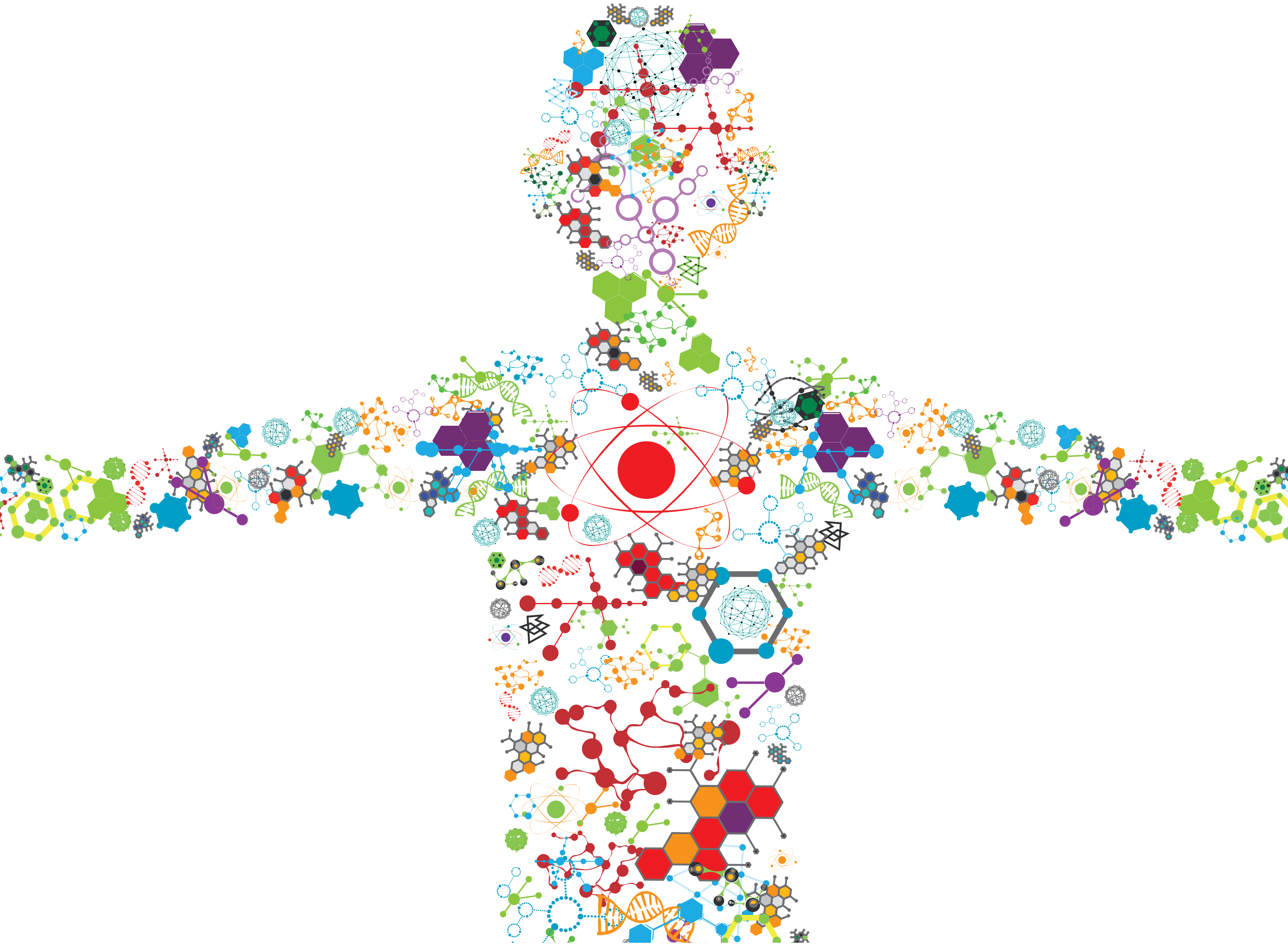

frontiers Research Topics

About Frontiers

Frontiers is more than just an open-access publisher of scholarly articles: it is a pioneering approach to the world of academia, radically improving the way scholarly research is managed. The grand vision of Frontiers is a world where all people have an equal opportunity to seek, share and generate knowledge. Frontiers provides immediate and permanent online open access to all its publications, but this alone is not enough to realize our grand goals.

Frontiers Journal Series

The Frontiers Journal Series is a multi-tier and interdisciplinary set of open-access, online journals, promising a paradigm shift from the current review, selection and dissemination processes in academic publishing. All Frontiers journals are driven by researchers for researchers; therefore, they constitute a service to the scholarly community. At the same time, the Frontiers Journal Series operates on a revolutionary invention, the tiered publishing system, initially addressing specific communities of scholars, and gradually climbing up to broader public understanding, thus serving the interests of the lay society, too.

Dedication to Quality

Each Frontiers article is a landmark of the highest quality, thanks to genuinely collaborative interactions between authors and review editors, who include some of the world's best academicians. Research must be certified by peers before entering a stream of knowledge that may eventually reach the public - and shape society; therefore, Frontiers only applies the most rigorous and unbiased reviews.
Frontiers revolutionizes research publishing by freely delivering the most outstanding research, evaluated with no bias from both the academic and social point of view. By applying the most advanced information technologies, Frontiers is catapulting scholarly publishing into a new generation.

What are Frontiers Research Topics?

Frontiers Research Topics are very popular trademarks of the Frontiers Journals Series: they are collections of at least ten articles, all centered on a particular subject. With their unique mix of varied contributions from Original Research to Review Articles, Frontiers Research Topics unify the most influential researchers, the latest key findings and historical advances in a hot research area! Find out more on how to host your own Frontiers Research Topic or contribute to one as an author by contacting the Frontiers Editorial Office: researchtopics@frontiersin.org

ISSN 1664-8714
ISBN 978-2-88963-114-8
DOI 10.3389/978-2-88963-114-8

MEDICAL AND INDUSTRIAL APPLICATIONS OF MICROFLUIDIC-BASED CELL/TISSUE CULTURE AND ORGANS-ON-A-CHIP: ADVANCES IN ORGANS-ON-A-CHIP AND ORGANOIDS TECHNOLOGIES

Topic Editors:
Qasem Ramadan, Agency for Science, Technology and Research (A*STAR), Singapore
Massimo Alberti, Agency for Science, Technology and Research (A*STAR), Singapore
Martin Dufva, Technical University of Denmark, Denmark
Yi-Chung Tung, Academia Sinica, Taiwan

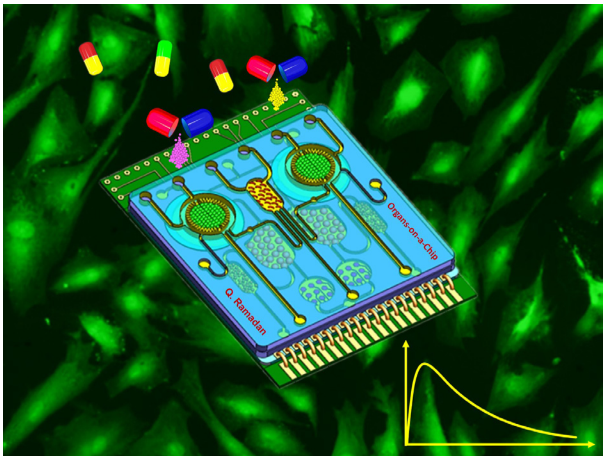

Multiple organs-on-a-chip for drug screening.
Image by Qasem Ramadan

Recent developments in microfluidics have demonstrated enormous potential of microscale cell culture for biology studies and recognized as instrumental in performing rapid and efficient experiments on small-sample volumes. Microfluidic-based cell culture is an area of research that keeps growing and gaining importance as a prominent technology, able to link scientific disciplines with industrial and clinical applications. In particular, organotypic cell culture and its integration in microfluidic devices would enable the realization of “in vivo-like” cell microenvironment within systems that are more amenable to automation and integration. Such remarkable advancement forms the foundation and motivation to transfer research from the laboratory to the field.

Although the microfluidics and cell culture technologies have influenced many areas of science, significant research efforts are currently focus on finding methods to transform drug screening and toxicity testing from a system reliant on high-dose animal studies to one based primarily on human-relevant in vitro models. In line with regulatory developments precluding the use of animal testing, as well as fundamental differences in animal versus human, human in vitro methodologies are required to replace the animal-based testes while permitting physiologically relevant model equivalents for superior prediction.

Organs-on-a-chip is an ambitious and rapidly growing technology that promise to bridge the gap between in vivo and in vitro studies and open wide possibilities in medical and industrial applications. However, many challenges are still ahead. This eBook present recent state-of-the-art works and critical reviews in organs-on-a-chip technology which highlight the new advances in this growing field with an emphasis on the interface between technological advancements and high impact applications.

Citation: Ramadan, Q., Alberti, M., Dufva, M., Tung, Y.-C., eds. (2019). Medical and Industrial Applications of Microfluidic-based Cell/Tissue Culture and Organs-on-a-Chip: Advances in Organs-on-a-Chip and Organoids Technologies. Lausanne: Frontiers Media. doi: 10.3389/978-2-88963-114-8

Table of Contents

frontiers
in Bioengineering and Biotechnology

EDITORIAL
published: 26 June 2019
doi: 10.3389/fbioe.2019.00151

Editorial: Medical and Industrial Applications of Microfluidic-Based Cell/Tissue Culture and Organs-on-a-Chip

Qasem Ramadan[1]*, **Massimo Alberti**[1], **Martin Dufva**[2] **and Yi-Chung Tung**[3]

[1] Agency for Science, Technology and Research (A*STAR), Singapore, Singapore, [2] Department of Health Technology, Technical University of Denmark, Kongens Lyngby, Denmark, [3] Research Center for Applied Sciences, Academia Sinica, Taipei, Taiwan

Keywords: cell culture, microfluidics, *in vitro*, organs-on-a-chip, drug, toxicology

Editorial on the Research Topic

Medical and Industrial Applications of Microfluidic-based Cell/Tissue Culture and Organs-on-a-Chip

Edited by:
Ranieri Cancedda,
Independent Researcher, Genova,
Italy

Reviewed by:
Andrea Banfi,
University of Basel, Switzerland

***Correspondence:**
Qasem Ramadan
qasemr@gmail.com

Specialty section:
This article was submitted to
Tissue Engineering and Regenerative
Medicine,
a section of the journal
Frontiers in Bioengineering and
Biotechnology

Received: 27 May 2019
Accepted: 10 June 2019
Published: 26 June 2019

Citation:
Ramadan Q, Alberti M, Dufva M and
Tung Y-C (2019) Editorial: Medical and
Industrial Applications of
Microfluidic-Based Cell/Tissue Culture
and Organs-on-a-Chip.
Front. Bioeng. Biotechnol. 7:151.
doi: 10.3389/fbioe.2019.00151

Cell culture on Petri dish remains the gold standard in basic research for screening drug candidates during one of the most expensive and lengthy industrial product development. However, the artifactual environment and the oversimplified structure of this one-cell-type culture system do not mimic the *in vivo* dynamic nature and heterogeneous architecture. Hence, it is not able to answer increasingly emerging biological questions. Animal models, on the other hand, provide systemic *in vivo* settings. However, despite the wealth of knowledge acquired from these models, many details of human pathogenesis cannot be addressed because of the differences between animal and human immune responses in preclinical studies vs. clinical trials (Mestas and Hughes, 2004; Zschaler et al., 2014). Costs associated with the failure in predicting the toxicity and efficacy of a drug candidate, particularly in the clinical trial stages, have become overwhelmingly expensive (Mullard, 2018). Therefore, the pharmaceutical industry needs to develop more predictive tools that reduce the chance of failure.

The past two decades have seen a rapid growth of microfluidics-based cell culture technology, with the ultimate aim to boost the development of fundamental bioscience and pharmaceutics. The versatile functionality and excellent spatiotemporal control over micro-environmental elements in microfluidic-based cell culture open up wide possibilities for tissue engineering and next-generation drug discovery. A remarkable development that is recently emerged is the ability to co-culture various type of cells in an integrated fluidic network to emulate a specific human tissue or organ simplified structure and function, called organs on a chip (OOC). A plethora of microfluidic-based culture models have been developed; however, the adaptation of this technology to address biological questions still scattered.

Here, we have assembled papers by contributors from prominent research labs that discuss fundamental questions and highlight the recent development in this emerging and rapidly advancing technology. There are five unique reviews, one perspective paper, and six original research papers in this issue that present a critical assessment of recent literature and demonstrate new advances in the field.

Avendano et al. discuss the effect of the physical microenvironment remodeling associated with cancer progression on mass transport in the tumor interstitial space. They examine the application and future opportunities of microfluidic models to better identify the physiochemical mediators of the mass transport. To maintain *in vivo*-like mass transfer and cell-cell communication *in vitro*, heterotypic cell co-culture is essential to mimic tissues and organs. Achieving such a heterotypic structure requires controlling the cell adhesion with desired patterns, Yaman et al. review the application of magnetic force-based cell manipulation in microfluidic devices and the potential use of this technique in guidance of cells into a specific location and creating heterotypic cellular structures in 2D and 3D organization.

Three papers in this collection focus on the brain tissue. *In vitro* modeling of the brain tissue, including the blood-brain barrier, and related diseases requires a high level of biological and fluidic design, as it is critical to replicate the complex network of different brain regions. Frimat and Luttge emphasize the advantages of combining engineered microsystems with stem cell (hiPSC) technology to improve the performances of brain-on-a-chip devices and their clinical relevance. Badiola-Mateos et al. address the challenges of modeling the neuromuscular circuit and recommend the combination of microfluidic systems, hiPSC and 3D culture to create patient-specific and reliable *in vitro* models. Qiao et al. discuss recent work on organoid-on-a-chip (Wang et al., 2018) as an alternative human-relevant neurodevelopmental model and its potential use for understanding the effects of prenatal nicotine exposure in the early stages of embryonic development, eliminating ethical concerns regarding human clinical trials in smoking pregnant women.

Spheroids and organoids have become popular tools for oncology and for basic and translational patient-specific tissue research. In order to grow large tissue models and organoids, the cells within the artificial tissue need continuous feeding through an *in vivo*-like capillary network. Mimicking the human vasculature, which can be viewed as a complex closed-loop perfusion system, represents one of the major *in vitro* challenges. Grebenyuk and Ranga reviewed the recent progress in generating *in vitro* vascularization. To date, nearly all fabrication techniques fall short to keep cells in 3D tissues alive during the slow fabrication process. Organ-on-a-Chip technology would enable the incorporation of the right cells at the right place, ultimately achieving perfusable organoids. An unconventional approach is reported by Bottaro et al. to demonstrate physical vein models by populating the surfaces of a PDMS mold with endothelial cells to simulate blood vessels and characterize the fluidic behavior of sclerosing foams.

Another significant challenge, especially when reconstructing epithelial tissues *in vitro*, is to obtain a realistic barrier function which is reviewed by Torras et al. Various epithelial barriers have been demonstrated *in vitro*, including lungs, intestine and skin. Bioprinting and photolithography are used for producing engineered complex basement membrane, recapitulate the properties of native epithelial tissues and provide robust predictive models.

Besides providing physiologically relevant cellular structure and fluidic environment, microfluidic devices also allow simulating the micro- and macro-mechanical features in human tissue. For instance, Felder et al. examined the effect of cyclic mechanical stress induced by respiratory motions, which was mimicked using a thin membrane, on alveolar wound repair. Recent breakthroughs in microbiology and medical sciences have highlighted the importance that the microbiota has on human health. Shin et al. demonstrated an *in vitro* anoxic-oxic interface of obligate anaerobic gut microbiome and human intestinal epithelial cells co-culture in a microfluidic chip and highlighted the importance of the host-microbiome crosstalk to the homeostasis of gastrointestinal functions.

Among all *in vitro* models, liver models play a central role in drug discovery. Accurate *in vitro* modeling of the liver is challenging because different hepatic functions are specific to the hepatocytes' spatial location within a liver lobule, which translate in different levels of gene expression and metabolic competence. Supported by a mathematical model, Tomlinson et al. used a Quasi Vivo system to create a zonated *in vitro* liver model in which primary rat hepatocytes cultured in three chambers are exposed to varying oxygen tension. This system provides a more accurate evaluation of pharmacological interventions at a zone-specific level.

Finally, in order to become widely accepted, these new culture systems need to overcome several drawbacks, such as the ability to control the concentrations of soluble factors, especially drugs. Lohasz et al. takes advantage of a tubing-free microfluidic device architecture to construct a microtissue culture system to generate gradual *in vivo*-like substance exposure profiles. The device not only eliminates the tedious interconnections for microfluidic device but also provides a great capability to control compound gradients in spatiotemporal domains.

This exciting collection of papers represent an excellent fit into the "Frontiers in Bioengineering and Biotechnology" with state-of-the-art contributions and critical reviews on the new advances in this growing field, with an emphasis on the interface between the technological advancements and high impact applications. We are delighted to be a part of this effort and witness the rapid expanding of the organ-on-a-chip technology toward opening the door to a variety of scientific and commercial avenues.

AUTHOR CONTRIBUTIONS

All authors listed have made a substantial, direct and intellectual contribution to the work, and approved it for publication.

REFERENCES

Mestas, J., and Hughes, C. C. W. (2004). Of mice and not men: differences between mouse and human immunology. *J. Immunol.* 172, 2731–2738. doi: 10.4049/jimmunol.172.5.2731

Mullard, A. (2018). How much do phase III trials cost? *Nat. Rev. Drug Discov.* 17: 777. doi: 10.1038/nrd.2018.198

Wang, Y., Wang, L., Zhu, Y., and Qin, J. (2018). Human brain organoid-on- a-chip to model prenatal nicotine exposure. *Lab Chip* 18, 851–860. doi: 10.1039/C7LC01084B

Zschaler, J., Schlorke, D., and Arnhold, J. (2014). Differences in innate immune response between man and mouse. *Crit. Rev. Immunol.* 34, 433–454. doi: 10.1615/CritRevImmunol.2014011600

Conflict of Interest Statement: The authors declare that the research was conducted in the absence of any commercial or financial relationships that could be construed as a potential conflict of interest.

frontiers
in Bioengineering and Biotechnology

PERSPECTIVE
published: 23 January 2019
doi: 10.3389/fbioe.2019.00006

Application of 3-D Microfluidic Models for Studying Mass Transport Properties of the Tumor Interstitial Matrix

Alex Avendano[1†], *Marcos Cortes-Medina*[1†] *and Jonathan W. Song*[2,3*]

[1] Department of Biomedical Engineering, The Ohio State University, Columbus, OH, United States, [2] Department of Mechanical and Aerospace Engineering, The Ohio State University, Columbus, OH, United States, [3] The Comprehensive Cancer Center, The Ohio State University, Columbus, OH, United States

The physical remodeling associated with cancer progression results in barriers to mass transport in the tumor interstitial space. This hindrance ultimately affects the distribution of macromolecules that govern cell fate and potency of cancer therapies. Therefore, knowing how specific extracellular matrix (ECM) and cellular components regulate transport in the tumor interstitium could lead to matrix normalizing strategies that improve patient outcome. Studies over the past decades have provided quantitative insights into interstitial transport in tumors by characterizing two governing parameters: (1) molecular diffusivity and (2) hydraulic conductivity. However, many of the conventional techniques used to measure these parameters are limited due to their inability to experimentally manipulate the physical and cellular environments of tumors. Here, we examine the application and future opportunities of microfluidic systems for identifying the physiochemical mediators of mass transport in the tumor ECM. Further advancement and adoption of microfluidic systems to quantify tumor transport parameters has potential to bridge basic science with translational research for advancing personalized medicine in oncology.

Keywords: tumor engineering, microfabrication, extracellular matrix, cellular microenvironment, therapeutic testing

Edited by:
Yi-Chung Tung,
Academia Sinica, Taiwan

Reviewed by:
Rui Cruz Pereira,
Fondazione Istituto Italiano di Technologia, Italy
Michela Pozzobon,
University of Padova, Italy

***Correspondence:**
Jonathan W. Song
song.1069@osu.edu

[†]These authors have contributed equally to this work

Specialty section:
This article was submitted to Tissue Engineering and Regenerative Medicine,
a section of the journal Frontiers in Bioengineering and Biotechnology

Received: *29 September 2018*
Accepted: *07 January 2019*
Published: *23 January 2019*

Citation:
Avendano A, Cortes-Medina M and Song JW (2019) Application of 3-D Microfluidic Models for Studying Mass Transport Properties of the Tumor Interstitial Matrix.
Front. Bioeng. Biotechnol. 7:6.
doi: 10.3389/fbioe.2019.00006

INTRODUCTION

Cancer has traditionally been described in terms of its molecular and genetic underpinnings, cellular heterogeneity, and network of signaling interactions during malignant progression (Hanahan and Weinberg, 2011). However, cancer can also be defined by its physicochemical features that arise due to function-altering mutations to the cellular constituents of the tumor microenvironment. For example, many solid tumor types, such as breast, pancreas, and liver, exhibit a desmoplastic response where stromal cells become hyperactivated leading to excessive extracellular matrix (ECM) production, growth of dense fibrotic tissue around the tumor (Trimboli et al., 2009; Kalluri, 2016), and subsequent tumor-promoting increases in mechanical stiffness (Leight et al., 2016; Reid et al., 2017). In addition to mechanical alterations, the tumor ECM may impede the distribution of macromolecules involved in regulating cell function (Netti et al., 2000). This hindrance to transport can also affect the ability of therapeutics to efficiently reach cancer cells. Consequently, the tumor ECM itself has emerged as a therapeutic target where the use of proteolytic enzymes and anti-fibrotic agents have been shown to normalize the ECM, improve drug penetration into the tumor, and increase patient survival (Nakai et al., 2012; Provenzano et al., 2012; Venning et al., 2015; Doherty et al., 2017; Papageorgis et al., 2017; Elahi-Gedwillo et al., 2018).

These newfound clinical implications of targeting the tumor ECM have heightened the importance of precise quantitative analysis of the mass transport properties of the tumor interstitial matrix. For this application, 3-D microfluidic systems, i.e., ones that integrate microscale technologies with 3-D tissue scaffolds, may provide a powerful approach because they possess the following desirable attributes : (1) bottom-up construction that enables tuning of ECM properties and spatial patterning of cellular constituents, (2) micron or cellular length scales where diffusive transport is critical, (3) controlled application of convective flow, and (4) typically favorable optical properties for real-time observation (Huh et al., 2011; Infanger et al., 2013; Akbari et al., 2017).

Here we highlight the application of microfluidic technologies for studying the transport properties of the tumor interstitium. To provide a balanced perspective, first we present a fundamental understanding of the physiological barriers to interstitial mass transport in tumors. We then discuss the parameters used to quantify transport in tumors and the established techniques used to measure these parameters. Lastly, we present prospective directions for the use of microfluidics as a tool for drug screening and development of targeted therapies. We note that in addition to the interstitium, other constituents of tumors such as the vasculature and transcellular membranes pose barriers to drug transport before reaching the intracellular space (Jain, 1987). For the foundational understanding of these other barriers in the context of tumors, we wish to direct the readers to these excellent review articles (Jain, 1988; Szakács et al., 2006; Dewhirst and Secomb, 2017).

FUNDAMENTALS OF MASS TRANSPORT IN THE TUMOR INTERSTITIUM

Physiological Barriers to Transport

The interstitial compartment (or interstitium) is comprised of an ECM, interstitial fluid, basement membrane proteins (e.g., collagen IV, laminin, elastin), and stromal cells (**Figure 1**). The interstitial ECM consists of a network of fibrous matrix proteins (e.g., collagen type I, fibronectin), glycosaminoglycans (GAGs) (e.g., hyaluronan, chondroitin sulfate), and proteoglycans (PGs) (e.g., versican, aggrecan, perlecan) (Wiig and Swartz, 2012; Theocharis et al., 2016; Xiong and Xu, 2016; Malandrino et al., 2018). Interstitial fluid is composed primarily of extravasated blood plasma and provides a medium for the transport of nutrients, waste products, and signaling molecules between cells of the interstitium.

The tumor interstitium poses unique barriers to transport which in turn can influence the delivery and uptake of therapeutic agents (Stylianopoulos et al., 2018). For example, the dense ECM of tumors hinders molecular diffusion (Jain, 1987; Pluen et al., 2001; Stylianopoulos et al., 2010; Zhang et al., 2017). In addition, tumors exhibit elevated interstitial fluid pressure (IFP) (Heldin et al., 2004; Elahi-Gedwillo et al., 2018) which can be attributed to excessive plasma leakage out of tumor blood vessels and impaired lymphatic function due to compressed vessels by growth-induced solid stress (Stylianopoulos et al., 2012; Nia et al., 2016). Uniformly high IFP in tumors limits interstitial convection as it abrogates the pressure difference between blood and lymphatic vessels. Also, fluid leakage from the tumor into surrounding tissue can result in outward radial flow that prevents transport of molecules into the tumor interior (Jain and Stylianopoulos, 2010). However, an important consideration is that these characteristics of tumors are highly heterogeneous, both within the same tumor and when comparing separate tumors (Jain and Stylianopoulos, 2010).

Transport through the tumor interstitial space relies on a combination of diffusion and convection (Jain, 1987; Netti et al., 1997; Kuszyk et al., 2001; Swartz and Fleury, 2007; Fan et al., 2014). The relative contributions of diffusive and convective transport can be quantified through the dimensionless parameter, the Peclet number (Pe):

$$Pe = \frac{convection}{diffusion} = \frac{Lv_{interstitial}}{D} \tag{1}$$

Where L is the characteristic length associated with the transport of the molecule, $v_{interstitial}$ is the interstitial fluid velocity, and D is the solute effective diffusion coefficient. In the interstitium, a typical L is $\sim 100\,\mu\text{m}$ (approximate distance between microvessels) (Dewhirst and Secomb, 2017). A typical $v_{interstitial}$ is $\sim 1\ \mu\text{m/s}$ (Wiig and Swartz, 2012), although this value can be much lower or higher depending on the region of the tumor (Kingsmore et al., 2018). Finally, a representative value for D is $\sim 10^{-7}\ \text{cm}^2/\text{s}$ (Chary and Jain, 1989) (reported for serum albumin in both normal and neoplastic tissues). Further considerations for diffusion and convective transport in the tumor interstitium are discussed below.

Diffusive Transport in the Tumor Interstitium

Molecular diffusion through the tumor interstitium is due to concentration gradients (Baish et al., 2011). Diffusive flux can be related to the concentration gradient through the effective diffusion coefficient D (cm^2/s). In the case of one dimensional transport, this relationship is given by Ficks' Law:

$$J_{diff} = -D\frac{\delta C}{\delta x} \tag{2}$$

Abbreviations: ECs, endothelial cells; ECM, extracellular matrix; FRAP, fluorescent recovery after photobleaching; GAGs, glycosaminoglycans; HAS3, hyaluronan synthase 3; HA, hyaluronic acid; HAdase, hyaluronidase; IFP, interstitial fluid pressure; PDGFR-α, platelet derived growth factor receptor alpha; PDMS, poly(dimethylsiloxane); PGs, proteoglycans; PTEN, phosphatase and tensin homolog; NPs, nanoparticles; SMO, smoothened; T-MOC, tumor microenvironment on a chip; TKI, tyrosine kinase inhibitor.

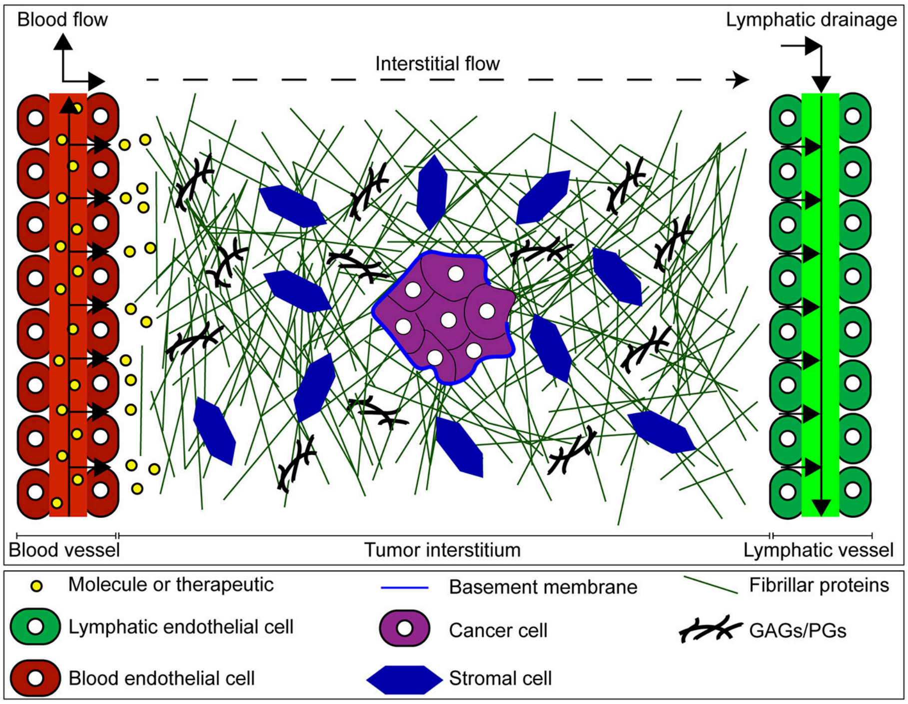

FIGURE 1 | Mass transport through the tumor interstitium. Once extravasated from the vascular space, molecules must cross the tumor interstitium, and eventually drain through the lymphatic vessels. The tumor interstitium is occupied by the interstitial matrix composed of fibrillar and non-fibrillar components such as collagen, glycosaminoglycans (GAGs), proteoglycans (PGs), and basement membrane produced by both cancer and stromal cells. This matrix imposes barriers to transport of molecules in tumors, contributing to a more hostile malignancy.

where $\frac{\delta C}{\delta x}$ denotes the concentration gradient. The effective diffusion coefficient in the interstitium (or interstitial diffusivity) is determined by properties of both the molecule of interest and the interstitial matrix (Jain and Stylianopoulos, 2010). Properties of the molecule that affect its interstitial diffusivity include size, charge, and configuration (Jain, 1999; Jain and Stylianopoulos, 2010; Wiig and Swartz, 2012). The properties of the ECM in the tumor interstitium that affect the diffusivity of molecules include viscoelasticity, geometrical arrangement (e.g., collagen fiber orientation), and electrostatic properties (Swartz and Fleury, 2007; Seo et al., 2014). These properties are a consequence of ECM composition (e.g., collagen, GAG, and PG content) with collagen being the major determinant of interstitial diffusion (Netti et al., 2000).

Convective Transport in the Tumor Interstitium

Convective transport of molecules through the tumor interstitium is driven by pressure gradients. The convective flux can be written as:

$$J_{conv} = v_{interstitial} f C \tag{3}$$

where C is the concentration of the particle/molecule, f is the retardation coefficient (ratio of particle to fluid velocity) which is often assumed to equal 1, and $v_{interstitial}$ is the interstitial fluid velocity. $v_{interstitial}$ can be determined by the solution to the Brinkman equation for flow through a porous medium (Equation 4):

$$\mu \nabla^2 v_{interstitial} - \frac{1}{K'} v_{interstitial} - \nabla p = 0 \tag{4}$$

where μ is the fluid viscosity, K' is the hydraulic conductivity, and ∇p is the pressure gradient across the interstitium. Due to the large magnitude of surface drag relative to viscous dissipation, the viscous term in the Brinkman equation can often be neglected resulting in the more familiar Darcy's law. Darcy's law can then be used to write the convective flux in terms of the pressure gradient and K':

$$J_{conv} = -CfK' \frac{\delta P}{\delta x} \tag{5}$$

where $\frac{\delta P}{\delta x}$ is the pressure gradient over a distance x. Thus, for a given $\frac{\delta P}{\delta x}$ the K' of the interstitial ECM is the major determinant of interstitial velocity. K' can also be expressed in terms of the Darcy permeability (also denoted as specific permeability) $K = \frac{K'}{\mu}$ where μ is the viscosity of the fluid. This parameter is mostly dependent on the properties of the interstitial ECM including composition, geometrical arrangement, charge, and hydration (Levick, 1987; Ng and Swartz, 2003; Ng et al., 2005; Wiig and Swartz, 2012). Compared to normal tissue, tumors typically exhibit reduced K' (Provenzano et al., 2012; Polydorou et al., 2014; Mpekris et al., 2017; Papageorgis et al., 2017).

MEASURING THE INTERSTITIAL TRANSPORT PARAMETERS IN TUMORS

Looking at the equations above for diffusive and convective fluxes, one can see that D and K' primarily determine the effectiveness of these mode of transport within tumors. A brief overview on how these two parameters have been experimentally measured is discussed below.

Interstitial Diffusivity (*D*)

Most techniques employed to measure D rely on measuring solute flux at a known concentration gradient or measuring relaxation of these gradients and fitting the diffusion equation to the data (Jain, 1999). Diffusion measurements *in vitro* have been performed using tissue slices or various gel or solution models of the interstitium (Jain, 1987; Pluen et al., 1999; Ramanujan et al., 2002). It should be noted that D is often lower than the diffusivity in free solution, and correlations have been developed that can relate both types (Swartz and Fleury, 2007). For *in vivo* settings, the use of intravital microscopy and fluorescence recovery after photobleaching (FRAP) has allowed the measurement of D (Chary and Jain, 2007). FRAP involves the use of a laser beam to artificially introduce a concentration gradient of a fluorescent tracer in a region of tissue and the relaxation of this gradient is analyzed to yield the diffusion coefficient and the convective velocity (Ramanujan et al., 2002).

Hydraulic Conductivity (*K′*)

Measurements of K' using Darcy's Law (Equation 5) involve estimating the flow rate under a known pressure gradient. This measurement is performed *in vitro* by applying flow across a tissue slice using an Ussing-style chamber (Hedbys and Mishima, 1962) or by ultracentrifugal sedimentation (Laurent and Pietruszkiewicz, 1961; Preston et al., 1965; Ethier, 1986). While measuring K' *in vivo* is comparatively more challenging, it has been achieved with the use of a micropore chamber (Swabb et al., 1974) as well as tail injections in rats (Swartz et al., 1999). K' can also be estimated by confined compression testing of excised tumor chunks *ex vivo* (Polydorou et al., 2014; Mpekris et al., 2015; Papageorgis et al., 2017).

APPLICATION OF MICROFLUIDIC MODELS FOR STUDYING TUMOR ECM TRANSPORT PROPERTIES

Representing the Tumor ECM in Microfluidic Devices

While the techniques described above have collectively provided the framework for our understanding of transport in tumors, they have several limitations that are worthy of consideration. First, it is often very difficult to apply controlled perturbations *in vivo*. With regards to quantifying transport within tumors, it is immensely challenging to independently specify concentration and pressure gradients and subsequently decouple the contributions of diffusion and convection. Second, intravital microscopy used for FRAP experiments requires specialized equipment and training that may not be readily available to most laboratories. This imaging modality is also limited to only thin tissues or for the superficial layer of thick tissues. Third, an overarching challenge with the analysis of tumor tissue, whether assessed *in situ* or *ex vivo*, is the high degree of morphological heterogeneity present in tumors that may lead to uncertainties when interpreting experimental results.

Compared to established techniques, microfluidic devices offer several advantageous characteristics for measuring the transport properties of the ECM (**Figure 2**). For instance, custom design and fabrication of microfluidic devices offer control over the length scale used to study transport phenomena and the formation of separate compartments that are representative of distinct regions of tumors. In addition, concentration and pressure gradients in microfluidic devices can be specified with relative ease and independently of each other, enabling precise control over convective and diffusive transport. Moreover, microfluidic devices fabricated by rapid prototyping of poly(dimethylsiloxane) (PDMS) permit visualization of the ECM since they are compatible with labeling and imaging techniques such as immunofluorescence, confocal reflectance microscopy, and second harmonic generation imaging. This important quality of PDMS microfluidic devices enables simultaneous interrogation of ECM composition and structure with the measurement of transport parameters. Lastly, microfluidic devices offer control over the spatial positioning of cells and the ECM composition. Of the reconstituted, biologically-derived ECM gels, collagen type I is most widely used due to its prominence as one of the main components of the tumor ECM (Sung et al., 2009; Burkel et al., 2016). However, other ECM gels such as fibrin and Matrigel are commonly used (Ng and Pun, 2008; Moreno-Arotzena et al., 2015). The biological function of the reconstituted matrices can be further modified through the incorporation of other ECM constituents such as GAGs, and PGs that were described in section Physiological Barriers to Transport (Stuart and Panitch, 2008; Yang et al., 2011; Manneschi et al., 2016; Narkhede et al., 2018). The use of cell derived matrices have also been used to provide a more representative tumor ECM in microfluidic devices (Gioiella et al., 2016; Brancato et al., 2018). Collectively these capabilities allow for the quantification of the contribution of each ECM constituent to transport properties. It is noted that the reconstituted ECM gels used for the desired studies can be subjected to material characterization tests (e.g., stiffness measurements, quantification of protein content) to ensure that they match the physiological properties of tumor tissue *in vivo*.

Given the importance of both D and K' as measures of transport through ECM, below we provide examples specific to the application of microfluidic platforms in quantifying these two governing parameters.

Interstitial Diffusivity (*D*)

Microfluidic devices used to measure values of D typically feature a compartmentalized 3-D ECM chamber that is flanked

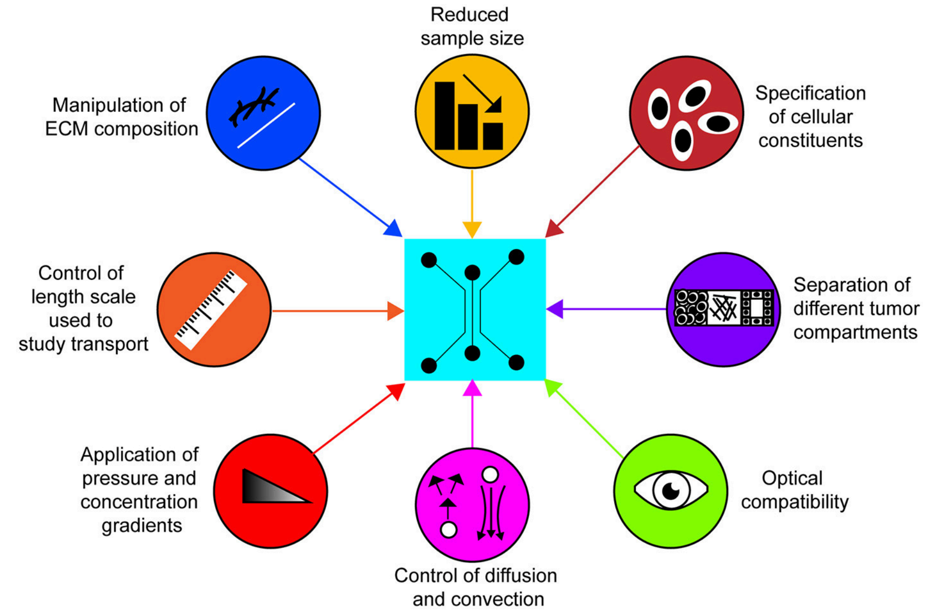

FIGURE 2 | Characteristics of 3-D microfluidic platforms for studying transport in the tumor ECM. Microfluidic platforms possess the capacity to readily integrate these attributes to efficiently quantify transport parameters of the tumor ECM *in vitro* and study how they are affected by different cellular and matrix constituents.

by channels or ports that enable controlled application of concentration gradients across the ECM (Zervantonakis et al., 2010; Evans et al., 2014; Wang et al., 2017). Measurement of D then involves applying a known concentration of a fluorescent tracer, measuring the concentration profile across the ECM compartment over time, and analyzing the data to obtain a value for D (Ghajar et al., 2008; Timp et al., 2008; Zervantonakis et al., 2010). Ghajar et al. demonstrated that increasing fibrin density significantly restricted D, which was attributed to increased matrix viscoelasticity (Ghajar et al., 2008). This study also demonstrated that the value for D is inversely proportional to the mass of the molecule of interest and presumably the hydrodynamic or Stokes radius (Seo et al., 2014). In a separate study, Albanese et al. incorporated tumor spheroids in a microfluidic device and monitored the accumulation of polystyrene nanoparticles (NPs) in the interstitial spaces as a property of NP size. This study also successfully bridged the gap between *in vitro* and *in vivo* studies by validating the results obtained in the microfluidic device with ones obtained in a murine model (Albanese et al., 2013). Kwak et al. implemented a tumor microenvironment on a chip (T-MOC) model that included capillary, interstitial, and lymphatic compartments with independent control of fluid pressure. This system demonstrated that NP transport is drastically hindered when IFP is higher than the capillary pressure (Kwak et al., 2014). Interestingly, addition of MCF7 breast cancer cells into the interstitial compartment reduced D by a factor of 3, presumably due to cell-mediated physical alterations to the ECM structure. Using a microfluidic model that incorporated cell-derived ECM, Gioiella et al. demonstrated that co-culture of MCF7 with normal breast fibroblasts generated an activated stromal tissue that reduced the D through the ECM (Gioiella et al., 2016). Taken together, microfluidic platforms have facilitated the quantification of D and how it is affected by both properties of the molecule and the ECM setting, with results agreeing with what has been observed *in vivo* (Tomasetti and Breunig, 2018).

Hydraulic Conductivity (K')

Several studies have leveraged the ability of microfluidic systems in specifying pressure gradients and ECM composition to quantify the hydraulic permeability (K) through application of Darcy's Law (Polacheck et al., 2011; Hammer et al., 2017). Typically, K' or K measurements in microfluidic devices involve the compartmentalization of ECM material in a microchannel and the application of a known pressure gradient to induce flow. The fluid velocity through the ECM can be approximated with the use of fluorescent tracers. Ng et al. looked at K as a measure of matrix integrity, demonstrating that Matrigel can support flow driven cultures for up to 6 h, with collagen matrices (2 mg/mL) also supporting such conditions (Ng and Pun, 2008). However, the reported value for K in Matrigel was below physiologically-relevant values. Tran et al. measured K through tumor cell aggregates in microfluidic devices at low and high pressures (Tran and Marcos, 2018). This study demonstrated that high intratumoral pressures can result in hydraulic fracturing of tumor aggregates, manifested by increased local K values.

K has also been estimated in microfluidic devices with the purpose of estimating interstitial flow and shear stress levels local to cells embedded in a 3-D matrix. This approach has shown that K can influence interstitial flow and consequently shear stresses on cells, thus altering cell behavior (Polacheck et al., 2011; Li R. et al., 2018). Lastly, K has also been used as a parameter for stromal cell-mediated ECM remodeling. Using this approach, Hammer et al. demonstrated that hyperactivation of platelet derived growth factor receptor alpha (PDGFRα) in the stroma reduced *K* and enhanced *in vivo* breast tumor growth (Hammer et al., 2017). Furthermore, it was shown that *K* was rescued to control levels by targeting PDGFR-α with the tyrosine kinase inhibitor (TKI) crenolanib, and extracellular hyaluronic acid (HA) deposited by stromal fibroblasts with hyaluronidase (HAdase). Recently, it was shown that pharmacologic inhibition of smoothened (SMO) in human pancreatic cancer fibroblasts with the compound GDC-0449 (or vismodegib) destabilized phosphatase and tensin homolog (PTEN) (Pitarresi et al., 2018). Moreover, gene expression analysis revealed that treatment of these fibroblasts with GDC-0449 increased hyaluronan synthase 3 (HAS3) expression levels while microfluidic analysis demonstrated that GDC-0449 treatment reduced *K*, which was rescued to control levels with application of HAdase. In this study, loss of PTEN in the stroma was also correlated with enhanced pancreatic tumor growth *in vivo* and reduced overall patient survival. Importantly, the functionality of microfluidics enabled precise control and manipulation of a biological target, and analysis of the functional outcomes of target modulation, which led to the discovery of previously unexplained adverse effects of PDGFR-α hyperactivation and loss of PTEN in stromal fibroblasts.

CONCLUSION AND FUTURE PERSPECTIVES

Microfluidic systems have successfully validated ECM transport properties obtained with other *in vitro* or *in vivo* models. However, we believe that there are numerous opportunities to utilize these systems for future novel discoveries. For instance, matrix normalizing strategies in oncology have so far focused on depleting collagen and HA in tumors, alleviating barriers to drug transport (Chauhan et al., 2011; Li X. et al., 2018). However, other ECM components may also have important and previously unknown roles in mediating drug transport, either directly as a physical barrier or indirectly by activating cells of tumors to deposit increased amounts of collagen and HA. Therefore, successfully elucidating these roles by ECM components besides collagen and HA may lead to new therapies for targeting the matrix that can improve drug transport and patient outcomes. We note that the application of microfluidic models has so far focused on describing the transport properties of desmoplastic tumors such as breast and pancreatic carcinomas that are rich in collagen and HA (Gioiella et al., 2016; Hammer et al., 2017; Brancato et al., 2018; Pitarresi et al., 2018). However, with increasing information on the different ECM compositions across various tumor types (Naba et al., 2016), measurements of the interstitial ECM transport properties can also be applied to non-desmoplastic tumors such as brain cancer to provide novel insights. Given the ability to systematically manipulate both ECM and cellular constituents, microfluidic systems are intrinsically modular, highly versatile, and therefore especially conducive for these types of studies.

Another prospective application for measuring D and K' within microfluidic devices can involve rapid screening to predict functional outcomes based on different genetic profiles of tumor or tumor-associated cells. For example, we previously demonstrated that hyperactivation of PDGFR-α in mammary fibroblasts and loss of PTEN in pancreatic fibroblasts resulted in increased deposition of HA with subsequent decreased K' in the ECM (Hammer et al., 2017; Pitarresi et al., 2018). Moreover, the therapeutic implications of this type of approach can be further extended through the incorporation of cancer patient-derived cells or ECM into the appropriate microfluidic system to predict drug response. While no current assays are ready for routine clinical practice (Shamir and Ewald, 2014), microfluidic systems can potentially provide personalized information on the determinants to drug transport. Thus, looking forward, microfluidic systems can serve as a nexus to bring together engineers, cancer researchers, and oncologists to foment advancements in cancer therapy.

AUTHOR CONTRIBUTIONS

All authors listed have made a substantial, direct and intellectual contribution to the work, and approved it for publication.

FUNDING

This work was supported by funding awarded to JS from an NSF CAREER Award (CBET-1752106), The American Cancer Society (IRG-67-003-50), Pelotonia Junior Investigator Award, NHLBI (R01HL141941), The American Heart Association (15SDG25480000), and The Ohio State University Materials Research Seed Grant Program, funded by the Center for Emergent Materials, an NSF-MRSEC, grant DMR-1420451, the Center for Exploration of Novel Complex Materials, and the Institute for Materials Research. AA acknowledges funding from the Pelotonia Graduate Fellowship Program. MC-M acknowledges funding from an OSU Graduate Enrichment Fellowship and Discovery Scholars Fellowship.

ACKNOWLEDGMENTS

We acknowledge the significant foundational work published beforehand that we regret that we cannot include here because of the limit on the number of words and references.

REFERENCES

Akbari, E., Spychalski, G. B., and Song, J. W. (2017). Microfluidic approaches to the study of angiogenesis and the microcirculation. *Microcirculation* 24:e12363. doi: 10.1111/micc.12363

Albanese, A., Lam, A. K., Sykes, E. A., Rocheleau, J. V., and Chan, W. (2013). Tumour-on-a-chip provides an optical window into nanoparticle tissue transport. *Nat. Commun.* 4:2718. doi: 10.1038/ncomms3718

Baish, J. W., Stylianopoulos, T., Lanning, R. M., Kamoun, W. S., Fukumura, D., Munn, L. L., et al. (2011). Scaling rules for diffusive drug delivery in tumor and normal tissues. *Proc Natl. Acad. Sci. U.S.A.* 108, 1799–1803. doi: 10.1073/pnas.1018154108

Brancato, V., Gioiella, F., Imparato, G., Guarnieri, D., Urciuolo, F., and Netti, P. A. (2018). 3D Breast Cancer Microtissue reveals the role of tumor microenvironment on the transport and efficacy of free-Doxorubicin *in vitro*. *Acta Biomater*. 75, 200–212. doi: 10.1016/j.actbio.2018.05.055

Burkel, B., Morris, B. A., Ponik, S. M., Riching, K. M., Eliceiri, K. W., and Keely, P. J. (2016). Preparation of 3D collagen gels and microchannels for the study of 3D interactions *in vivo*. *J. Vis. Exp.* e53989 doi: 10.3791/53989

Chary, S. R., and Jain, R. K. (1989). Direct measurement of interstitial convection and diffusion of albumin in normal and neoplastic tissues by fluorescence photobleaching. *Proc. Natl. Acad. Sci. U.S.A.* 86, 5385–5389. doi: 10.1073/pnas.86.14.5385

Chary, S. R., and Jain, R. K. (2007). analysis of diffusive and convective recovery of fluorescence after photobleaching—effect of uniform flow field. *Chem. Eng. Commun.* 55, 235–249. doi: 10.1080/00986448708911930

Chauhan, V. P., Stylianopoulos, T., Boucher, Y., and Jain, R. K. (2011). Delivery of molecular and nanoscale medicine to tumors: transport barriers and strategies. *Chem Biomol. Eng.* 2, 281–298. doi: 10.1146/annurev-chembioeng-061010-114300

Dewhirst, M. W., and Secomb, T. W. (2017). Transport of drugs from blood vessels to tumour tissue. *Nat. Rev. Cancer* 17, 738–750. doi: 10.1038/nrc.2017.93

Doherty, G. J., Tempero, M., and Corrie, P. G. (2017). HALO-109–301: a Phase III trial of PEGPH20 (with gemcitabine and nab-paclitaxel) in hyaluronic acid-high stage IV pancreatic cancer. *Future Oncol.* 14, 13–22. doi: 10.2217/fon-2017-0338

Elahi-Gedwillo, K. Y., Carlson, M., Zettervall, J., and Provenzano, P. P. (2018). Antifibrotic therapy disrupts stromal barriers and modulates the immune landscape in pancreatic ductal adenocarcinoma. *Cancer Res.* doi: 10.1158/0008-5472.can-18-1334. [Epub ahead of print].

Ethier, C. (1986). The hydrodynamic resistance of hyaluronic acid: estimates from sedimentation studies. *Biorheology* 23, 99–113.

Evans, S. M., Litzenberger, A. L., Ellenberger, A. E., Maneval, J. E., Jablonski, E. L., and Vogel, B. M. (2014). A microfluidic method to measure small molecule diffusion in hydrogels. *Mater. Sci. Eng. C* 35, 322–334. doi: 10.1016/j.msec.2013.10.035

Fan, D., Creemers, E. E., and Kassiri, Z. (2014). Matrix as an interstitial transport system. *Circ. Res.* 114, 889–902. doi: 10.1161/circresaha.114.302335

Ghajar, C. M., Chen, X., Harris, J. W., Suresh, V., Hughes, C. C., Jeon, N., et al. (2008). The effect of matrix density on the regulation of 3-D capillary morphogenesis. *Biophys. J.* 94, 1930–1941. doi: 10.1529/biophysj.107.120774

Gioiella, F., Urciuolo, F., Imparato, G., Brancato, V., and Netti, P. A. (2016). An engineered breast cancer model on a chip to replicate ECM-activation *in vitro* during tumor progression. *Adv. Healthc. Mater.* 5, 3074–3084. doi: 10.1002/adhm.201600772

Hammer, A. M., Sizemore, G., Shukla, V. C., Avendano, A., Sizemore, S. T., Chang, J. J., et al. (2017). Stromal PDGFR-α activation enhances matrix stiffness, impedes mammary ductal development, and accelerates tumor growth. *Neoplasia* 19, 496–508. doi: 10.1016/j.neo.2017.04.004

Hanahan, D., and Weinberg, R. A. (2011). Hallmarks of cancer: the next generation. *Cell* 144, 646–674. doi: 10.1016/j.cell.2011.02.013

Hedbys, B. O., and Mishima, S. (1962). Flow of water in the corneal stroma. *Exp. Eye Res.* 1, 262–275. doi: 10.1016/s0014-4835(62)80010-4

Heldin, C. H., Rubin, K., Pietras, K., and Ostman, A. (2004). High interstitial fluid pressure — an obstacle in cancer therapy. *Nat. Rev. Cancer* 4, 806–813. doi: 10.1038/nrc1456

Huh, D., Hamilton, G. A., and Ingber, D. E. (2011). From 3D cell culture to organs-on-chips. *Trends Cell Biol.* 21, 745–754. doi: 10.1016/j.tcb.2011.09.005

Infanger, D. W., Lynch, M. E., and Fischbach, C. (2013). Engineered culture models for studies of tumor-microenvironment interactions. *Annu. Rev. Biomed. Eng.* 15, 29–53. doi: 10.1146/annurev-bioeng-071811-150028

Jain, R. (1987). Transport of molecules in the tumor interstitium: a review. *Cancer Res.* 47, 3039–3051.

Jain, R. (1988). Determinants of tumor blood flow: a review. *Cancer Res.* 48, 2641–2658.

Jain, R. K. (1999). Transport of molecules, particles, and cells in solid tumors. *Biomed. Eng.* 1, 241–263. doi: 10.1146/annurev.bioeng.1.1.241

Jain, R. K., and Stylianopoulos, T. (2010). Delivering nanomedicine to solid tumors. *Nat. Rev. Clin. Oncol.* 7, 653. doi: 10.1038/nrclinonc.2010.139

Kalluri, R. (2016). The biology and function of fibroblasts in cancer. *Nat. Rev. Cancer* 16, 582–598. doi: 10.1038/nrc.2016.73

Kingsmore, K. M., Vaccari, A., Abler, D., Cui, S. X., Epstein, F. H., Rockne, R. C., et al. (2018). MRI analysis to map interstitial flow in the brain tumor microenvironment. *Appl. Bioeng* 2:031905. doi: 10.1063/1.5023503

Kuszyk, B., Corl, F. M., Franano, F. N., Bluemke, D. A., Hofmann, L. V., Fortman, B. J., et al. (2001). Tumor transport physiology: implications for imaging and imaging-guided therapy. *AJR Am. J. Roentgenol.* 177, 747–753. doi: 10.2214/ajr.177.4.1770747

Kwak, B., Ozcelikkale, A., Shin, C. S., Park, K., and Han, B. (2014). Simulation of complex transport of nanoparticles around a tumor using tumor-microenvironment-on-chip. *J. Control. Release* 194, 157–167. doi: 10.1016/j.jconrel.2014.08.027

Laurent, T. C., and Pietruszkiewicz, A. (1961). The effect of hyaluronic acid on the sedimentation rate of other substances. *Biochim. Biophys. Acta* 49, 258–264. doi: 10.1016/0006-3002(61)90125-1

Leight, J. L., Drain, A. P., and Weaver, V. M. (2016). Extracellular matrix remodeling and stiffening modulate tumor phenotype and treatment response. *Annu. Rev. Cancer Biol.* 1, 313–334. doi: 10.1146/annurev-cancerbio-050216-034431

Levick, J. (1987). Flow through interstitium and other fibrous matrices. *Q. J. Exp. Physiol.* 72, 409–437. doi: 10.1113/expphysiol.1987.sp003085

Li, R., Serrano, J. C., Xing, H., Lee, T. A., Azizgolshani, H., Zaman, M., et al. (2018). Interstitial flow promotes macrophage polarization toward an M2 phenotype. *Mol. Biol. Cell* 29 1927–1940. doi: 10.1091/mbc.e18-03-0164

Li, X., Shepard, H. M., Cowell, J. A., Zhao, C., Osgood, R. J., Rosengren, S., et al. (2018). Parallel accumulation of tumor hyaluronan, collagen and other drivers of tumor progression. *Clin. Cancer Res.* 24:clincanres.3284.2017. doi: 10.1158/1078-0432.ccr-17-3284

Malandrino, A., Mak, M., Kamm, R. D., and Moeendarbary, E. (2018). Complex mechanics of the heterogeneous extracellular matrix in cancer. *Extreme Mech. Lett.* 21, 25–34. doi: 10.1016/j.eml.2018.02.003

Manneschi, C., Pereira, R., Marinaro, G., Bosca, A., Francardi, M., and Decuzzi, P. (2016). A microfluidic platform with permeable walls for the analysis of vascular and extravascular mass transport. *Microfluid Nanofluid* 20, 113. doi: 10.1007/s10404-016-1775-5

Moreno-Arotzena, O., Meier, J. G., Del Amo, C., and García-Aznar, J. M. (2015). Characterization of fibrin and collagen gels for engineering wound healing models. *Materials* 8, 1636–1651. doi: 10.3390/ma8041636

Mpekris, F., Angeli, S., Pirentis, A. P., and Stylianopoulos, T. (2015). Stress-mediated progression of solid tumors: effect of mechanical stress on tissue oxygenation, cancer cell proliferation, and drug delivery. *Biomech. Model Mech.* 14, 1391–1402. doi: 10.1007/s10237-015-0682-0

Mpekris, F., Papageorgis, P., Polydorou, C., Voutouri, C., Kalli, M., Pirentis, A. P., et al. (2017). Sonic-hedgehog pathway inhibition normalizes desmoplastic tumor microenvironment to improve chemo- and nanotherapy. *J. Control. Release* 261, 105–112. doi: 10.1016/j.jconrel.2017.06.022

Naba, A., Clauser, K. R., Ding, H., Whittaker, C. A., Carr, S. A., and Hynes, R. O. (2016). The extracellular matrix: tools and insights for the "omics" era. *Matrix Biol.* 49, 10–24. doi: 10.1016/j.matbio.2015.06.003

Nakai, Y., Isayama, H., Ijichi, H., Sasaki, T., Kogure, H., Yagioka, H., et al. (2012). Phase I trial of gemcitabine and candesartan combination therapy in normotensive patients with advanced pancreatic cancer: GECA1. *Cancer Sci.* 103, 1489–1492. doi: 10.1111/j.1349-7006.2012.02311.x

Narkhede, A. A., Crenshaw, J. H., Manning, R. M., and Rao, S. S. (2018). The influence of matrix stiffness on the behavior of brain metastatic breast cancer cells in a biomimetic hyaluronic acid hydrogel platform. *J. Biomed. Mater. Res. A* 106, 1832–1841. doi: 10.1002/jbm.a.36379

Netti, P. A., Baxter, L. T., Boucher, Y., Skalak, R., and Jain, R. K. (1997). Macro- and microscopic fluid transport in living tissues: application to solid tumors. *AIChE J.* 43, 818–834. doi: 10.1002/aic.690430327

Netti, P. A., Berk, D. A., Swartz, M. A., Grodzinsky, A. J., and Jain, R. K. (2000). Role of extracellular matrix assembly in interstitial transport in solid tumors. *Cancer Res.* 60, 2497–2503. Available online at: http://cancerres.aacrjournals.org/content/60/9/2497

Ng, C., and Swartz, M. A. (2003). Fibroblast alignment under interstitial fluid flow using a novel 3-D tissue culture model. *Am. J. Physiol.* 284, H1771–H1777. doi: 10.1152/ajpheart.01008.2002

Ng, C. P., Hinz, B., and Swartz, M. A. (2005). Interstitial fluid flow induces myofibroblast differentiation and collagen alignment *in vitro*. *J. Cell Sci.* 118, 4731–4739. doi: 10.1242/jcs.02605

Ng, C. P., and Pun, S. H. (2008). A perfusable 3D cell–matrix tissue culture chamber for *in situ* evaluation of nanoparticle vehicle penetration and transport. *Biotechnol. Bioeng.* 99, 1490–1501. doi: 10.1002/bit.21698

Nia, H. T., Liu, H., Seano, G., Datta, M., Jones, D., Rahbari, N., et al. (2016). Solid stress and elastic energy as measures of tumour mechanopathology. *Nat. Biomed. Eng.* 1:0004. doi: 10.1038/s41551-016-0004

Papageorgis, P., Polydorou, C., Mpekris, F., Voutouri, C., Agathokleous, E., Kapnissi-Christodoulou, C. P., et al. (2017). Tranilast-induced stress alleviation in solid tumors improves the efficacy of chemo- and nanotherapeutics in a size-independent manner. *Sci. Rep.* 7:46140. doi: 10.1038/srep46140

Pitarresi, J. R., Liu, X., Avendano, A., Thies, K. A., Sizemore, G. M., Hammer, A. M., et al. (2018). Disruption of stromal hedgehog signaling initiates RNF5-mediated proteasomal degradation of PTEN and accelerates pancreatic tumor growth. *Life Sci. Alliance* 1:e201800190. doi: 10.26508/lsa.201800190

Pluen, A., Boucher, Y., Ramanujan, S., McKee, T. D., Gohongi, T., di Tomaso, E., et al. (2001). Role of tumor–host interactions in interstitial diffusion of macromolecules: cranial vs. subcutaneous tumors. *Proc. Natl. Acad. Sci.* 98, 4628–4633. doi: 10.1073/pnas.081626898

Pluen, A., Netti, P. A., Jain, R. K., and Berk, D. A. (1999). Diffusion of macromolecules in agarose gels: comparison of linear and globular configurations. *Biophys. J.* 77, 542–552. doi: 10.1016/s0006-3495(99)76911-0

Polacheck, W. J., Charest, J. L., and Kamm, R. D. (2011). Interstitial flow influences direction of tumor cell migration through competing mechanisms. *Proc. Natl. Acad. Sci.* 108, 11115–11120. doi: 10.1073/pnas.1103581108

Polydorou, C., Mpekris, F., Papageorgis, P., Voutouri, C., and Stylianopoulos, T. (2014). Pirfenidone normalizes the tumor microenvironment to improve chemotherapy. *Oncotarget* 5, 24506–24517. doi: 10.18632/oncotarget.15534

Preston, B. N., Davies, M., and Ogston, A G. (1965). The composition and physicochemical properties of hyaluronic acids prepared from ox synovial fluid and from a case of mesothelioma. *Biochem. J.* 96, 449–474. doi: 10.1042/bj0960449

Provenzano, P. P., Cuevas, C., Chang, A. E., Goel, V. K., Von Hoff, D. D., and Hingorani, S. R. (2012). Enzymatic targeting of the stroma ablates physical barriers to treatment of pancreatic ductal adenocarcinoma. *Cancer Cell* 21, 418–429. doi: 10.1016/j.ccr.2012.01.007

Ramanujan, S., Pluen, A., McKee, T. D., Brown, E. B., Boucher, Y., and Jain, R. K. (2002). Diffusion and convection in collagen gels: implications for transport in the tumor interstitium. *Biophys. J.* 83, 1650–1660. doi: 10.1016/S0006-3495(02)73933-7

Reid, S. E., Kay, E. J., Neilson, L. J., Henze, A. T., Serneels, J., McGhee, E. J., et al. (2017). Tumor matrix stiffness promotes metastatic cancer cell interaction with the endothelium. *EMBO J.* 36, 2373–2389. doi: 10.15252/embj.201694912

Seo, B. R., DelNero, P., and Fischbach, C. (2014). *In vitro* models of tumor vessels and matrix: engineering approaches to investigate transport limitations and drug delivery in cancer. *Adv. Drug Delivery Rev.* 69, 205–216. doi: 10.1016/j.addr.2013.11.011

Shamir, E. R., and Ewald, A. J. (2014). Three-dimensional organotypic culture: experimental models of mammalian biology and disease. *Nat. Rev. Mol. Cell Biol.* 15, 647–664. doi: 10.1038/nrm3873

Stuart, K., and Panitch, A. (2008). Influence of chondroitin sulfate on collagen gel structure and mechanical properties at physiologically relevant levels. *Biopolymers* 89, 841–851. doi: 10.1002/bip.21024

Stylianopoulos, T., Martin, J. D., Chauhan, V. P., Jain, S. R., Diop-Frimpong, B., Bardeesy, N., et al. (2012). Causes, consequences, and remedies for growth-induced solid stress in murine and human tumors. *Proc. Natl. Acad. Sci. U.S.A.* 109, 15101–15108. doi: 10.1073/pnas.1213353109

Stylianopoulos, T., Munn, L. L., and Jain, R. K. (2018). Reengineering the physical microenvironment of tumors to improve drug delivery and efficacy: from mathematical modeling to bench to bedside. *Trends Cancer* 4, 292–319. doi: 10.1016/j.trecan.2018.02.005

Stylianopoulos, T., Poh, M. Z., Insin, N., Bawendi, M. G., Fukumura, D., Munn, L. L., et al. (2010). Diffusion of particles in the extracellular matrix: the effect of repulsive electrostatic interactions. *Biophys. J.* 99, 1342–1349. doi: 10.1016/j.bpj.2010.06.016

Sung, K. E., Su, G., Pehlke, C., Trier, S. M., Eliceiri, K. W., Keely, P. J., et al. (2009). Control of 3-dimensional collagen matrix polymerization for reproducible human mammary fibroblast cell culture in microfluidic devices. *Biomaterials* 30, 4833–4841. doi: 10.1016/j.biomaterials.2009.05.043

Swabb, E. A., Wei, J., and Gullino, P. M. (1974). Diffusion and convection in normal and neoplastic tissues. *Cancer Res.* 34, 2814–2822.

Swartz, M. A., and Fleury, M. E. (2007). Interstitial flow and its effects in soft tissues. *Biomed. Eng.* 9, 229–256. doi: 10.1146/annurev.bioeng.9.060906.151850

Swartz, M. A., Kaipainen, A., Netti, P. A., Brekken, C., Boucher, Y., Grodzinsky, A. J., et al. (1999). Mechanics of interstitial-lymphatic fluid transport: theoretical foundation and experimental validation. *J. Biomech.* 32, 1297–1307. doi: 10.1016/S0021-9290(99)00125-6

Szakács, G., Paterson, J. K., Ludwig, J. A., Booth-Genthe, C., and Gottesman, M. M. (2006). Targeting multidrug resistance in cancer. *Nat. Rev. Drug Discov.* 5, 219–234. doi: 10.1038/nrd1984

Theocharis, A. D., Skandalis, S. S., Gialeli, C., and Karamanos, N. K. (2016). Extracellular matrix structure. *Adv. Drug Delivery Rev.* 97, 4–27. doi: 10.1016/j.addr.2015.11.001

Timp, W., Mirsaidov, U., Matsudaira, P., and Timp, G. (2008). Jamming prokaryotic cell-to-cell communications in a model biofilm. *Lab. Chip* 9, 925–934. doi: 10.1039/b810157d

Tomasetti, L., and Breunig, M. (2018). Preventing obstructions of nanosized drug delivery systems by the extracellular matrix. *Adv. Healthc. Mater.* 7:1700739. doi: 10.1002/adhm.201700739

Tran, Q. D., Marcos, and Gonzalez-Rodriguez, D. (2018). Permeability and viscoelastic fracture of a model tumor under interstitial flow. *Soft Mater.* 14, 6386–6392. doi: 10.1039/c8sm00844b

Trimboli, A. J., Cantemir-Stone, C. Z., Li, F., Wallace, J. A., Merchant, A., Creasap, N., et al. (2009). Pten in stromal fibroblasts suppresses mammary epithelial tumours. *Nature* 461, 1084–1091. doi: 10.1038/nature08486

Venning, F. A., Wullkopf, L., and Erler, J. T. (2015). Targeting ECM disrupts cancer progression. *Front. Oncol.* 5:224. doi: 10.3389/fonc.2015.00224

Wang, X., Liu, Z., and Pang, Y. (2017). Concentration gradient generation methods based on microfluidic systems. *RSC Adv.* 7, 29966–29984. doi: 10.1039/c7ra04494a

Wiig, H., and Swartz, M. A. (2012). Interstitial fluid and lymph formation and transport: physiological regulation and roles in inflammation and cancer. *Physiol. Rev.* 92, 1005–1060. doi: 10.1152/physrev.00037.2011

Xiong, G.-F., and Xu, R. (2016). Function of cancer cell-derived extracellular matrix in tumor progression. *J. Cancer Metastasis Treat.* 2, 357–364. doi: 10.20517/2394-4722.2016.08

Yang, Y. L., Sun, C., Wilhelm, M. E., Fox, L. J., Zhu, J., and Kaufman, L. J. (2011). Influence of chondroitin sulfate and hyaluronic acid on structure, mechanical properties, and glioma invasion of collagen I gels. *Biomaterials* 32, 7932–7940. doi: 10.1016/j.biomaterials.2011.07.018

Zervantonakis, I., Chung, S., Sudo, R., Zhang, M., Charest, J., and Kamm, R. (2010). Concentration gradients in microfluidic 3D matrix cell culture systems. *Int. J. Micro Nano Scale Transplant.* 1, 27–36. doi: 10.1260/1759-3093.1.1.27

Zhang, B., Hu, Y., and Pang, Z. (2017). Modulating the tumor microenvironment to enhance tumor nanomedicine delivery. *Front. Pharmacol.* 8:952. doi: 10.3389/fphar.2017.00952

Conflict of Interest Statement: The authors declare that the research was conducted in the absence of any commercial or financial relationships that could be construed as a potential conflict of interest.

frontiers
in Bioengineering and Biotechnology

REVIEW
published: 19 December 2018
doi: 10.3389/fbioe.2018.00192

Magnetic Force-Based Microfluidic Techniques for Cellular and Tissue Bioengineering

Sena Yaman, Muge Anil-Inevi, Engin Ozcivici*† and H. Cumhur Tekin*†

Department of Bioengineering, Izmir Institute of Technology, Izmir, Turkey

Live cell manipulation is an important biotechnological tool for cellular and tissue level bioengineering applications due to its capacity for guiding cells for separation, isolation, concentration, and patterning. Magnetic force-based cell manipulation methods offer several advantages, such as low adverse effects on cell viability and low interference with the cellular environment. Furthermore, magnetic-based operations can be readily combined with microfluidic principles by precisely allowing control over the spatiotemporal distribution of physical and chemical factors for cell manipulation. In this review, we present recent applications of magnetic force-based cell manipulation in cellular and tissue bioengineering with an emphasis on applications with microfluidic components. Following an introduction of the theoretical background of magnetic manipulation, components of magnetic force-based cell manipulation systems are described. Thereafter, different applications, including separation of certain cell fractions, enrichment of rare cells, and guidance of cells into specific macro- or micro-arrangements to mimic natural cell organization and function, are explained. Finally, we discuss the current challenges and limitations of magnetic cell manipulation technologies in microfluidic devices with an outlook on future developments in the field.

Keywords: magnetic manipulations, microfluidics, rare cell separation, cell culture, tissue engineering

OPEN ACCESS

Edited by:
Qasem Ramadan,
*Agency for Science, Technology and Research (A*STAR), Singapore*

Reviewed by:
Pu Chen,
Stanford University, United States
Arnaud Scherberich,
Universitätsspital Basel, Switzerland

***Correspondence:**
Engin Ozcivici
enginozcivici@iyte.edu.tr
H. Cumhur Tekin
cumhurtekin@iyte.edu.tr

†These author have contributed equally to this work

Specialty section:
This article was submitted to Tissue Engineering and Regenerative Medicine, a section of the journal Frontiers in Bioengineering and Biotechnology

Received: *30 August 2018*
Accepted: *23 November 2018*
Published: *19 December 2018*

Citation:
Yaman S, Anil-Inevi M, Ozcivici E and Tekin HC (2018) Magnetic Force-Based Microfluidic Techniques for Cellular and Tissue Bioengineering. Front. Bioeng. Biotechnol. 6:192. doi: 10.3389/fbioe.2018.00192

INTRODUCTION

The manipulation of living cells by an external stimulus is an important tool for separation or detection of cells of interest and to guide cells in tissue engineering applications. Together with recent advances in engineering and technology, systems and designs varying in size, shape, complexity, and cost have been developed for various cell manipulation applications. These applications include blood cell separation (Ji et al., 2008), rare cell (e.g., circulating tumor cells) isolation in blood (Huang et al., 2013; Karabacak et al., 2014), detection of pathogens (Ho, 2014; Huang et al., 2017), cell counting for disease monitoring (e.g. CD4$^+$ T cell counting for HIV progression) (Cheng et al., 2007; Boyle et al., 2012), stem cell enrichment (Stephens et al., 1996; Muslimov et al., 2017) and organization of cells into designed spatial arrangements in two or three dimensional cultures (Ger et al., 2013; Tseng et al., 2014).

Most cell manipulation techniques are based on physical and/or affinity-based approaches. Physical manipulation techniques are driven by intrinsic cell properties (e.g., deformability, density, electrical capacitance, or resistance, size, magnetic susceptibility, mass, morphology) while affinity-based techniques use "labels" (e.g., particle-antibody conjugates specific to a membrane protein) to manipulate cells of interest. Operation principles include electrical (Fuhr et al., 1994; Voldman, 2006; CemaŽar et al., 2016), mechanical (Lo et al., 2000; Chronis and Lee, 2005; Kim et al., 2008b), affinity (Jin et al., 2009), acoustic (Coakley et al., 1989; Laurell et al., 2007; Lenshof et al., 2017), optical (Ashkin et al., 1987; Grier, 2003; Cheng et al., 2017), and magnetic (Pamme and Manz, 2004; Pamme, 2006; Zhao et al., 2016) forces or combined application of these factors (Wiklund et al., 2006).

The basic principle of magnetic force-based manipulation relies on a magnetic field strength, field gradient, and a magnetic susceptibility difference between the cell of interest and the surrounding environment (**Data Sheet 1** in the Supplementary Material). This strategy offers several advantages compared to its alternatives. First, the non-contact nature of the technique minimizes potential hazardous effects that could reduce cell viability/integrity (Morais et al., 2006). Second, the generation of a magnetic field does not depend on complex or expensive instrumentation as it can be created with an externally located, simple, low-cost rare earth magnet (Zeng et al., 2013; Durmus et al., 2015). Third, magnetic manipulation has low sensitivity to internal and external factors such as ionic strength, surface charges, pH and temperature (Nguyen, 2012).

Movement of cells under a magnetic field is usually referred to as magnetophoresis which can be performed in two ways. Cells are migrated to a region of high magnetic field strength (positive magnetophoresis) or escape from such a region (negative magnetophoresis). Since most cells are not inherently magnetic in nature, researchers generally exploit extrinsic magnetic properties for positive magnetophoresis by labeling cells with magnetic nanoparticles. In bio-separation applications, magnetic nanoparticles (MNPs) are commonly preferred as labels due to their unique magnetic properties, large surface to volume ratio, ability to selectively bind to target cell with the recognition ligands coupled onto their surface, and biocompatibility (Jiang et al., 2004; Gu et al., 2006; Issa et al., 2013). In terms of cell separation, magnetically-activated cell sorting (MACS) is a widely accepted technique in which MNPs decorated with cell membrane antigen-specific antibodies are used (Thiel et al., 1998). Although most sorting techniques rely on labeling cells with MNPs via cell surface antigens, it is also possible to contrast cells that contain different magnetic bead distributions based on their endocytotic capacity such as monocytes and macrophages (Robert et al., 2011). In addition, intrinsic magnetic properties of erythrocytes with iron-containing hemoglobin have been exploited in positive magnetophoresis for cell separation (Zborowski et al., 2003).

Positive magnetophoresis is a useful tool in the field of two and three dimensional (2D and 3D) cell culture and can be used to assemble cells into 3D cellular spheroids as building blocks (Mattix et al., 2014a; Parfenov et al., 2018), to pattern cells in culture for a suitable cellular microenvironment (Ino et al., 2009; Whatley et al., 2014), to guide cells into sheet-like structures for close cellular contact (Ito et al., 2004b; Ishii et al., 2014) and to enhance the seeding efficiency of cells into scaffolds in tissue engineering applications (Thevenot et al., 2008). However, since positive magnetophoresis heavily rely on the labeling of cells with magnetic particles, problems related to adequate and standard cellular internalization (Küstermann et al., 2008; Wildgruber et al., 2009), time consuming experimental steps (Chen et al., 2013; Calero et al., 2014) and possible biological interference of magnetic labels (Kostura et al., 2004; Peyman et al., 2009; Kedziorek et al., 2010) stand out as the most common limiting factors.

In recent years, a label-free magnetic manipulation alternative based on negative magnetophoresis has been developed to eliminate the adverse effects of cell labeling. In this method, cells are placed in a medium containing either a paramagnetic salt solution (Peyman et al., 2009) or a ferrofluid (Zhu et al., 2010). Since cells magnetize less than the medium, cells are focused in the lower magnetic field regions when placed under a magnetic field (Shen et al., 2012). Thereby, cells can be manipulated based on the arranged magnetic field pattern. This method was successfully used to trap bacteria (Wang et al., 2016b), to separate tumor cells (Zhao et al., 2017a,b), and to detect lipid-accumulating bone marrow cells (Sarigil et al., 2018) and cells with impaired function (e.g., sickle cells) (Knowlton et al., 2015). Moreover, there are successful applications of this technique to create ordered cellular structures such as the assembly of cells into linear arrangements (Krebs et al., 2009) or spheroids (Akiyama and Morishima, 2011a) and levitation of cell encapsulated polymers (Tasoglu et al., 2015b).

The motivation of this review is to address the fundamental principles, advantages, and challenges of recent studies applying labeled or label-free magnetic force-based techniques with state-of-the-art design or technology for cell and tissue manipulation. This review discusses the major applications of *in vitro* magnetophoresis from a cellular and tissue bioengineering perspective, namely, 1) rare cell separation, and 2) 2D and 3D cell culture.

REVIEW OF MAGNETIC MANIPULATION APPLICATIONS

The importance of efficient *in vitro* cell detection and sorting platforms has increased in parallel with the growing demand for the diagnosis of cancer and infectious diseases, enrichment of rare cells, and monitoring of environmental safety and public health (Mairhofer et al., 2009; Pratt et al., 2011; Chen et al., 2012; Foudeh et al., 2012). Consequently, a variety of magnetic cell sorting and detection methods and devices have been developed over the past few decades. Besides *in vitro* sorting and detection, the magnetic guidance of cells has been exploited in the organization of cells to mimic natural cell arrangements and functions. Magnetic cell manipulation methods are useful tools to form 3D cellular assemblies, to guide single cells or 3D building blocks into a desired pattern, to create cell sheets with tight cellular contacts and to enhance cell seeding efficiency into scaffolds. Lately, the combination of magnetism and microfluidic concepts, which is termed "magnetofluidics" (Lenshof and Laurell, 2010; Nguyen, 2012; Hejazian and Nguyen, 2016) has advanced rapidly due to several advantages: (1) an external magnetic force can be created with a simple, small-sized permanent magnet (Hejazian and

Nguyen, 2016), (2) micro- or nano-sized magnetic labels can be readily used for manipulating biological components inside microfluidic channels (Kwak et al., 2017), (3) magnetofluidics enables continuous-flow separation of cells (e.g., continuous separation of erythrocytes and leukocytes from the whole blood) (Pamme and Wilhelm, 2006) and (4) the magnetic field can pass through various components of microfluidic systems such as glass, metals, plastics, and liquids, which allows contactless manipulation of cells (Bhuvanendran Nair Gourikutty et al., 2016b). Considering the growing trend, the following part of the review focuses on the recent advancements and challenges in magnetofluidic detection, sorting and cell culture.

Rare Cell Screening: Isolation and Enrichment of Rare Cells

Rare cells are defined as those which are present at fewer than 1,000 cells in 1 mL of sample (Dharmasiri et al., 2010) such as clinically important stem cells (e.g., hematopoietic stem cells) and circulating tumor cells (CTCs) (Chen et al., 2014). CTC detection and isolation techniques have opened a new era in cancer prognosis and development of personalized chemotherapy or radiotherapy (Greene et al., 2012; Toss et al., 2014). CTC-derived organoid cultures have potential applications in disease modeling with a structure that more closely resembles natural organ systems compared to 2D cell cultures (Boj et al., 2015). Stem cells (SCs), on the other hand, are promising candidates for regenerative medicine. They are isolated and reinjected to promote natural repair mechanisms in the body (Sasaki et al., 2008). In fact, cell regeneration approaches for the treatment of several diseases and disorders such as cardiac, neurodegenerative, kidney, and lung diseases are under clinical investigation (Chen and Hou, 2016; Mathur et al., 2016; Kumar et al., 2017; Li et al., 2017). Given that tumor and stem cells have great therapeutic and regenerative potential, there is a crucial need for developing efficient detection and isolation methods for pure and transferable rare cell populations.

Most magnetic rare cell separation methods depend on targeting surface antigens on cells using antibody coupled-magnetic labels (**Figure 1** and **Table 1**). On the other hand, label-free techniques are beneficial in collecting cells without perturbing their functions. These techniques are also advantageous when the specific marker for the target cell is not fully known (Dharmasiri et al., 2010). Label-free manipulation is commonly achieved with one of two strategies: (1) direct sorting of target cells using the cells' intrinsic properties without labels (Durmus et al., 2015) and (2) indirect sorting of target cells by depleting unwanted cells in the surrounding medium (Iinuma

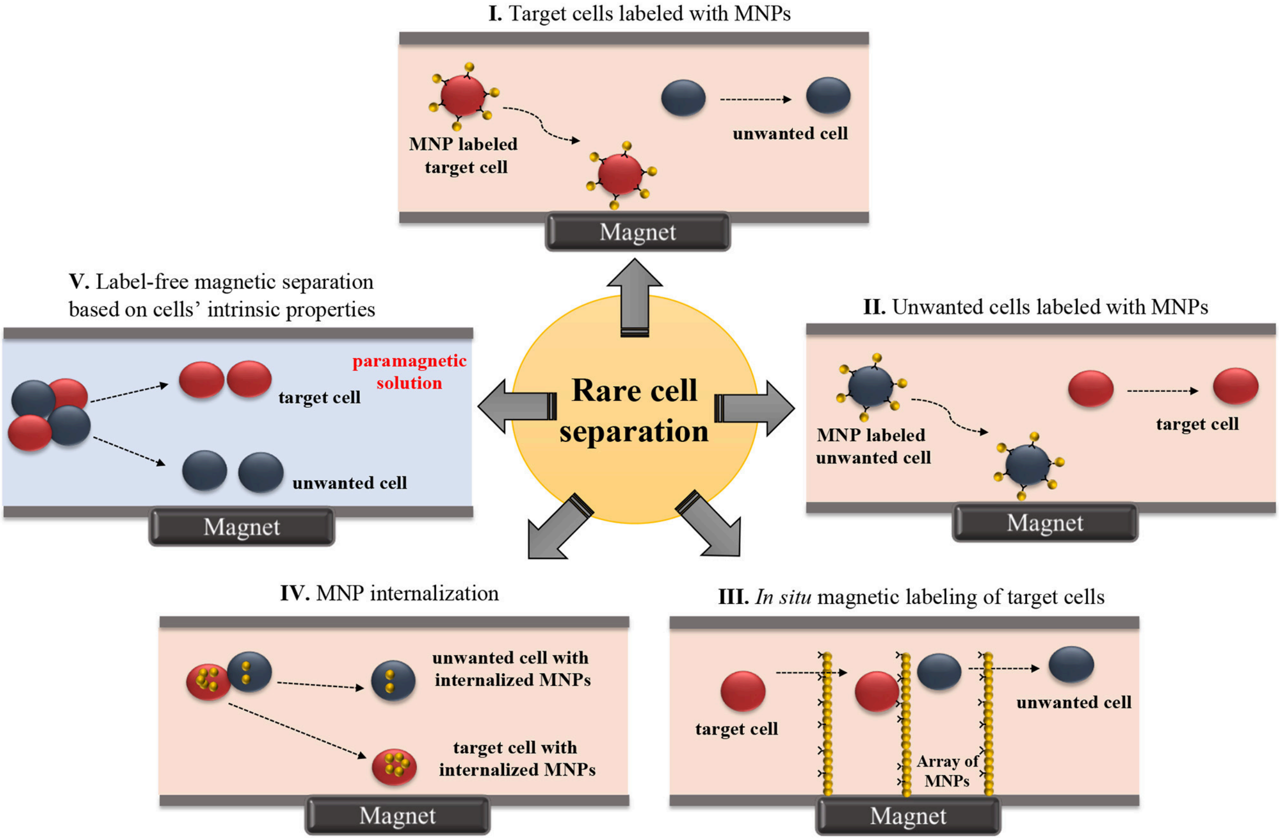

FIGURE 1 | Schematic illustration of microfluidic-based rare cell isolation methods. **(I)** Target cells labeled with MNPs, **(II)** Unwanted cells labeled with MNPs, **(III)** *In situ* magnetic labeling of target cells, **(IV)** MNP internalization, and **(V)** Label-free magnetic separation based on cells' intrinsic properties.

TABLE 1 | Microfluidic rare cell separation applications based on positive and negative magnetophoresis.

Cell type	Method	Surface marker	Magnetic element	Purity	Cell concentration	Capture rate	Throughput	Viability	References
STEM AND PROGENITOR CELLS									
Endothelial progenitor cells (EPCs)	PM -MNP internalization (positive enrichment)	NU	NdFeB permanent magnet	NR	NR	40%	0.3 mL h^{-1}	No difference between treated and untreated cells after 24 h in viability and tube formation function was reported	Kim et al., 2009
Hematopoietic stem cells (HSCs)	PM -MNP labeling (positive enrichment)	CD34	Permanent magnet	NR	5×10^7 cells mL^{-1}	88%	0.15 mL h^{-1}	NR	Wu et al., 2010
Hematopoietic stem cells (HSCs) and endothelial progenitor cells (EPCs)	PM -MNP labeling(positive enrichment)	CD133	Electromagnetic wire	NR	HSC: ~6750 cells mL^{-1} EPC: ~1190 cells mL^{-1}	HSC: > 96% EPC: > 95%	>14 mL h^{-1}	No adverse effect on cell viability	Plouffe et al., 2012
Mouse lung multipotent stem cells (MLSCs)	PM -MNP labeling (negative and positive enrichment)	CD45 (-) CD31 (-) FITC (+)	Magnet	96–99%	NR	NR	1.2 mL h^{-1}	Good self-renewal and proliferation capacity was obtained	Zeng et al., 2015
TUMOR CELLS									
Human colon adenocarcinoma cells (COLO205) and human breast cancer cells (SKBR3)	PM - MNP labeling (positive enrichment)	EpCAM	NdFeB permanent magnet	NR	5–1,000 cells mL^{-1} (TC: RBC= ~1: 10^7 - 10^9)	COLO205: 90% SKBR3: 86%	10 mL h^{-1}	NR	Hoshino et al., 2011
Mouse metastatic breast cancer cells (M6C)	PM - MNP labeling (positive enrichment)	EpCAM	NdFeB permanent magnet	<0.4% WBC capture	2–80 cells mL^{-1}	~90%	1.2 mL h^{-1}	> 90%	Kang et al., 2012
Breast cancer cells (MCF-7) and lung cancer cells (HCC827)	PM -MNP labeling (positive enrichment)	EpCAM	Permanent magnet	NR	~10 cells mL^{-1}	~80%	NR	NR	Yoo et al., 2016
Human breast cancer cells (MCF-7 and MDA-MB-23)	PM -MNP labeling (positive enrichment)	EpCAM	Permanent magnet	NR	10^3- 10^5 cells mL^{-1} (MCF-7: MDA-MB-231=1:1)	MCF-7: 95.7% MDA-MB-23: 79.3%	3 mL h^{-1}	NR	Kwak et al., 2017
Human acute monocytic leukemia cells (THP-1)	PM -MNP labeling (positive enrichment)	CD45	NdFeB permanent magnet	NR	10^6 cells mL^{-1}	NR	4.2 mL h^{-1}	NR	Huang et al., 2018
Human colon cancer cells (COLO205)	PM -MNP labeling (positive enrichment)	EpCAM	Permanent magnet + nickel micromagnets	NR	~60 cells mL^{-1}	Increased by 19% compared to no-micromagnet condition	2.5 mL h^{-1}	NR	Chen et al., 2015

(Continued)

TABLE 1 | Continued

Cell type	Method	Surface marker	Magnetic element	Purity	Cell concentration	Capture rate	Throughput	Viability	References
Breast cancer cells (SKBR-3)	PM -MNP labeling (positive enrichment)	EpCAM	NdFeB permanent magnet + ferromagnetic nickel-iron wires	97%	7×10^1-6×10^4 cells mL^{-1}	90%	2–5 mL h^{-1}	100% of the isolated cells were intact	Kim et al., 2013b
Breast cancer cells (MCF-7)	PM -MNP labeling (positive enrichment)	EpCAM	NdFeB permanent magnet + ferromagnetic nickel-cobalt wires	NR	$1.25-2.5\times 10^5$ cells mL^{-1}	93%	2.4–6 mL h^{-1}	NR	Park et al., 2015
Breast cancer cells (MCF-7)	PM -MNP labeling (positive enrichment)	EpCAM	NdFeB permanent magnet + ferromagnetic nickel-iron wires	6.9–67.9%	1–10 cells mL^{-1}	99.08%	4 mL h^{-1}	NR	Cho et al., 2016
Human lung cancer cells (A549)	PM -MUNP labeling (positive enrichment)	EpCAM	Permanent magnet + silicon wires	NR	5×10^3 cells mL^{-1}	~90%	~1 mL h^{-1}	Re-collected cells showed almost the same morphology compared to control cells	Wang et al., 2015
(i) Lung cancer cells (H-1650) (ii) Lung cancer cells (HCC827 and H-1650), breast cancer cells (MCF-7), human prostate cancer cells (LNCaP and PC-3) and human bladder cancer cells (T24) (EpCAM epxression levels: ~2000/cell to ~500,000/cell)	PM -MNP labeling (positive enrichment)	EpCAM	NdFeB permanent magnet + nickel-iron coated magnetic sifter	NR	(i) 4–470 cells mL^{-1} (ii) 50-100 cells mL^{-1} (>90% for >100 k EpCAM/cell)	H-1650: 95.7% HCC827, H-1650, MCF-7, LNCaP: 90% PC-3: 48%, T24: 17.7%	10 mL h^{-1}	Unchanged cell viability was obtained	Earhart et al., 2014
Human ovarian cancer cells (HeLa)	PM -MNP labeling (positive enrichment)	EpCAM	Nickel-iron -based microstripline	NR	10^6 cells mL^{-1}	79%	0.06 mL h^{-1}	100% cell viability was obtained with cooling	Wong et al., 2016
B lymphoid cells (Raji cell line) (target) T lymphoid cells (Jurkat cell line) (non-target)	PM *-in situ* magnetic labeling (positive enrichment)	CD19	Cooled electromagnet coil + microcontact printed ferrofluidic dots	96%	2×10^6 cells mL^{-1} (Raji cells to total=33%)	94%	3.6×10^4 – 3.6×10^5 total cells h^{-1}	Viable cells with ability to move and divide were reported	Saliba et al., 2010

(Continued)

TABLE 1 | Continued

Cell type	Method	Surface marker	Magnetic element	Purity	Cell concentration	Capture rate	Throughput	Viability	References
Human lung cancer cells (A549)	PM - *in situ* magnetic labeling (positive enrichment)	WGA modification	Magnetic solenoid coil + nickel micropillars	~93%	1.5×10^5 cells mL^{-1}	62–74%	NR	NR	Liu et al., 2007
Human T-lymphocytic leukemic cells (JM) and human ovarian cancer cell (HeLa)	PM -MNP labeling (positive enrichment)	CD4	NdFeB permanent magnet	>90%	$\sim 2 \times 10^6$ mL^{-1}	NR	$\sim 3.6 \times 10^5$ cells h^{-1}	NR	Mizuno et al., 2013
Breast cancer cells (MCF-7)	PM -MNP labeling (positive enrichment)	EpCAM	NdFeB permanent magnets +	NR	10^3–3.3×10^4 cells mL^{-1}	up to 88%	~0.1 mL h^{-1}	NR	Kirby et al., 2015
Lung carcinoma cells (H1299-GFP)	PM -MNP labeling (negative enrichment)	CD45	Permanent magnet	~50%	10^1-10^5 cells mL^{-1}	~90%	60 mL h^{-1}	>90%	Jiang et al., 2017
Human ovarian cancer cells (HeLa)	PM -MNP internalization (positive enrichment)	NU	NdFeB permanent magnet	NR	5×10^5 cells mL^{-1}	NR	NR	NR	Pamme and Wilhelm, 2006
Breast cancer cells (MDA-MB-231)	PM -magnetic susceptibility difference (negative enrichment)	NU	Permanent magnet +ferromagnetic nickel wire	NR	NR	94.8%	0.0025–0.0200 mL h^{-1}	NR	Han et al., 2006
Breast cancer cells (SKBR3, MDA-MB-231) Prostate cancer cells (PC3-9)	PM -MNP labeling (positive enrichment)	EpCAM	Quadrupole magnetic circuit	>3.5-log purification resulted in 1,500 WBCs mL^{-1}	200–1,000 cells mL^{-1}	SKBR3: 98.6 ± 4.3% MDA-MB-231: 77.8 ± 7.8% PC3-9: 89.7 ± 4.5%	8 mL h^{-1} (3.6×10^{10} cells h^{-1})	Viable cells were obtained	Ozkumur et al., 2013
Human breast cancer cells (MCF10A and MCF10A-LBX1)	PM -MNP labeling (negative enrichment)	CD45 CD15		2.5-log purification resulted in 32,000 WBCs mL^{-1}		MCF10A: 96.7 ± 1.9% MCF10A: 97.0 ± 1.7%			
Human melanoma cells (WM164), breast cancer cells (MB231, SKBR3), human lung cancer cells (PC9) and prostate cancer cells (PC3-9)	PM -MNP labeling (negative enrichment)	CD66b CD45	Permanent magnet	3.8-log purification	$\sim 10^3$ cells mL^{-1}	97%	8 mL h^{-1} (3.6×10^{10} cells h^{-1})	NR	Karabacak et al., 2014

(Continued)

TABLE 1 | Continued

Cell type	Method	Surface marker	Magnetic element	Purity	Cell concentration	Capture rate	Throughput	Viability	References
Human melanoma cells (SkMel28), lung cancer cells (H1650, H1975, H3122), prostate cancer cells (NCAP, PC3, PC3-9, VCAP) and breast cancer cells (MB231, MCF-7, SkBR)	PM -MNP labeling (negative enrichment)	CD66b CD45 CD16	Magnetic circuit	Purification resulted in 445 WBC mL^{-1}	19–5,000 cells mL^{-1}	99.5%	5.4–7.2 × 10^{10} cells h^{-1}	NR	Fachin et al., 2017
Human colon cancer cells (HCT8)	PM -MNP labeling (negative enrichment)	CD45	Permanent magnet	Purification resulted in 83.99± 1.00% WBC depletion	10^4 cells mL^{-1}	70 ± 5% (for single round of depletion)	NR	Unchanged cell viability when a pulsation frequency of 0.05 Hz was used	Luo et al., 2015
Colorectal adenocarcinoma cells (HT29)	PM -MNP labeling (negative enrichment)	CD45	Magnet + layer of NdFeB magnetic grains	NR	50- 250 cells mL^{-1}	87–96%	5 mL h^{-1}	NR	Chung et al., 2013
Oncogenic human monocyte cells (U937)	NM	NU	NdFeB permanent magnet + nickel microstructure	>90%	8 × 10^7 cells mL^{-1} (U937: RBC=1:400)	NR	10^5 cells h^{-1}	NR	Shen et al., 2012
Breast cancer cells (MDA-MB-231), colorectal cancer cells (HCT116 and HT29), lung cancer cells (HCC827) and esophageal cancer cells (JHEsoAD1)	NM	NU	NdFeB permanent magnet	NR	NR	NR	No flow	Unchanged cell viability for long term cultivation in paramagnetic medium was reported	Durmus et al., 2015
Breast cancer cells (MDAMB-231), lung cancer cells (A549), ovarian cancer cells (HEYA8) and prostate cancer cells (PC-3)	NM	NU	NdFeB permanent magnet	NR	NR	NR	0.36 mL h^{-1}	NR	Amin et al., 2017

PM, positive magnetophoresis; NM, negative magnetophoresis.
NR, not reported; NU, not used.
Capture rate, the ratio of the number of cells collected after separation to the total number of cells loaded to the chip.
Purity, the ratio of the number of target cells collected after separation to the total number of collected cells.

et al., 2000; Lara et al., 2004; Bhuvanendran Nair Gourikutty et al., 2016a). Recently, microfluidic systems employing labeled or label-free sorting of rare cells have progressed to offer higher levels of control, purity, rapidness, and portability required for research and clinical applications (**Table 1**).

Stem Cells

Innovative designs using microfluidic principles for separation of SCs have been mostly tested with immunomagnetic labels. Kim et al. designed a microfluidic system to model a blood vessel, aiming to solve losses in injected number of SCs for therapeutic *in vivo* applications (Kim et al., 2009). Localization of endothelial progenitor cells (EPCs) to a specific site within a polydimethylsiloxane (PDMS)-based microfluidic channel was simulated. The method included the incorporation of *Magnetospirillum* sp. AMB-1-based magnetic nanoparticles (10 μg MNP /10^4 cells) into EPCs. About 40% of magnetically-tagged EPCs flowing in the channel adhered to the microfluidic channel wall under an external magnetic field. Most of the EPCs maintained their viability and tube formation function. Later, Wu et al. developed a microfluidic platform consisting of isolation, counting, and sorting modules on a single chip for isolation of hematopoietic stem cells (HSCs) from cord blood (Wu et al., 2010). Plouffe et al. also studied the isolation of HSCs and EPCs from whole blood in a PDMS-based chip containing an electromagnetic wire array (Plouffe et al., 2012) (**Figure 2**). First, HSCs and EPCs were pre-labeled and isolated using anti-CD133 functionalized MNPs from whole blood. For further identification of isolated HSCs and EPCs, cells were labeled with antibodies against CD34, CD45 and kinase insert domain receptor (KDR). A magnetic field was created by two wires on the top and bottom of the microfluidic separation chamber. Under the magnetic field, labeled HSCs (CD133+/CD34+/CD45+/KDR-) and EPCs (CD133+/CD34+/CD45-/KDR+) were deflected from the two lateral sample streams to a central buffer stream according to the magnetic properties of individual cells. Separation efficiency was determined as >96%. Another immunomagnetic microfluidic sorting was performed for the isolation of mouse lung multipotent stem cells (MLSCs) (Zeng et al., 2015). First, magnetically-labeled cells (i.e., CD45+ and CD31+) were directed into the isolation zone of the microfluidic platform (IsoFlux^{TM}) using an external magnet, whereas unlabeled cells flowed through the unlabeled cell zone. Second, the unlabeled cells were collected and labeled with FITC-coupled Sca-1 (Stem cell antigen-1) antibody. Then, using anti-FITC magnetic beads, MLSCs (CD45-, CD31-, and Sca-1+) were collected at the isolation zone. The efficiency was determined as 96–99% by FITC signal and isolated MLSCs retained their capacity for self-renewal and differentiation.

Circulating Tumor Cells

Positive magnetophoresis based on labeling cells with MNPs have been applied frequently in the last decade for CTC sorting. Hoshino et al. developed a PDMS-based microchip using anti-EpCAM antibody-functionalized MNP (Veridex Ferrofluid^{TM}) to separate COLO205 and SKBR3 cancer cells spiked in the blood (Hoshino et al., 2011). The chip captured MNP-conjugated cancer cells by an array of three permanent magnets with alternating polarities. Average capture rates were 90% and 86% for COLO205 and SKBR3 cells, respectively. Kang et al. also used anti EpCAM-functionalized magnetic beads (2.8 μm) to separate EpCAM + breast cancer cells (BCCs) from blood in a microfluidic chip (Kang et al., 2012). The design consisted of

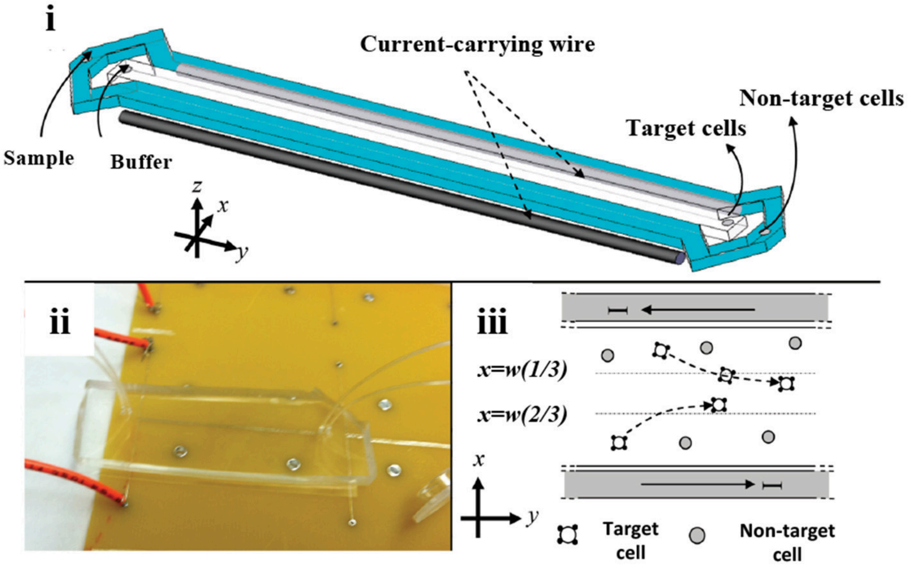

FIGURE 2 | Microfluidic stem cell separation device. Magnetophoretic HSC and EPC separation based on anti-CD133-conjugated magnetic labeling. **(i)** Illustration and **(ii)** photograph of the device. **(iii)** Magnetic field created by electromagnetic wires deflects magnetically-labeled stem cells into a center collection stream. Reprinted with permission from Plouffe et al. (2012). Copyright (2012) American Chemical Society.

an inlet, the main channel and double collection channels before the outlet. The inlet channel contained a micropillar array (50 × 50 µm) that filter the sample fluid from cell and bead clusters to prevent clogging. Main and double collection channels were lined by rows of dead-end collection side chambers. Magnetically-labeled BCCs were pulled from the flow through the collection side chambers while white blood cells (WBCs) moved through the channel with the sample flow under an external magnetic field. The BCCs were separated with high efficiency (87%), specificity (<0.4% WBC capture) of WBC captured, and viability (>90%). Later, Yoo et al. used anti-EpCAM magnetic particles in a system containing separation and collection wells for vertical magnetic isolation of spiked CTCs (MCF-7 and HCC827) in plasma-depleted blood (Yoo et al., 2016). Recently, Kwak et al. used anti-EpCAM MNPs to isolate human BCCs with different EpCAM expression levels [i.e., MCF-7 (EpCAM +) and MDA-MB-231 (EpCAM -)] in the microchannels with five serpentine-trapping segments (Kwak et al., 2017). Trapping segments with 30 rectangular subsegments were perpendicular to the flow. A magnetic field gradient was created perpendicular to the flow at the end of the trapping segments. CTCs flowing in the chip were collected at different segments depending on the extent of their magnetic label. For instance, high EPCAM-expressing MCF-7 bore higher anti-EpCAM magnetic particles and they were attracted by the magnetic force and collected mostly at the segments located most distantly from the magnet. The chip separated CTCs with an average yield of 97.5% and 79.3% for EpCAM+ and EpCAM- CTCs, respectively. Recently, anti-CD45-based immunomagnetic labels were used in a microfluidic device containing an attached microwell layer between a microchannel and a permanent magnet to collect individual THP-1 cells in the microwells (Huang et al., 2018).

Modulating a magnetic field using microscale magnetic elements is important in various applications (Lee et al., 2001, 2004; Kimura et al., 2004), including cell sorting. An example of these devices was a 2D micromagnet array for CTCs (Chen et al., 2015). In the device, patterned thin-film micromagnets were used together with an external magnet to enhance the effect of the external magnetic field locally and create discontinuous capture sites for CTCs. The array was tested with magnetically-tagged human colon cancer cells (COLO205) spiked in blood samples. Throughout the assay, blood cells moved with the flow in the microfluidic chamber while anti-EpCAM magnetic label-CTC complexes were captured alongside the array. The results revealed that pattern integration increased the average capture rate and distribution uniformity by 19% and 14%, respectively, compared to the device without micromagnets. Another approach was developed including the use of inlaid ferromagnetic wires and an external permanent magnet in a microseparator device (Kim et al., 2013b). Anti-EpCAM labeled CTCs (SKBR-3) were separated from blood cells, and directed to a separate outlet in the device (**Figure 3A**). Spiked CTCs were isolated with a purity of 97% and a yield of 90%. The device was also tested for the peripheral blood of breast and lung cancer patients. Based on a principle similar to Kim et al., Park et al. used ferromagnetic Ni-Co nanowires in a microdevice for MCF-7 cells. Under an external magnetic field, anti-EpCAM MNP-labeled MCF-7 cells were collected from whole blood with a purity of 93% (Park et al., 2015). Cho et al. also used ferromagnetic wires together with two permanent magnets for separation of anti-EpCAM magnetic bead-conjugated MCF-7 cells from red blood cell (RBC) -lysed whole blood (CTC-µChip) (Cho et al., 2016). The average recovery rate was 99.08%, and the purity of CTCs was in the range of 6.9–67.9% depending on the spiked CTC concentration. Another design included a magnetic sifter-based microstructure having arrays of 40 × 40 µm pores in a honey comb format to separate cancer cells (Earhart et al., 2014). MNP-anti-EpCAM-labeled H-1650 lung tumor cells spiked in whole blood were pushed with a fluid flow toward the patterned pores of the sifter. Magnetically-labeled cancer cells were captured on the magnetized sifter while other cells passed through the pores. The device separated tumor cells with a 91.4% efficiency. Later, the device was tested for cells (HCC827, H-1650, MCF-7, LNCaP, PC-3, T24) spiked in whole blood with varying EpCAM expression levels (∼2000/cell to ∼500,000/cell). For the cells with high EpCAM expression levels (HCC827, H-1650, MCF-7, LNCaP), the yield of the separation was as high as 90%; however, low EpCAM expressing PC-3 and T24 cells were captured with efficiencies of 48% and 17.7%, respectively. The device was also tested for enumeration of CTCs in the blood of non-small cell lung cancer patients as preliminary attempts. Microstrip lines, which are typically current conducting elements fixed on the device substrate, can produce a high magnetic field gradient in a tunable manner instead of simple off-chip permanent magnets. It was shown that deflection of magnetically-tagged (COMPEL^{TM} 8 µm) human ovarian cancer (HeLa) cells by microstrip lines could achieve a separation with an efficiency of 79% (Wong et al., 2016). Lately, magnetic upconversion nanoparticles (MUNPs) have received much attention as novel probes for sensitive detection of biomolecules due to lack of autofluorescence. Wang et al. integrated anti-EPCAM-conjugated MUNPs in a microfluidic device with silicon-nanowire-arrays and an external magnet to capture a small number of cancer cells in spiked blood samples and also in clinical samples from lung cancer patients (Wang et al., 2015).

In addition to the batch-wise mixing of magnetic beads with cells, creating magnetic self-assembly bead arrays in a microfluidic chip using monoclonal antibody (mAb)-functionalized magnetic beads was reported for sorting of cancer cells (Ephesia) (Saliba et al., 2010) (**Figure 3B**). In the chip, beads were organized onto a microcontact printed ferrofluid dot pattern under a magnetic field. On the pattern, the dipole-dipole interaction between the beads created 3D-array of magnetic beads oriented in the direction of the field. The chip with the array of magnetic beads bearing anti CD-19 mAb was tested for a mixture of CD19- Jurkat and CD19+ Raji cells. Raji cells were captured by the array of beads with a yield of 94% while Jurkat cells moved with the flow. Another microfluidic device without off-chip labeling was developed to isolate A549 cancer cells from RBCs (Liu et al., 2007). First, superparamagnetic particles (260 nm) were trapped at the zone of a hexagonal array of Ni micropillars generating a strong magnetic field gradient under a controlled external magnetic field. Then, magnetic particles

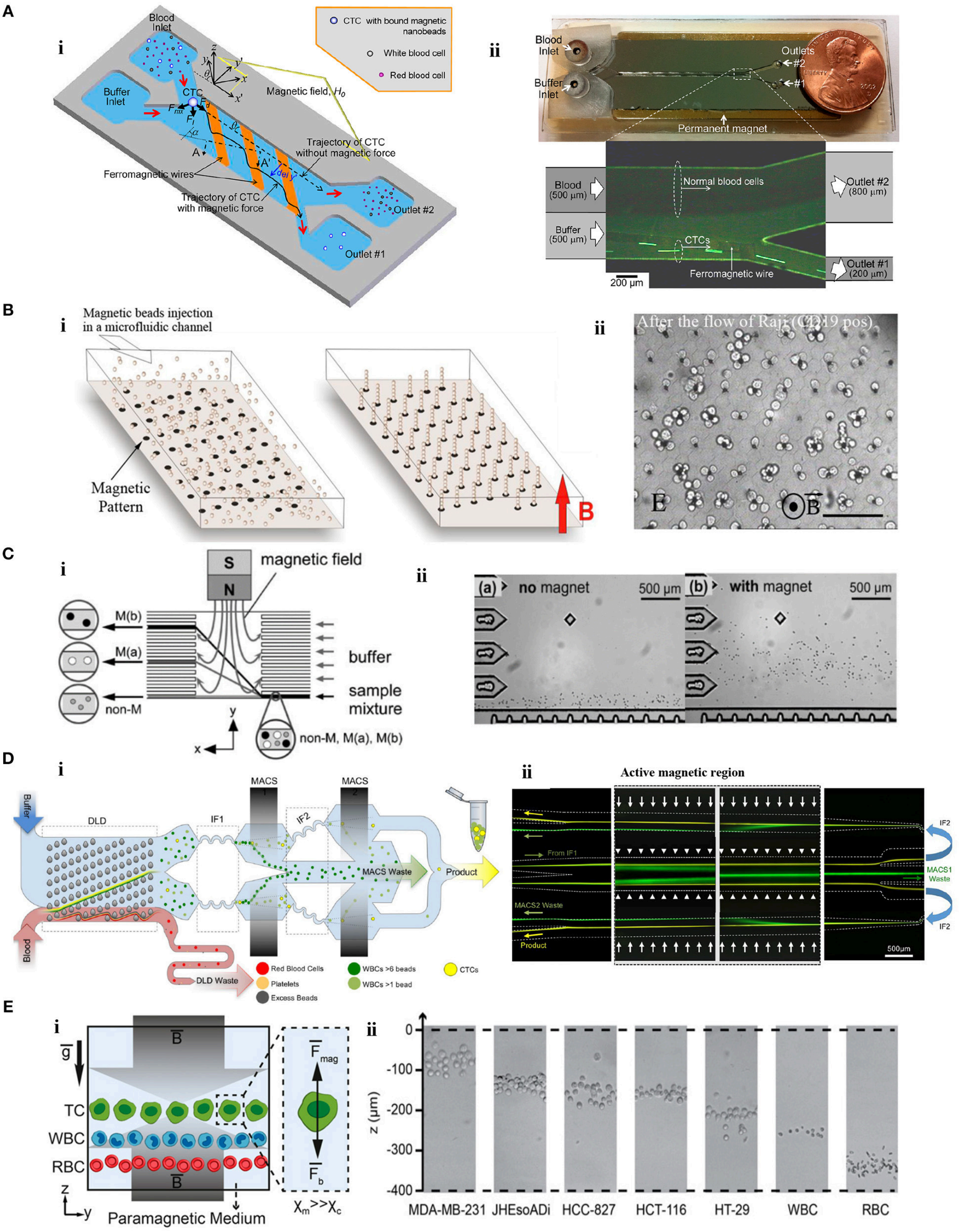

FIGURE 3 | Microfluidic tumor cell separation devices. **(A)** Separation of magnetically-labeled target cells. **(i)** Design and **(ii)** optical micrograph of the positive tumor cell (SKBR-3) enrichment device using anti-EpCAM-coupled magnetic nanoparticles. Reprinted with permission from Kim et al. (2013b). Copyright (2013) American

(Continued)

FIGURE 3 | Chemical Society. **(B)** *In situ* magnetic labeling of tumor cells (Ephesia). **(i)** The magnetic beads are located on ferrofluid dots in the microfluidic channel to create a self-assembled magnetic bead array under the applied magnetic field. **(ii)** Cells are captured on the magnetic bead array during the sample flow. Reprinted from Saliba et al. (2010). **(C)** Separation of tumor cells (HeLa) based on MNP uptake extent. **(i)** The schematic illustration of the device. **(ii)** HeLa cells are deflected from the laminar flow according to their magnetic load. Reprinted with permission from Pamme and Wilhelm (2006). Copyright (2006) The Royal Society of Chemistry. **(D)** Separation of cancer cells by depleting other cells. **(i)** A monolithic microfluidic chip for negative enrichment of tumor cells through the depletion of magnetically-labeled WBCs. In the deterministic lateral displacement (DLD) part, RBCs, platelets, and free beads are eliminated. Following the inertial focusing 1 (IF1), magnetophoresis (MACS1) is applied to deplete magnetic labeled WBCs having more than ∼6 beads. Another set of inertial focusing (IF2) and magnetophoresis (MACS2) is applied to deplete WBCs that contain at least one magnetic bead. **(ii)** Image of cell streaks captured using fluorescence microscopy on different areas of the chip. Green and yellow colors represent WBCs and CTCs, respectively. Reprinted from Fachin et al. (2017). **(E)** Tumor cell separation using cells' intrinsic properties in a paramagnetic solution. **(i)** The design of the label-free magnetophoresis platform (MagLev). **(ii)** Alignment of tumor cells at different heights (*z-axis*) in the device. Reprinted from Durmus et al. (2015).

were functionalized *in situ* with corresponding antibodies, and A549 cancer cells were trapped and enriched by 133-fold (A549 to RBC ratio= 1:10).

Integrated microfluidic systems combining forces of differing natures have also been tested for CTCs. Mizuno et al. developed a 2D sorting device combining hydrodynamic filtration for size-based sorting and magnetophoresis for surface marker-based (CD4+) sorting of cancer cells (Mizuno et al., 2013). Kirby et al. merged magnetophoretic and centrifugal forces on a disposable PDMS cartridge as a lab-on-a-disc format for the separation of EpCAM+ MCF-7 cancer cells from blood (Kirby et al., 2015). Magnetically-tagged MCF-7 cells and blood were placed into the disc and rotated at a rate of 17 Hz. Under centrifugal and magnetic forces, 80% of tagged cancer cells were routed to a capture chamber. Lately, Jiang et al. combined deterministic lateral displacement (DLD) and immunomagnetic separation in a microfluidic device (Jiang et al., 2017). The CTCs (H1299-GFP) spiked in blood samples were captured with an efficiency and purity of ∼90 and 50%, respectively. The device was also tested with the blood of cancer patients and revealed promising results for potential clinical applications.

Besides manipulation depending on surface marker expression, magnetic particle uptake extent was utilized to distinguish cancer cells using a microfluidic chip (Pamme and Wilhelm, 2006) (**Figure 3C**). The chip contained a separation chamber in which a laminar flow was provided perpendicular to the direction of the magnetic field. Magnetic nanoparticle-loaded [i.e., maghemite nanoparticles (γFe_2O_3)] HeLa cells that differ in their uptake capacity were deflected under an external magnetic field (∼400 mT) from the laminar flow toward the different levels of the separation chamber according to their magnetic moment and size.

Another application of positive magnetophoresis is the enrichment of CTCs through depletion of unwanted cells by either labeling them (e.g., WBCs) with magnetic particles or using their intrinsic properties (e.g., RBC). An example of the latter was as a hybrid microsystem which included a paramagnetic capture module (PCM) and micro-electrical impedance spectroscopy (μ-EIS) (Han et al., 2006). The microsystem was tested for three BCCs (MCF-7, MDA-MB-231, and MDA-MB-435). In PCM (200 mT), deoxyhemoglobin RBCs with inherent paramagnetic properties were attracted by a ferromagnetic wire and depleted from the solution. Then in μ-EIS module, the impedance analysis of cancer cells was performed at the single cell level. Results revealed that 94.8% of the BCCs were separated and characterized in a continuous manner. Enrichment of tumor cells based on depletion of magnetically-labeled CD45+ lymphocytes was tested in an integrated device with micropumps and mixers (Luo et al., 2015). CD45- cancer cells (HCT8) were recovered with a 70% efficiency for a single round of enrichment. Similarly, in a magnetic/size-sorting device, a layer of magnetic grains depleted magnetically-labeled CD45+ leukocytes and a size-sorter captured and collected individual cancer cells (HT29) at predefined locations (Chung et al., 2013). In a device offering both positive and negative enrichment modes (Ozkumur et al., 2013; Karabacak et al., 2014), leukocytes labeled with magnetic beads were depleted from a blood sample in the negative enrichment mode (^{neg}CTC-iChip). The ^{neg}CTC-iChip platform consisted of two serial modules. In the first module, nucleated cells (WBCs and tumor cells) were separated from RBCs, platelets, and unbound beads by their sizes using DLD. In the second module, cells were lined-up by inertial focusing for better manipulation. Then, permanent magnets in a quadrupole orientation depleted WBCs. The chip isolated cancer cells with a 97% efficiency (Karabacak et al., 2014). Afterwards, the CTC-iChip was improved for better throughput and purity (Fachin et al., 2017) (**Figure 3D**). In this case, WBCs were depleted using two stages of magnetophoresis. In the first magnetic region (200 T/m), WBCs labeled with more than ∼6 beads were depleted from the sample. Following a second set of inertial focusing, WBCs containing at least 1 magnetic bead were depleted in the second region (425 T/m).

In contrast to approaches with labels, negative magnetophoresis exploiting intrinsic physical biomarkers of cells, and therefore independent of magnetic tags or labels, is a simple and affordable technique. U937 cells were separated from RBCs by tuning resolution capacity of magnetophoresis in gadolinium (Gd) diethylenetriamine penta-acetic acid (DTPA)-based paramagnetic solutions (0–80 mM) (Shen et al., 2012). Under an external magnetic field applied perpendicular to the direction of flow and a Ni microstructure, cells were deflected laterally due to the magnetic repulsion force. The most efficient separation was achieved at 40 mM Gd–DTPA with a >90% purity. Gd-based paramagnetic solutions (0–100 mM) was tested for density-based, label-free, and real-time imaging of cells in a non-flow magnetic levitation platform as well (MagDense) (Durmus et al., 2015) (**Figure 3E**). Tumor and blood cells were levitated in a capillary between two opposing magnets (1.45 T).

The characteristic levitation height depended on the intrinsic signatures of the cells: magnetic susceptibility and density. All types of tumor cells (i.e., HT29, HCT116, HCC827, JHesoAD1, and MDA-MB-231) spiked in Gd-based medium were levitated at distinguishably higher positions than blood cells. In addition, heterogeneity among seemingly homogeneous tumor cells populations was demonstrated at the single cell level. Recently, this density-based magnetic focusing has been applied in a platform made of a 3D-printed smartphone module and built-in camera for real time monitoring and spatial separation of cancer and blood cells (Amin et al., 2017; Knowlton et al., 2017).

2D and 3D Cell Culture

To meet functional requirements, organs arrange one or more cell types in specific forms (Rivron et al., 2009). Manipulation of cells in 2D and 3D cell culture that aims biomimicry is therefore crucial to reflect appropriate form and function. Thus, development of techniques to organize cells in targeted arrangements in convenient microenvironments is one of the most important trends in cell culture technologies. Magnetic cell manipulation techniques have been used for various purposes in 2D and 3D cell culture (**Figure 4**) such as; to form 3D cellular assembly (**Table 2**) as building blocks (Mattix et al., 2014a), to organize cells or spheroids into a targeted pattern (Ino et al., 2009; Whatley et al., 2014), to create cell sheets for a tight and close cellular contact (Ishii et al., 2014) and to increase cell seeding efficiency into scaffolds (Thevenot et al., 2008). Here, we reviewed recent advances in magnetic-based 2D and 3D cell culturing techniques that were either used in microfluidic devices or represent potency for future microfluidic applications.

3D Cellular Assembly

3D cellular spheroid culture is a valuable tool to mimic the tissue-specific properties of cells (Lin and Chang, 2008). Magnetic force-based guidance of cells into spheroids offers a unique way to form 3D arrangements in a non-contact mode. Cells can be aggregated into spheroids using positive magnetophoresis by assembly of cells at a certain location on the surface of a culture chamber above permanent magnets with a multi-step seeding process (**Figure 5A**) where cluster shape is determined by cell type used (Ghosh et al., 2016). Positive magnetophoresis can also assemble cells at the air–medium interface (**Figure 5B**) (Souza et al., 2010; Jaganathan et al., 2014) with magnetic levitation. Souza et al. reported this levitation-based 3D cell culture method using a bioinorganic hydrogel comprised of filamentous bacteriophage, MNPs and gold nanoparticles (Souza et al., 2010). Hydrogel-treated cells were levitated to the air–medium interface with a permanent magnet and manipulated for the formation of different 3D geometries and cellular compositions by spatial variations in the magnetic field. A second-generation, bacteriophage-free hydrogel was also described to enable the magnetization of cells without the use of any toxic or infectious agents (Souza, 2013) and commercialized under the trade name NANOSHUTTLE^{TM} (NS) and the Bio-Assembler^{TM} kit that contains the NS solution and a magnetic drive.

There are several examples that use magnetic cell guidance to form tissue-specific constructs. Daquinag et al. developed a 3D tissue culture system based on cell levitation via MNP-labeling to model white adipose tissue development (Daquinag et al., 2012). 3T3-L1 preadipocytes remained viable in levitated spheroids for extended periods, while 2D cultured cells died after reaching confluence. Adipogenic-induced adipospheres

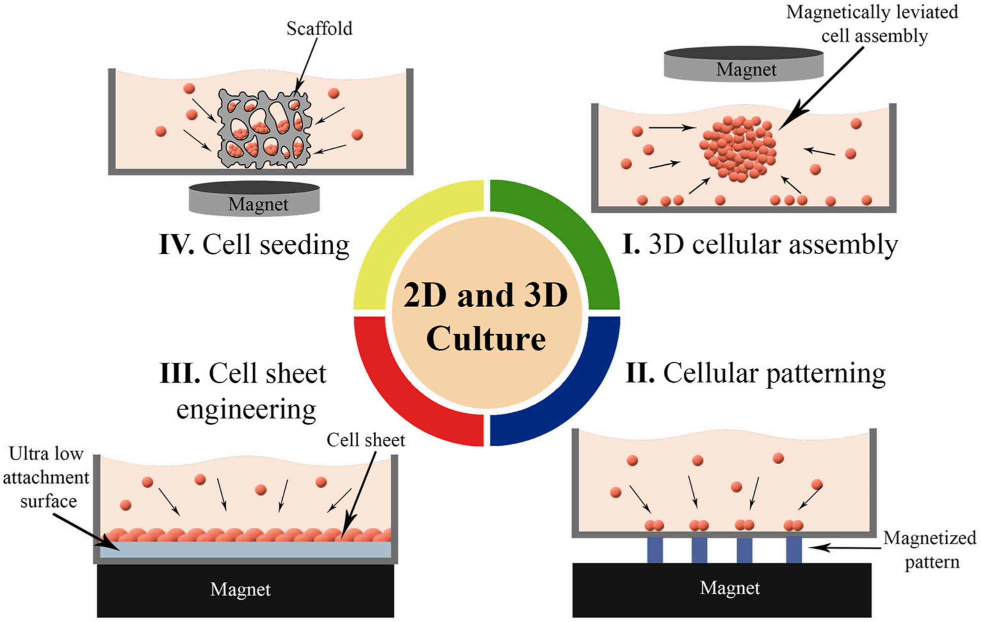

FIGURE 4 | Magnetic force-based 2D and 3D cell culture techniques. **(I)** Formation of 3D cellular assembly as building blocks, **(II)** Organizing cells or spheroids into a targeted pattern, **(III)** Guiding cells into sheet-like structures for a close cellular contact, and **(IV)** Enhancing the seeding efficiency of the cells into scaffolds.

TABLE 2 | Summary of 3D cellular assembly applications.

Manipulation strategy	Cell type	Biofabrication output	Microfluidic	References
PM (labeling cells via internalization using bovine serum albumin coated MNP)	Human prostate cancer epithelial (PC-3) cells and human lung fibroblast (HFL-1) cells	Multilayer sheet structures for epithelial cells, tightly packed spheroids for fibroblasts after 24 h of manipulation.	-	Ghosh et al., 2016
PM (labeling cells via a hydrogel consisting of gold, iron oxide MNP and filamentous bacteriophage)	Normal human astrocytes and human glioblastoma (LN-229 or U-251MG)	Spheroids with ~ 930 µm diameter after 10.5 days of levitation	-	Souza et al., 2010
PM (labeling cells via NANOSHUTTLE^{TM})	Preadipocyte cells (3T3-L1) and endothelial cells (bEND.3)	Adiposphere-based coculture with a vascular-like network assembly and lipogenesis in perivascular cells.	-	Daquinag et al., 2012
PM (labeling cells via NANOSHUTTLE^{TM})	Primary human epithelial cells, smooth muscle cells, pulmonary fibroblasts, and pulmonary endothelial cells	3D bronchiole coculture consisting of four cell types together in a layered assembly after 7 days of levitation culture	-	Tseng et al., 2013
PM (labeling cells via NANOSHUTTLE^{TM})	Primary porcine valvular interstitial cells and endothelial cells	3D layered co-culture model of the aortic valve with ~ 2800 µm diameter after 3 days of levitation	-	Tseng et al., 2014
PM (labeling cells via NANOSHUTTLE^{TM})	Breast cancer cells (SUM159, MDA-MB-231) and fibroblasts (293T, Hs578bst, human pulmonary fibroblasts and patient derived tumor associated fibroblasts)	Large-sized (millimeter in diameter) co-culture model of breast tumor within 24 h	-	Jaganathan et al., 2014
PM (labeling cells via MNP)	Bone marrow-derived human MSCs	Random mixed, core-shell, and fused spheroids composed of cells stained with two different dyes with 100–200 µm in diameter	-	Kim et al., 2013a
PM (labeling cells via NANOSHUTTLE^{TM})	Rat vascular smooth muscle cells (A10) and primary human aortic smooth muscle cells	Contractile rings with ~ 3 mm in outer diameter	-	Tseng et al., 2016
PM (labeling cells via magnetite cationic liposomes)	Mouse myoblast cells (C2C12)	Cell sheets with 0.63 cm^2 area after 24 h, cell strings with ~150 µm in longitudinal direction after 24 h, cell rings with 12 mm in diameter after 48 h	-	Yamamoto et al., 2009, 2010
PM (labeling cells via magnetite cationic liposomes)	Primary neonatal rat cardiomyocytes	Cardiac tissue rings with ~250 µm thickness after 7-day cultivation	-	Akiyama et al., 2010
PM (labeling 3D cellular spheroids via incorporation of magnetoferritin nanoparticles into spheroids)	Primary rat aortic smooth muscle cells	Tissue rings formed by fusion of spheroids over 4 days (~ 13 mm in diameter)	-	Mattix et al., 2014a
PM (labeling 3D cellular spheroids via incorporation of MNP into ECM of spheroids)	Primary rat aortic smooth muscle cells	Tissue rings (from 2 mm up to 10 mm) and custom patterns (square and Clemson University Tiger Paw) formed by fusion of magnetic labeled spheroids over 4 days	-	Mattix et al., 2014b
PM (labeling cells via deposition of poly(allylamine)-stabilized MNP on cell membranes)	Primary human skin fibroblasts (HSF) and human lung carcinoma epithelial cells (A549)	Layered planar tissue constructs (~100 µm thick, round, and 3 mm in diameter) after 24 h incubation of surface-engineered magnetic cells	-	Dzamukova et al., 2015
PM (forming magnetic 3D cellular structures via adhesion of cells to magnetic iron oxide-encapsulated nano/microparticle substrates)	Human epidermoid tumor KB cells	Tumor cell spheroids with an increase in volume during 10-day culture period	-	Lee et al., 2011
PM (forming magnetic 3D cellular structures via adhesion of cells to magnetic collagen hydrogel beads)	Mouse fibroblast cells (NIH-3T3) and human hepatocellular carcinoma cells (Hep G2)	Magnetically manipulable cells adhered on the collagen beads	-	Sugaya et al., 2012
PM (labeling biotinylated cells via streptavidin paramagnetic particles)	Human embryonic kidney cells (HEK293) and human breast cancer cells (MCF-7)	Magnetically orientable cells and spheroids in hanging drop culture to target and immobilize spheroids for a facilitated media change and therapeutic screening, covering different cells onto preformed spheroids	-	Ho et al., 2013

(Continued)

TABLE 2 | Continued

Manipulation strategy	**Cell type**	**Biofabrication output**	**Microfluidic**	**References**
NM (suspension of cells in paramagnetic solution containing gadolinium diethylenetriaminepentaacetic acid)	Bovine carotid artery cells (HH)	Egg-shaped cellular structure with 510 μm diameter and 690 μm height in 20 min	-	Akiyama and Morishima, 2011a
NM (suspension of cells in paramagnetic solution containing gadoteric acid)	Bovine carotid artery cells (HH)	Spheroids with ~400 μm in diameter after one day of culture (25 spheroids in each batch)	-	Akiyama and Morishima, 2011b
NM (suspension of cells in paramagnetic solution containing gadoteric acid)	Mouse myoblast cells (C2C12)	Spheroids with ~250 μm diameter within 1 min	+	Akiyama and Morishima, 2012
NM (suspension of cells in paramagnetic solution containing gadolinium diethylenetriaminepentaacetic acid)	Whole blood cells	Rectangular bar, three-pointed star shaped cellular structures and spheroids of varying sizes (600–1,000 μm)	-	Abdel Fattah et al., 2016
NM (suspension of cells in paramagnetic solution containing Gadavist®)	Murine fibroblasts (NIH 3T3)	Cellular clusters (100–260 μm) formed by magnetic levitation after 48 h, merged preformed-spheroids after 4 days and assembly of cells compartmentalized in the water-in-oil droplets after 24 h	+	Tocchio et al., 2017
NM (suspension of spheroids in paramagnetic solution containing Omniscan™)	Primary sheep chondrocytes	Fused chondrospheres	-	Parfenov et al., 2018
NM (suspension of cells in paramagnetic solution containing Gadavist®)	Bone marrow stem cells (D1 ORL UVA) and breast cancer cells (MDA-MB-231)	Cellular blocks up to ~2.7 cm in length (with ~280 μm thickness) formed by magnetic levitation after 48 h and biphasic cellular structures in a single device	+	Anil-Inevi et al., 2018
NM (suspension of cells in paramagnetic solution containing Gadavist®)	Mouse fibroblast cells (NIH 3T3) and non-small-cell lung cancer cells (HCC827)	Cell spheroids and cell strings with increase in cell number during 168-h culture	+	Türker et al., 2018
PM (forming magnetic 3D cellular structures via encapsulation of cell within paramagnetic hydrogel)	Mouse fibroblast cells (NIH 3T3)	Magnetically controllable cell-encapsulating hydrogels with manufacturability in different sizes (150 μm in thickness and 200–1,000 μm in side dimension)	-	Tasoglu et al., 2013
NM (suspension of cells in paramagnetic solution containing gadolinium diethylenetriaminepentaacetic acid)	Mouse fibroblast cells (NIH 3T3)	Assembled building blocks; cell encapsulating hydrogels (2 mm round with 150 μm thickness) and cell seeded microbeads	-	Tasoglu et al., 2015b
PM (manipulation of cell encapsulating hydrogels via motion of the magnetic microrobots)	Human umbilical vein endothelial cells (HUVECs), mouse fibroblast cells (NIH 3T3), cardiomyocyte	2D and 3D heterogeneous assembly of cell encapsulating hydrogels.	-	Tasoglu et al., 2014

PM, positive magnetophoresis; NM, negative magnetophoresis; MNP, magnetic nanoparticles; NANOSHUTTLE™, assembly of iron oxide and gold nanoparticles cross-linked with poly-l-lysine.
–, The shortest dimension of the cell culture chamber > 1 mm.
+, The shortest dimension of the cell culture chamber ≤ 1 mm.

composed of 3T3-L1 cells successfully mimicked *in vivo* white adipocytes by formation of large lipid droplets unlike 2D cultured ones. Magnetic levitation with MNPs was also used to assemble a 3D co-culture structure of the bronchiole with sequential layers of epithelial cells, smooth muscle cells, pulmonary fibroblasts, and pulmonary endothelial cells in a similar organization to native tissue (Tseng et al., 2013). The resulting co-culture maintained the phenotype and induced extracellular matrix (ECM) formation in contrast to 2D culture. Same levitation-based co-culture model was also successfully utilized in creating sequentially assembled 3D structures of aortic valve cells; valvular interstitial and endothelial cells (Tseng et al., 2014). The resulting 3D model maintained cell phenotype and function, and synthesized relevant ECM molecules. Additionally, a novel *in vitro* model mimicking heterogeneous breast tumors was developed by 3D cellular assembly of BCCs and fibroblasts by magnetic levitation, which can control tumor composition for microenvironment in an effort to test anti-cancer drugs (Jaganathan et al., 2014). A magnetic pin-array system was also developed to assemble MNP-incorporated cells into 3D spheroids (Kim et al., 2013a). In this system, an iron pin and magnet were combined to generate a concentrated and strong magnetic field at a specific point and thus to reinforce cell-cell contact in 3D spheroids (**Figure 5C**). The method provided accurate control over spheroid size and had versatile applications as it was able to create random mixed, core-shell, and fused. In addition to 3D spheroids, another group of studies reported guiding magnetically-labeled cells were guided into ring-shaped structures at the macro level. In these studies, ring-shaped muscle tissues were created either by a system that allowed the cells to accumulate around a cylindrical plug by a magnet under the culture plate (**Figure 5D**) (Yamamoto et al., 2009, 2010; Akiyama et al., 2010) or by using a ring-shaped magnet (**Figure 5E**) (Tseng et al., 2016).

Applications that require magnetic functionalization of cells by internalization of MNPs through endocytosis, cause concerns regarding potential cytotoxicicity of MNPs (Tomitaka et al., 2011). Several strategies have been suggested to reduce potential toxicity of magnetic functionalization. It was showed that compared to iron oxide MNPs, magnetoferritin as a biological MNP provided magnetic functionality provided with higher cell viability (Mattix et al., 2014a). In another study, Mattix et al. also presented a Janus structure of magnetic cellular spheroids with two distinct domains: cells and MNPs in the extracellular region (Mattix et al., 2014b). To assemble this structure, iron oxide MNPs, collagen and cell suspension were combined and magnetic cellular spheroids were formed by a hanging drop method. Study revealed that cellular internalization of MNPs in Janus magnetic spheroids is notably lower (35%) than uptake spheroids (83%), and that the Janus method contributed to better maintenance of spheroid viability ($\geq$82%) in long-term cultivation. Janus magnetic spheroids were also successfully manipulated by an external magnetic field to assemble and fuse into a vascular tissue construct. Another approach to avoid the cytotoxicity of MNP internalization is cell surface engineering with MNPs. Dzamukova et al. described a cell surface engineering method based on the deposition of poly(allylamine)-stabilized MNPs on cell membranes without penetration to the cytoplasm (Dzamukova et al., 2015). The method did not affect membrane integrity or fundamental cellular functions (i.e., adhesion, proliferation, apoptosis) in either cancer or healthy cells and was used to generate layered cell sheets and 3D multicellular spheroids. It is also possible to manipulate label-free cells on a magnetic support. Lee et al. reported a magnetic cell levitation technique using iron-oxide encapsulated polymeric micro/nanoparticles as a substrate for 3D culture of tumor cells (Lee et al., 2011). Sugaya et al. described a manipulation method of cells and cellular spheroids via cell-size collagen hydrogel microbeads (Sugaya et al., 2012). Following the preparation of magnetic collagen hydrogel beads ($> 20\,\mu$m) using microfluidic water-in-oil droplets, cells were attached to the collagen bead surfaces and cell-bead complexes were manipulated with a magnetic field.

Cells can be manipulated with a completely label-free principle based on negative magnetophoresis (**Figures 5F–I**) leading to a powerful alternative to eliminate acute and long-term cytotoxicity concerns due to cell binding or uptake of magnetic particles. Firstly, 3D cellular aggregates were formed by negative magnetophoresis using a paramagnetic medium (Akiyama and Morishima, 2011a). The experimental setup consisted of a culture chamber on four cubic NdFeB magnets (side dimension of 10 mm), placed with opposite poles next to each other. For cellular assembly, cells were suspended in a Gd-DTPA containing culture medium (34.6 mM) to enhance the diamagnetic property of the cells and poured into the chamber. Cells were aggregated into an egg-shaped structure in the center of the magnets, the area of lowest magnetic flux density, in 20 min. They also demonstrated another device for spheroid array formation that was able to form larger numbers of spheroids using the same principle (Akiyama and Morishima, 2011b). In this system, a cell culture chamber was set on a magnet array composed of 6 × 6 NdFeB magnets (3 × 3 × 10 mm), corresponding to 25 array spots with low magnetic flux densities at equal distance from each other. Furthermore, this magnetic cell manipulation principle was combined with microfluidic technology to generate rapid and high throughput systems for spheroid formation (Akiyama and Morishima, 2012). This microfluidic chip was composed of a cell aggregation chamber (8 mm in wide and 0.5 mm in deep) on a similar magnet array with 2 × 3 aggregation spots and a syringe pump for medium perfusion after aggregation. Cells assembled into spheroids within 1 min in the chip and most of the cells were alive in spheroids after 12 h of culture with medium perfusion. It is also possible to control the shape and size of cellular assemblies with the negative magnetophoresis principle. Abdel Fattah et al. placed two magnets, facing the same poles, on both sides of the cell culture chamber to form a rectangular bar-shaped cellular assembly and used also an arrangement of three magnets with 120° pole angles placed next to each other to form a three-pointed star-shaped cellular assembly (Abdel Fattah et al., 2016). Besides organizing cells into these different shapes, a strategy was developed that could control the size of spheroids generated by placing magnets under the cell culture chamber. This strategy involved the formation of larger spheroids by increasing the distance between the cell culture chamber and the magnet under the chamber, and consequently lowering the magnetic field strength (Abdel Fattah et al., 2016).

Negative magnetophoresis is also a convenient technology for assembly of cells by a complete levitation of cells. Firstly, a system, composed of two permanent NdFeB magnets with the same poles facing each other and a container filled with a solution of paramagnetic ions between these magnets, was described for levitation of non-living materials (Mirica et al., 2009, 2010, 2011). Durmus et al. used a miniaturized magnetic levitation system, consisting of a glass capillary (with 1 mm inner diameter) between two NdFeB magnets to load cells in a paramagnetic medium, and two 45° tilted mirrors added to the sides to observe cells in real time, as a cell densitometry platform (Durmus et al., 2015; Tasoglu et al., 2015a). Following the study showing that the magnetic levitation system was suitable for the levitation of living cells, several studies aiming at manipulation of 3D living building

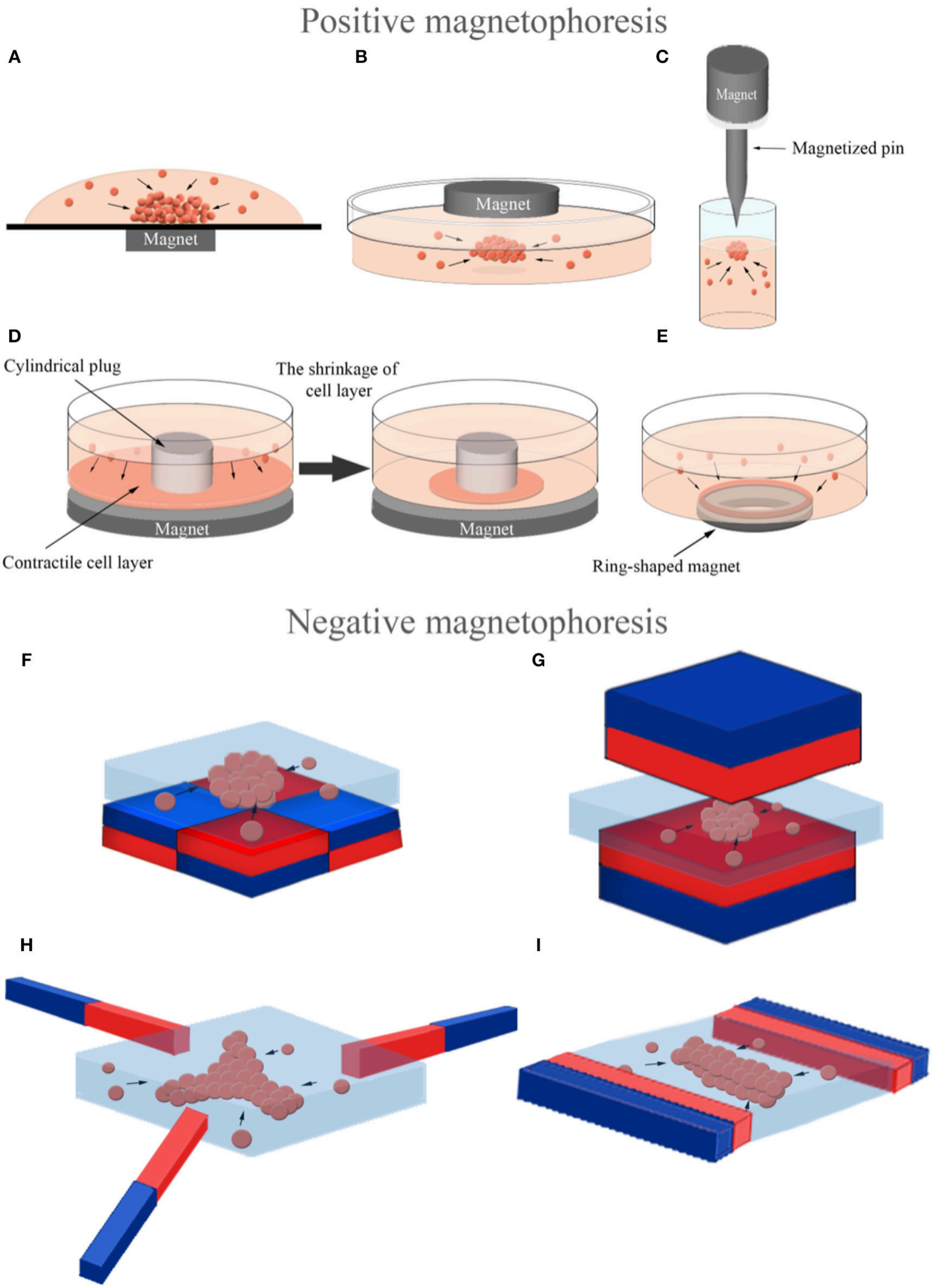

FIGURE 5 | Magnetic force-based manipulation of magnetically labeled cells (positive magnetophoresis) and label-free diamagnetic cells (negative magnetophoresis). 3D assembly of magnetically labeled cells into a spheroid by a magnet **(A)** under the culture chamber, **(B)** on the top of the culture chamber and **(C)** by a magnetized pin beneath the magnet to concentrate the magnetic field for attracting cells in a focused direction. 3D assembly of magnetically labeled cells into a ring-shaped structure **(D)** using a cylindrical plug and a magnet under it to accumulate contractile cells around the plug and **(E)** using a ring-shaped magnet. 3D assembly of label-free diamagnetic cells into **(F,G)** spheroid, **(H)** three-pointed star and **(I)** rectangular bar in a magnetic liquid with different configurations of magnets to produce a spatially varying field along the culture chamber (The north poles: red, the south poles: blue).

blocks were conducted using this strategy. Cellular clusters of varying sizes were formed by changing the number of cells loaded into the capillaries within this system and fabricated tissue strings with patterning spheroids, already assembled with ultra-low attachment microplates (**Figure 6A**) (Tocchio et al., 2017). They also described a droplet-based magnetic levitation assembly design to form a larger number of 3D cellular structures. In this design, cells were compartmentalized in water-in-oil droplets generated by alternate aspiration of mineral oil and cell suspension, in the magnetic levitation device and assembled into individual 3D architecture within 24 h. This cellular assembly process resulted in faster cellular aggregation and enhanced shape uniformity of biological structures. As an alternative, Parfenov et al. designed a new installation consisting of 2 ring-shape NdFeB magnets (external diameter: 85 mm, internal diameter: 20 mm, thickness: 24 mm), oriented to each other with the same poles, a glass container (12 × 12 × 50 mm), inserted into the hole of the magnets and a camera system for label-free magnetic levitation of tissue spheroids (Parfenov et al., 2018). Besides the manipulation and fusion of the pre-formed 3D living structures, the manipulation of individual cells and formation of *in situ* 3D aggregates with controllable structures were also achieved in a magnetic levitation system (Anil-Inevi et al., 2018). In this study, the label-free magnetic levitation protocol was optimized by performing levitation of cells with several commercially available chelate forms and concentrations of gadolinium. A macrocyclic ligand containing the non-ionic form of gadolinium (gadobutrol) provided higher cell viability and higher levitation height. The optimal concentration (100 mM) of gadobutrol determined by considering the same evaluation criteria was found to be suitable for maintaining the viability of bone marrow stem cells cultured with magnetic levitation for 5 days. Furthermore, this protocol was shown to be convenient for the formation of larger cellular blocks up to ∼2.7 cm in length, and for biofabrication and culture of various biphasic cellular structures consisting of bone marrow stem cells and breast cancer cells in a single magnetic levitation device (**Figure 6B**). It was also reported that fibroblast cells and lung cancer cells formed 3D structures and were cultured for 7 days using the magnetic levitation principle (Türker et al., 2018).

As cells can be manipulated without using MNPs, cells that form living structures with a desired shape and size in/on a support material can also be manipulated by magnetic forces. Tasoglu et al. first fabricated microscale photo-crosslinkable paramagnetic hydrogels with different sizes, assembled hydrogels in a controllable manner by manually moving the magnets above the liquid surface in a fluidic chamber and stabilized the resulting assembled gels by a secondary crosslinking step (Tasoglu et al., 2013). After all of the hydrogel fabrication and assembly stages, cell viability was still above 82%. In another

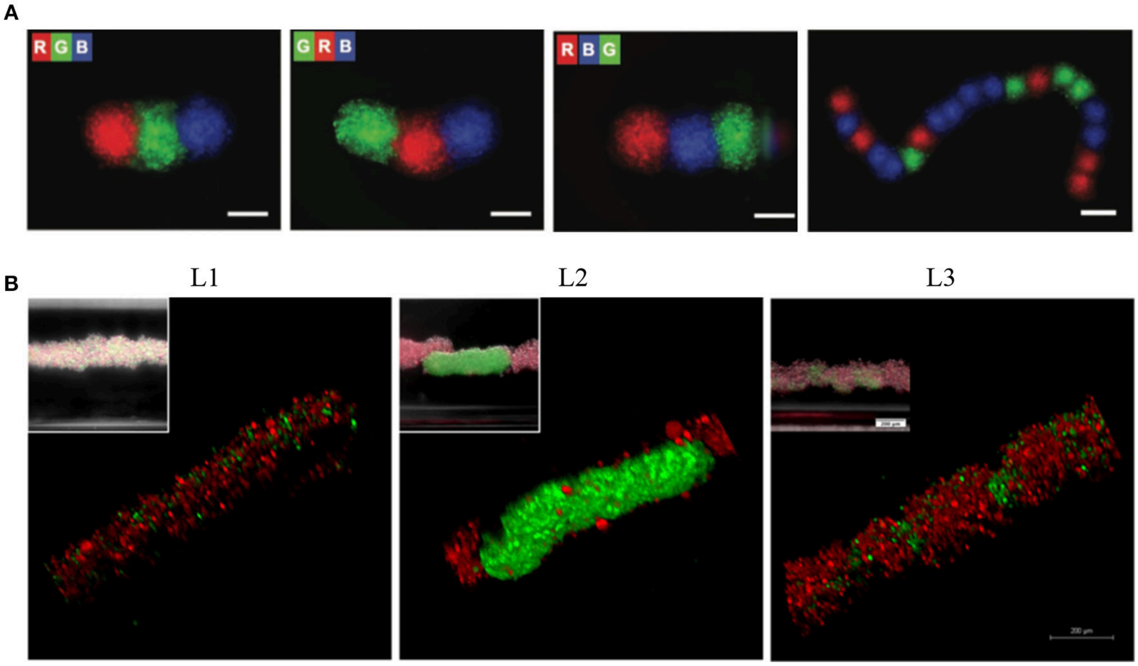

FIGURE 6 | Levitation of diamagnetic cells with negative magnetophoresis; patterning of pre-formed spheroids into the tissue strings and *in situ* 3D cellular assembly. **(A)** Serial coding of spatially controlled spheroids. Spheroids were formed separately and then inserted into the levitation device (spheroids; R, red; G, green; B, blue) Scale bars, 100 µm. Reprinted from Tocchio et al. (2017). Copyright (2017) John Wiley & Sons, Inc. **(B)** Cellular assembly of D1 ORL UVA^{eGFP} and MDA-MB-231^{dsRed} cells under microgravity. Confocal and conventional fluorescence microscopy (upper left) images showing self-assembled coculture clusters formed with magnetic levitation (100 mM Gd-BT-DO3A) and different cell loading strategies; L1: simultaneously loading of MDA-MB-231^{dsRed} and D1 ORL UVA^{eGFP} cells, L2: MDA-MB-231^{dsRed} cells onto D1 ORL UVA^{eGFP} clusters formed with magnetic levitation and L3: D1 ORL UVA^{eGFP} cells onto MDA-MB-231^{dsRed} clusters formed with magnetic levitation (total 50,000 cells/culture chamber). Scale bars: 200 µm. Reprinted from Anil-Inevi et al. (2018).

study, microgels composed of photo-crosslinkable polymers (methacrylated gelatin or polyethylene glycol dimethacrylate) and laminin-coated microbeads were levitated in a paramagnetic medium within a magnetic setup composed of a reservoir between two permanent magnets with the same poles facing each other (Tasoglu et al., 2015b). Then, cell encapsulating hydrogels and cell seeded microbeads were used as building blocks for magnetic assembly within the device. They also described a method using an untethered magnetic micro-robot remotely controlled by magnetic fields for 2D and 3D manipulation of cell-encapsulating hydrogels (Tasoglu et al., 2014). In the system, motion of the magnetic microrobots ($750 \times 750 \times 225\,\mu$m), polyurethane-encapsulated NdFeB particles, was guided by an electromagnet system surrounding the workspace and used to manipulate cellular building units.

2D and 3D Cellular Patterning

Patterning is an important tool to mimic natural homotypic or heterotypic cellular arrangements for cell biology and tissue engineering applications (Guillotin and Guillemot, 2011). Precise spatiotemporal control and guidance of individual cells via micromanipulation techniques have great potential to provide convenient cellular microenvironments and accurately imitate *in vivo* chemical and physical cues (El-Ali et al., 2006). It is possible to pattern both adherent and suspension cells in the culture. Patterning of adherent cells is conventionally performed via material surface modification with cell-adhesion ligands to guide cells toward adhesive areas (Veiseh et al., 2007). For the patterning of suspension cells, tools that generate an external force such as a strongly focused beam of light (Grier, 2003), an electric field (Matsue et al., 1997) or a magnetic field (Ino et al., 2007) are used. Among all these techniques, the patterning of cells with magnetic force provides minimized interference with the biochemical functions of cells (Lai et al., 2010). Firstly, cells labeled with magnetite cationic liposomes (MCLs) were manipulated to form curved, parallel, or crossing patterns through a setup, composed of steel plates (L: 30 mm; H: 2 mm; T: 200 μm) on a magnet (Ino et al., 2007). They also patterned HUVECs on Matrigel to form cord-like structures. Using a similar technology, line patterning of HUVECs was formed on monolayer cells, skin tissues and different types of cell sheets (Akiyama et al., 2009). Furthermore, they achieved incorporation of patterned HUVECs into layered myoblast sheets. To generate these 3D constructs, magnetic accumulation of myoblasts into cell sheets and magnetic patterning of HUVECs on each sheet layer were alternated. Fujita et al. demonstrated that the magnetic cell pattern could be used to produce scaffold-free contractile skeletal muscle (Fujita et al., 2010). In the study, magnetite-incorporated myogenic cells were patterned linearly on a monolayer of fibroblast cells, using a magnetic field concentrator. The tendon structure was modeled by two collagen films that were fixed on a culture dish. Alignment of myotubes was enhanced through linear patterning of the cells and fibroblast monolayer prevented the construct shrinkage. Furthermore, construct had the presence of sarcomere structures, expression of muscle proteins and the exhibition of active tension (~1 μN) when stimulated with electric pulses.

Magnetic force-based cell patterning technology also allows studies related to the behavior of individual cells. Ino et al. developed single cell culture arrays composed of a pin holder (soft iron) with more than 6,000 pillars ($100 \times 100 \times 300\,\mu$m) placed on a magnet to concentrate the magnetic flux density on the culture dish areas right above the pillars (Ino et al., 2008). MCL-labeled cells were allocated on the pillars and single cell patterning was obtained when the number of cells seeded was sufficiently reduced. Cellular aggregates were also successfully collected from the culture using a micromanipulator. In addition, the same system was used to investigate cell–cell interactions between HUVECs (Ino et al., 2009). Following the demonstration that the labeling of cells with MCLs had no effect on the viability and function of HUVECs, they changed the distance of the cellular aggregates on spots (center-to-center distance: 250 and 350 μm) using magnetized pin holder devices with different configurations and showed the effect of distance between cells on tubular formation. This magnetic patterning system also allowed for analysis of the invasive capacity of cancer model cells. Magnetically-labeled BALB/3T3 mouse fibroblast cells transformed with *v-Src* were seeded into a culture dish with a thin layer of collagen gel (Okochi et al., 2009). After patterning of cells into an array by placing the culture dish on a magnetized pin holder device (center-to-center distance: 250 μm), cells were further embedded with collagen gel to form the 3D cell array. For the culture of 3D aggregates, the magnetized pin holder was removed from the culture dish and this *in vivo*-like 3D model was used to investigate the invasive capacity of cells under different conditions. Another cell patterning method was presented for biochip applications (Ger et al., 2013). Cell culture arrangements were achieved through diamond-shaped magnetic thin films (size of each diamond: $90 \times 50\,\mu$m). When an external magnetic field was applied along the long axis of the thin film, the magnetically-labeled cells were successfully pulled toward the tips of the diamond-shaped thin film structure and formed a linear pattern.

An alternative approach for cell patterning is hydrogel-based magnetic cell patterning techniques. Fu and co-workers described a patterning method based on magnetic force and photoresponsive hydrogels (Fu et al., 2011). Hydrogels were magnetized with magnetic particles, and magnetic hydrogel blocks with the desired pattern were fabricated by photolithography. First, magnetic blocks were pulled toward the cell adhesion surface with a magnet and the first type of cells were seeded to adhere to the region not covered by the hydrogel. To form heterotypic cell pattern, the hydrogel on the surface was removed using a magnetic probe and the second type of cells was seeded to adhere to the empty area on the culture surface. Grogan et al. reported another magnetic cell patterning technique that relied on the alignment of magnetically-labeled cells in hydrogel by specifically orientated external magnetic fields (Grogan et al., 2012). Cellular arrangements were altered by manipulating the strength of the magnetic field, distribution of field lines and using calcium chloride crosslinking gradients in alginate hydrogels. Magnetically-labeled cells in this tissue engineering structure could be monitored using magnetic resonance imaging *in vivo*.

Besides manipulation and patterning of individual cells, patterning of spheroids is critical to form complex tissue-mimicking structures. Lin et al. presented an organoid patterning apparatus composed of a magnetic field–defining steel construct, that was fabricated by machining according to the targeted patterns on a permanent magnet and patterned preformed magnetically-labeled spheroids into rings, lines, and arrays (Lin et al., 2008). Stem cell spheroids were also patterned into various configurations (circle, distinct islands, four-leaf clover or line) to enable the study of fundamental principles in developmental biology (Bratt-Leal et al., 2011). In the study, cells were labeled by physical entrapment of magnetic particles in the extracellular space of spheroids during formation to allow assembly without directly perturbing intracellular processes. Magnetically guided patterning of spheroids were also achieved using functionalized super paramagnetic iron oxide nanoparticles (SPIONs) to label cells with enhanced cytocompatibility (Whatley et al., 2014). The desired patterns were obtained through magnetic templates fabricated from magnetic sheets using a computer controlled cutting device.

Although most of the applications for magnetic force-based patterning of cells or cellular spheroids have been achieved by positive magnetophoresis, based on magnetic labeling of cells, they can also be patterned in a label-free manner by negative magnetophoresis. It was shown that HUVEC cells that were suspended in an inert and biocompatible ferrofluid were aligned parallel to the applied magnetic field and the linear cellular structures were stable even after removal of the ferrofluid and magnetic field (Krebs et al., 2009). Tocchio et al. levitated and patterned preformed spheroids with more than 15 repeating units in a paramagnetic medium through magnetic field gradient between two permanent magnets placed on the top and bottom of a culture capillary channel (**Figure 6A**) (Tocchio et al., 2017). To achieve spheroid-to-spheroid contact and thus formation of tissue string with the desired order, spheroids were successively inserted into the capillary and the levitation setup was temporarily tilted for ∼5 min. Although patterning of cells with negative magnetophoresis eliminates the drawbacks arising from cell labeling, it limits the flexibility of the pattern variety as the cell or spheres are directed toward the area where the magnetic field is low and this area cannot be controlled easily.

Other Applications

Magnetic cell manipulation techniques can be used for further auxiliary purposes in cell culture systems for various tissue engineering applications and study of fundamental biological principles in a controlled manner. One of these applications is cell sheet engineering, that aims to keep cells and ECM together via formation of living sheet structures and thus to constitute *in vivo*-like models for various specific tissues (Yamato and Okano, 2004; Yang et al., 2005). Although the formation of tissues by combining spheroids as building blocks is a promising approach to construct complex structures, it has been shown that thin tissue sheets composed of cell layers are also functional and useful for some applications such as tissue engineering in heart (Matsuura et al., 2014) and cornea (Umemoto et al., 2013). Cell sheet engineering that can maintain the intact cell matrix provides a convenient microenvironment for vascularization. Magnetic force-based cell sheet engineering eliminates the need for thermosensitive surfaces that are used in conventional methods to form cell sheets.

It was reported that magnetic force-based manipulation of cells could be used to construct and harvest keratinocyte sheets (Ito et al., 2004a). MCL-labeled human keratinocytes were cultured in a low-attachment plate with a cylindrical NdFeB magnet positioned under the plate to create a magnetic force vertical to the plate. After 24 h of culture, 5-layered keratinocyte sheets were formed, and keratinocytes were further stratified into 10-layered epidermal sheets by additional cultivation in high-calcium medium. This technology was also used to construct a heterotypic, layered co-culture system of hepatocytes and endothelial cells (Ito et al., 2004b) or mesenchymal cells (Ito et al., 2007) to obtain tight and close cellular contact. This tight layered co-culture structure exhibited enhanced albumin secretion by hepatocytes compared to homotypic culture or heterotypic co-cultures produced without using magnetic manipulation of cells.

Retinal pigment epithelium (RPE) cells present another example that needs formation of sheet-like structures due to microscale transplant requirements. Magnetically-labeled human RPE cells were guided into sheets and 15-layered cell sheets were formed after 24 h of culture via the same magnetic manipulation technique (Ito et al., 2005a). Furthermore, magnetic force-based cell sheet engineering technology was used for bone tissue engineering (Shimizu et al., 2007c). In this work, magnetically-labeled mesenchymal stem cells (MSCs) were formed into multilayered sheet-like structures after 24 h of magnetic guidance, the sheets were then differentiated into osteoblasts for 21 days. Differentiated sheets were transplanted into the bone defect in the crania of nude rats and new bone formation in the defect area was observed in 2 weeks after the transplantation. Magnetic cell sheet engineering was used in a regenerative medicine strategy for ischemic heart disease (Ishii et al., 2014). Isolated mouse adipose-derived regenerative cells (ADRCs) were labeled with MCLs, mixed with an ECM precursor solution and cultured in an ultra-low attachment plate with a magnet placed underneath the plate to accumulate ADRCs at the bottom of the culture. Multilayered cell sheets formed after 24 h of culture, which were subsequently transplanted onto the infarcted myocardium and resulted in functional and structural improvements in ischemic hearts. Similarly, magnetite tissue engineering technology was used to create induced pluripotent stem (iPS) cell sheets for reparative angiogenesis, and revascularization was shown to be promoted after engraftment of engineered sheets into the ischemic tissues of nude mice (Kito et al., 2013). In addition to these studies that illustrate the unmodified use of cellular sheets, preformed magnetic cell sheets can also be magnetically directed to the desired macrostructures. Ito et al., for example, rolled a cylindrical magnet in a silicone tube over the cell sheet to form a cellular tube (Ito et al., 2005b).

Another application of magnetic cell guidance in cell culture is magnetic force-based cell seeding into scaffolds. The complex architecture of scaffolds can cause technical difficulties in cell seeding and this results in a non-uniform and inadequate migration of cells into the depth of the structure (Melchels et al., 2010). Shimizu et al. seeded magnetically-labeled fibroblasts on varying pore size scaffolds with with a magnet (400 mT) positioned under the scaffold (Shimizu et al., 2006). Presence of magnetic forces improved cell-seeding efficiency for all scaffold types. Cell seeding efficiency was further increased when a high-intensity magnet (1,000 mT) was used. Shortly after, the same group increased seeding efficiency of magnetically-labeled fibroblasts onto porcine decellularized common carotid artery (dCCA) by inserting a cylindrical magnet into the lumen of dCCA (Shimizu et al., 2007a). System not only increased the number of cell attached to the scaffold, but also enhanced infiltration and distribution (Thevenot et al., 2008). Magnetic cell seeding technique was also applied to bone tissue engineering using bone marrow stromal cells and 3D hydroxyapatite scaffolds and cultured cells in the osteogenic induction medium for 2 weeks (Shimizu et al., 2007b). The results indicated that cells seeded with magnetic cell manipulation expressed higher levels of osteogenic markers than cells seeded with static technique. Although studies on the use of magnetic cell manipulation for cell seeding on the scaffolds have so far aimed at the formation of large living structures, this technique has potential to be used to direct cells into desired regions of the 3D structures in miniaturized systems.

DISCUSSION AND CONCLUSION

Sorting rare cells with high purity provide a huge application potential in medical pursuits including regenerative medicine, personalized therapy as well as diagnostics (Tanaka et al., 2009; Toss et al., 2014; Kumar et al., 2017). Classical cell separation methods include membrane-based filtration and centrifugation, and have been applied to the separation of clinically relevant cells such as tumor cells (Vona et al., 2000) and bone marrow (BM) micrometastatic cells in cancer patients (Choesmel et al., 2004). However, filtration, in general, is limited by the pores of the membrane that are prone to clogging. Centrifugation, on the other hand, may induce phenotype affecting shear stresses on cells (Autebert et al., 2012). Moreover, these two techniques lack automation and not suitable for single cell operations. Modern tools such as fluorescence-activated cell sorting (FACS) (Picot et al., 2012) and MACS (Grützkau and Radbruch, 2010) offer more powerful, robust and high-throughput cell sorting. In FACS, cells labeled with antibody-conjugated fluorescence molecules are identified via fluorescence signal coming from each cell in a flow cytometry system. But FACS requires sophisticated and expensive machines. Besides, direct separation of rare cells from whole blood is not applicable using conventional FACS. MACS, which requires labeling of cells with magnetic particles and subsequent flow through high magnetic gradient columns, is a rather simple and inexpensive method compared to FACS. However, it shows an insufficient sensitivity when applied to low abundance subpopulations in the sample (Leary et al., 2002). These limitations have led the development of microfluidic devices that could allow cost-effective, sensitive, and high-throughput separation and subsequent analysis of different cell types.

Active cell sorting devices which use external forces for cell manipulation are comprised of optical, dielectrophoretic, acoustic, and magnetic fields (Bhagat et al., 2010). Optical platforms are the least portable since they require an optic system and a high-power laser source (Wang et al., 2004). Dielectrophoresis (DEP) represents a good alternative if target cells have distinct intrinsic electric properties (Pohl and Hawk, 1966; Pohl and Crane, 1971). However, DEP may cause Joule heating that harm cells suspended in a culture medium that have high electric conductivity (Tang et al., 2014). Acoustophoresis (ACP) uses sound waves to manipulate cells based on their size, density and compressibility (Petersson et al., 2005). Compared to DEP, ACP affects cell viability less (Hultström et al., 2007) and has been used to separate CTCs from WBCs (Li et al., 2015). However, compressibility of the many rare cells is not well-documented. One of the assets of magnetic techniques over its counterparts is that the separation could be achieved with minimal damage to cells (Kim et al., 2013b). Besides, simplicity of inserting an inexpensive permanent magnet or an electromagnet makes magnetophoresis more suitable for on-chip/microfluidic separation applications. In contrast to DEP and ACP, magnetophoresis may include the use of magnetic labels which are rather advantageous compared to fluorescent labels since they are more stable and do not require light excitation (Hahm, 2011).

A wide range of basic and advanced techniques has been currently available to assemble cells into 3D structures. Conventional methods of cellular assembly into 3D, such as cell hanging drop (Timmins et al., 2004) and liquid overlay (Lei et al., 2017) are labor intensive, time consuming and only allow low throughput. The methods that enhance throughput, such as spinner culture (Nyberg et al., 2005) and rotating cell culture (Nishi et al., 2013), cause loss of control over the size and uniformity of the generated 3D living structures. Alternatively, external forces can also be employed to assemble cells into 3D via dielectrophoresis (Voldman, 2006), acoustophoresis (Petersson et al., 2007; Bouyer et al., 2016), and magnetophoresis. Magnetophoresis retain the advantages it presents for cell separation in 3D assembly of cells as well, involving cell health, instrumentation, and cost.

Patterning of cells for 2D or 3D culture currently can be carried out by chemical, physical, or combinatorial techniques. Surface chemistry-based methods provide a high precision way to collocate cells on surfaces in predesigned patterns taking advantage of recognition-based cell adhesion (Ogaki et al., 2010). However, the need for a pre-treated surface requires additional steps such as the fabrication and characterization of the surface. In addition, these methods can be applied only for surface-dependent cell cultures. Although this limitation can be surpassed by guiding cells by cell-repellent interfaces, the application loses recognition-based high precision. Physical guidance of cells into targeted patterns is possible via dielectrophoresis, acoustophoresis, and alternatively bioprinting techniques, such as inkjet printing (Xu et al., 2013) and laser-based techniques (Schiele et al., 2010). Precise cell patterning applications without cellular damage by bioprinting techniques require large instrumentations and complex set-ups. Magnetophoresis eliminates the need for these complex instrumentations and offers nozzle free arrangement of the cells in the desired organization without affecting their viability and function.

Despite the advantages of the magnetic force-based cell manipulation methods reviewed here, the biological effects of its components acting on biological systems should not be overlooked, especially for long-term cell culture. The magnetic field, which is an important component of magnetic-based cell manipulation systems in both positive and negative magnetophoresis, can have different effects on living cells. The impact of the magnetic field on cells depends on magnetic field intensity (Zhang et al., 2014, 2016), type (static or dynamic) and spatial distribution of magnetic fields (homogeneous or inhomogeneous) (Zhang et al., 2017c), exposure time (Sullivan et al., 2011), cell type and density (Zhang et al., 2017b), and cellular infection (Nam et al., 2013). Several cellular processes are influenced by the magnetic field, such as membrane properties (Lin et al., 2013), cell shape and cytoskeletal organization (Chionna et al., 2005), cell cycle (Mo et al., 2013), cell viability and proliferation (Wang et al., 2016a; Maredziak et al., 2017), cell orientation (Kim et al., 2008a), cell adhesion, migration (Mo et al., 2016) and differentiation (Zhang et al., 2014). Evidence from several studies has shown that the biological effects of magnetic fields are correlated with their intensity. While weak or moderate magnetic fields (<1 T) have only slight effects on cells (Glade and Tabony, 2005; Zhang et al., 2016), strong magnetic fields (>20 T) can have drastic effects such as altering mitotic spindle orientation (Zhang et al., 2017a). Despite the fact that the magnetic field used for cell manipulation is usually weak or moderate, the magnitude of the applied magnetic field and the duration of the magnetic field exposure must be considered as these factors may affect the success of the application depending on cell type.

An important component of negative magnetophoresis is magnetic liquids, i.e., ferrofluid (Zhu et al., 2010, 2012), or paramagnetic salt solution (Shen et al., 2012; Abdel Fattah et al., 2016). Magnetic liquids are needed to increase the repulsive magnetic forces on diamagnetic cells through enhancing medium magnetic susceptibility and thus eliminate problems arising from the use of high magnetic field exposure. However, the biocompatibility of magnetic liquids is an important and challenging issue for tissue engineering applications. Studies that were carried out to understand the biocompatibility of paramagnetic salt solutions and ferrofluids, are summarized in **Table 3**. Although the effect of magnetic fluids on cell viability is under investigation, and some biocompatible magnetic fluids have been reported, other cellular influences should be considered specifically depending on application.

Positive magnetophoresis-based cell manipulation using magnetic labels usually offers high purity, selectivity and recovery rate for cell separation and high manipulation flexibility for guidance of cells into pre-designed organizations in 2D and 3D cell culture. However, it should be noted that long-term retention of magnetic labels might affect cellular function, viability and phenotypic characteristics of some sensitive cell populations such as stem cells and progenitor cells (Farrell et al., 2008; Mahmoudi et al., 2011; Plouffe et al., 2015). In addition, internalization of small particles (<100 nm) creates reactive oxygen species (ROS) (Soenen and De Cuyper, 2010), which could damage the structure and function of cellular components when produced at elevated levels (Sharifi et al., 2012; Liu et al., 2013). In cell culture applications, although cellular alterations arising from MNPs internalization may be minimized by several strategies such as the usage of biological MNPs and forming Janus structure, these methods also require different additional steps that need to be well characterized, and still time-consuming. It is also challenging to detach MNPs after separation (Hosic et al., 2016). But one of the biggest challenge regarding rare cell separation in clinical settings is selecting the target cells baring several surface markers from an initial bulk of cells (Plouffe et al., 2015). In case of CTCs that show genetic and phenotypic heterogeneity (Baccelli et al., 2013; Yu et al., 2013), surface marker-based magnetic detection and isolation techniques become challenging. At this point, negative magnetophoresis-based label-free cell manipulation strategies becomes an attractive option. Nevertheless, this technique has been scarcely exploited for microfluidic magnetic sorting of key rare cells such as stem cells and tumor cells (**Table 1**). Improvements in negative magnetophoresis could open a new window for accurate and high-throughput handling of rare cells based on cells' intrinsic properties.

Lately, the use of magnetic forces has become a favorable approach in miniaturized microfluidic systems that offer minimal size, cost, and analysis time compared to complex and expensive laboratory equipment and also enhance magnetic flux density with magnetizable on-chip micropatterns (Tekin and Gijs, 2013; Shields et al., 2015). Nevertheless, microfluidic cell sorting systems usually have lower throughput compared to FACS system (50,000 cells s^{-1}) and therefore require further improvement (Dharmasiri et al., 2010). In this context, attempts to increase the throughput of the microfluidic systems, such as chip parallelization could be implemented (Hosic et al., 2016). So far, many of the works related to magnetically-guided cell separation were proof-of-principle demonstrations of the systems and designs with low medium complexity or user defined mixtures (e.g., biological samples spiked with cancer cells). Even though pioneering results were reported, each concept should be validated using complex cell suspensions (e.g., whole blood) to be successfully translated to real-world applications in near future. Magnetic manipulation is performed by permanent or electromagnets which are either placed outside or integrated into the chip. Obtaining a desired magnetic field gradient at a certain location within the microfluidic platform is necessary for repeatable results. For delicate control of magnetic fields in microfluidic channels, external magnets should be aligned to the channel with high-precision. Integrated micromagnets on microfluidic channel provides enhanced control of magnetic field. However, these micromagnets require costly microfabrication steps (Pamme, 2006).

In addition to obtaining the cell subpopulation of interest from a bulk population, magnetic cell manipulation is a crucial tool to guide cells into the natural-like structures for culture. The future of 2D and 3D cell culture for bottom-up tissue engineering applications, fundamental biological and pharmaceutical research lies in the generation of complex cellular

TABLE 3 | Biocompatibility of magnetic liquids.

Magnetic liquids	Structures	Short-term biocompatibility	Long-term biocompatibility	References
Gadolinium diethylenetriaminepentaacetic acid	Linear ionic	NR	+	Winkleman et al., 2004
		++	NR	Rodríguez-Villarreal et al., 2011
		+ + ++	NR	Abdel Fattah et al., 2016
Gadoteridol	Macrocyclic nonionic	NR	+ + +	Kauffmann et al., 2011
Gadabutrol (Gadavist®)	Macrocyclic nonionic	NR	+ + ++	Durmus et al., 2015; Anil-Inevi et al., 2018
		NR	+ + +	Tocchio et al., 2017
Gadodiamide (Omniscan™)	Linear nonionic	NR	++	Anil-Inevi et al., 2018
Gadopentetate dimeglumine (Magnevist®)	Linear ionic	NR	+ + +	Anil-Inevi et al., 2018
Gadoterate meglumine (Dotarem®)	Macrocyclic ionic	NR	++	Kauffmann et al., 2011
		NR	+ + +	Anil-Inevi et al., 2018
Gadobenate dimeglumine (Multihance®)	Linear ionic	NR	±	Kauffmann et al., 2011
		NR	+ + +	Anil-Inevi et al., 2018
BSA (bovine serum albumin) coated ferrofluid	Globular protein-magnetite nanoparticles	±	NR	Krebs et al., 2009
Citrate stabilized ferrofluid	Citrate anion-Cobalt-ferrite nanoparticles	–	NR	Kose et al., 2009
EMG 408 ferrofluid	Anionic surfactant-magnetite nanoparticles	+ + ++	NR	Zhu et al., 2012
Graft copolymer functionalized ferrofluid	Nonionic polymers-maghemite nanoparticles	+ + ++ + + ++	NR	Zhao et al., 2015
		++	NR	Zhao et al., 2017a,b

Cell viability which was not statistically different from the control group, or above 80% was assessed as good cell viability. Good cell viability levels were scored as– (<10 mM), ± (10–25 mM), + (25–50 mM), ++ (50–100 mM), + + + (100–200 mM) or + + ++ (>200 mM) for paramagnetic salt solutions. Good cell viability in ferrofluids were scored as– (good cell viability: <0.06%, volume fraction of magnetic particles), ± (0.06–0.12%), + (0.12–0.25%), ++ (0.25–0.5%), + + + (0.5–1%) or + + ++ (>1%). NR stands for "not reported," respectively.

organizations in a spatiotemporally controllable manner, and magnetic force-based methods provide a relatively new and precise contactless cell manipulation with minimized biological effects. Moreover, the mechanical support-free nature of the technology provides an opportunity to eliminate the biological effects of the support material. Although most studies have involved application of magnetic cell guidance on a macroscale, recent efforts have focused on combining magnetic force-based cell manipulation with microfluidic technology for creation of concentrated and strong magnetic forces with inexpensive setups, more precise control of cellular interactions and dynamic microenvironment, reduced consumption of reagents, and efficient high throughput experimentation. The recent applications of this concept involve using magnetic levitation technology as a label-free biofabrication method (Tocchio et al., 2017; Anil-Inevi et al., 2018; Türker et al., 2018). This label-free magnetic cell guidance technique has great potential in several exciting applications. Recent research shows that cellular building blocks can be fused in a nozzle-free manner to produce functional and large-sized tissues (Parfenov et al., 2018), and this progress presents a preview of the immediate future for application of magnetic-based cell manipulation in tissue engineering.

Among the applications of magnetic levitation, ground-based facilities for simulation of microgravity through magnetic levitation (Qian et al., 2013) must be mentioned due to their promise to improve our understanding of the biological effects of microgravity as an alternative to expensive and rare spaceflight experiments. Not all magnetic levitation technologies are suitable for this purpose. Specifically, magnetic levitation by labeling diamagnetic cells with magnetic particles cannot properly simulate microgravity owing to the fact that magnetic force cannot be applied to all cellular units homogeneously (Souza et al., 2010; Haisler et al., 2013). On the contrary, magnetic levitation of diamagnetic cells by negative magnetophoresis creates forces acting on all cellular structures. While other ground-based techniques to simulate microgravity, such as the rotating-wall vessel (RWV) platform (Rucci et al., 2002), 2D clinostats (Qian et al., 2012), and Random Positioning Machines (RPM) (Wuest et al., 2015), generate fluid shear stress on the cells as a result of rotation and interrupts the cellular response (Pavalko et al., 1998; Kaysen et al., 1999), the magnetic levitation principle does not create such additional forces on the cells. Furthermore, magnetic levitation presents an alternative to the use of earth-based animal models (Ozcivici et al., 2007, 2010; Ozcivici and Judex, 2014), which are limited by expensive setups, high variation at the molecular/cellular level, and ethical concerns. In conclusion, magnetic levitation is a powerful technique that can potentially be applied to test unique hypotheses in gravitational biology and tissue engineering research.

In this review, we highlighted magnetofluidic cell manipulation applications including rare cell separation and 2D and 3D cell culture. Although some improvements in throughput, purity and viability are required for current techniques, the rapid growth in the field could spread magnetofluidic-based rare cell separation tools from the research laboratory to industry in the future. Furthermore, progressive development in magnetic cell manipulation techniques and recent attempts for integration of these techniques with microfluidic technology represent exciting tools in near future for more complex and precise tissue engineering and cell biology research. Based on the studies highlighted in this review, we envision that the future trend of magnetic force-based microfluidic systems will be toward the development of label-free cell separation platforms that perform series of all necessary tasks (such as filtration, separation, and analysis of cells) on a single chip and the improvement of cell culture systems for scaffold- and nozzle-free biofabrication of 3D living constructs, simulation of microgravity and simultaneous monitoring of drug effects.

AUTHOR CONTRIBUTIONS

EO and HCT designed the content of the article; all authors performed literature survey and wrote the article. SY and MA-I prepared the figures and tables. EO and HCT edited and reviewed the article before submission.

ACKNOWLEDGMENTS

Financial support by The Scientific and Technological Research Council of Turkey for 116M298 (HCT) and 215S862 (EO) grants is gratefully acknowledged. Authors also extend warm regards to Anne Frary, Ph.D. for critically reviewing the manuscript.

SUPPLEMENTARY MATERIAL

The Supplementary Material for this article can be found online at: https://www.frontiersin.org/articles/10.3389/fbioe.2018.00192/full#supplementary-material

REFERENCES

Abdel Fattah, A. R., Meleca, E., Mishriki, S., Lelic, A., Geng, F., Sahu, R. P., et al. (2016). *In situ* 3D label-free contactless bioprinting of cells through diamagnetophoresis. *ACS Biomater. Sci. Eng.* 2, 2133–2138. doi: 10.1021/acsbiomaterials.6b00614

Akiyama, H., Ito, A., Kawabe, Y., and Kamihira, M. (2009). Fabrication of complex three-dimensional tissue architectures using a magnetic force-based cell patterning technique. *Biomed. Microdevices* 11, 713–721. doi: 10.1007/s10544-009-9284-x

Akiyama, H., Ito, A., Sato, M., Kawabe, Y., and Kamihira, M. (2010). Construction of cardiac tissue rings using a magnetic tissue fabrication technique. *Int. J. Mol. Sci.* 11, 2910–2920. doi: 10.3390/ijms11082910

Akiyama, Y., and Morishima, K. (2011a). Label-free cell aggregate formation based on the magneto-Archimedes effect. *Appl. Phys. Lett.* 98:163702. doi: 10.1063/1.3581883

Akiyama, Y., and Morishima, K. (2011b). "Spheroid array formation by non-label cell manipulation using magneto-Archimedes effect," in *Micro-NanoMechatronics and Human Science (MHS), 2011 International Symposium on: IEEE)* (Nagoya), 45–50.

Akiyama, Y., and Morishima, K. (2012). "Label-free ultrarapid spheroid formation in microfluidic chip using magneto-Archimedes effect," in *Micro Electro Mechanical Systems (MEMS), 2012 IEEE 25th International Conference on: IEEE)* (Paris), 116–119.

Amin, R., Knowlton, S., Dupont, J., Bergholz, J. S., Joshi, A., Hart, A., et al. (2017). 3D-printed smartphone-based device for label-free cell separation. *J. 3D Print. Med.* 1, 155–164. doi: 10.2217/3dp-2016-0007

Anil-Inevi, M., Yaman, S., Yildiz, A. A., Mese, G., Yalcin-Ozuysal, O., Tekin, H. C., et al. (2018). Biofabrication of *in situ* self assembled 3d cell cultures in a weightlessness environment generated using magnetic levitation. *Sci. Rep.* 8:7239. doi: 10.1038/s41598-018-25718-9

Ashkin, A., Dziedzic, J. M., and Yamane, T. (1987). Optical trapping and manipulation of single cells using infrared laser beams. *Nature* 330, 769–771.

Autebert, J., Coudert, B., Bidard, F. C., Pierga, J. Y., Descroix, S., Malaquin, L., et al. (2012). Microfluidic: an innovative tool for efficient cell sorting. *Methods* 57, 297–307. doi: 10.1016/j.ymeth.2012.07.002

Baccelli, I., Schneeweiss, A., Riethdorf, S., Stenzinger, A., Schillert, A., Vogel, V., et al. (2013). Identification of a population of blood circulating tumor cells from breast cancer patients that initiates metastasis in a xenograft assay. *Nat. Biotechnol.* 31, 539–544. doi: 10.1038/nbt.2576

Bhagat, A. A., Bow, H., Hou, H. W., Tan, S. J., Han, J., and Lim, C. T. (2010). Microfluidics for cell separation. *Med. Biol. Eng. Comput.* 48, 999–1014. doi: 10.1007/s11517-010-0611-4

Bhuvanendran Nair Gourikutty, S., Chang, C. P., and Poenar, D. P. (2016a). An integrated on-chip platform for negative enrichment of tumour cells. *J. Chromatogr. B Analyt. Technol. Biomed. Life Sci.* 1028, 153–164. doi: 10.1016/j.jchromb.2016.06.016

Bhuvanendran Nair Gourikutty, S., Chang, C. P., and Puiu, P. D. (2016b). Microfluidic immunomagnetic cell separation from whole blood. *J. Chromatogr. B Analyt. Technol. Biomed. Life Sci.* 1011, 77–88. doi: 10.1016/j.jchromb.2015.12.016

Boj, S. F., Hwang, C.I., Baker, L. A., Chio, I. I., Engle, D. D., Corbo, V., et al. (2015). Organoid models of human and mouse ductal pancreatic cancer. *Cell* 160, 324–338. doi: 10.1016/j.cell.2014.12.021

Bouyer, C., Chen, P., Güven, S., Demirta,ş, T. T., Nieland, T. J., Padilla, F., et al. (2016). A bio-acoustic levitational (BAL) assembly method for engineering of multilayered, 3d brain-like constructs, using human embryonic stem cell derived neuro-progenitors. *Adv. Mater.* 28, 161–167. doi: 10.1002/adma.201503916

Boyle, D. S., Hawkins, K. R., Steele, M. S., Singhal, M., and Cheng, X. (2012). Emerging technologies for point-of-care CD4 T-lymphocyte counting. *Trends Biotechnol.* 30, 45–54. doi: 10.1016/j.tibtech.2011.06.015

Bratt-Leal, A. M., Kepple, K. L., Carpenedo, R. L., Cooke, M. T., and McDevitt, T. C. (2011). Magnetic manipulation and spatial patterning of multi-cellular stem cell aggregates. *Integr. Biol.* 3, 1224–1232. doi: 10.1039/c1ib00064k

Calero, M., Gutiérrez, L., Salas, G., Luengo, Y., Lázaro, A., Acedo, P., et al. (2014). Efficient and safe internalization of magnetic iron oxide nanoparticles: two fundamental requirements for biomedical applications. *Nanomedicine* 10, 733–743. doi: 10.1016/j.nano.2013.11.010

CemaŽar, J., Douglas, T. A., Schmelz, E. M., and Davalos, R.V. (2016). Enhanced contactless dielectrophoresis enrichment and isolation platform via cell-scale microstructures. *Biomicrofluidics* 10, 14109–14109. doi: 10.1063/1.4939947

Chen, C., and Hou, J. (2016). Mesenchymal stem cell-based therapy in kidney transplantation. *Stem Cell Res. Ther.* 7:16. doi: 10.1186/s13287-016-0283-6

Chen, C. C. V., Ku, M. C., D. M. J, Lai, J. S., Hueng, D. Y., and Chang, C. (2013). Simple SPION incubation as an efficient intracellular labeling method for tracking neural progenitor cells using MRI. *PLoS ONE* 8:e56125. doi: 10.1371/journal.pone.0056125

Chen, J., Li, J., and Sun, Y. (2012). Microfluidic approaches for cancer cell detection, characterization, and separation. *Lab Chip* 12, 1753–1767. doi: 10.1039/c2lc21273k

Chen, P., Huang, Y. Y., Hoshino, K., and Zhang, J. X. (2015). Microscale magnetic field modulation for enhanced capture and distribution of rare circulating tumor cells. *Sci. Rep.* 5, 8745–8745. doi: 10.1038/srep08745

Chen, Y., Li, P., Huang, P.H., Xie, Y., Mai, J. D., Wang, L., et al. (2014). Rare cell isolation and analysis in microfluidics. *Lab Chip* 14, 626–645. doi: 10.1039/c3lc90136j

Cheng, J., Rahman, M. A., and Ohta, A. T. (2017). "Optical manipulation of cells BT - microtechnology for cell manipulation and sorting," in *Microtechnology for Cell Manipulation and Sorting, Microsystems and Nanosystems,* eds W. Lee, P. Tseng, and D. Di Carlo (Cham: Springer International Publishing), 93–128.

Cheng, X., Irimia, D., Dixon, M., Ziperstein, J. C., Demirci, U., Zamir, L., et al. (2007). A microchip approach for practical label-free CD4+ T-cell counting of HIV-infected subjects in resource-poor settings. *J. Acquir. Immune Defic. Syndr.* 45, 257–261. doi: 10.1097/QAI.0b013e3180500303

Chionna, A., Tenuzzo, B., Panzarini, E., Dwikat, M. B., Abbro, L., and Dini, L. (2005). Time dependent modifications of Hep G2 cells during exposure to static magnetic fields. *Bioelectromagnetics* 26, 275–286. doi: 10.1002/bem.20081

Cho, H., Kim, J., Han, S.I., and Han, K.H. (2016). Analytical evaluation for somatic mutation detection in circulating tumor cells isolated using a lateral magnetophoretic microseparator. *Biomed. Microdevices* 18, 91–91. doi: 10.1007/s10544-016-0116-5

Choesmel, V., Pierga, J. Y., Nos, C., Vincent-Salomon, A., Sigal-Zafrani, B., Thiery, J. P., et al. (2004). Enrichment methods to detect bone marrow micrometastases in breast carcinoma patients: clinical relevance. *Breast Cancer Res.* 6, R556–R570. doi: 10.1186/bcr898

Chronis, N., and Lee, L. P. (2005). Electrothermally activated SU-8 microgripper for single cell manipulation in solution. *J. Microelectromech. Syst.* 14, 857–863. doi: 10.1109/JMEMS.2005.845445

Chung, J., Issadore, D., Ullal, A., Lee, K., Weissleder, R., and Lee, H. (2013). Rare cell isolation and profiling on a hybrid magnetic/size-sorting chip. *Biomicrofluidics* 7:054107. doi: 10.1063/1.4821923

Coakley, W. T., Bardsley, D. W., Grundy, M. A., Zamani, F., and Clarke, D. J. (1989). Cell manipulation in ultrasonic standing wave fields. *J. Chem. Technol. Biotechnol.* 44, 43–62. doi: 10.1002/jctb.280440106

Daquinag, A. C., Souza, G. R., and Kolonin, M. G. (2012). Adipose tissue engineering in three-dimensional levitation tissue culture system based on magnetic nanoparticles. *Tissue Eng. Part C Methods* 19, 336–344. doi: 10.1089/ten.tec.2012.0198

Dharmasiri, U., Witek, M. A., Adams, A. A., and Soper, S. A. (2010). Microsystems for the capture of low-abundance cells. *Annu. Rev. Anal. Chem.* 3, 409–431. doi: 10.1146/annurev.anchem.111808.073610

Durmus, N. G., Tekin, H. C., Guven, S., Sridhar, K., Arslan Yildiz, A., Calibasi, G., et al. (2015). Magnetic levitation of single cells. *Proc. Natl. Acad. Sci.* 112, E3661–E3668. doi: 10.1073/pnas.1509250112

Dzamukova, M. R., Naumenko, E. A., Rozhina, E. V., Trifonov, A. A., and Fakhrullin, R. F. (2015). Cell surface engineering with polyelectrolyte-stabilized magnetic nanoparticles: a facile approach for fabrication of artificial multicellular tissue-mimicking clusters. *Nano Res.* 8, 2515–2532. doi: 10.1007/s12274-015-0759-1

Earhart, C. M., Hughes, C. E., Gaster, R. S., Ooi, C. C., Wilson, R. J., Zhou, L. Y., et al. (2014). Isolation and mutational analysis of circulating tumor cells from lung cancer patients with magnetic sifters and biochips. *Lab Chip* 14, 78–88. doi: 10.1039/C3LC50580D

El-Ali, J., Sorger, P. K., and Jensen, K. F. (2006). Cells on chips. *Nature* 442, 403–411. doi: 10.1038/nature05063

Fachin, F., Spuhler, P., Martel-Foley, J. M., Edd, J. F., Barber, T. A., Walsh, J., et al. (2017). Monolithic chip for high-throughput blood cell depletion to sort rare circulating tumor cells. *Sci. Rep.* 7:10936. doi: 10.1038/s41598-017-11119-x

Farrell, E., Wielopolski, P., Pavljasevic, P., van Tiel, S., Jahr, H., Verhaar, J., et al. (2008). Effects of iron oxide incorporation for long term cell tracking on MSC differentiation *in vitro* and *in vivo*. *Biochem. Biophys. Res. Commun.* 369, 1076–1081. doi: 10.1016/j.bbrc.2008.02.159

Foudeh, A. M., Fatanat Didar, T., Veres, T., and Tabrizian, M. (2012). Microfluidic designs and techniques using lab-on-a-chip devices for pathogen detection for point-of-care diagnostics. *Lab Chip* 12, 3249–3266. doi: 10.1039/c2lc40630f

Fu, C. Y., Lin, C. Y., Chu, W. C., and Chang, H. Y. (2011). A simple cell patterning method using magnetic particle-containing photosensitive poly (ethylene glycol) hydrogel blocks: a technical note. *Tissue Eng. Part C Methods* 17, 871–877. doi: 10.1089/ten.tec.2010.0690

Fuhr, G., Glasser, H., Müller, T., and Schnelle, T. (1994). Cell manipulation and cultivation under a.c. electric field influence in highly conductive culture media. *Biochim. Biophys. Acta* 1201, 353–360. doi: 10.1016/0304-4165(94)90062-0

Fujita, H., Shimizu, K., Yamamoto, Y., Ito, A., Kamihira, M., and Nagamori, E. (2010). Fabrication of scaffold-free contractile skeletal muscle tissue using magnetite-incorporated myogenic C2C12 cells. *J. Tissue Eng. Regen. Med.* 4, 437–443. doi: 10.1002/term.253

Ger, T.-R., Huang, C.-Y., and Lai, M.-F. (2013). Cell culture arrangement using ferromagnetic diamond-shaped thin films. *IEEE Trans. Magn.* 49, 3453–3455. doi: 10.1109/TMAG.2013.2245865

Ghosh, S., Kumar, S.R, Puri, I.K, and Elankumaran, S. (2016). Magnetic assembly of 3D cell clusters: visualizing the formation of an engineered tissue. *Cell Prolif.* 49, 134–144. doi: 10.1111/cpr.12234

Glade, N., and Tabony, J. (2005). Brief exposure to high magnetic fields determines microtubule self-organisation by reaction–diffusion processes. *Biophys. Chem.* 115, 29–35. doi: 10.1016/j.bpc.2004.12.048

Greene, B. T., Hughes, A. D., and King, M. R. (2012). Circulating tumor cells: the substrate of personalized medicine? *Front. Oncol.* 2:69. doi: 10.3389/fonc.2012.00069

Grier, D. G. (2003). A revolution in optical manipulation. *Nature* 424, 810–816. doi: 10.1038/nature01935

Grogan, S. P., Pauli, C., Chen, P., Du, J., Chung, C. B., Kong, S. D., et al. (2012). *In situ* tissue engineering using magnetically guided three-dimensional cell patterning. *Tissue Eng. Part C Methods* 18, 496–506. doi: 10.1089/ten.tec.2011.0525

Grützkau, A., and Radbruch, A. (2010). Small but mighty: how the MACS-technology based on nanosized superparamagnetic particles has helped to analyze the immune system within the last 20 years. *Cytometry A* 77A, 643–647. doi: 10.1002/cyto.a.20918

Gu, H., Xu, K., Xu, C., and Xu, B. (2006). Biofunctional magnetic nanoparticles for protein separation and pathogen detection. *Chem. Commun.* 941–949. doi: 10.1039/b514130c

Guillotin, B., and Guillemot, F. (2011). Cell patterning technologies for organotypic tissue fabrication. *Trends Biotechnol.* 29, 183–190. doi: 10.1016/j.tibtech.2010.12.008

Hahm, J. I. (2011). Functional polymers in protein detection platforms: optical, electrochemical, electrical, mass-sensitive, and magnetic biosensors. *Sensors* 11, 3327–3355. doi: 10.3390/s110303327

Haisler, W. L., Timm, D. M., Gage, J. A., Tseng, H., Killian, T.C, and Souza, G. R. (2013). Three-dimensional cell culturing by magnetic levitation. *Nat. Protoc.* 8, 1940–1949. doi: 10.1038/nprot.2013.125

Han, K. H., Han, A., and Frazier, A. B. (2006). Microsystems for isolation and electrophysiological analysis of breast cancer cells from blood. *Biosens. Bioelectron.* 21, 1907–1914. doi: 10.1016/j.bios.2006.01.024

Hejazian, M., and Nguyen, N. T. (2016). Magnetofluidic concentration and separation of non-magnetic particles using two magnet arrays. *Biomicrofluidics* 10:044103. doi: 10.1063/1.4955421r

Ho, P.-L. (2014). Magnetic nanoparticles for pathogen detection. *Pathology* 46:S45. doi: 10.1097/PAT.0000000000000060

Ho, V. H., Guo, W. M., Huang, C. L., Ho, S. F., Chaw, S. Y., Tan, E. Y., et al. (2013). Manipulating magnetic 3D spheroids in hanging drops for applications in tissue engineering and drug screening. *Adv. Healthc. Mater.* 2, 1430–1434. doi: 10.1002/adhm.201200408

Hoshino, K., Huang, Y. Y., Lane, N., Huebschman, M., Uhr, J. W., Frenkel, E. P., et al. (2011). Microchip-based immunomagnetic detection of circulating tumor cells. *Lab Chip* 11, 3449–3449. doi: 10.1039/c1lc20270g

Hosic, S., Murthy, S. K., and Koppes, A. N. (2016). Microfluidic sample preparation for single cell analysis. *Anal. Chem.* 88, 354–380. doi: 10.1021/acs.analchem.5b04077

Huang, G., Huang, Q., Xie, L., Xiang, G., Wang, L., Xu, H., et al. (2017). A rapid, low-cost, and microfluidic chip-based system for parallel identification of multiple pathogens related to clinical pneumonia. *Sci. Rep.* 7:6441. doi: 10.1038/s41598-017-06739-2

Huang, N.-T., Hwong, Y.-J., and Lai, R. L. (2018). A microfluidic microwell device for immunomagnetic single-cell trapping. *Microfluid. Nanofluidics* 22:16. doi: 10.1007/s10404-018-2040-x

Huang, S. B., Wu, M. H., Lin, Y. H., Hsieh, C. H., Yang, C. L., Lin, H. C., et al. (2013). High-purity and label-free isolation of circulating tumor cells (CTCs) in a microfluidic platform by using optically-induced-dielectrophoretic (ODEP) force. *Lab Chip* 13, 1371–1383. doi: 10.1039/c3lc41256c

Hultström, J., Manneberg, O., Dopf, K., Hertz, H. M., Brismar, H., and Wiklund, M. (2007). Proliferation and viability of adherent cells manipulated by standing-wave ultrasound in a microfluidic chip. *Ultrasound Med. Biol.* 33, 145–151. doi: 10.1016/j.ultrasmedbio.2006.07.024

Iinuma, H., Okinaga, K., Adachi, M., Suda, K., Sekine, T., Sakagawa, K., et al. (2000). Detection of tumor cells in blood using CD45 magnetic cell separation followed by nested mutant allele-specific amplification of p53 and K-ras genes in patients with colorectal cancer. *Int. J. Cancer.* 89, 337–344. doi: 10.1002/1097-0215(20000720)89:4<337::AID-IJC4>3.0.CO;2-R

Ino, K., Ito, A., and Honda, H. (2007). Cell patterning using magnetite nanoparticles and magnetic force. *Biotechnol. Bioeng.* 97, 1309–1317. doi: 10.1002/bit.21322

Ino, K., Okochi, M., and Honda, H. (2009). Application of magnetic force-based cell patterning for controlling cell–cell interactions in angiogenesis. *Biotechnol. Bioeng.* 102, 882–890. doi: 10.1002/bit.22104

Ino, K., Okochi, M., Konishi, N., Nakatochi, M., Imai, R., Shikida, M., et al. (2008). Cell culture arrays using magnetic force-based cell patterning for dynamic single cell analysis. *Lab Chip* 8, 134–142. doi: 10.1039/B712330B

Ishii, M., Shibata, R., Shimizu, Y., Yamamoto, T., Kondo, K., Inoue, Y., et al. (2014). Multilayered adipose-derived regenerative cell sheets created by a novel magnetite tissue engineering method for myocardial infarction. *Int. J. Cardiol.* 175, 545–553. doi: 10.1016/j.ijcard.2014.06.034

Issa, B., Obaidat, I. M., Albiss, B. A., and Haik, Y. (2013). Magnetic nanoparticles: Surface effects and properties related to biomedicine applications. *Int. J. Mol. Sci.* 14, 21266–21305. doi: 10.3390/ijms141121266

Ito, A., Hayashida, M., Honda, H., Hata, K., Kagami, H., Ueda, M., et al. (2004a). Construction and harvest of multilayered keratinocyte sheets using magnetite nanoparticles and magnetic force. *Tissue Eng.* 10, 873–880. doi: 10.1089/1076327041348446

Ito, A., Hibino, E., Kobayashi, C., Terasaki, H., Kagami, H., Ueda, M., et al. (2005a). Construction and delivery of tissue-engineered human retinal pigment epithelial cell sheets, using magnetite nanoparticles and magnetic force. *Tissue Eng.* 11, 489–496. doi: 10.1089/ten.2005.11.489

Ito, A., Ino, K., Hayashida, M., Kobayashi, T., Matsunuma, H., Kagami, H., et al. (2005b). Novel methodology for fabrication of tissue-engineered tubular constructs using magnetite nanoparticles and magnetic force. *Tissue Eng.* 11, 1553–1561. doi: 10.1089/ten.2005.11.1553

Ito, A., Jitsunobu, H., Kawabe, Y., and Kamihira, M. (2007). Construction of heterotypic cell sheets by magnetic force-based 3-D coculture of HepG2 and NIH3T3 cells. *J. Biosci. Bioeng.* 104, 371–378. doi: 10.1263/jbb.104.371

Ito, A., Takizawa, Y., Honda, H., Hata, K., Kagami, H., Ueda, M., et al. (2004b). Tissue engineering using magnetite nanoparticles and magnetic force: heterotypic layers of cocultured hepatocytes and endothelial cells. *Tissue Eng.* 10, 833–840. doi: 10.1089/1076327041348301

Jaganathan, H., Gage, J., Leonard, F., Srinivasan, S., Souza, G. R., Dave, B., et al. (2014). Three-dimensional *in vitro* co-culture model of breast tumor using magnetic levitation. *Sci. Rep.* 4:6468. doi: 10.1038/srep06468

Ji, H. M., Samper, V., Chen, Y., Heng, C. K., Lim, T. M., and Yobas, L. (2008). Silicon-based microfilters for whole blood cell separation. *Biomed. Microdevices* 10, 251–257. doi: 10.1007/s10544-007-9131-x

Jiang, J., Zhao, H., Shu, W., Tian, J., Huang, Y., Song, Y., et al. (2017). An integrated microfluidic device for rapid and high-sensitivity analysis of circulating tumor cells. *Sci. Rep.* 7:42612. doi: 10.1038/srep42612

Jiang, W., Yang, H. C., Yang, S. Y., Horng, H. E., Hung, J. C., Chen, Y. C., et al. (2004). Preparation and properties of superparamagnetic nanoparticles with narrow size distribution and biocompatible. *J. Magn. Magn. Mater.* 283, 210–214. doi: 10.1016/j.jmmm.2004.05.022

Jin, A., Ozawa, T., Tajiri, K., Obata, T., Kondo, S., Kinoshita, K., et al. (2009). A rapid and efficient single-cell manipulation method for screening antigen-specific antibody–secreting cells from human peripheral blood. *Nat. Med.* 15, 1088–1092. doi: 10.1038/nm.1966

Kang, J. H., Krause, S., Tobin, H., Mammoto, A., Kanapathipillai, M., and Ingber, D. E. (2012). A combined micromagnetic-microfluidic device for rapid capture and culture of rare circulating tumor cells. *Lab Chip* 12, 2175–2175. doi: 10.1039/c2lc40072c

Karabacak, N. M., Spuhler, P. S., Fachin, F., Lim, E. J., Pai, V., Ozkumur, E., et al. (2014). Microfluidic, marker-free isolation of circulating tumor cells from blood samples. *Nat. Protoc.* 9, 694–694. doi: 10.1038/nprot.2014.044

Kauffmann, P., Ith, A., O'Brien, D., Gaude, V., Boué, F., Combe, S., et al. (2011). Diamagnetically trapped arrays of living cells above micromagnets. *Lab Chip* 11, 3153–3161. doi: 10.1039/c1lc20232d

Kaysen, J. H, Campbell, W. C, Majewski, R. R, Goda, F. O, Navar, G. L, Lewis, F. C, et al. (1999). Select de novo gene and protein expression during renal epithelial cell culture in rotating wall vessels is shear stress dependent. *J. Membr. Biol.* 168, 77–89. doi: 10.1007/s002329900499

Kedziorek, D. A., Muja, N., Walczak, P., Ruiz-Cabello, J., Gilad, A. A., Jie, C. C., et al. (2010). Gene expression profiling reveals early cellular responses to intracellular magnetic labeling with superparamagnetic iron oxide nanoparticles. *Magn. Reson. Med.* 63, 1031–1043. doi: 10.1002/mrm.22290

Kim, J. A., Choi, J. H., Kim, M., Rhee, W. J., Son, B., Jung, H. K., et al. (2013a). High-throughput generation of spheroids using magnetic nanoparticles for three-dimensional cell culture. *Biomaterials* 34, 8555–8563. doi: 10.1016/j.biomaterials.2013.07.056

Kim, J. A., Lee, H. J., Kang, H. J., and Park, T. H. (2009). The targeting of endothelial progenitor cells to a specific location within a microfluidic channel using magnetic nanoparticles. *Biomed. Microdevices* 11, 287–296. doi: 10.1007/s10544-008-9235-y

Kim, S., Han, S. I., Park, M. J., Jeon, C. W., Joo, Y. D., Choi, I. H., et al. (2013b). Circulating tumor cell microseparator based on lateral magnetophoresis and immunomagnetic nanobeads. *Anal. Chem.* 85, 2779–2786. doi: 10.1021/ac303284u

Kim, S., Im, W. S., Kang, L., Lee, S. T., Chu, K., and Kim, B. I. C, (2008a). The application of magnets directs the orientation of neurite outgrowth in cultured human neuronal cells. *J. Neurosci. Methods* 174, 91–96. doi: 10.1016/j.jneumeth.2008.07.005

Kim, S. M., Lee, S. H., and Suh, K. Y. (2008b). Cell research with physically modified microfluidic channels: a review. *Lab Chip* 8, 1015–1023. doi: 10.1039/b800835c

Kimura, T., Yamato, M., and Nara, A. (2004). Particle trapping and undulation of a liquid surface using a microscopically modulated magnetic field. *Langmuir* 20, 572–574. doi: 10.1021/la035768m

Kirby, D., Glynn, M., Kijanka, G., and Ducrée, J. (2015). Rapid and cost-efficient enumeration of rare cancer cells from whole blood by low-loss centrifugo-magnetophoretic purification under stopped-flow conditions. *Cytometry Part A* 87, 74–80. doi: 10.1002/cyto.a.22588

Kito, T., Shibata, R., Ishii, M., Suzuki, H., Himeno, T., Kataoka, Y., et al. (2013). iPS cell sheets created by a novel magnetite tissue engineering method for reparative angiogenesis. *Sci. Rep.* 3:1418. doi: 10.1038/srep01418

Knowlton, S., Joshi, A., Syrrist, P., Coskun, A. F., and Tasoglu, S. (2017). 3D-printed smartphone-based point of care tool for fluorescence- and magnetophoresis-based cytometry. *Lab Chip* 17, 2839–2851. doi: 10.1039/C7LC00706J

Knowlton, S. M, Sencan, I., Aytar, Y., Khoory, J., Heeney, M. M, Ghiran, I. C, et al. (2015). Sickle cell detection using a smartphone. *Sci. Rep.* 5:15022. doi: 10.1038/srep15022

Kose, A. R., Fischer, B., Mao, L., and Koser, H. (2009). Label-free cellular manipulation and sorting via biocompatible ferrofluids. *Proc. Natl. Acad. Sci. U.S.A.* 106, 21478–21483. doi: 10.1073/pnas.0912138106

Kostura, L., Kraitchman, D. L., Mackay, A. M., Pittenger, M. F., and Bulte, J. W. (2004). Feridex labeling of mesenchymal stem cells inhibits chondrogenesis but not adipogenesis or osteogenesis. *NMR Biomed.* 17, 513–517. doi: 10.1002/nbm.925

Krebs, M. D., Erb, R. M., Yellen, B. B., Samanta, B., Bajaj, A., Rotello, V. M., et al. (2009). Formation of ordered cellular structures in suspension via label-free negative magnetophoresis. *Nano Lett.* 9, 1812–1817. doi: 10.1021/nl803757u

Kumar, A., Narayanan, K., Chaudhary, R. K., Mishra, S., Kumar, S., Vinoth, K. J., et al. (2017). Current perspective of stem cell therapy in neurodegenerative and metabolic diseases. *Mol. Neurobiol.* 54, 7276–7296. doi: 10.1007/s12035-016-0217-4

Küstermann, E., Himmelreich, U., Kandal, K., Geelen, T., Ketkar, A., Wiedermann, D., et al. (2008). Efficient stem cell labeling for MRI studies. *Contrast Media Mol. Imaging* 3, 27–37. doi: 10.1002/cmmi.229

Kwak, B., Lee, J., Lee, D., Lee, K., Kwon, O., Kang, S., et al. (2017). Selective isolation of magnetic nanoparticle-mediated heterogeneity subpopulation of circulating tumor cells using magnetic gradient based microfluidic system. *Biosens. Bioelectron.* 88, 153–158. doi: 10.1016/j.bios.2016.08.002

Lai, M.-F., Chen, C.-Y., Lee, C.-P., Huang, H.-T., Ger, T.-R., and Wei, Z.-H. (2010). Cell patterning using microstructured ferromagnetic thin films. *Appl. Phys. Lett.* 96:183701. doi: 10.1063/1.3383229

Lara, O., Tong, X., Zborowski, M., Chalmers, J. J., Lara, O., Tong, X., et al. (2004). Enrichment of rare cancer cells through depletion of normal cells using density and ow-through, immunomagnetic cell separation. *Exp. Hematol.* 32, 891–904. doi: 10.1016/j.exphem.2004.07.007

Laurell, T., Petersson, F., and Nilsson, A. (2007). Chip integrated strategies for acoustic separation and manipulation of cells and particles. *Chem. Soc. Rev.* 36, 492–506. doi: 10.1039/B601326K

Leary, J. F., Szaniszlo, P., Prow, T. W., Reece, L. M., Wang, N., and Asmuth, D. M. (2002). "Importance of high-throughput cell separation technologies for genomics/proteomics-based clinical diagnostics," in *International Symposium on Biomedical Optics: SPIE* (San Jose, CA), 8.

Lee, C. S., Lee, H., and Westervelt, R. M. (2001). Microelectromagnets for the control of magnetic nanoparticles. *Appl. Phys. Lett.* 79, 3308–3310. doi: 10.1063/1.1419049

Lee, H., Purdon, A. M., and Westervelt, R. M. (2004). Manipulation of biological cells using a microelectromagnet matrix. *Appl. Phys. Lett.* 85, 1063–1065. doi: 10.1063/1.1776339

Lee, W. R., Oh, K. T., Park, S. Y., Yoo, N. Y., Ahn, Y. S., Lee, D. H., et al. (2011). Magnetic levitating polymeric nano/microparticular substrates for three-dimensional tumor cell culture. *Colloids and Surfaces B* 85, 379–384. doi: 10.1016/j.colsurfb.2011.02.021

Lei, K. F., Lin, B.-Y., and Tsang, N.-M. (2017). Real-time and label-free impedimetric analysis of the formation and drug testing of tumor spheroids formed via the liquid overlay technique. *RSC Adv.* 7, 13939–13946. doi: 10.1039/C7RA00209B

Lenshof, A., Johannesson, C., Evander, M., Nilsson, J., and Laurell, T. (2017). "Acoustic cell manipulation BT - microtechnology for cell manipulation and sorting," in *Microtechnology for Cell Manipulation and Sorting, Microsystems and Nanosystems,* eds W. Lee, P. Tseng, and D. Di Carlo (Cham: Springer International Publishing), 129–173.

Lenshof, A., and Laurell, T. (2010). Continuous separation of cells and particles in microfluidic systems. *Chem. Soc. Rev.* 39, 1203–1217. doi: 10.1039/b915999c

Li, P., Mao, Z., Peng, Z., Zhou, L., Chen, Y., Huang, P. H., et al. (2015). Acoustic separation of circulating tumor cells. *Proc. Natl. Acad. Sci. U.S.A.* 112, 4970–4975. doi: 10.1073/pnas.1504484112

Li, X., Yue, S., and Luo, Z. (2017). Mesenchymal stem cells in idiopathic pulmonary fibrosis. *Oncotarget* 8, 102600–102616. doi: 10.18632/oncotarget.18126

Lin, C. Y., Wei, P. L., Chang, W. J., Huang, Y. K., Feng, S. W., Lin, C. T., et al. (2013). Slow freezing coupled static magnetic field exposure enhances cryopreservative efficiency—A study on human erythrocytes. *PLoS ONE* 8:e58988. doi: 10.1371/journal.pone.0058988

Lin, R. Z., Chu, W. C., Chiang, C. C., Lai, C. H., and Chang, H. Y. (2008). Magnetic reconstruction of three-dimensional tissues from multicellular spheroids. *Tissue Eng. Part C Methods* 14, 197–205. doi: 10.1089/ten.tec.2008.0061

Lin, R. Z., and Chang, H. Y. (2008). Recent advances in three-dimensional multicellular spheroid culture for biomedical research. *Biotechnol. J.* 3, 1172–1184. doi: 10.1002/biot.200700228

Liu, G., Gao, J., Ai, H., and Chen, X. (2013). Applications and potential toxicity of magnetic iron oxide nanoparticles. *Small* 9, 1533–1545. doi: 10.1002/smll.201201531

Liu, Y. J., Guo, S. S., Zhang, Z. L., Huang, W. H., Baigl, D., Xie, M., et al. (2007). A micropillar-integrated smart microfluidic device for specific capture and sorting of cells. *Electrophoresis* 28, 4713–4722. doi: 10.1002/elps.200700212

Lo, C. M., Wang, H. B., Dembo, M., and Wang, Y. L. (2000). Cell movement is guided by the rigidity of the substrate. *Biophys. J.* 79, 144–152. doi: 10.1016/S0006-3495(00)76279-5

Luo, W.-Y., Tsai, S.-C., Hsieh, K., and Lee, G.-B. (2015). An integrated microfluidic platform for negative selection and enrichment of cancer cells. *J. Micromech. Microeng.* 25, 084007–084007. doi: 10.1088/0960-1317/25/8/084007

Mahmoudi, M., Azadmanesh, K., Shokrgozar, M. A., Journeay, W. S., and Laurent, S. (2011). Effect of nanoparticles on the cell life cycle. *Chem. Rev.* 111, 3407–3432. doi: 10.1021/cr1003166

Mairhofer, J., Roppert, K., and Ertl, P. (2009). Microfluidic systems for pathogen sensing: a review. *Sensors* 9, 4804–4823. doi: 10.3390/s90604804

Maredziak, M., Tomaszewski, K., Polinceusz, P., Lewandowski, D., and Marycz, K. (2017). Static magnetic field enhances the viability and proliferation rate of adipose tissue-derived mesenchymal stem cells potentially through activation of the phosphoinositide 3-kinase/Akt (PI3K/Akt) pathway. *Electromagn. Biol. Med.* 36, 45–54. doi: 10.3109/15368378.2016.1149860

Mathur, A., Ma, Z., Loskill, P., Jeeawoody, S., and Healy, K. E. (2016). *In vitro* cardiac tissue models: current status and future prospects. *Adv. Drug Deliv. Rev.* 96, 203–213. doi: 10.1016/j.addr.2015.09.011

Matsue, T., Matsumoto, N., and Uchida, I. (1997). Rapid micropatterning of living cells by repulsive dielectrophoretic force. *Electrochim. Acta* 42, 3251–3256. doi: 10.1016/S0013-4686(97)00175-8

Matsuura, K., Shimizu, T., and Okano, T. (2014). Toward the development of bioengineered human three-dimensional vascularized cardiac tissue using cell sheet technology. *Int. Heart J.* 55, 1–7. doi: 10.1536/ihj.13-337

Mattix, B., Olsen, T. R., Gu, Y., Casco, M., Herbst, A., Simionescu, D. T., et al. (2014a). Biological magnetic cellular spheroids as building blocks for tissue engineering. *Acta Biomater.* 10, 623–629. doi: 10.1016/j.actbio.2013.10.021

Mattix, B. M., Olsen, T. R., Casco, M., Reese, L., Poole, J. T., Zhang, J., et al. (2014b). Janus magnetic cellular spheroids for vascular tissue engineering. *Biomaterials* 35, 949–960. doi: 10.1016/j.biomaterials.2013.10.036

Melchels, F. P., Barradas, A. M., van Blitterswijk, C. A., de Boer, J., Feijen, J., and Grijpma, D. W. (2010). Effects of the architecture of tissue engineering scaffolds on cell seeding and culturing. *Acta Biomater.* 6, 4208–4217. doi: 10.1016/j.actbio.2010.06.012

Mirica, K. A., Ilievski, F., Ellerbee, A. K., Shevkoplyas, S. S., and Whitesides, G. M. (2011). Using magnetic levitation for three dimensional self-assembly. *Adv. Mater.* 23, 4134–4140. doi: 10.1002/adma.201101917

Mirica, K. A., Phillips, S. T., Mace, C. R., and Whitesides, G. M. (2010). Magnetic levitation in the analysis of foods and water. *J. Agric. Food Chem.* 58, 6565–6569. doi: 10.1021/jf100377n

Mirica, K. A., Shevkoplyas, S. S., Phillips, S. T., Gupta, M., and Whitesides, G. M. (2009). Measuring densities of solids and liquids using magnetic levitation: fundamentals. *J. Am. Chem. Soc.* 131, 10049–10058. doi: 10.1021/ja900920s

Mizuno, M., Yamada, M., Mitamura, R., Ike, K., Toyama, K., and Seki, M. (2013). Magnetophoresis-integrated hydrodynamic filtration system for size- and surface marker-based two-dimensional cell sorting. *Anal. Chem.* 85, 7666–7673. doi: 10.1021/ac303336f

Mo, W. C., Zhang, Z., j. Liu, Y., Bartlett, P. F., and He, R. Q. (2013). Magnetic shielding accelerates the proliferation of human neuroblastoma cell by promoting G1-phase progression. *PLoS ONE* 8:e54775. doi: 10.1371/journal.pone.0054775

Mo, W.-C., Zhang, Z.-J., Wang, D.-L., Liu, Y., Bartlett, P. F., and He, R.-Q. (2016). Shielding of the geomagnetic field alters actin assembly and inhibits cell motility in human neuroblastoma cells. *Sci. Rep.* 6:22624. doi: 10.1038/srep22624

Morais, P. C., Santos, R. L., Pimenta, A. C. M., Azevedo, R. B., and Lima, E. C. D. (2006). Preparation and characterization of ultra-stable biocompatible magnetic fluids using citrate-coated cobalt ferrite nanoparticles. *Thin Solid Films* 515, 266–270. doi: 10.1016/j.tsf.2005.12.079

Muslimov, A. R., Timin, A. S., Petrova, A. V., Epifanovskaya, O. S., Shakirova, A. I., Lepik, K. V., et al. (2017). Mesenchymal stem cells engineering: microcapsules-assisted gene transfection and magnetic cell separation. *ACS Biomater. Sci. Eng.* 3, 2314–2324. doi: 10.1021/acsbiomaterials.7b00482

Nam, J., Huang, H., Lim, H., Lim, C., and Shin, S. (2013). Magnetic separation of malaria-infected red blood cells in various developmental stages. *Anal. Chem.* 85, 7316–7323. doi: 10.1021/ac4012057

Nguyen, N. T. (2012). Micro-magnetofluidics: interactions between magnetism and fluid flow on the microscale. *Microfluid. Nanofluidics* 12, 1–16. doi: 10.1007/s10404-011-0903-5

Nishi, M., Matsumoto, R., Dong, J., and Uemura, T. (2013). Engineered bone tissue associated with vascularization utilizing a rotating wall vessel bioreactor. *J. Biomed. Mater. Res. Part A* 101, 421–427. doi: 10.1002/jbm.a.34340

Nyberg, S. L., Hardin, J., Amiot, B., Argikar, U. A., Remmel, R. P., and Rinaldo, P. (2005). Rapid, large-scale formation of porcine hepatocyte spheroids in a novel spheroid reservoir bioartificial liver. *Liver Transpl.* 11, 901–910. doi: 10.1002/lt.20446

Ogaki, R., Alexander, M., and Kingshott, P. (2010). Chemical patterning in biointerface science. *Materialstoday* 13, 22–35. doi: 10.1016/S1369-7021(10)70057-2

Okochi, M., Takano, S., Isaji, Y., Senga, T., Hamaguchi, M., and Honda, H. (2009). Three-dimensional cell culture array using magnetic force-based cell patterning for analysis of invasive capacity of BALB/3T3/v-src. *Lab Chip* 9, 3378–3384. doi: 10.1039/b909304d

Ozcivici, E., Garman, R., and Judex, S. (2007). High-frequency oscillatory motions enhance the simulated mechanical properties of non-weight bearing trabecular bone. *J. Biomech.* 40, 3404–3411. doi: 10.1016/j.jbiomech.2007.05.015

Ozcivici, E., and Judex, S. (2014). Trabecular bone recovers from mechanical unloading primarily by restoring its mechanical function rather than its morphology. *Bone* 67, 122–129. doi: 10.1016/j.bone.2014.05.009

Ozcivici, E., Luu, Y. K., Rubin, C. T., and Judex, S. (2010). Low-level vibrations retain bone marrow's osteogenic potential and augment recovery of trabecular bone during reambulation. *PLoS ONE* 5:e11178. doi: 10.1371/journal.pone.0011178

Ozkumur, E., Shah, A. M., Ciciliano, J. C., Emmink, B. L., Miyamoto, D. T., Brachtel, E., et al. (2013). Inertial focusing for tumor antigen–dependent and –independent sorting of rare circulating tumor cells. *Sci. Transl. Med.* 5:179ra147. doi: 10.1126/scitranslmed.3005616

Pamme, N. (2006). Magnetism and microfluidics. *Lab Chip* 6, 24–38. doi: 10.1039/B513005K

Pamme, N., and Manz, A. (2004). On-chip free-flow magnetophoresis: continuous flow separation of magnetic particles and agglomerates. *Anal. Chem.* 76, 7250–7256. doi: 10.1021/ac049183o

Pamme, N., and Wilhelm, C. (2006). Continuous sorting of magnetic cells via on-chip free-flow magnetophoresis. *Lab Chip* 6, 974–974. doi: 10.1039/b604542a

Parfenov, V. A., Koudan, E. V., Bulanova, E. A., Karalkin, P. A., DAS Pereira, F., Norkin, N. E., et al. (2018). Scaffold-free, label-free and nozzle-free biofabrication technology using magnetic levitational assembly. *Biofabrication* 10:034104. doi: 10.1088/1758-5090/aac900

Park, J. W., Lee, N. R., Cho, S. M., Jung, M. Y., Ihm, C., and Lee, D. S. (2015). Microdevice for separation of circulating tumor cells using embedded magnetophoresis with v-shaped Ni-Co nanowires and immuno-nanomagnetic beads. *ETRI J.* 37, 233–240. doi: 10.4218/etrij.15.0114.0572

Pavalko, F. M., Chen, N. X., Turner, C. H., Burr, D. B., Atkinson, S., Hsieh, Y. F., et al. (1998). Fluid shear-induced mechanical signaling in MC3T3-E1 osteoblasts requires cytoskeleton-integrin interactions. *Am. J. Physiol.* 275, C1591–C1601. doi: 10.1152/ajpcell.1998.275.6.C1591

Petersson, F., Aberg, L., Swärd-Nilsson, A. M., and Laurell, T. (2007). Free flow acoustophoresis: microfluidic-based mode of particle and cell separation. *Anal. Chem.* 79, 5117–5123. doi: 10.1021/ac070444e

Petersson, F., Nilsson, A., Jönsson, H., and Laurell, T. (2005). Carrier medium exchange through ultrasonic particle switching in microfluidic channels. *Anal. Chem.* 77, 1216–1221. doi: 10.1021/ac048394q

Peyman, S. A., Kwan, E. Y., Margarson, O., Iles, A., and Pamme, N. (2009). Diamagnetic repulsion—a versatile tool for label-free particle handling in microfluidic devices. *J. Chromatogr. A* 1216, 9055–9062. doi: 10.1016/j.chroma.2009.06.039

Picot, J., Guerin, C. L., Le Van Kim, C., and Boulanger, C. M. (2012). Flow cytometry: retrospective, fundamentals and recent instrumentation. *Cytotechnology* 64, 109–130. doi: 10.1007/s10616-011-9415-0

Plouffe, B. D., Mahalanabis, M., Lewis, L. H., Klapperich, C. M., and Murthy, S. K. (2012). Clinically relevant microfluidic magnetophoretic isolation of rare-cell populations for diagnostic and therapeutic monitoring applications. *Anal. Chem.* 84, 1336–1344. doi: 10.1021/ac2022844

Plouffe, B. D., Murthy, S. K., and Lewis, L. H. (2015). Fundamentals and application of magnetic particles in cell isolation and enrichment. *Rep. Prog. Phys.* 78:016601. doi: 10.1088/0034-4885/78/1/016601

Pohl, H. A., and Crane, J. S. (1971). Dielectrophoresis of cells. *Biophys. J.* 11, 711–727. doi: 10.1016/S0006-3495(71)86249-5

Pohl, H. A., and Hawk, I. (1966). Separation of living and dead cells by dielectrophoresis. *Science* 152, 647–649. doi: 10.1126/science.152.3722.647-a

Pratt, E. D., Huang, C., Hawkins, B. G., Gleghorn, J. P., and Kirby, B. J. (2011). Rare cell capture in microfluidic devices. *Chem. Eng. Sci.* 66, 1508–1522. doi: 10.1016/j.ces.2010.09.012

Qian, A. R, Li, D., Han, J., Gao, X., Di, S. Mi, Zhang, W., et al. (2012). Fractal dimension as a measure of altered actin cytoskeleton in MC3T3-E1 cells under simulated microgravity using 3-D/2-D clinostats. *IEEE Trans. Biomed. Eng.* 59, 1374–1380. doi: 10.1109/TBME.2012.2187785

Qian, A., Yin, D., Yang, P., Lv, Y., Tian, Z., and Shang, P. (2013). Application of diamagnetic levitation technology in biological sciences research. *IEEE Trans. Appl. Superconduct.* 23:3600305. doi: 10.1109/TASC.2012.2232919

Rivron, N. C., Rouwkema, J., Truckenmüller, R., Karperien, M., De Boer, J., and Van Blitterswijk, C. A. (2009). Tissue assembly and organization: developmental mechanisms in microfabricated tissues. *Biomaterials* 30, 4851–4858. doi: 10.1016/j.biomaterials.2009.06.037

Robert, D., Pamme, N., Conjeaud, H., Gazeau, F., Iles, A., and Wilhelm, C. (2011). Cell sorting by endocytotic capacity in a microfluidic magnetophoresis device. *Lab Chip* 11, 1902–1910. doi: 10.1039/c0lc00656d

Rodríguez-Villarreal, A. I., Tarn, M. D., Madden, L. A., Lutz, J. B., Greenman, J., Samitier, J., et al. (2011). Flow focussing of particles and cells based on their intrinsic properties using a simple diamagnetic repulsion setup. *Lab Chip* 11, 1240–1248. doi: 10.1039/C0LC00464B

Rucci, N., Migliaccio, S., Zani, B. M., Taranta, A., and Teti, A. (2002). Characterization of the osteoblast-like cell phenotype under microgravity conditions in the NASA-approved rotating wall vessel bioreactor (RWV). *J. Cell. Biochem.* 85, 167–179. doi: 10.1002/jcb.10120

Saliba, A. E., Saias, L., Psychari, E., Minc, N., Simon, D., Bidard, F. C., et al. (2010). Microfluidic sorting and multimodal typing of cancer cells in self-assembled magnetic arrays. *Proc. Nat. Acad. Sci. U.S.A.* 107, 14524–14529. doi: 10.1073/pnas.1001515107

Sarigil, O., Anil-Inevi, M., Mese, G., Tekin, H. C., and Ozcivici, E. (2018). Label-free density-based detection of adipocytes of bone marrow origin using magnetic levitation. *Biorxiv [Preprint]*. doi: 10.1101/462002

Sasaki, M., Abe, R., Fujita, Y., Ando, S., Inokuma, D., and Shimizu, H. (2008). Mesenchymal stem cells are recruited into wounded skin and contribute to wound repair by transdifferentiation into multiple skin cell type. *J. Immunol.* 180, 2581–2587. doi: 10.4049/jimmunol.180.4.2581

Schiele, N. R., Corr, D. T., Huang, Y., Raof, N. A., Xie, Y., and Chrisey, D. B. (2010). Laser-based direct-write techniques for cell printing. *Biofabrication* 2:032001. doi: 10.1088/1758-5082/2/3/032001

Sharifi, S., Behzadi, S., Laurent, S., Laird Forrest, M., Stroeve, P., and Mahmoudi, M. (2012). Toxicity of nanomaterials. *Chem. Soc. Rev.* 41, 2323–2343. doi: 10.1039/C1CS15188F

Shen, F., Hwang, H., Hahn, Y. K., and Park, J. K. (2012). Label-free cell separation using a tunable magnetophoretic repulsion force. *Anal. Chem.* 84, 3075–3081. doi: 10.1021/ac201505j

Shields, C. W., Reyes, C. D., and López, G. P. (2015). Microfluidic cell sorting: a review of the advances in the separation of cells from debulking to rare cell isolation. *Lab Chip* 15, 1230–1249. doi: 10.1039/C4LC01246A

Shimizu, K., Ito, A., Arinobe, M., Murase, Y., Iwata, Y., Narita, Y., et al. (2007a). Effective cell-seeding technique using magnetite nanoparticles and magnetic force onto decellularized blood vessels for vascular tissue engineering. *J. Biosci. Bioeng.* 103, 472–478. doi: 10.1263/jbb.103.472

Shimizu, K., Ito, A., and Honda, H. (2006). Enhanced cell-seeding into 3D porous scaffolds by use of magnetite nanoparticles. *J. Biomed. Mater. Res. B Appl. Biomater.* 77, 265–272. doi: 10.1002/jbm.b.30443

Shimizu, K., Ito, A., and Honda, H. (2007b). Mag-seeding of rat bone marrow stromal cells into porous hydroxyapatite scaffolds for bone tissue engineering. *J. Biosci. Bioeng.* 104, 171–177. doi: 10.1263/jbb.104.171

Shimizu, K., Ito, A., Yoshida, T., Yamada, Y., Ueda, M., and Honda, H. (2007c). Bone tissue engineering with human mesenchymal stem cell sheets constructed using magnetite nanoparticles and magnetic force. *J. Biomed. Mater. Res. B Appl. Biomat.* 82, 471–480. doi: 10.1002/jbm.b.30752

Soenen, S. J., and De Cuyper, M. (2010). Assessing iron oxide nanoparticle toxicity *in vitro*: current status and future prospects. *Nanomedicine* 5, 1261–1275. doi: 10.2217/nnm.10.106

Souza, G. R. (2013). *3D Cell Viability Assay*. U.S. Patent Application No. 13/995,610. Google Patents.

Souza, G. R., Molina, J. R., Raphael, R. M., Ozawa, M. G., Stark, D. J., Levin, C. S., et al. (2010). Three-dimensional tissue culture based on magnetic cell levitation. *Nat. Nanotechnol.* 5, 291–296. doi: 10.1038/nnano.2010.23

Stephens, M., Talary, M. S., Pethig, R., Burnett, A. K., and Mills, K. I. (1996). The dielectrophoresis enrichment of CD34+ cells from peripheral blood stem cell harvests. *Bone Marrow Transplant.* 18, 777–782.

Sugaya, S., Yamada, M., and Seki, M. (2012). "Manipulation of cells and cell spheroids using collagen hydrogel microbeads prepared by microfluidic devices," in *Micro-NanoMechatronics and Human Science (MHS), 2012 International Symposium on: IEEE)* (Nagoya), 435–438.

Sullivan, K., Balin, A. K., and Allen, R. G. (2011). Effects of static magnetic fields on the growth of various types of human cells. *Bioelectromagnetics* 32, 140–147. doi: 10.1002/bem.20624

Tanaka, F., Yoneda, K., Kondo, N., Hashimoto, M., Takuwa, T., Matsumoto, S., et al. (2009). Circulating tumor cell as a diagnostic marker in primary lung cancer. *Clin. Cancer Res.* 15, 6980–6986. doi: 10.1158/1078-0432.CCR-09-1095

Tang, S. Y., Zhang, W., Soffe, R., Nahavandi, S., Shukla, R., and Khoshmanesh, K. (2014). High resolution scanning electron microscopy of cells using dielectrophoresis. *PLoS ONE* 9:e104109. doi: 10.1371/journal.pone.0104109

Tasoglu, S., Diller, E., Guven, S., Sitti, M., and Demirci, U. (2014). Untethered micro-robotic coding of three-dimensional material composition. *Nat. Commun.* 5:3124. doi: 10.1038/ncomms4124

Tasoglu, S., Kavaz, D., Gurkan, U. A., Guven, S., Chen, P., Zheng, R., et al. (2013). Paramagnetic levitational assembly of hydrogels. *Adv. Mater.* 25, 1137–1143. doi: 10.1002/adma.201200285

Tasoglu, S., Khoory, J. A., Tekin, H. C., Thomas, C., Karnoub, A. E., Ghiran, I. C., et al. (2015a). Levitational image cytometry with temporal resolution. *Adv. Mater.* 27, 3901–3908. doi: 10.1002/adma.201405660

Tasoglu, S., Yu, C. H., Liaudanskaya, V., Guven, S., Migliaresi, C., and Demirci, U. (2015b). Magnetic levitational assembly for living material fabrication. *Adv. Health. Mater.* 4, 1469–1476. doi: 10.1002/adhm.201500092

Tekin, H. C., and Gijs, M. A. (2013). Ultrasensitive protein detection: a case for microfluidic magnetic bead-based assays. *Lab Chip* 13, 4711–4739. doi: 10.1039/c3lc50477h

Thevenot, P., Sohaebuddin, S., Poudyal, N., Liu, J. P., and Tang, L. (2008). "Magnetic nanoparticles to enhance cell seeding and distribution in tissue engineering scaffolds," in *Nanotechnology, 2008. NANO'08. 8th IEEE Conference on: IEEE* (Arlington, TX), 646–649.

Thiel, A., Scheffold, A., and Radbruch, A. (1998). Immunomagnetic cell sorting-pushing the limits. *Immunotechnology* 4, 89–96. doi: 10.1016/S1380-2933(98)00010-4

Timmins, N. E, Dietmair, S., and Nielsen, L. (2004). Hanging-drop multicellular spheroids as a model of tumour angiogenesis. *Angiogenesis* 7, 97–103. doi: 10.1007/s10456-004-8911-7

Tocchio, A., Durmus, N. G., Sridhar, K., Mani, V., Coskun, B., El Assal, R., et al. (2017). Magnetically guided self-assembly and coding of 3D living architectures. *Advan. Mater*. 30:1705034. doi: 10.1002/adma.201705034

Tomitaka, A., Koshi, T., Hatsugai, S., Yamada, T., and Takemura, Y. (2011). Magnetic characterization of surface-coated magnetic nanoparticles for biomedical application. *J. Magn. Magn. Mater.* 323, 1398–1403. doi: 10.1016/j.jmmm.2010.11.054

Toss, A., Mu, Z., Fernandez, S., and Cristofanilli, M. (2014). CTC enumeration and characterization: moving toward personalized medicine. *Ann. Transl. Med.* 2:108. doi: 10.3978/j.issn.2305-5839.2014.09.06

Tseng, H., Balaoing, L. R., Grigoryan, B., Raphael, R. M., Killian, T. C., Souza, G. R., et al. (2014). A three-dimensional Co-culture model of the aortic valve using magnetic levitation. *Acta Biomater.* 10, 173–182. doi: 10.1016/j.actbio.2013.09.003

Tseng, H., Gage, J. A., Haisler, W. L., Neeley, S. K., Shen, T., Hebel, C., et al. (2016). A high-throughput *in vitro* ring assay for vasoactivity using magnetic 3D bioprinting. *Sci. Rep.* 6:30640. doi: 10.1038/srep30640

Tseng, H., Gage, J. A., Raphael, R. M., Moore, R. H., Killian, T. C., Grande-Allen, K. J., et al. (2013). Assembly of a three-dimensional multitype bronchiole coculture model using magnetic levitation. *Tissue Eng. Part C Methods* 19, 665–675. doi: 10.1089/ten.tec.2012.0157

Türker, E., Demirçak, N., and Arslan-Yildiz, A. (2018). Scaffold-free three-dimensional cell culturing using magnetic levitation. *Biomater. Sci.* 6, 1745–1753. doi: 10.1039/c8bm00122g

Umemoto, T., Yamato, M., Nishida, K., and Okano, T. (2013). Regenerative medicine of cornea by cell sheet engineering using temperature-responsive culture surfaces. *Chin. Sci. Bull.* 58, 4349–4356. doi: 10.1007/s11434-013-5742-1

Veiseh, M., Veiseh, O., Martin, M. C., Asphahani, F., and Zhang, M. (2007). Short peptides enhance single cell adhesion and viability on microarrays. *Langmuir* 23, 4472–4479. doi: 10.1021/la062849k

Voldman, J. (2006). Electrical forces for microscale cell manipulation. *Annu. Rev. Biomed. Eng.* 8, 425–454. doi: 10.1146/annurev.bioeng.8.061505.095739

Vona, G., Sabile, A., Louha, M., Sitruk, V., Romana, S., Schútze, K., et al. (2000). Isolation by size of epithelial tumor cells: a new method for the immunomorphological and molecular characterization of circulatingtumor cells. *Am. J. Pathol.* 156, 57–63. doi: 10.1016/S0002-9440(10)64706-2

Wang, C., Ye, M., Cheng, L., Li, R., Zhu, W., Shi, Z., et al. (2015). Simultaneous isolation and detection of circulating tumor cells with a microfluidic silicon-nanowire-array integrated with magnetic upconversion nanoprobes. *Biomaterials* 54, 55–62. doi: 10.1016/j.biomaterials.2015.03.004

Wang, J., Xiang, B., Deng, J., Freed, D. H., Arora, R. C., and Tian, G. (2016a). Inhibition of viability, proliferation, cytokines secretion, surface antigen expression, and adipogenic and osteogenic differentiation of adipose-derived stem cells by seven-day exposure to 0.5 T static magnetic fields. *Stem Cells Int.* 2016:7168175. doi: 10.1155/2016/7168175

Wang, M. M., Tu, E., Raymond, D. E., Yang, J. M., Zhang, H., Hagen, N., et al. (2004). Microfluidic sorting of mammalian cells by optical force switching. *Nat. Biotechnol.* 23:83. doi: 10.1038/nbt1050

Wang, Z. M., Wu, R. G., Wang, Z. P., and Ramanujan, R. V. (2016b). Magnetic trapping of bacteria at low magnetic fields. *Sci. Rep.* 6:26945. doi: 10.1038/srep26945

Whatley, B. R., Li, X., Zhang, N., and Wen, X. (2014). Magnetic-directed patterning of cell spheroids. *J. Biomed. Mater. Res. A* 102, 1537–1547. doi: 10.1002/jbm.a.34797

Wiklund, M., Günther, C., Lemor, R., Jäger, M., Fuhr, G., and Hertz, H. M. (2006). Ultrasonic standing wave manipulation technology integrated into a dielectrophoretic chip. *Lab Chip* 6, 1537–1544. doi: 10.1039/B612064B

Wildgruber, M., Lee, H., Chudnovskiy, A., Yoon, T.J., Etzrodt, M., Pittet, M. J., et al. (2009). Monocyte subset dynamics in human atherosclerosis can be profiled with magnetic nano-sensors. *PLoS ONE* 4:e5663. doi: 10.1371/journal.pone.0005663

Winkleman, A., Gudiksen, K. L., Ryan, D., Whitesides, G. M., Greenfield, D., and Prentiss, M. (2004). A magnetic trap for living cells suspended in a paramagnetic buffer. *Appl. Phys. Lett.* 85, 2411–2413. doi: 10.1063/1.1794372

Wong, Q. Y., Liu, N., Koh, C. G., Li, H. Y., and Lew, W. S. (2016). Isolation of magnetically tagged cancer cells through an integrated magnetofluidic device. *Microfluid. Nanofluidics* 20, 1–9. doi: 10.1007/s10404-016-1804-4

Wu, H. W., Hsu, R. C., Lin, C. C., Hwang, S. M., and Lee, G. B. (2010). An integrated microfluidic system for isolation, counting, and sorting of hematopoietic stem cells. *Biomicrofluidics* 4:024112. doi: 10.1063/1.3454767

Wuest, S. L., Richard, S., Kopp, S., Grimm, D., and Egli, M. (2015). Simulated microgravity: critical review on the use of random positioning machines for mammalian cell culture. *Biomed. Res. Int.* 2015:971474. doi: 10.1155/2015/971474

Xu, T., Zhao, W., Zhu, J. M., Albanna, M. Z., Yoo, J. J., and Atala, A. (2013). Complex heterogeneous tissue constructs containing multiple cell types prepared by inkjet printing technology. *Biomaterials* 34, 130–139. doi: 10.1016/j.biomaterials.2012.09.035

Yamamoto, Y., Ito, A., Fujita, H., Nagamori, E., Kawabe, Y., and Kamihira, M. (2010). Functional evaluation of artificial skeletal muscle tissue constructs fabricated by a magnetic force-based tissue engineering technique. *Tissue Eng. Part A* 17, 107–114. doi: 10.1089/ten.tea.2010.0312

Yamamoto, Y., Ito, A., Kato, M., Kawabe, Y., Shimizu, K., Fujita, H., et al. (2009). Preparation of artificial skeletal muscle tissues by a magnetic force-based tissue engineering technique. *J. Biosci. Bioeng.* 108, 538–543. doi: 10.1016/j.jbiosc.2009.05.019

Yamato, M., and Okano, T. (2004). Cell sheet engineering. *Materialstoday* 7, 42–47. doi: 10.1016/S1369-7021(04)00234-2

Yang, J., Yamato, M., Kohno, C., Nishimoto, A., Sekine, H., Fukai, F., et al. (2005). Cell sheet engineering: recreating tissues without biodegradable scaffolds. *Biomaterials* 26, 6415–6422. doi: 10.1016/j.biomaterials.2005.04.061

Yoo, C. E., Park, J. M., Moon, H. S., Joung, J. G., Son, D. S., Jeon, H. J., et al. (2016). Vertical magnetic separation of circulating tumor cells for somatic genomic-alteration analysis in lung cancer patients. *Sci. Rep.* 6: 37392. doi: 10.1038/srep37392

Yu, M., Bardia, A., Wittner, B. S., Stott, S. L., Smas, M. E., Ting, D. T., et al. (2013). Circulating breast tumor cells exhibit dynamic changes in epithelial and mesenchymal composition. *Science* 339, 580–584. doi: 10.1126/science.1228522

Zborowski, M., Ostera, G. R., Moore, L. R., Milliron, S., Chalmers, J. J., and Schechter, A. N. (2003). Red blood cell magnetophoresis. *Biophys. J.* 84, 2638–2645. doi: 10.1016/S0006-3495(03)75069-3

Zeng, J., Deng, Y., Vedantam, P., Tzeng, T. R., and Xuan, X. (2013). Magnetic separation of particles and cells in ferrofluid flow through a straight microchannel using two offset magnets. *J. Magn. Magn. Mater.* 346, 118–123. doi: 10.1016/j.jmmm.2013.07.021

Zeng, L., Qiu, L., Yang, X. T., Zhou, Y. H., Du, J., Wang, H. Y., et al. (2015). Isolation of lung multipotent stem cells using a novel microfluidic magnetic activated cell sorting system. *Cell Biol. Int.* 39, 1348–1353. doi: 10.1002/cbin.10513

Zhang, J., Ding, C., and Shang, P. (2014). Alterations of mineral elements in osteoblast during differentiation under hypo, moderate and high static magnetic fields. *Biol. Trace Elem. Res.* 162, 153–157. doi: 10.1007/s12011-014-0157-7

Zhang, L., Hou, Y., Li, Z., Ji, X., Wang, Z., Wang, H., et al. (2017a). 27 T ultra-high static magnetic field changes orientation and morphology of mitotic spindles in human cells. *Elife* 6:e22911. doi: 10.7554/eLife.22911

Zhang, L., Ji, X., Yang, X., and Zhang, X. (2017b). Cell type-and density-dependent effect of 1 T static magnetic field on cell proliferation. *Oncotarget* 8:13126. doi: 10.18632/oncotarget.14480

Zhang, L., Wang, J., Wang, H., Wang, W., Li, Z., Liu, J., et al. (2016). Moderate and strong static magnetic fields directly affect EGFR kinase domain orientation to inhibit cancer cell proliferation. *Oncotarget* 7:41527. doi: 10.18632/oncotarget.9479

Zhang, X., Yarema, K., and Xu, A. (2017c). "Parameters of magnetic fields and their differential biological effects," in *Biological Effects of Static Magnetic Fields* (Singapore: Springer), 3–25.

Zhao, W., Cheng, R., Jenkins, B. D., Zhu, T., Okonkwo, N. E., Jones, C. E., et al. (2017a). Label-free ferrohydrodynamic cell separation of circulating tumor cells. *Lab Chip*. 17, 3097–3111. doi: 10.1039/C7LC00680B

Zhao, W., Cheng, R., Lim, S. H., Miller, J. R., Zhang, W., Tang, W., et al. (2017b). Biocompatible and label-free separation of cancer cells of cell culture lines from white blood cells in ferrofluids. *Lab Chip*. 17, 2243–2255. doi: 10.1039/C7LC00327G

Zhao, W., Cheng, R., Miller, J. R., and Mao, L. (2016). Label-free microfluidic manipulation of particles and cells in magnetic liquids. *Adv. Funct. Mater.* 26, 3916–3932. doi: 10.1002/adfm.201504178

Zhao, W., Zhu, T., Cheng, R., Liu, Y., He, J., Qiu, H., et al. (2015). Label-free and continuous-flow ferrohydrodynamic separation of HeLa cells and blood cells in biocompatible ferrofluids. *Adv. Funct. Mater.* 26, 3990–3998. doi: 10.1002/adfm.201503838

Zhu, T., Cheng, R., Lee, S. A., Rajaraman, E., Eiteman, M. A., Querec, T. D., et al. (2012). Continuous-flow ferrohydrodynamic sorting of particles and cells in microfluidic devices. *Microfluid. Nanofluidics* 13, 645–654. doi: 10.1007/s10404-012-1004-9

Zhu, T., Marrero, F., and Mao, L. (2010). Continuous separation of non-magnetic particles inside ferrofluids. *Microfluid. Nanofluidics* 9, 1003–1009. doi: 10.1007/s10404-010-0616-1

Conflict of Interest Statement: The authors declare that the research was conducted in the absence of any commercial or financial relationships that could be construed as a potential conflict of interest.

frontiers
in Bioengineering and Biotechnology

REVIEW
published: 07 May 2019
doi: 10.3389/fbioe.2019.00100

The Need for Physiological Micro-Nanofluidic Systems of the Brain

Jean-Philippe Frimat[1,2] *and Regina Luttge*[1*]

[1] Neuro-Nanoscale Engineering Group, Microsystems Section & ICMS Institute for Complex Molecular Systems, Eindhoven University of Technology, Eindhoven, Netherlands, *[2] Department of Neurosurgery, Maastricht University Medical Centre, School for Mental Health and Neuroscience, Eindhoven, Netherlands*

In this article, we review brain-on-a-chip models and associated underlying technologies. Micro-nanofluidic systems of the brain can utilize the entire spectrum of organoid technology. Notably, there is an urgent clinical need for a physiologically relevant microfluidic platform that can mimic the brain. Brain diseases affect millions of people worldwide, and this number will grow as the size of elderly population increases, thus making brain disease a serious public health problem. Brain disease modeling typically involves the use of *in vivo* rodent models, which is time consuming, resource intensive, and arguably unethical because many animals are required for a single study. Moreover, rodent models may not accurately predict human diseases, leading to erroneous results, thus rendering animal models poor predictors of human responses to treatment. Various clinical researchers have highlighted this issue, showing that initial physiological descriptions of animal models rarely encompass all the desired human features, including how closely the model captures what is observed in patients. Consequently, such animal models only mimic certain disease aspects, and they are often inadequate for studying how a certain molecule affects various aspects of a disease. Thus, there is a great need for the development of the brain-on-a-chip technology based on which a human brain model can be engineered by assembling cell lines to generate an organ-level model. To produce such a brain-on-a-chip device, selection of appropriate cells lines is critical because brain tissue consists of many different neuronal subtypes, including a plethora of supporting glial cell types. Additionally, cellular network bio-architecture significantly varies throughout different brain regions, forming complex structures and circuitries; this needs to be accounted for in the chip design process. Compartmentalized microenvironments can also be designed within the microphysiological cell culture system to fulfill advanced requirements of a given application. On-chip integration methods have already enabled advances in Parkinson's disease, Alzheimer's disease, and epilepsy modeling, which are discussed herein. In conclusion, for the brain model to be functional, combining engineered microsystems with stem cell (hiPSC) technology is specifically beneficial because hiPSCs can contribute to the complexity of tissue architecture based on their level of differentiation and thereby, biology itself.

Keywords: brain models, brain-on-a-chip, micro- and nanofluidics, organ-on-a-chip, organoids

Edited by:
Massimo Alberti,
*Agency for Science, Technology and Research (A*STAR), Singapore*

Reviewed by:
Abhigyan Satyam,
Harvard Medical School, United States
Dilip Thomas,
Stanford University, United States

***Correspondence:**
Regina Luttge
r.luttge@tue.nl

Specialty section:
This article was submitted to Tissue Engineering and Regenerative Medicine,
a section of the journal Frontiers in Bioengineering and Biotechnology

Received: *03 September 2018*
Accepted: *18 April 2019*
Published: *07 May 2019*

Citation:
Frimat J-P and Luttge R (2019) The Need for Physiological Micro-Nanofluidic Systems of the Brain.
Front. Bioeng. Biotechnol. 7:100.
doi: 10.3389/fbioe.2019.00100

INTRODUCTION

We suggest that there is an urgent medical need for physiologically relevant microfluidic platforms that can mimic the brain. Therefore, what are the technical arguments for following such a radically new approach? A previous World Health Organization (WHO) report showed that neurological disorders, ranging from epilepsy, Alzheimer's disease, and stroke to headache, affect up to one billion people worldwide (Dua et al., 2006). An estimated 6.8 million people die every year due to neurological disorders. In 2004, the economic cost of neurological diseases in Europe was estimated at between 139 and 386 billion euros (Andlin-Sobocki et al., 2005).

Research with models of brain disorders typically involves the use of rodents *in vivo*, which is time consuming, resource intensive, and arguably unethical because many animals are required for a single study (Festing and Wilkinson, 2007). Moreover, rodent models may not accurately predict human disease and may lead to erroneous results (i.e., false positives; Perrin, 2014), rendering such animal models as poor predictors of human responses. Various clinical researchers have highlighted this issue, showing that the initial physiological descriptions of animal models rarely encompass all of the desired human features, including how closely the model captures what is observed in patients. Consequently, such animal models are often inadequate for studying how a certain molecule affects various aspects of a disease (Perrin, 2014). Thus, there is presently a great need for the development of better models to investigate the brain and its diseases.

In neurobiological research, microfluidic channels and various interconnected compartment geometries have been used to study axon guidance (Francisco et al., 2007) and neuronal regeneration processes (Taylor et al., 2003, 2005). Spatiotemporal investigations of electrophysiological function have also been performed on microelectrode arrays (MEAs) (Ban et al., 2007; van Vliet et al., 2007). We recently introduced organ-on-a-chip technology, which yields miniaturized systems that support two- and three-dimensional (2D and 3D) cell culture formats (Frimat et al., 2015; Bastiaens et al., 2018; Moonen et al., 2018; Xie et al., 2018). These on-chip low-volume culture systems can forward-engineer brain-like tissues as well as other organ features from a small number of human cells and simply rely on internal diffusion facilitated by the microfluidic approach (Ronaldson-Bouchard and Vunjak-Novakovic, 2018). A lung-on-a-chip study demonstrated the use of stem cells assembled to provide an organotypic model resembling full organ structure rather than only mimicking certain aspects of organ function (Huh et al., 2010). Although this study is a fascinating development of our era, it had a basic science scope concerning disease modeling. Micro- and nanotechnologies have significantly contributed to the development of better human organ and disease models. However, to successfully engineer a brain-on-a-chip model, researchers must produce an *in vitro* model that accurately mimics critical cellular events observed *in vivo*. Therefore, to construct functional brain tissue within a miniaturized system, certain criteria must be met.

Considering that brain disorders are the number one factor reducing quality of life in aging societies, we review the advances in and requirements of microsystems that mimic brain function. First, we summarize the literature concerning the essential technical features involved in the design of brain-on-a-chip systems. Second, we address the clinical requirements of and medical need for brain-on-a-chip systems by reviewing previous applied studies. Finally, we argue that there is not only a clear need for brain-on-a-chip technology in biomedical research, but also, given the dedicated efforts of engineers to improve the performance of brain-on-a-chip devices as well as their high biological and clinical relevance, technological solutions can be achieved.

BRAIN-ON-A-CHIP TECHNOLOGY AND BRAIN MODELS

As previously mentioned, a brain-on-a-chip is a micro-engineered chip platform that mimics the physiological microenvironment and tissue of a particular brain region. In this section, we discuss detailed brain-on-a-chip design features and culture methods, including their applications to brain disease modeling.

Conventional Methods for 3D Neuronal Cell Cultures

When designing brain models, cellular mass transport (Yamada and Cukierman, 2007) is an essential aspect to consider to engineer the correct microenvironment for different cellular events (**Figure 1A**). Various technologies exist that mainly attempt to mimic the *in vivo* microenvironment of the central nervous system (CNS). Alépée et al. (2014) reviewed the conventional methods for designing organotypic brain models (**Figure 1B**). For example, electrophysiological recordings of neuronal tissues primarily rely on rodent brain slices (Qi et al., 2019). Co-culture models with a glial cell layer overlaid by a second neuron layer have also been studied (Viviani, 2006). To model the blood-brain barrier, transwell culture systems have been developed in which neurons and endothelial cells separated by a porous membrane can be grown and permeability assays as well as transendothelial electrical resistance (TEER) measurements can be performed (Patabendige et al., 2013). Dissociated rodent brain cells have also been used with the development of methods to isolate and re-aggregate 3D brain cell cultures (Bart Schurink and Luttge, 2013). Moreover, neurospheres can be grown on low-adherence plastic plates and then replated onto an adhesive substrate, which supports the outgrowth of radial glia and migrating neurons (Jensen and Parmar, 2006). Finally, using stem cell technology, neuronal tissue can spontaneously self-assemble into organoids (Lancaster et al., 2013), which will be discussed in section Human Induced Pluripotent Stem Cell Technology. However, these methods are insufficient and too reductionist for disease modeling.

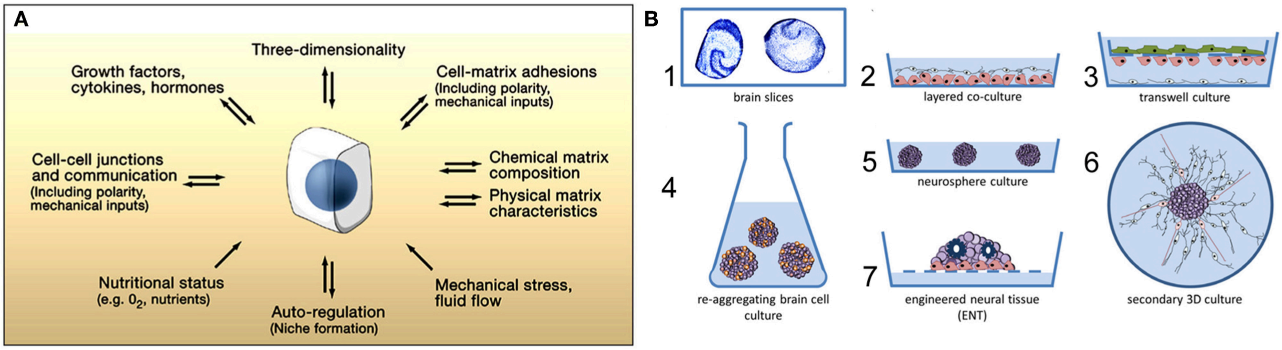

FIGURE 1 | (A) Microenvironmental factors affecting cell behavior. Numerous spatially and temporally changing microenvironmental aspects may affect how accurately a 3D model reflects cellular behavior *in vivo*. Conversely, cells (center) can actively modify their local microenvironment. Figure reprinted with permission, previously published in Cell, Yamada and Cukierman (2007). **(B)** Conventional methods for designing 3D *in vitro* models of the nervous system. The first 3D *in vitro* models used rodent brain slices (1) or co-culture models consisting of neurons placed directly on top of a glial cell layer (2). Transwell culture models are also used to mimic the blood-brain barrier *in vitro* (3). Re-aggregating brain cell culture models can also be formed by the spontaneous re-aggregation of dissociated rodent brain cells (4). Neurospheres can be generated and kept in low-adherence plastic plates (5) with secondary 3D cultures being produced by plating these neurospheres onto a planar adhesive substrate (6). Engineered neural tissue is generated by growing highly concentrated stem cell suspensions on a membrane floating at the air-liquid interface. This tissue is polarized (e.g., astrocytes at the bottom), consists of several neuronal subtypes, and shows rosettes as neural tube-like structures (7). Figure reprinted with permission, previously published in ALTEX, Alépée et al. (2014).

Chip Technologies Using Various Combination of Microfluidics, Electrode Arrays, and 3D Cell Cultures

To a large extent, brain model advances have been limited due to a lack of controlled environments which recreate CNS microenvironment characteristics. The established cell culture models mimicking brain function are too simplistic, whereas more physiologically relevant approaches, such as the use of *ex vivo* brain slices or *in vivo* experiments, provide limited control and make information extraction difficult. Therefore, advances in nano- and microfabrication technology have increased the developmental potential of brain-on-a-chip devices (**Figures 2A–D**; Park et al., 2006). These advances include microfluidic platforms that have been engineered for different neuroscience research needs, such as greater visualization (Lu et al., 2012) and quantification (Park et al., 2014; Zhao et al., 2014), network formation control (Frimat et al., 2010; Dinh et al., 2013), studying neuronal co-culture effects (**Figures 2E,F**; Dinh et al., 2013), improving brain slice culture performance, and examining on-chip electrophysiology (Massobrio et al., 2016). The development of compartmental culturing platform for primary neurons, which combines microfluidics with surface patterning (**Figure 2**), has allowed for real-time monitoring of axons (Zhao et al., 2014) and synapses (Taylor et al., 2010) as well as studies of brain injury and trauma (Taylor et al., 2005). Another important platform is the transwell assay, which enables the study of organ membrane function (Jang et al., 2013). The development of microfabrication methods yielding novel platforms for complex tissue constructs, such as the blood brain barrier (BBB), has received considerable attention (Banks, 2016).

These platform technology advances have enabled the production of various brain structures, including the cerebral cortical layers, which were engineered by intercalating neuron-hydrogel layers with plain hydrogel layers (**Figure 3A**; Kunze et al., 2011a). These engineered cortical layers exhibited different synaptic densities per layer as well as chemical gradients of growth factors (Cheng et al., 2007; Wong et al., 2008; Kunze et al., 2011c). In addition, neurospheroids, which are 3D non-hydrogel-based brain models, have also been developed (Choi et al., 2010). Choi et al. (2010) cultured cells from all six layers of the rat cortex at the bottom of concave microwells and investigated network formation inside of the neurospheroids. More detailed 3D brain models have also attempted to include the BBB using microfluidic approaches. The BBB is a 3D multicellular structure of the brain which regulates the passage of molecules from the blood to the brain and has profound implications for modeling disease responses to drugs (Vandenhaute et al., 2012; Banks, 2016). In BBB models, intersecting microfluidic channels are separated by a porous polycarbonate membrane upon which endothelial cells (vascular) and astrocytes (brain) are cultured on opposite sides, which essentially mimics the BBB (Griep et al., 2013). This membrane also allows for TEER measurements for barrier characterization (Odijk et al., 2015; van der Helm et al., 2016). Alternatively, a hollow fiber-like design (i.e., synthetic microvasculature, SyM-BBB) with enhanced visual capabilities has also been developed (Achyuta et al., 2013; Prabhakarpandian et al., 2013). These models have elucidated how drugs or toxins can breach the BBB and enter the brain microenvironment. Another brain model platform combines 3D cell cultures or samples with MEA systems, which allows for real-time electrical readouts of cells as well as the identification of electrical signatures associated with neurotoxicity (Pancrazio et al., 2003; Wölfer et al., 2006). Further advancement in this area has led to the development of 3D MEAs (**Figure 3B**) which convey 3D connectivity information (Köhling et al., 2005; Musick et al., 2009). Moreover, a system has been established that allows for 3D perfusion by using an

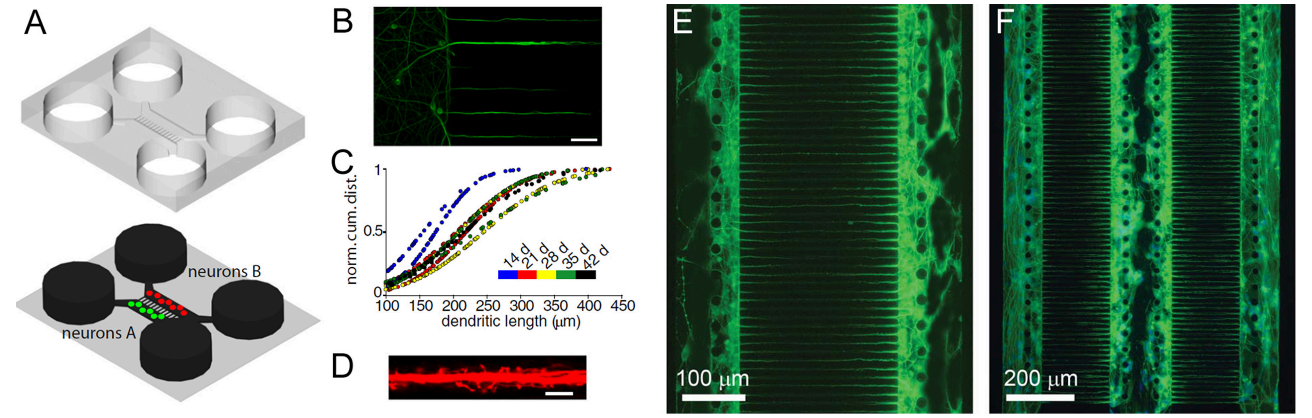

FIGURE 2 | Dendrites grow into the microgrooves of microfluidic chambers. **(A)** Schematic of a microfluidic chamber. **(B)** Fluorescence image of dendrites extending into microgrooves (MAP2, green; scale bar, 50 μm). **(C)** Dendritic length within microgrooves as a function of days in culture. **(D)** Fluorescence image of dendritic spines within microgrooves (scale bar, 10 μm). Figure reprinted with permission, previously published in Neuron, Taylor et al. (2010). Highly interconnected SH-SY5Y co-cultures in two **(E)** and three **(F)** compartments. Neurons and neurite outgrowths are immunostained for β-III tubulin following culture for 5 days. Figure reprinted with permission, previously published in Lab on a Chip, Dinh et al. (2013).

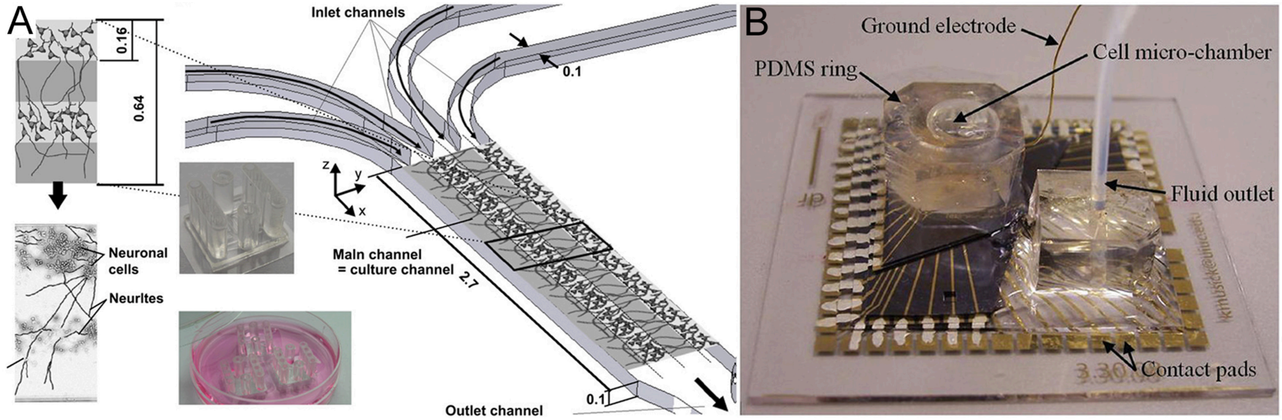

FIGURE 3 | (A) Three-dimensional layers of the cerebral cortex, which were engineered using intercalating neuron-hydrogel layers. This drawing illustrates the layered structure of the 3D neural cell culture. The hydrogel or cell-loaded hydrogel flow through four inlet, main, and outlet channels. The two inserts show the final microfluidic device fabricated using polydimethylsiloxane (top insert) and three devices placed in a Petri dish for incubation during cell culture (bottom insert). Figure reprinted with permission, previously published in Biomaterials, Kunze et al. (2011a). **(B)** Three-dimensional microelectrode array for recording dissociated neuronal cultures. Figure reprinted with permission, previously published in Lab on a Chip, Musick et al. (2009).

active 3D microscaffold system with fluid perfusion for culturing *in vitro* neuronal networks (Rowe et al., 2007).

Human Induced Pluripotent Stem Cell Technology

An alternative brain model that utilizes 3D culture involves the use of stem cell technology to engineer neural tissues which grow directly from neurospheres, yielding organoids (Lancaster et al., 2013). Although the aforementioned technologies allow for the development of brain-on-a-chip platforms, the cell sources used in such models must be carefully considered. Stem cell technology has been a giant-leap forward in the design of brain organoids; however, human induced pluripotent stem cells (hiPSCs) are an attractive alternative for on-chip brain modeling. HiPSCs have several advantages over immortalized neuronal cell lines or primary animal brain cells. HiPSCs can be obtained from human somatic cells (Takahashi et al., 2007) as an inexhaustible cellular resource. Moreover, hiPSCs can be cultured and differentiated into multiple brain cell types and are genetically matched with the patient (Dolmetsch and Geschwind, 2011). HiPSCs differentiated into neural lineages allow for neurotoxicological or neurodevelopmental assays as well as the analysis of mature human neuronal networks by exploiting self-organization during neural differentiation. Kilic et al. (2016) demonstrated the feasibility of differentiating pluripotent human cells (NTERA2) into neuronal clusters containing astrocytes, which interfaced with a layer of human brain microvascular endothelial cells that had BBB characteristics. This 3D multicellular on-chip environment enhanced chemotactic cue-induced human neural progenitor migration (i.e., CXCL12 expressed during embryonic brain development and in pathological CNS tissues). A promising development in iPSC technology is the use of patient-derived iPSCs containing single mutations that lead to disease (e.g., familial dysautonomia; Lee et al., 2009). In such patients, the IKBKAP encoding gene contains a point mutation that is directly correlated with the loss of autonomic and sensory neurons. Through healthy vs. diseased hiPSC screening, the collection of patient-derived iPSCs can allow for diagnosis and *in vitro* drug treatment prior to patient treatment, which could lead to more personal and efficient diagnoses and drug treatments (Park et al., 2008; Dolmetsch and Geschwind, 2011).

Disease Models

Neurodegenerative diseases and disorders, such as Parkinson's disease (PD) and Alzheimer's disease (AD), lead to the destruction or degradation of synaptic connections, whereas neurological diseases, such as epilepsy, are thought to be related to dysfunctional network responses. Although epilepsy-on-a-chip has not been established yet, brain-on-a-chip technology has been applied to PD and AD modeling. In the following sections, we discuss the main technical features of the brain-on-a-chip platforms utilized for these disease models.

Alzheimer's Disease-On-A-Chip

In AD, synaptic dysfunction is usually related to malfunctions of proteins, such as tau and amyloid beta (amyloid-β) (Pascoal et al., 2016). Therefore, some AD models have focused on modulating these proteins with respect to their influence on synapse formation and glial cell communication (Hai et al., 2010). Three-dimensional neuronal tissue models, including the aforementioned networked neurospheres (Choi et al., 2010), have also been used for AD studies investigating amyloid-β protein expression and network formation (Choi et al., 2013). Platforms and systems offering real-time analyses of neuronal activity, co-culturing, and chemotaxis gradients have been used to model AD. Previously, microfluidics were successfully used to demonstrate the role of amyloid-β in neuronal connections (Deleglise et al., 2014) and glial cells (Cho et al., 2013). Using these models, these studies showed that amyloid-β accumulation in cortical neurons led to the occurrence of synaptic anomalies at the level of neurotransmitter signaling pathways, which represented the onset of AD. Tau protein hyperphosphorylation is a hallmark trait of AD (Pascoal et al., 2016), and studies combining microfluidics and co-cultures demonstrated that different tau phosphorylation states could be modeled within interconnected microfluidic neuronal cell compartments (Kunze et al., 2011b; Cho et al., 2013). In another AD model study, microfluidic devices were used to demonstrate neuron-to-neuron wild-type tau protein transfer through trans-synaptic mechanisms (Dujardin et al., 2014). More recently, an 3D on-chip AD model was proposed (Park et al., 2015; **Figure 4**). The use of microfluidic technologies allowed for culture media perfusion to assess perfused amyloid-β effects on network formation (Park et al., 2015). This chip contained concave microwells for the formation of homogeneous 3D neurospheroids of a uniform size. Its osmotic micropump system was connected to the outlet to provide a continuous flow of medium. By providing 3D cytoarchitecture and interstitial flow, this chip approximated the microenvironment of normal and AD brains, which facilitated the investigation of amyloid-β effects on 3D neural tissue. On the microfluidic chip, normal (i.e., healthy) neurospheroids were cultured under dynamic conditions with a flow of normal medium containing oxygen and nutrients for 10 d. AD neurospheroids were cultured on the microfluidic chip under dynamic conditions with a flow of normal medium containing oxygen and nutrients for 7 d. Following this, the AD neurospheroids were incubated with a medium containing 5 μM of synthetic amyloid-β for 3 d. Compared with the normal model, the AD model had decreased cell viability and increased neural destruction and synaptic dysfunction, which are pathophysiological features of AD *in vivo*.

Parkinson's Disease-On-A-Chip

An on-chip PD model that allowed for monitoring of mitochondrial transport on single dopaminergic axons was also proposed (Lu et al., 2012). This device consisted of two open chambers connected via microchannels in which axon growth was monitored and labeled mitochondria were visualized. The device promoted oriented axon growth into a separate axonal compartment for analysis. Moreover, this device improved upon the culture of more sensitive neurons (i.e., primary midbrain dopaminergic neurons). Although this work was limited to mitochondrial transport, vesicular transport, and microtubule fragmentation, which also contribute to dopaminergic fiber loss, could also be analyzed with this device. This is an important development because such studies are difficult to perform using traditional cell culture approaches and PD brain lesions are always associated with dopaminergic fiber loss. To date, this device does not support co-culture or 3D cell cultures but instead uses microfluidics to align axons. This approach highlights the axonal degeneration mechanisms potentially underlying PD pathophysiology as well as those underlying other major neurodegenerative diseases.

Another potential on-chip PD model using 3D phase-guided microfluidic cell culture bioreactors was recently developed as a personalized biomedical approach to PD (Moreno et al., 2015). These authors differentiated human neuroepithelial stem cells into dopaminergic neurons in microfluidic cell culture bioreactors and suggested that this platform could be used to study substantia nigra dopaminergic neuron degeneration, a hallmark of PD.

Epilepsy

Epilepsy is characterized by excessive synchronized electrical activity within the brain. MEAs in combination with brain slices have been the best technology used so far to monitor, study, and detect epileptic activity *in vitro*. This technology consists of rapid high-throughput static platforms used for drug discovery and toxicology studies. Recently, an *in vitro* model of spontaneous epilepsy was proposed in which cells cultured from transgenic mice expressing β2-V287L were used with MEA technology to

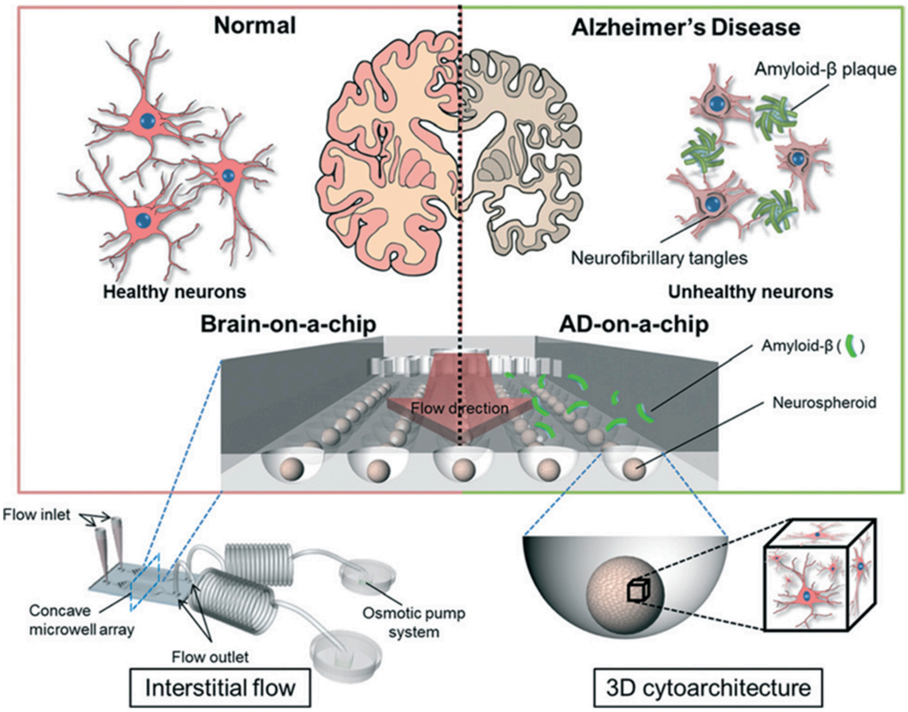

FIGURE 4 | Schematic diagram of a 3D Alzheimer's disease brain-on-a-chip with an interstitial level of flow. The chip contains a concave microwell array for the formation of homogeneous neurospheroids of a uniform size with 3D cytoarchitecture. The osmotic micropump system is connected to the outlet to provide a continuous flow of medium at the level of interstitial flow. By providing 3D cytoarchitecture and interstitial flow, this chip approximates the microenvironment of normal and Alzheimer's disease brains, which facilitates the investigation of amyloid-β effects on 3D neural tissue. Figure reprinted with permission, previously published in Lab on a Chip, Park et al. (2015).

assess the role of Bβ2-V287L in synaptic formation (Gullo et al., 2014). With this β2-V287L model, the authors showed that it is possible to produce murine models with human channelopathy *in vitro*. In addition, MEAs coupled with microfluidics have been proposed to monitor neuronal network activity under different conditions and exposures (Morin et al., 2006; Ravula et al., 2006). These brain slice-based models can be used as chronic models of spontaneous hyperexcitability (i.e., epileptiform) activity, which does not require pre-treatment with pharmacological agents to trigger seizures. However, these models have questionable clinical relevance. Given the recent advances combining brain-on-a-chip and iPSC technologies, epilepsy-on-a-chip may become a reality. Genetic factors play an important etiological role in epilepsy development. Harvesting hiPSCs from patients with Dravet syndrome, in which a single SCN1A gene mutation causes epilepsy (Selmer et al., 2009), holds great promise for enhancing treatment options and improving quality of life.

FUTURE DIRECTIONS OF CLINICALLY VALIDATED ON-CHIP BRAIN MODELS

Although tremendous progress has been made with brain-on-a-chip technology and its applications, challenges remain with respect to the translational and clinical value of such systems. To recreate the critical features of the *in vivo* human brain microenvironment, several factors must be addressed. First, advanced cell composition reflecting the type, ratio, and 3D architecture of cells within brain tissue must be achieved by incorporating stem cell technologies (Lancaster et al., 2013; Berger et al., 2018). Another important aspect of validating brain-on-a-chip models is to identify the functional readouts of the healthy or pathological states of these systems. As previously discussed, MEA-based electrophysiological measurements should be appropriate for 3D microphysiological cell culture systems. Alternatively, advanced neuroprobe microtechnologies (Xie et al., 2015) are useful for assessing brain function; however, these tools remain to be implemented in brain-on-a-chip models. Progress in neuroprobe technology has been reviewed elsewhere (Seymour et al., 2017).

Despite the current limitations, most modern microscale platforms have already identified known pathological mechanisms and pathways; however, they have yet to contribute to novel therapeutic solutions. Thus, the clinical relevance of brain-on-a-chip technology remains limited; however, the pharmaceutical industry has started to examine these new technologies for drug discovery and testing. Nonetheless, these systems show great promise in more closely representing the diseased human tissue microenvironment *in vitro* compared with standard tissue culture tests. Resolving the aforementioned critical features as well as mimicking blood flow and the

BBB, or neurovascular unit, will be important steps toward advancing clinically relevant brain-on-a-chip models. The next sections will describe an idealized schematic of a brain-on-a-chip concept, which details its desired physiological features. Moreover, we address novel assay development routes that exploit 3D engineered tissue architecture and provide a market outlook.

Nano- and Microfabrication Challenges With Brain-On-a-Chip Technology

Essentially, a brain-on-a-chip is a miniaturized dish-type construct placed on a microscope slide, which hosts neuronal tissue supported by a medium replenishment unit and integrated microfluidics. To produce such a device, the appropriate cells must first be selected. This step is critical because brain tissue consists of many different neuronal subtypes (Brodal, 2010). Moreover, a plethora of supporting glial cell types, including microglia, astrocytes and oligodendrocytes, are also required to design advanced brain-on-a-chip models. To further complicate matters, cellular network bio-architecture significantly varies throughout different brain regions, forming complex structures and circuitries. Importantly, different cell types appear in precise ratios in different brain regions, where, for example, glial cells influence apoptosis and repair mechanisms and can accumulate following brain trauma (Eskes et al., 2003; Giordano et al., 2009; Kuegler et al., 2012). Glial cells also determine the overall reaction of tissue to injury by phagocytosing dying neurons and neurite debris (Hirt and Leist, 2003). Therefore, brain injury models need to reflect these altered conditions instead of only modeling healthy brain function. In addition, several metabolic pathways in the brain involve different cell types. For example, astrocytes take up glutamate, transform it to glutamine, and provide it to neurons. Astrocytes also provide neurons with specific energy substrates or essential thiols. Therefore, co-culturing of different cells must be performed in diseased or healthy brain-on-a-chip models.

For the brain model to be functional, all cell types must be present and supported by the engineered construct (**Figure 5**). This may be achieved by combining engineered microsystems with hiPSC technology. HiPSC-derived neuronal cell cultures are beneficial in this respect because they can contribute to a specific tissue architecture based on their level of differentiation. Differentiation can be induced within particular compartmentalized microenvironments specifically designed within the microphysiological cell culture system to fulfill the requirements of a given application. Preliminary successes in this area have been recently demonstrated, amongst others, by Fleming and his team who utilized the Mimetas platform (Moreno et al., 2015). However, in that system, the 3D space was limited to a few hundred micrometers and there was no electrical readout.

Unlike organoid culture in flasks (Lancaster et al., 2013), brain-on-a-chip models have only been developed with a maximum of two or three cell types, which is not sufficient to achieve fully functional brain tissue. In addition to cell type and complexity issues, the host environment must allow for sufficient medium exchange with different cell types that may require dedicated media and growth factors. For example, neuron and astrocyte culture media differ during differentiation, which often requires a flow barrier that prevents direct co-culture and connection between the two cell types. Future micro- and nanofluidic systems of the brain should specifically address these technical challenges to obtain representative physiological behavior within brain-on-a-chip models and, thus, advance their clinical relevance.

3D Engineered Tissue Architecture-Based Assays

In brain-on-a-chip models, the cell construct architecture should resemble the spatial distribution of cells within tissue, allowing for 3D culture instead of the conventional 2D conformation produced by many high-throughput cell culture screening platforms (Frimat et al., 2010; Hardelauf et al., 2011). A 3D conformation will affect the neuronal network (i.e., connectivity) and consequently, the signals sent between cells (Frega et al., 2014). This, in turn, would lead to changes in metabolism and neuron activity. Three-dimensional models often result in improved structure, which is demonstrated by cellular outgrowths (i.e., neuronal processes) and enhanced cell-to-cell connectivity. Moreover, 3D cultures often show enhanced survival and richer neuronal differentiation compared with traditional monolayer cultures (Peretz et al., 2007). Local secretion and paracrine signaling of neurotrophic factors (e.g., nerve growth factor and brain-derived neurotrophic factor) together with other intercellular communication events are also desired features that are important for recreating brain function within a model (Maurel and Salzer, 2000; Michailov et al., 2004). Designing 3D *in vitro* models to enable this type of bio-architecture is therefore an important consideration for brain-on-a-chip development. Functional synapses have been observed earlier in 3D neuronal cultures in collagen hydrogel compared with 2D models (O'Shaughnessy et al., 2003). Furthermore, stem cell-derived neurons cultured in 3D showed increased differentiation compared with 2D cultures (Paavilainen et al., 2018). Morphology at the single-cell level is also different in 3D, where cells adopt a round shape compared with cells that spread on 2D surfaces, which influences cells at the genetic level (Li et al., 2007). For example, genetic and morphological microarray analysis of neurons growing in gels (3D) compared with those cultured on standard tissue culture plates (2D) demonstrated that cells cultured in 3D exhibited differential expression of 1,766 genes, including those relevant to cytoskeleton, extracellular matrix, and neurite outgrowth (e.g., filamin A, actinin 1a1, capping protein a2, fibronectin 1, and midkine; Li et al., 2007). In addition, when 3D cultured in gels (e.g., collagen, Matrigel, or Puramatrix), neurons and other cell types adopted a more *in vivo*-like phenotype, including more branched and thicker neuronal processes compared with those cultured in 2D (Ylä-Outinen et al., 2014). The *in vivo* structural features of brain tissue bio-architecture support network formation and regionally compartmentalize the brain to connect different regions and allow for cognitive processing (Honegger et al.,

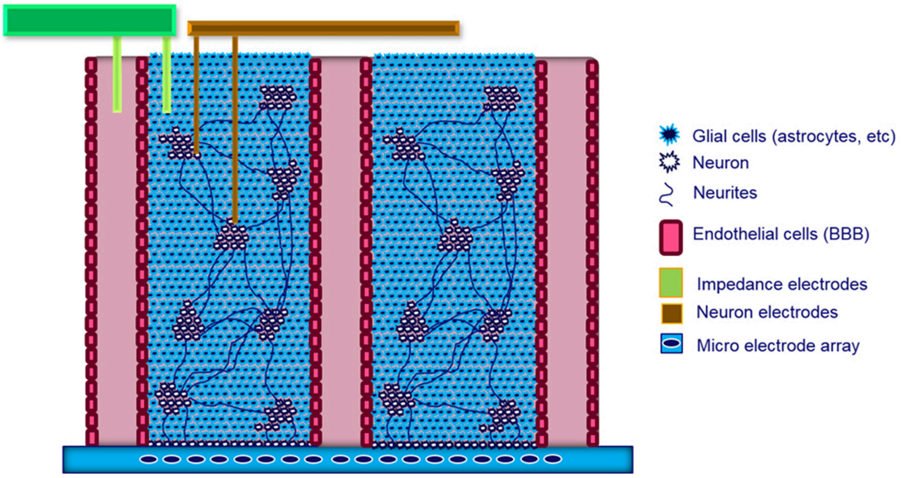

FIGURE 5 | Schematic side view of the ideal brain model. This model has a cell composition of 10% neurons and 90% glial cells. The 3D architecture, which includes the blood-brain barrier (BBB), is interfaced with a microelectrode array (MEA). Additional output measurements can be made using external electrodes.

2016). Therefore, the architecture of the brain is not random, and during development, 3D structural modification occurs inside the brain. Moreover, brain architecture is highly heterogeneous and does not have repeating units or exhibit clear structural patterns. Therefore, to generate a brain model *in vitro*, different brain regions (e.g., the medulla, pons, hypothalamus, thalamus, cerebellum, optic tectum, pallium, hippocampus, basal ganglia, and olfactory bulb) should be modeled separately at first to develop minimal brain model concepts. These regionally specified brain-on-a-chip models should be arranged and interconnected in a way resembling a real brain to permit cross-talk between regions, which could potentially be facilitated by an electronic link (Panuccio et al., 2016).

Considering the above issues, 3D assays must be developed. Nano- and microfabrication technologies can help to reach this goal with nano-patterning (e.g., nanoimprint and microcontact printing; Martínez et al., 2012), additive manufacturing routes (e.g., microprinting; Marga et al., 2012; Ye et al., 2018), and hydrogel templating (Matsusaki et al., 2007) approaches. These techniques can subsequently assist in deriving the desired 3D assemblies for augmenting cell-to-cell and cell-to-substrate interactions. Our research has shown that nanogroove substrates produced by replica molding from a nanoimprint lithography template can impact culture organization in 3D (Frimat et al., 2015). Moreover, self-assembly of cell-laden hydrogel beads, produced by flow-focusing microfluidics, can yield novel 3D cell culture arrangements, which can facilitate assay development due to the regular ordering of neurons in culture (Bastiaens, 2019).

Potential for Micro-Nanofluidics Systems of the Brain

BBB devices are often considered to be brain-on-a-chip models; however, they are not. BBB-type devices monitor what enters and exits the brain and, although BBB function can be mimicked *in vitro* (Griep et al., 2013; van der Helm et al., 2016), it is usually not coupled with a brain model. Given that the BBB is essential for the brain and its functions, it should be included in brain models as a building block for the compartmentalization of different brain regions. A stand-alone human BBB-on-a-chip, or neurovascular unit, was recently developed and serves as a first step toward improving drug development (Heidari and Taylor, 2018). The structural components of BBB blood vessels can serve as feeding channels for more advanced culture models including immune system cells. Optimizing the 3D *in vitro* brain microenvironment, which should include extracellular matrix (ECM) modeling to recreate *in vivo* brain physiology better than that of the current state-of-the art, can be achieved by including micro- and nanofluidic technology in addition to the appropriate cell types. Continuous medium supply and realistic 3D conformation are prerequisites for differentiating multiple cell types within a model and sustaining 3D cultures for prolonged time periods. A vascular ECM-type scaffold design may allow for highly specific cellular niches to be established by providing continuous or local access to growth factors, correct cell matrix adhesion (i.e., polarity), nutrition, cell-to-cell junction formation, and immune system (i.e., T-cell) modeling (Kipnis and Schwartz, 2005). With exquisite mimicking facilitated by micro- and nanofluidics, such 3D reconstructions could eventually provide an economical platform to model stem cell niches, which would enable specific cell compositions and signaling molecule gradients. These developments would provide a highly defined environment (e.g., enriched or deprived of certain signaling molecules) for the development and functioning of cultured brain tissues, which could overcome current difficulties in securing scarcely available brain tissue slices. During neuronal development, signaling molecule gradients are particularly important for cell migration and differentiation and, thus, overall brain structure patterning. From a clinical perspective, 3D cell culture systems have obvious advantages over 2D systems when modeling for a specific research question is the major objective (Fuchs et al., 2004; Morrison and Spradling, 2008). However, if a 3D cell culture model is not engineered properly or its matrix (typically hydrogels) is not porous enough, there can be limited diffusion of chemicals and nutrients and signals can be lost. In the brain, a cell is never more than 200 μm away from a blood vessel. This feature should be replicated in brain-on-a-chip applications to create marketable products and services with highly robust experimental designs.

CONCLUSION

Although the union of micro- and nanotechnologies with neuroscience has been demonstrated by a number of microfluidic devices, the lack of a deeper understanding of the brain still hampers the selection of appropriate design criteria. To overcome these design bottlenecks, it is important to understand the clinical and pharmaceutical requirements for organ-on-a-chip technologies, which can revolutionize biology and personal medicine. Conventional neuronal cell culture methods have limited relevance for brain disease modeling. The combination of microfluidic, MEA, and iPSC technologies has had a significant impact on the development of brain-on-a-chip technology. We have discussed microfluidic technologies that emulate the BBB, or neurovascular unit, and establish nutrient replenishment routes with distinguishable growth factor gradients as well as compartmentalized culture systems. Furthermore, current brain-on-a-chip models are limited to immunostaining or 2D MEA readouts. Therefore, 3D culture could benefit from the integration of advanced neuroprobe technology and 3D cultures. In addition, stem cell technology must improve the differentiation methods for multicellular tissue constructs. Overall, on-chip integration methods have already enabled advances in AD, PD, and epilepsy modeling. In AD modeling, microfluidic approaches have provided drug screening advantages. Moreover, cell soma and axon compartmentalization and visualization have been greatly improved in PD models. In epilepsy, electrode integration and genetic manipulation will allow for new insights into specific disease mechanisms. Integrating different features into one compact brain-on-a-chip model is a major technical challenge in this field. For actual brain models, the integration of microfluidic neurovascular units and electrophysiological readouts in 3D multicellular tissue constructs will be important steps forward.

AUTHOR CONTRIBUTIONS

J-PF and RL: conceptualization and design of the review, preparation of manuscript, and final approval of the version to be published. RL: acquired the funding.

FUNDING

This work was financially supported by the European Research Council (ERC), MESOTAS Grant No. 280281, MESOTAS-SIEVE, Grant No. 713732, and ZONMW Off road Grant No. 40-0812598160.

ACKNOWLEDGMENTS

The authors gratefully acknowledge the many fruitful discussions on this topic with biomedical experts working in the Organ-on-a-Chip community.

REFERENCES

Achyuta, A. K., Conway, A. J., Crouse, R. B., Bannister, E. C., Lee, R. N., Katnik, C. P., et al. (2013). A modular approach to create a neurovascular unit-on-a-chip. *Lab Chip* 13, 542–553. doi: 10.1039/C2LC41033H

Alépée, N., Bahinski, A., Daneshian, M., De Wever, B., Fritsche, E., Goldberg, A., et al. (2014). State-of-the-art of 3D cultures (organs-on-a-chip) in safety testing and pathophysiology. *ALTEX* 31, 441–477. doi: 10.14573/altex 1406111

Andlin-Sobocki, P., Jönsson, B., Wittchen, H. U., and Olesen, J. (2005). Costs of disorders of the brain in Europe. *Eur. J. Neurol.* 12, 1–27. doi: 10.1111/j.1468-1331.2005.01202.x

Ban, J., Bonifazi, P., Pinato, G., Broccard, F. D., Studer, L., Torre, V., et al. (2007). Embryonic stem cell-derived neurons form functional networks *in vitro*. *Stem Cells* 25, 738–749. doi: 10.1634/stemcells.2006-0246

Banks, W. A. (2016). From blood–brain barrier to blood–brain interface: new opportunities for CNS drug delivery. *Nat. Rev. Drug Dis.* 15, 275–292. doi: 10.1038/nrd.2015.21

Bart Schurink, B., and Luttge, R. (2013). Hydrogel/poly-dimethylsiloxane hybrid bioreactor facilitating 3D cell culturing. *J. Vac. Sci. Technol. B.* 31:06F903. doi: 10.1116/1.4831762

Bastiaens, A. J. (2019). *Nano- and Microengineered Neuronal Cell Networks for Brain-on-Chip Technology,* PhD thesis. Eindhoven: Eindhoven University of Technology. ISBN: 978-90-386-4676-3.

Bastiaens, A. J., Frimat, J. P., van Nunen, T., Schurink, B., Homburg, E., and Luttge, R. (2018). Advancing a MEMS-based 3D cell culture system for in vitro neuro-electrophysiological recordings. *Front. Cell. Neurosci.* 12:415. doi: 10.3389/fncel.2018.00415

Berger, E., Magliaro, C., Paczia, N., Monzel, A. S., Antony, P., Linster, C. L., et al. (2018). Millifluidic culture improves human midbrain organoid vitality and differentiation. *Lab Chip* 18, 3172–3183. doi: 10.1039/C8LC00206A

Brodal, P. (2010). *The Central Nervous System: Structure and Function,* 4th Ed. Oslo: Oxford University Press.

Cheng, S. Y., Heilman, S., Wasserman, M., Archer, S., Shuler, M. L., and Wu, M. (2007). A hydrogel-based microfluidic device for the studies of directed cell migration. *Lab Chip* 7, 763–769. doi: 10.1039/b618463d

Cho, H., Hashimoto, T., Wong, E., Hori, Y., Wood, L. B., Zhao, L., et al. (2013). Microfluidic chemotaxis platform for differentiating the roles of soluble and bound amyloid-beta on microglial accumulation. *Sci. Rep.* 3:1823. doi: 10.1038/srep01823

Choi, Y. J., Park, J., and Lee, S. H. (2013). Size-controllable networked neurospheres as a 3D neuronal tissue model for Alzheimer's disease studies. *Biomaterials* 34, 2938–2946. doi: 10.1016/j.biomaterials.2013.01.038

Choi, Y. Y., Chung, B. G., Lee, D. H., Khademhosseini, A., Kim, J. H., and Lee, S. H. (2010). Controlled-size embryoid body formation in concave microwell arrays. *Biomaterials* 31, 4296–4303. doi: 10.1016/j.biomaterials.2010.01.115

Deleglise, B., Magnifico, S., Duplus, E., Vaur, P., Soubeyre, V., Belle, M., et al. (2014). β-Amyloid induces a dying-back process and remote trans-synaptic alterations in a microfluidic–based reconstructed neuronal network. *Acta Neuropathol. Commun.* 2:145. doi: 10.1186/PREACCEPT-4848873741397798

Dinh, N. D., Chiang, Y. Y., Hardelauf, H., Baumann, J., Jackson, E., Waide, S., et al. (2013). Microfluidic construction of minimalistic neuronal co-cultures. *Lab Chip* 13, 1402–1412. doi: 10.1039/c3lc41224e

Dolmetsch, R., and Geschwind, D. H. (2011). The human brain in a dish: the promise of iPSC-derived neurons. *Cell* 145, 831–834. doi: 10.1016/j.cell.2011.05.034

Dua, T., Janca, A., and Muscetta, A. (2006). *Neurological Disorders: Public Health Challenges*. World Health Organization. ISBN 92 4 156 336 2.

Dujardin, S., Lecolle, K., Caillierez, R., Begard, S., Zommer, N., Lachaud, C., et al. (2014). Neuron-to-neuron wild-type Tau protein transfer through a trans-synaptic mechanism: relevance to sporadic tauopathies. *Acta Neuropathol. Commun*. 30:14. doi: 10.1186/2051-5960-2-14

Eskes, C., Juillerat-Jeanneret, L., Leuba, G., Honegger, P., and Monnet-Tschudi, F. (2003). Involvement of microglia-neuron interactions in the tumor necrosis factor-alpha release, microglial activation, and neurodegeneration induced by trimethyltin. *J. Neurosci. Res*. 71, 583–590. doi: 10.1002/jnr.10508

Festing, S., and Wilkinson, R. (2007). The ethics of animal research. Talking point on the use of animals in scientific research. *EMBO Rep*. 8, 526–530. doi: 10.1038/sj.embor.7400993

Francisco, H., Yellen, B. B., Halverson, D. S., Friedman, G., and Gallo, G. (2007). Regulation of axon guidance and extension by three-dimensional constraints. *Biomaterials* 28, 3398–3407. doi: 10.1016/j.biomaterials.2007.04.015

Frega, M., Tedesco, M., Massobrio, P., Pesce, M., and Martinoia, S. (2014). Network dynamics of 3D engineered neuronal cultures: a new experimental model for *in-vitro* electrophysiology. *Sci. Rep*. 4:5489. doi: 10.1038/srep05489

Frimat, J. P., Sisnaiske, J., Subbiah, S., Menne, K., Godoy, P., Lampen, P., et al. (2010). The network formation assay: a spatially standardized neurite outgrowth analytical display for neurotoxicity screening. *Lab Chip* 10, 701–709. doi: 10.1039/b922193j

Frimat, J. P., Xie, S., Bastiaens, A., Schurink, B., Wolbers, F., den Toonder, J. M. J., et al. (2015). Advances in 3D neuronal cell culture. *J. Vac. Sci. Technol. B Nanotechnol. Microelectron*. 33:06F902. doi: 10.1116/1.4931636

Fuchs, E., Tumbar, T., and Guasch, G. (2004). Socializing with the neighbors: stem cells and their niche. *Cell* 116, 769–778. doi: 10.1016/S0092-8674(04)00255-7

Giordano, G., Kavanagh, T. J., and Costa, L. G. (2009). Mouse cerebellar astrocytes protect cerebellar granule neurons against toxicity of the polybrominated diphenyl ether (PBDE) mixture DE-71. *Neurotoxicology* 30, 326–329. doi: 10.1016/j.neuro.2008.12.009

Griep, L. M., Wolbers, F., de Wagenaar, B., ter Braak, P. M., Weksler, B. B., Romero, I. A., et al. (2013). BBB on chip: microfluidic platform to mechanically and biochemically modulate blood-brain barrier function. *Biomed. Microdev*. 15, 145–150. doi: 10.1007/s10544-012-9699-7

Gullo, F., Manfredi, I., Lecchi, M., Casari, G., Wanke, E., and Becchetti, A. (2014). Multi-electrode array study of neuronal cultures expressing nicotinic beta2-V287L subunits, linked to autosomal dominant nocturnal frontal lobe epilepsy. An *in vitro* model of spontaneous epilepsy. *Front. Neural Circuits* 8:87. doi: 10.3389/fncir.2014.00087

Hai, A., Shappir, J., and Spira, M. E. (2010). In-cell recordings by extracellular micro-electrodes. *Nat. Methods* 7, 200–202. doi: 10.1038/nmeth.1420

Hardelauf, H., Frimat, J. P., Stewart, J. D., Schormann, W., Chiang, Y. Y., Lampen, P., et al. (2011). Microarrays for the scalable production of metabolically-relevant tumour spheroids: a tool for modulating chemosensitivity traits. *Lab Chip* 11, 419–428. doi: 10.1039/C0LC00089B

Heidari, H., and Taylor, H. (2018). Review article: capturing the physiological complexity of the brain's neuro-vascular unit *in vitro*. *Biomicrofluidics* 12:051502. doi: 10.1063/1.5045126

Hirt, U. A., and Leist, M. (2003). Rapid, noninflammatory and PS-dependent phagocytic clearance of necrotic cells. *Cell Death Differ*. 10, 1156–1164. doi: 10.1038/sj.cdd.4401286

Honegger, T., Thielen, M. I., Feizi, S., Sanjana, N. E., and Voldman, J. (2016). Microfluidic neurite guidance to study structure-function relationships in topologically-complex population-based neural networks. *Sci. Rep*. 22, 28384. doi: 10.1038/srep28384

Huh, D., Matthews, B. D., Mammoto, A., Montoya-Zavala, M., Hsin, H. Y., and Ingber, D. E. (2010). Reconstituting organ-level lung functions on a chip. *Science* 328, 1662–1668. doi: 10.1126/science.1188302

Jang, K., Mehr, A. P., Hamilton, G. A., McPartlin, L. A., Chung, S., Suh, K. Y., et al. (2013). Human kidney proximal tubule-on-a-chip for drug transport and nephrotoxicity assessment. *Integr. Biol*. 5:1119. doi: 10.1039/c3ib40049b

Jensen, J. B., and Parmar, M. (2006). Strengths and limitations of the neurosphere culture system. *Mol. Neurobiol*. 34, 153–161. doi: 10.1385/MN:34:3:153

Kilic, O., Pamies, D., Lavell, E., Schiapparelli, P., Feng, Y., Hartung, T., et al. (2016). Brain-on-a-chip model enables analysis of human neuronal differentiation and chemotaxis. *Lab Chip* 16, 4152–4162. doi: 10.1039/C6LC00946H

Kipnis, J., and Schwartz, M. (2005). Controlled autoimmunity in CNS maintenance and repair: naturally occurring CD4+CD25+ regulatory T-cells at the crossroads of health and disease. *Neuromolecular Med*. 7, 197–206. doi: 10.1385/NMM:7:3:197

Köhling, R., Melani, R., Koch, U., Speckmann, E. J., Koudelka-Hep, M., Thiébaud, P., et al. (2005). Detection of electrophysiological indicators of neurotoxicity in human and rat brain slices by a three-dimensional microelectrode array. *Altern. Lab. Anim*. 33, 579–589. doi: 10.1177/026119290503300613

Kuegler, P. B., Baumann, B. A., Zimmer, B., Keller, S., Marx, A., Kadereit, S., et al. (2012). GFAP-independent inflammatory competence and trophic functions of astrocytes generated from murine embryonic stem cells. *Glia* 60, 218–228. doi: 10.1002/glia.21257

Kunze, A., Giugliano, M., Valero, A., and Renaud, P. (2011a). Micropatterning neural cell cultures in 3D with a multi-layered scaffold. *Biomaterials* 32, 2088–2098. doi: 10.1016/j.biomaterials.2010.11.047

Kunze, A., Meissner, R., Brando, S., and Renaud, P. (2011b). Co-pathological connected primary neurons in a microfluidic device for Alzheimer studies. *Biotechnol. Bioeng*. 108, 2241–2245. doi: 10.1002/bit.23128

Kunze, A., Valero, A., Zosso, D., and Renaud, P. (2011c). Synergistic NGF/B27 gradients position synapses heterogeneously in 3D micropatterned neural cultures. *PLoS ONE*. 6:e26187. doi: 10.1371/journal.pone.0026187

Lancaster, M. A., Renner, M., Martin, C. A., Wenzel, D., Bicknell, L. S., Hurles, M. E., et al. (2013). Cerebral organoids model human brain development and microcephaly. *Nature* 501, 373–379. doi: 10.1038/nature12517

Lee, G., Papapetrou, E. P., Kim, H., Chambers, S. M., Tomishima, M. J., Fasano, C. A., et al. (2009). Modelling pathogenesis and treatment of familial dysautonomia using patient-specific iPSCs. *Nature* 461, 402–406. doi: 10.1038/nature08320

Li, G. N., Livi, L. L., Gourd, C. M., Deweerd, E. S., and Hoffman-Kim, D. (2007). Genomic and morphological changes of neuroblastoma cells in response to three-dimensional matrices. *Tissue Eng*. 13, 1035–1047. doi: 10.1089/ten.2006.0251

Lu, X., Kim-Han, J. S., O'Malley, K. L., and Sakiyama-Elbert, S. E. (2012). A microdevice platform for visualizing mitochondrial transport in aligned dopaminergic axons. *J. Neurosci. Methods* 209, 35–39. doi: 10.1016/j.jneumeth.2012.05.021

Marga, F., Jakab, K., Khatiwala, C., Shepherd, B., Dorfman, S., Hubbard, B., et al. (2012). Toward engineering functional organ modules by additive manufacturing. *Biofabrication* 4:022001. doi: 10.1088/1758-5082/4/2/022001

Martínez, E., Pla-Roca, M., and Samitier, J. (2012). Micro/nanopatterning of proteins using a nanoimprint-based contact printing technique. *Methods Mol. Biol*. 811, 79–87. doi: 10.1007/978-1-61779-388-2_5

Massobrio, P., Massobrio, G., and Martinoia, S. (2016). Interfacing cultured neurons to microtransducers arrays: a review of the neuro-electronic junction models. *Front. Neurosci*. 10:282. doi: 10.3389/fnins.2016.00282

Matsusaki, M., Yoshida, H., and Akashi, M. (2007). The construction of 3D-engineered tissues composed of cells and extracellular matrices by hydrogel template approach. *Biomaterials* 28, 2729–2737. doi: 10.1016/j.biomaterials.2007.02.015

Maurel, P., and Salzer, J. L. (2000). Axonal regulation of Schwann cell proliferation and survival and the initial events of myelination requires PI 3-kinase activity. *J. Neurosci*. 20, 4635–4645. doi: 10.1523/JNEUROSCI.20-12-04635.2000

Michailov, G. V., Sereda, M. W., Brinkmann, B. G., Fischer, T. M., Haug, B., Birchmeier, C., et al. (2004). Axonal neuregulin-1 regulates myelin sheath thickness. *Science* 304, 700–703. doi: 10.1126/science.1095862

Moonen, E., Luttge, R., and Frimat, J. P. (2018). Single cell trapping by capillary pumping using NOA81 replica moulded stencils. *Microelectron Eng*. 197, 1–7. doi: 10.1016/ j.mee.2018.04.010

Moreno, E., Hachi, S., Hemmer, K., Trietsch, S. J., Baumuratov, A. S., Hankemeier, T., et al. (2015). Differentiation of neuroepithelial stem cells into functional dopaminergic neurons in 3D microfluidic cell culture. *Lab Chip* 15, 2419–2428. doi: 10.1039/C5LC00180C

Morin, F., Nishimura, N., Griscom, L., Le Pioufle, B., Fujita, H., Takamura, Y., et al. (2006). Constraining the connectivity of neuronal networks cultured on microelectrode arrays with microfluidic techniques: a step towards neuron-based functional chips. *Biosens. Bioelectron*. 21, 1093–1100. doi: 10.1016/j.bios.2005.04.020

Morrison, S. J., and Spradling, A. C. (2008). Stem cells and niches: mechanisms that promote stem cell maintenance throughout life. *Cell* 132, 598–611. doi: 10.1016/j.cell.2008.01.038

Musick, K., Khatami, D., and Wheeler, B. C. (2009). Three-dimensional microelectrode array for recording dissociated neuronal cultures. *Lab Chip* 9, 2036–2042. doi: 10.1039/b820596e

Odijk, M., van der Meer, A. D., Levener, D., Kim, H. J., and van der Helm, M. W., Segerink, et al. (2015). Measuring direct current trans-epithelial electrical resistance in organ-on-a-chip microsystems. *Lab Chip* 7, 745–752. doi: 10.1039/C4LC01219D

O'Shaughnessy, T. J., Lin, H. J., and Ma, W. (2003). Functional synapse formation among rat cortical neurons grown on three-dimensional collagen gels. *Neurosci. Lett*. 340, 169–172. doi: 10.1016/S0304-3940(03)00083-1

Paavilainen, T., Pelkonen, A., Mäkinen, M. E., Peltola, M., Huhtala, H., Fayuk, D., et al. (2018). Effect of prolonged differentiation on functional maturation of human pluripotent stem cell-derived neuronal cultures. *Stem Cell Res*. 27, 151–161. doi: 10.1016/j.scr.2018.01.018

Pancrazio, J. J., Gray, S. A., Shubin, Y. S., Kulagina, N., Cuttino, D. S., Shaffer, K. M., et al. (2003). A portable microelectrode array recording system incorporating cultured neuronal networks for neurotoxin detection. *Biosens. Bioelectron*. 18, 1339–1347. doi: 10.1016/S0956-5663(03)00092-7

Panuccio, G., Semprini, M., and Chiappalone, M. (2016). Intelligent biohybrid systems for functional brain repair. *Eur. J. Mol. Clin. Med*. 3, 162–174. doi: 10.1016/j.nhtm.2016.10.001

Park, I. H., Arora, N., Huo, H., Maherali, N., Ahfeldt, T., Shimamura, A., et al. (2008). Disease-specific induced pluripotent stem cells. *Cell* 134, 877–886. doi: 10.1016/j.cell.2008.07.041

Park, J., Kim, S., Park, S. I., Choe, Y., Li, J., and Han, A. (2014). A microchip for quantitative analysis of CNS axon growth under localized biomolecular treatments. *J. Neurosci. Methods* 221, 166–174. doi: 10.1016/j.jneumeth.2013.09.018

Park, J., Lee, B. K., Jeong, G. S., Hyun, J. K., Lee, C. J., and Lee, S. H. (2015). Three-dimensional brain-on-a-chip with an interstitial level of flow and its application as an *in vitro* model of Alzheimer's disease. *Lab Chip* 15, 141–150. doi: 10.1039/C4LC00962B

Park, J. W., Vahidi, B., Taylor, A. M., Rhee, S. W., and Jeon, N. L. (2006). Microfluidic culture platform for neuro-science research. *Nat. Protoc*. 1, 2128–2136. doi: 10.1038/nprot.2006.316

Pascoal, T. A., Mathotaarachchi, S., Mohades, S., Benedet, A. L., Chung, C. O., Shin, M., et al. (2016). Amyloid-β and hyperphosphorylated tau synergy drives metabolic decline in preclinical Alzheimer's disease. *Mol. Psychiatry* 22, 1–6. doi: 10.1038/mp.2016.37

Patabendige, A., Skinner, R. A., and Abbott, N. J. (2013). Establishment of a simplified in vitro porcine blood-brain barrier model with high transendothelial electrical resistance. *Brain Res*. 1521, 1–15. doi: 10.1016/j.brainres.2012.06.057

Peretz, H., Talpalar, A. E., Vago, R., and Baranes, D. (2007). Superior survival and durability of neurons and astrocytes on 3-dimensional aragonite biomatrices. *Tissue Eng*. 13, 461–472. doi: 10.1089/ten.2005.0522

Perrin, S. (2014). Preclinical research: make mouse studies work. *Nature* 507, 423–425. doi: 10.1038/507423a

Prabhakarpandian, B., Shen, M. C., Nichols, J. B., Mills, I. R., Sidoryk-Wegrzynowicz, M., Aschner, M., et al. (2013). SyM-BBB: a microfluidic blood brain barrier model. *Lab Chip* 13, 1093–1101. doi: 10.1039/c2lc41208j

Qi, X. R., Verwer, R. W. H., Bao, A. M., Balesar, R. A., Luchetti, S., Zhou, J. N., et al. (2019). Human brain slice culture: a useful tool to study brain disorders and potential therapeutic compounds. *Neurosci. Bull*. 35, 244–252. doi: 10.1007/s12264-018-0328-1

Ravula, S. K., McClain, M. A., Wang, M. S., Glass, J. D., and Frazier, A. B. (2006). A multielectrode microcompartment culture platform for studying signal transduction in the nervous system. *Lab Chip* 6, 1530–1153. doi: 10.1039/b612684g

Ronaldson-Bouchard, K., and Vunjak-Novakovic, G. (2018). Organs-on-a-chip: a fast track for engineered human tissues in drug development. *Cell Stem Cell*. 22, 310–324. doi: 10.1016/j.stem.2018.02.011

Rowe, L., Almasri, M., Lee, K., Fogleman, N., Brewer, G. J., Nam, Y., et al. (2007). Active 3-D microscaffold system with fluid perfusion for culturing *in vitro* neuronal networks. *Lab Chip* 7, 475–482. doi: 10.1039/b700795g

Selmer, K. K., Eriksson, A. S., Brandal, K., Egeland, T., Tallaksen, C., and Undlien, D. E. (2009). Parental SCN1A mutation mosaicism in familial Dravet syndrome. *Clin. Genet*. 76, 398–403. doi: 10.1111/j.1399-0004.2009.01208.x

Seymour, J. P., Wu, F., Wise, K. D., and Yoon, E. (2017). State-of-the-art MEMS and microsystem tools for brain research. *Microsys. Nanoeng*. 3:16066. doi: 10.1038/micronano.2016.66

Takahashi, K., Tanabe, K., Ohnuki, M., Narita, M., Ichisaka, T., Tomoda, K., et al. (2007). Induction of pluripotent stem cells from adult human fibroblasts by defined factors. *Cell* 131, 861–872. doi: 10.1016/j.cell.2007.11.019

Taylor, A. M., Blurton-Jones, M., Rhee, S. W., Cribbs, D. H., Cotman, C. W., and Jeon, N. L. (2005). A microfluidic culture platform for CNS axonal injury, regeneration and transport. *Nat. Methods* 2, 599–605. doi: 10.1038/nmeth777

Taylor, A. M., Dieterich, D. C., Ito, H. T., Kim, S. A., and Schuman, E. M. (2010). Microfluidic local perfusion chambers for the visualization and manipulation of synapses. *Neuron* 66, 57–68. doi: 10.1016/j.neuron.2010.03.022

Taylor, A. M., Rhee, S. W., Tu, C. H., Cribbs, D. H., Cotman, C. W., and Jeon, N. L. (2003). Microfluidic multicompartment device for neuroscience research. *Langmuir*. 19, 1551–1556. doi: 10.1021/la026417v

van der Helm, M. W., Odijk, M., Frimat, J. P., van der Meer, A. D., Eijkel, J. C., van den Berg, A., et al. (2016). Direct quantification of transendothelial electrical resistance in organs-on-chips. *Biosens. Bioelectron*. 15, 924–929. doi: 10.1016/j.bios.2016.06.014

van Vliet, E., Stoppini, L., Balestrino, M., Eskes, C., Griesinger, C., Sobanski, T., et al. (2007). Electrophysiological recording of re-aggregating brain cell cultures on multi-electrode arrays to detect acute neurotoxic effects. *Neurotoxicology* 28, 1136–1146. doi: 10.1016/j.neuro.2007.06.004

Vandenhaute, E., Sevin, E., Hallier-Vanuxeem, D., Dehouck, M. P., and Cecchelli, R. (2012). Case study: adapting *in vitro* blood-brain barrier models for use in early-stage drug discovery. *Drug Discov. Today* 17, 285–290. doi: 10.1016/j.drudis.2011.10.006

Viviani, B. (2006). Preparation and coculture of neurons and glial cells. *Curr. Protoc. Cell Biol*. 32, 2–7. doi: 10.1002/0471143030.cb0207s32

Wölfer, J., Bantel, C., Köhling, R., Speckmann, E. J., Wassmann, H., and Greiner, C. (2006). Electrophysiology in ischemic neocortical brain slices: species differences vs. influences of anaesthesia and preparation. *Eur. J. Neurosci*. 23, 1795–1800. doi: 10.1111/j.1460-9568.2006.04696.x

Wong, A. P., Perez-Castillejos, R., Christopher Love, J., and Whitesides, G. M. (2008). Partitioning microfluidic channels with hydrogel to construct tunable 3-D cellular microenvironments. *Biomaterials* 29, 1853–1861. doi: 10.1016/j.biomaterials.2007.12.044

Xie, C., Liu, J., Fu, T. M., Dai, X., Zhou, W., and Lieber, C. M. (2015). Three-dimensional macroporous nanoelectronic networks as minimally invasive brain probes. *Nat. Mater*. 14, 1286–1292. doi: 10.1038/nmat4427

Xie, S., Gardeniers, J. G. E., and Luttge, R. (2018). Nanoscale membrane actuator for in vitro mechano-stimuli responsive studies of neuronal cell networks on chip. *J. Micromech. Microeng*. 28:085011. doi: 10.1088/1361-6439/aabf7e

Yamada, K. M., and Cukierman, E. (2007). Modeling tissue morphogenesis and cancer in 3D. *Cell* 130, 601–610. doi: 10.1016/j.cell.2007.08.006

Ye, K., Kaplan, D. L., Bao, G., Bettinger, C., Forgacs, G., Dong, C., et al. (2018). Advanced cell and tissue biomanufacturing. *ACS Biomat. Sci. Eng*. 4, 2292–2307. doi: 10.1021/acsbiomaterials.8b00650

Ylä-Outinen, L., Joki, T., Varjola, M., Skottman, H., and Narkilahti, S. (2014). Three-dimensional growth matrix for human embryonic stem cell-derived neuronal cells. *J. Tissue Eng. Regen. Med*. 8, 186–194. doi: 10.1002/term.1512

Zhao, X., Zhou, Y., Weissmiller, A. M., Pearn, M. L., Mobley, W. C., and Wu, C. (2014). Real-time imaging of axonal transport of quantum dot-labeled BDNF in primary neurons. *J. Vis. Exp*. 15:51899. doi: 10.3791/51899

Conflict of Interest Statement: The authors declare that the research was conducted in the absence of any commercial or financial relationships that could be construed as a potential conflict of interest.

frontiers
in Bioengineering and Biotechnology

MINI REVIEW
published: 11 December 2018
doi: 10.3389/fbioe.2018.00194

Challenges and Future Prospects on 3D *in-vitro* Modeling of the Neuromuscular Circuit

Maider Badiola-Mateos [1,2], Arnau Hervera [1,3,4,5], José Antonio del Río [1,3,4,5] and Josep Samitier [1,2,6]*

[1] Institute for Bioengineering of Catalonia-Barcelona Institute of Science and Technology, Barcelona, Spain, [2] Department of Electronics and Biomedical Engineering, Faculty of Physics, Universitat de Barcelona, Barcelona, Spain, [3] Department of Cell Biology, Physiology and Immunology, Faculty of Biology, Universitat de Barcelona, Barcelona, Spain, [4] Centro de Investigación Biomédica en Red sobre Enfermedades Neurodegenerativas, Barcelona, Spain, [5] Institut de Neurociències de la Universitat de Barcelona, Barcelona, Spain, [6] Centro de Investigación Biomédica en Red en Bioingeniería, Biomateriales y Nanomedicina, Madrid, Spain

Edited by:
Massimo Alberti,
*Agency for Science, Technology and Research (A*STAR), Singapore*

Reviewed by:
Michela Pozzobon,
Università degli Studi di Padova, Italy
Abhigyan Satyam,
Harvard Medical School, United States

***Correspondence:**
Josep Samitier
jsamitier@ibecbarcelona.eu

Specialty section:
This article was submitted to Tissue Engineering and Regenerative Medicine,
a section of the journal Frontiers in Bioengineering and Biotechnology

Received: *31 August 2018*
Accepted: *27 November 2018*
Published: *11 December 2018*

Citation:
Badiola-Mateos M, Hervera A, del Río JA and Samitier J (2018) Challenges and Future Prospects on 3D in-vitro Modeling of the Neuromuscular Circuit.
Front. Bioeng. Biotechnol. 6:194.
doi: 10.3389/fbioe.2018.00194

Movement of skeletal-muscle fibers is generated by the coordinated action of several cells taking part within the locomotion circuit (motoneurons, sensory-neurons, Schwann cells, astrocytes, microglia, and muscle-cells). Failures in any part of this circuit could impede or hinder coordinated muscle movement and cause a neuromuscular disease (NMD) or determine its severity. Studying fragments of the circuit cannot provide a comprehensive and complete view of the pathological process. We trace the historic developments of studies focused on *in-vitro* modeling of the spinal-locomotion circuit and how bioengineered innovative technologies show advantages for an accurate mimicking of physiological conditions of spinal-locomotion circuit. New developments on compartmentalized microfluidic culture systems (cμFCS), the use of human induced pluripotent stem cells (hiPSCs) and 3D cell-cultures are analyzed. We finally address limitations of current study models and three main challenges on neuromuscular studies: (i) mimic the whole spinal-locomotion circuit including all cell-types involved and the evaluation of independent and interdependent roles of each one; (ii) mimic the neurodegenerative response of mature neurons *in-vitro* as it occurs *in-vivo*; and (iii) develop, tune, implement, and combine cμFCS, hiPSC, and 3D-culture technologies to ultimately create patient-specific complete, translational, and reliable NMD *in-vitro* model. Overcoming these challenges would significantly facilitate understanding the events taking place in NMDs and accelerate the process of finding new therapies.

Keywords: neuromuscular circuit, compartmentalized microfluidic culture systems (cμFCS), hiPSC, 3D-culture, *in-vitro* models

INTRODUCTION

From the physiological and anatomical points of view, the mechanosensory-motor circuit is complex, involving several cell-types with specific natural environments. Traditionally, it has been studied coculturing different cell-types on the same platform from animal origin in 2D (Vilmont et al., 2016; Charoensook et al., 2017; Happe et al., 2017) and 3D (Morimoto et al., 2013; Martin et al., 2015; Smith et al., 2016), or from human origin (Guo et al., 2011; Demestre et al., 2015), or mixed species (Yoshida et al., 2015; Prpar Mihevc et al., 2017). These models provide valuable information in understanding some of the mechanisms underlying the system; but to the date they have not been able to replicate the exact human complexity of physiological functional-units formed by the connection of different cell-types, arising from separated microenvironments. Compartmentalized microfluidic culture systems (cμFCS) (Bhatia and Ingber, 2014) represent an alternative to overcome those problems and, combined with 3D-culture techniques and the use of human induced pluripotent stem cells, they could help recreating neuromuscular physiology of humans *in-vitro*.

This review aims to: (i) provide basic insights about the locomotion circuit and neuromuscular diseases required for its *in-vitro* modeling; (ii) review the breakthrough of bioengineered technologies for neuromuscular-systems; (iii) discuss the limitations and challenges of current study models and future prospects.

LOCOMOTION CIRCUIT AND NEUROMUSCULAR DISEASES (NMDs)

Locomotion circuit, also known as mechanosensory-motor circuit or reflex-arc circuit, is responsible for executing voluntary, and reflex skeletal-muscle movement, alternating flexion, and extension of the muscle (McCrea, 2001; Purves et al., 2004; Kiehn and Dougherty, 2013). The coordinated-action of cells taking part within is what generates movement: (i) motor-neurons (MN) are in charge of carrying information from the central nervous system to the muscle (Kandel et al., 2013); (ii) sensory-neurons (SN) carry information from the periphery of the body (the muscle in this case) to the central nervous system (Kandel et al., 2013); (iii) interneurons innervate motoneurons and are linked to their pattern of sensory input (Côté et al., 2018); (iv) Schwann cells are small cells that form a myelin-sheath around MN and SN axons that insulates them and enhances signal conduction (Kandel et al., 2013); (v) astrocytes maintain synapses, modulate the transmission of the signal, regulate blood flow, and availability of oxygen, nutrients, and survival factors onto neurons (Rindt et al., 2015); (vi) microglia are phagocytic and immunocompetent cells within the central nervous system, able to induce MN cell-death (Sargsyan et al., 2005; Frakes et al., 2014); (vii) skeletal-muscle cells are multinucleated and elongated cells, with sarcomeric striations that form muscle-fibers distributed in fascicle fashion and are the last executors of voluntary and reflex skeletal-muscle movement (Marieb, 2015; Tortora and Derrickson, 2017).

The events that take part within the neuromuscular-circuit to guide the movement in mammals could be resumed as follows. Once the brain takes the decision of initiating a movement, the signal is transmitted from neocortical projecting neurons through the spinal-cord. Then the spinal-locomotion circuit takes part of guiding the voluntary and reflex skeletal-muscle movement (Purves et al., 2004; Kandel et al., 2013; Tortora and Derrickson, 2017): (1) somatic α-motoneurons (MNs) arising from the ventral-horns of spinal-cord, send the input to the synaptic end-bulbs, triggering calcium flows inwards, and the release of the neurotransmitter acetylcholine (ACh) in the neuromuscular junction (NMJ) between the motoneuron and the motor-end plate of extrafusal muscle-fibers; (2) ACh binds specifically to the skeletal-muscle motor-end plates' ACh-receptors (AChR), inducing contraction of sarcolemma, releasing calcium into the sarcoplasm, that binds to troponin on the thin filaments, facilitating myosin-actin binding, and triggering muscle contraction; (3) intrafusal muscle fibers, located interspersed parallel to extrafusal fibers, change in length as the whole muscle changes; (4) sensory-neurons (SN) sense muscle fiber elongation through muscle-spindle—formed by SN nerve endings wrapped around central areas of intrafusal fibers—, and contraction through Golgi tendon organ—formed by encapsulated structures of collagen fibers located at the joint between muscle fibers and tendons that compress innervating a single SN axon—propagating an impulse signal back to the spinal-cord where is modulated by local interneurons and; (5) γ-motoneurons modulate excitatory input adjusting the contractibility of the muscle-spindle by stimulating intrafusal fibers adapting them to an appropriate length; (6) the integration of both afferent signals from the muscle-spindle and the Golgi tendon organ travels through the spinal-cord to the brain to have awareness of the position of the muscle and movement (muscle extension-flexion state), coordinating movements.

Failures in any part of this circuit can hamper coordinated muscle movement and be the cause of neuromuscular diseases (NMDs) or be the consequence that defines their severity (Gogliotti et al., 2012). The term of NMD comprises several diseases with different origins and affectations (such as muscular dystrophy, amyotrophic lateral sclerosis, myasthenia gravis, or spinal muscular atrophy). The effects of NMDs are reflected in the mechanosensory-motor circuit at different cellular levels—including sensory and motor neurons (Jablonka et al., 2006; Gogliotti et al., 2012), Schwann cells (Hunter et al., 2016; Vilmont et al., 2016; Santosa et al., 2018), astrocytes (Rindt et al., 2015), microglia (Frakes et al., 2014; Cooper-Knock et al., 2017), muscle (Martínez-Hernández et al., 2014; Maimon et al., 2018)—, as well as in the connections among them—NMJ (Uzel et al., 2016b; Maimon et al., 2018; Santhanam et al., 2018), muscle spindle (Rumsey et al., 2010; Guo et al., 2017)—, or intraspinal circuits. However, they all share symptoms such as: peripheral hypotonia, muscle weakness, and orthopedic deformities, among others (Bhatt, 2016; Morrison, 2016; Mary et al., 2018). These symptoms impoverishes patient's life-quality (Mary et al., 2018). There is still no treatment for them. Current study models are far from mimicking physiology and therefore are limited on helping to find cures. The technologies here reviewed (**Figure 1**) aim to help on that direction.

MIMICKING *IN-VITRO* HUMAN SPINAL-LOCOMOTION CIRCUIT WITH hiPSCs IN 3D

NMD and NMJ *in-vitro* models have gone through a long evolution history (Thomson et al., 2012): the use of primary

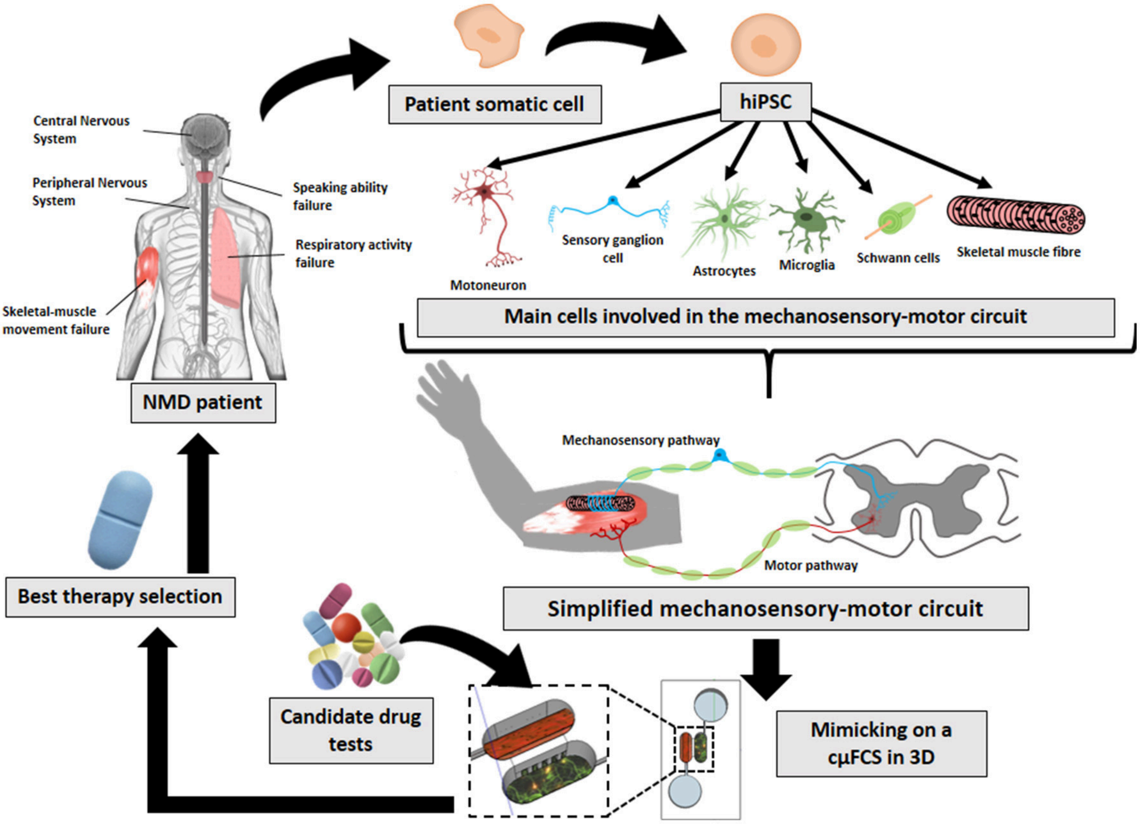

FIGURE 1 | Future prospects on *in-vitro* neuromuscular disease modeling. The implementation and combination of later innovative technologies (hiPSCs, cμFCS, 3D cell-culture) would facilitate the recreation of patient's physiological conditions with his own disease-carrying cells mimicking the mechanosensory-motor circuit in 3D inside a microfluidic compartmentalized device. And finally, it would serve to find specific treatments for each NMD.

cells, cell lines and stem cells; animal-animal cocultures, human-human cocultures, xeno-cocultures; and disease-specific studies. But as reported, most of the research has been done until now by coculturing healthy and diseased cells; primary cells or cell lines with stem cells; and mostly on rodent models or xeno-cultures (human-animal models). However, rodent models offer limited benefit translated into clinic as they do not carry human genetic background. Therefore, personalized medicine needs patient-specific isogenic disease models. In this regard, human induced pluripotent stem cells (hiPSCs) offer the possibility of obtaining different isogenic cell-types from patient's somatic cells, by overexpressing some transcription factors (Takahashi and Yamanaka, 2006), later reviewed (Amabile and Meissner, 2009). They can serve both for creating study models that mimic the physiopathology of the patient, with the further development of future therapeutic transplantation strategies (Su et al., 2013).

The use of induced pluripotent stem cells for disease-modeling, drug-screening, and regenerative therapies of NMDs has widely evolved in the last years (Selvaraj and Perlingeiro, 2018). Nevertheless, few studies have cultured hiPSC-derived motoneurons with hiPSC-derived skeletal-muscle cells *in-vitro* (Demestre et al., 2015; Puttonen et al., 2015; Maffioletti et al., 2018; Osaki et al., 2018). Puttonen et al. (2015) reported a method for the simultaneous differentiation of motoneurons and myotubes from patient-specific hiPSCs, obtaining neuronal differentiation, multinucleated spontaneously contracting myotubes, and functional NMJs on a 2D monolayer. In contrast, Demestre et al. used hiPSCs from healthy donors differentiated separately to motoneurons and myotubes, and subsequently cocultured in 2D. They observed AChR formation in the muscle and neurites outgrowing from motoneurons within the first weeks; but AChR aggregation, maturation of muscle cells, and NMJ formation was not detected until 3 weeks of monolayer cocultures (Demestre et al., 2015).

The advantages and disadvantages between 2D and 3D hiPSC cultures for neurodegenerative disease studies were recently reviewed (Centeno et al., 2018). Briefly, the main outstanding contributions of 3D cultures on NMDs are that: (**i**) it has been proved that 2D monolayers present in some cases altered gene expression whereas 3D cultures display a genotype more relevant to *in-vivo* (Smith et al., 2012; Centeno et al., 2018); (**ii**) cells cultured in 3D acquire more *in-vivo* like phenotype (lower proliferation rate, areas with different levels of oxygen distribution, higher cell-to-cell, and cell-extracellular matrix interactions, increased viability, proliferation, differentiation, and response to stimuli of other cells) (LaPlaca et al., 2010;

Antoni et al., 2015; Centeno et al., 2018); **(iii)** some higher-order processes, such as angiogenesis, occur inherently in 3D (Baker and Chen, 2012; Centeno et al., 2018). But so far, only two studies have been able to mimic the NMJ in 3D using hiPSC-derived motoneurons and skeletal-muscle cells *in-vitro* (Maffioletti et al., 2018; Osaki et al., 2018). Maffioletti et al. (2018) used somatic cells from muscular dystrophy patients to create hiPSC-derived isogenic multilineages (skeletal-muscle cells, vascular endothelial cells, pericytes, and motoneurons), subsequently cocultured embedded in fibrin hydrogels. Osaki et al. (2018) created an ALS microphysiological 3D model culturing ALS-hiPSC-derived neural stem cells with hiPSC-derived skeletal-myoblasts embedded in collagen-Matrigel composites.

However, there are still no studies utilizing hiPSC-derived sensory-neurons and hiPSC-derived muscle-cells to mimic the sensory pathway of the spinal reflex-arc circuit. The latest advances on this respect were published by the group of J.J. Hickman using sensory-neurons derived from human neural progenitor cells and intrafusal fibers generated from human skeletal-muscle stem cells, cocultured on a 2D monolayer (Guo et al., 2017).

COMPARTMENTALIZED MICROFLUIDIC CULTURE SYSTEMS (CμFCS) FOR SPINAL-LOCOMOTION CIRCUIT *IN-VITRO*

Traditional coculture methods do not consider: (i) the different microenvironment requirements of muscle, nerves, and neurons; (ii) the distal connections as they are physically separated *in-vivo*. Furthermore, finding a medium composition compatible for the long-term coculture of both cell-types could be challenging, as several medium components ideal for MN are incompatible with long-term maintenance of skeletal-muscle cells (Thomson et al., 2012; Tong et al., 2014). Hence, a coculture system between neurons and muscle offers limited benefits on mimicking the pathophysiology of NMDs.

The use of compartmentalized microfluidic culture systems (cμFCS) is increasingly growing for neurobiology studies due to the advantages offered compared to classical coculture systems, reviewed in **Box 1**.

Most relevantly, they enable independent culture conditions for neurons and muscle cells, each supplied by its own microenvironment requirements in different interconnected but fluidically isolated compartments, whilst axons can still go through microgroves connecting cells of both compartments.

First compartmentalized microfluidic culture system (cμFCS) for neurobiology studies on neurotrophic effects of dorsal rood ganglion cells (Campenot, 1977) used Teflon-made open compartments, silicone-glue, and microchannels shattered in glass. Since then, and after soft-lithography fabrication improvements, cμFCS have widely evolved in the last 10 years for spinal-locomotion circuit studies (**Supplementary Table 1**). Most compartmentalized cocultures are nowadays performed onto polydimethylsiloxane (PDMS)-based platforms with two cellular compartments separated through microchannels or, as described in the only two publications found using a 3D cell coculture, through a gel region (Uzel et al., 2016b; Osaki et al., 2018). Different cell sources are used for MN (predominantly mouse embryonic primary cells) and muscle-cells (using equally rodent hind limb primary skeletal-muscle cells and C2C12 cell-line).

Besides, there are progressively more commercial cμFCS on the market (Zhang and Radisic, 2017), available for neuromuscular and other neurobiology studies in 2D or 3D, connecting two compartments through microchannels, microposts, or membranes, from the following companies: (i) Xona neuron devices (Xona Microfluidics, California), used in some neuromuscular studies (Southam et al., 2013; Blizzard et al., 2015); (ii) ANANDA Neuro-Device and Coculture-Device (Advanced Nano Design Applications Devices, Canada) employed by Magdesian et al. (2016) combined with AFM measurements to study neuronal growth; (iii) OrganoPlates for 3D culture (Mimetas BV, Netherlands) used to differentiate stem cells into neurons in 3D (Moreno et al., 2015) or for high-throughput evaluation of compounds in glia and neuronal 3D culture (Wevers et al., 2016); (iv) AIM 3D culture chips (AimBiotech, Singapore), employed mostly in cancer-research (Jenkins et al., 2018), although with a great potential to be used in neuromuscular studies, as performed by Uzel et al. (2016b) with a similar custom made device; (v) Neural Diode (MicroBrain Biotech, France) to reconstruct oriented neural network monolayer cultures (Peyrin et al., 2011; Deleglise et al., 2014); (vi) Idealized coculture chips (Synvivo, USA), with different options of radial slits or pillars utilized in many cases to mimic the BBB (Prabhakarpandian et al., 2013), or linear slits for compartmentalization purposes.

However, and despite the advantages offered by both hiPSC and cμFCS technologies, at the moment only two studies have attempted to mimic the spinal-locomotion circuit combining both technologies (Osaki et al., 2018; Santhanam et al., 2018). Santhanam et al. (2018) seed healthy donor's hiPSC-derived MN and human skeletal-muscle fibers in 2D, for dose-evaluation study of toxins affecting the NMJ. Osaki et al. create an ALS microphysiological 3D *in-vitro* study-model and compare it with a healthy model (muscle contraction, recovery, and response to drugs administered via endothelial cell barrier).

LIMITATIONS OF CURRENT STUDY MODELS AND MAIN CHALLENGES

Combination of hiPSCs, cμFCS, and 3D-Culture Technologies

Uzel et al. (2016b) combine cμFCS with 3D cell-culture techniques for neuromuscular studies. Additionally, Santhanam et al. (2018) have attempted to mimic the spinal-locomotion circuit combining hiPSCs and cμFCS technologies. And Maffioletti et al. (2018) perform 3D culture of hiPSCs for NMD studies. But thus far, there is one single study combining 3D culture, hiPSCs and cμFCS as NMD models (Osaki et al., 2018). The three innovative technologies offer advantages (**Figure 1**), but the novelty itself comes with the challenge of developing,

Box 1 | Top 10 advantages of compartmentalized microfluidic culture systems (cμFCS) compared to traditional coculture systems for mimicking spinal-locomotion circuit *in-vitro*.

1. **Fluidic control.** Compartmentalization enables to control de fluidic environment and provide each cell-type required nutrients to efficiently mature, facilitating survival, functionality, and long-term coculture (Park et al., 2006; Tong et al., 2014).
2. **Experiment feasibility.** Ease to study, enhance, control, and monitor some processes (cell proliferation, differentiation, directional growth, migration, and media diffusion from one compartment to the other) (Kamm and Bashir, 2014; Esch et al., 2015).
3. **Microenvironment spatiotemporal control and monitoring.** Independent manipulation of each compartment cells or extracellular matrix hydrogels could be a critical point to assess some processes. Compartmentalized platforms make possible to dissect molecular and cellular events occurring in somal vs. axonal compartments (effect of compounds, drug-sensitivitiy test, etc.) (Yang et al., 2009; Hur et al., 2011; Zahavi et al., 2015); to track individual axons through microchannels (Hosmane et al., 2011); and to assess axon-specific molecules through immunostaining, protein lisate isolation, and mRNA isolation (Saal et al., 2014; Zahavi et al., 2015).
4. **Customisability of cμFCS designs.** Control over microchannel geometry and dimensions (and therefore sifting of cells or compounds that can pass from one compartment to the other), number of compartments (and therefore number or different microenvironments, if required), compartment division tool (micochannels, microgrooves, membranes), distance between compartments, possibility to include reservoirs, covered, or opened compartments, scalability, and device size (Park et al., 2009; Yang et al., 2009; Hosmane et al., 2010; Uzel et al., 2016b).
5. **Customisable engineering features.** Possibility to integrate and take control over parameters: shear-stress flows (Joanne Wang et al., 2008; Shin, 2009); mechanical (Hosmane et al., 2011), optical (Renault et al., 2015; Jang et al., 2016), and electrical stimuli (Hallfors et al., 2013); topographical cues or micropatterns (Hoffman-Kim et al., 2010); chemical gradients (Uzel et al., 2016a); and sensory systems (Shen et al., 2004; Jeong et al., 2018).
6. **Cost-effectiveness.** Low volume of cells and reagents are required (Millet et al., 2007).
7. **Control over the polarity of neural development.** Culturing somas on one compartment makes possible to take control over axon and dendrite polarity during the development, and hence, to mimic axon injuries and study post-injury regeneration easily (Peyrin et al., 2011; Tong et al., 2015; Renault et al., 2016).
8. **Possibility to mimic neural distal connections.** Neurons growing on one compartment can extend their axons to interact with the other compartment cells, mimicking distal connections (Yang et al., 2009; Zahavi et al., 2015; Maimon et al., 2018).
9. **Possibility to integrate control over the polarity of myocyte differentiation.** Skeletal-muscle cells usually adopt randomized distribution *in-vitro*, whereas the presence of aligned micropatterns for 2D culture, cantilevers for 3D culture, or some stimuli methods (mechanical, electrical, or optical) integrated on the cμFCS can enhance its appropriate differentiation and functionality (Tourovskaia et al., 2008; Hume et al., 2012; Uzel et al., 2014, 2016b).
10. **Better mimicking of physiological conditions and possibility to connect with other microfluidic platforms.** This facilitates the study interactions between different physiological functional-units (Maschmeyer et al., 2015), as well as to integrate blood-flow effects (Maoz et al., 2018), or in a future, to mimic a full human-on-a-chip (Williamson et al., 2013; Kamm and Bashir, 2014), enhancing the development of therapies or diagnostic tools (Esch et al., 2014, 2015; Kamm and Bashir, 2014).

tuning, and implementing them together in a unique and biologically reproducible functional platform.

Consideration of Main Actors and Roles From the Spinal-Locomotion Circuit

The co-culture of main cell-types participating in the spinal-locomotion circuit is mandatory to provide a native microenvironment, including the inherent release of growth-factors, as well as to support the viability and maturation of both muscle and neurons, and axon elongation of MNs (Gingras et al., 2008). For instance, spinal MNs cannot achieve proper maturation even after long-term maintenance, unless cultured with muscle-cells, and Schwann cells, as previously reviewed (Bucchia et al., 2018).

Besides, both SN and MN could be altered in particular NMDs (Jablonka et al., 2006; Rumsey et al., 2010; Guo et al., 2017), but not being many available studies focused on the muscle spindle (Taylor et al., 2005; Dagberg and Alstermark, 2006; Rumsey et al., 2010; Bewick and Banks, 2015; Matthews, 2015; Guo et al., 2017) challenges the task of mimicking and characterizing the mechanosensory spinal-locomotion circuit. Additionally, glial cells are also affected and involved in several neuromuscular pathologies (Lobsiger and Cleveland, 2007; Vilmont et al., 2016; Bucchia et al., 2018). Yet, most publications do not consider them.

Most *in-vitro* NMD studies are focused on the α-MN-muscle connection (**Supplementary Table 1**), very few on the γ-MN-muscle connection (Colón et al., 2017), and some on the SN-muscle connection (Taylor et al., 2005; Dagberg and Alstermark, 2006; Rumsey et al., 2010; Bewick and Banks, 2015; Matthews, 2015; Guo et al., 2017; Levin et al., 2017) and fewer on the internal SN-MN connection (Schwab and Ebert, 2014). But there is still very little known about what happens beyond those connections, to what extent cell-strategies for synaptic-specificity contribute on the formation of a functional connection (Fukuhara et al., 2013; Maimon et al., 2018).

Studying parts of the circuit cannot provide a comprehensive and complete view of the pathological process, and functional alterations occurring within it. The big challenge that remains out there on NMD studies is the modeling of the whole spinal-locomotion circuit with all cell-types involved, and the evaluation of independent and interdependent roles of each part of the circuit on the development of a particular NMD.

Modeling Neurodegeneration in NMDs

In a broad sense, neurodegeneration is a process characterized by the progressive functional loss of a population of neurons by intrinsic cell-death or the loss of support cells (i.e., oligodendrocytes or astrocytes). Most NMDs are characterized by this devastating phenomenon (i.e., motoneuron diseases: amyotrophic lateral sclerosis, or spinal muscular atrophy, etc.).

Indeed, studying only functional changes in MNs cannot give a comprehensive and complete picture of the process as it is also regulated by non-neuronal cells (Lobsiger and Cleveland, 2007; Bucchia et al., 2018; Maimon et al., 2018). For instance, a recent study performed by Maimon et al. (2018) demonstrated that axon degeneration only occurred with both MN and muscle cells carrying the genetic mutation indicative of the disorder. Furthermore, the morphology of spinal MN axons *in-vitro* differs from the one presented *in-vivo*: contrary to *in-vivo*, axonal terminals *in-vitro* manifest growth-cones, and are prone to regenerate and lengthen in response to neurotrophic factors required for the *in-vitro* maintenance of the culture (Bucchia et al., 2018). On top of that, another caveat is the fact that extrapolating effects of short-term studies to longer-term disease processes is often not correlated. Therefore, mimicking neurodegeneration response *in-vitro* as it occurs *in-vivo* endures to this day as a challenge. And consequently, there is no effective treatment for neurodegenerative NMDs to promote axonal regeneration yet.

CONCLUSIONS AND FUTURE PROSPECTS

Finding causes and treatment for NMD requires an accurate modeling of the microphysiological conditions that the patient is suffering. But reproducing the complete spinal-locomotion (reflex-arc) circuit *in-vitro* is very complex. Later progresses in neuromuscular-mimicking *in-vitro* systems, have been achieved incorporating increasingly evolving technologies of hiPSCs, cμFCS, and 3D cell-culture techniques here reviewed. The combination of novel technologies in the proper manner has proved to result in the acquisition of more reliable results (Uzel et al., 2016b; Maffioletti et al., 2018; Osaki et al., 2018; Santhanam et al., 2018). But there is still room for improvement. Future studies should focus on addressing unsolved questions related to: mimicking the whole spinal-locomotion circuit (including all cell-types involved, as well as evaluating the independent and interdependent roles of each one), defining the specific role of the factors that determine the NMD and their severity; mimicking neurodegeneration processes; and above all, finding treatments for NMD.

AUTHOR CONTRIBUTIONS

MB-M wrote the manuscript with contributions from AH, JdR, and JS.

FUNDING

This work was supported by Networking Biomedical Research Center (CIBER), Spain. CIBER is an initiative funded by the VI National R&D Plan 2008–2011, Iniciativa Ingenio 2010, Consolider Program, CIBER Actions, and the Instituto de Salud Carlos III, with the support of the European Regional Development Fund. This work was funded by the CERCA Programme and by the Commission for Universities and Research of the Department of Innovation, Universities, and Enterprise of the Generalitat de Catalunya (2017 SGR 1079). This work was funded by the Spanish Ministry of Economy and Competitiveness (MINECO) through the projects MINDS (Proyectos I+D Excelencia + FEDER): TEC2015-70104-P and BIOBOT (Programa Explora Ciencia/Tecnología): TEC2015-72718-EXP. This research was supported by grants from the Spanish Ministry of Economy, Industry and Competitiveness (MEICO / FEDER) (BFU2015-67777-R), the Spanish Prion Network (Prionet Spain, AGL2015-71764-REDT and AGL2017-90665-REDT), the Generalitat de Catalunya (SGR2017-648), CIBERNED (PRY-2016-2, MFDEND), CERCA Programme/Generalitat de Catalunya and La Marató de TV3 to JADR. AH was supported by a fellowship from the Juan de la Cierva program from MINECO.

SUPPLEMENTARY MATERIAL

The Supplementary Material for this article can be found online at: https://www.frontiersin.org/articles/10.3389/fbioe.2018.00194/full#supplementary-material

REFERENCES

Amabile, G., and Meissner, A. (2009). Induced pluripotent stem cells: current progress and potential for regenerative medicine. *Trends Mol. Med.* 15, 59–68. doi: 10.1016/j.molmed.2008.12.003

Antoni, D., Burckel, H., Josset, E., and Noel, G. (2015). Three-dimensional cell culture: a breakthrough *in vivo*. *Int. J. Mol. Sci.* 16, 5517–5527. doi: 10.3390/ijms16035517

Baker, B. M., and Chen, C. S. (2012). Deconstructing the third dimension – how 3D culture microenvironments alter cellular cues. *J. Cell Sci.* 125, 3015–3024. doi: 10.1242/jcs.079509

Bewick, G. S., and Banks, R. W. (2015). Mechanotransduction in the muscle spindle. *Pflügers Arch. Eur. J. Physiol.* 467, 175–190. doi: 10.1007/s00424-014-1536-9

Bhatia, S. N., and Ingber, D. E. (2014). Microfluidic organs-on-chips. *Nat. Biotechnol.* 32, 760–772. doi: 10.1038/nbt.2989

Bhatt, J. M. (2016). The epidemiology of neuromuscular diseases. *Neurol. Clin.* 34, 999–1021. doi: 10.1016/j.ncl.2016.06.017

Blizzard, C. A., Southam, K. A., Dawkins, E., Lewis, K. E., King, A. E., Clark, J. A., et al. (2015). Identifying the primary site of pathogenesis in amyotrophic lateral sclerosis - vulnerability of lower motor neurons to proximal excitotoxicity. *Dis. Model. Mech.* 8, 215–224. doi: 10.1242/dmm.018606

Bucchia, M., Merwin, S. J., Re, D. B., and Kariya, S. (2018). Limitations and challenges in modeling diseases involving spinal motor neuron degeneration *in vitro*. *Front. Cell. Neurosci.* 12:61. doi: 10.3389/fncel.2018.00061

Côté, M. P., Murray, L. M., and Knikou, M. (2018). Spinal control of locomotion: individual neurons, their circuits and functions. *Front. Physiol.* 9:784. doi: 10.3389/fphys.2018.00784

Campenot, R. B. (1977). Local control of neurite development by nerve growth factor (chemotaxis/culture methods/retrograde transport/sympathetic ganglia). *Cell Biol.* 74, 4516–4519.

Centeno, E. G. Z., Cimarosti, H., and Bithell, A. (2018). 2D versus 3D human induced pluripotent stem cell-derived cultures for neurodegenerative disease modelling. *Mol. Neurodegener.* 13:27. doi: 10.1186/s13024-018-0258-4

Charoensook, S. N., Williams, D. J., Chakraborty, S., Leong, K. W., and Vunjak-Novakovic, G. (2017). Bioreactor model of neuromuscular junction with electrical stimulation for pharmacological potency testing. *Integr. Biol.* 9, 956–967. doi: 10.1039/C7IB00144D

Colón, A., Guo, X., Akanda, N., Cai, Y., and Hickman, J. J. (2017). Functional analysis of human intrafusal fiber innervation by human γ-motoneurons. *Sci. Rep.* 7:17202. doi: 10.1038/s41598-017-17382-2

Cooper-Knock, J., Green, C., Altschuler, G., Wei, W., Bury, J. J., Heath, P. R., et al. (2017). A data-driven approach links microglia to pathology and prognosis in amyotrophic lateral sclerosis. *Acta Neuropathol. Commun.* 5:23. doi: 10.1186/s40478-017-0424-x

Dagberg, B., and Alstermark, B. (2006). Improved organotypic cell culture model for analysis of the neuronal circuit involved in the monosynaptic stretch reflex. *J. Neurosci. Res.* 84, 460–469. doi: 10.1002/jnr.20888

Deleglise, B., Magnifico, S., Duplus, E., Vaur, P., Soubeyre, V., Belle, M., et al. (2014). β-amyloid induces a dying-back process and remote trans-synaptic alterations in a microfluidic-based reconstructed neuronal network. *Acta Neuropathol. Commun.* 2:145. doi: 10.1186/s40478-014-0145-3

Demestre, M., Orth, M., Föhr, K. J., Achberger, K., Ludolph, A. C., Liebau, S., et al. (2015). Formation and characterisation of neuromuscular junctions between hiPSC derived motoneurons and myotubes. *Stem Cell Res.* 15, 328–336. doi: 10.1016/j.scr.2015.07.005

Esch, E. W., Bahinski, A., and Huh, D. (2015). Organs-on-chips at the frontiers of drug discovery. *Nat. Rev. Drug Discov.* 14, 248–260. doi: 10.1038/nrd4539

Esch, M. B., Smith, A. S., Prot, J. M., Oleaga, C., Hickman, J. J., and Shuler, M. L. (2014). How multi-organ microdevices can help foster drug development. *Adv. Drug Deliv. Rev.* 69–70, 158–169. doi: 10.1016/j.addr.2013.12.003

Frakes, A. E., Ferraiuolo, L., Haidet-Phillips, A. M., Schmelzer, L., Braun, L., Miranda, C. J., et al. (2014). Microglia induce motor neuron death via the classical NF-κB pathway in amyotrophic lateral sclerosis. *Neuron* 81, 1009–1023. doi: 10.1016/j.neuron.2014.01.013

Fukuhara, K., Imai, F., Ladle, D. R., Katayama, K. I., Leslie, J. R., Arber, S., et al. (2013). Specificity of monosynaptic sensory-motor connections imposed by repellent Sema3E-PlexinD1 signaling. *Cell Rep.* 5, 748–758. doi: 10.1016/j.celrep.2013.10.005

Gingras, M., Beaulieu, M. M., Gagnon, V., Durham, H. D., and Berthod, F. (2008). *In vitro* study of axonal migration and myelination of motor neurons in a three-dimensional tissue-engineered model. *Glia* 56, 354–364. doi: 10.1002/glia.20617

Gogliotti, R. G., Quinlan, K. A., Barlow, C. B., Heier, C. R., Heckman, C. J., and DiDonato, C. J. (2012). Motor neuron rescue in spinal muscular atrophy mice demonstrates that sensory-motor defects are a consequence, not a cause, of motor neuron dysfunction. *J. Neurosci.* 32, 3818–3829. doi: 10.1523/JNEUROSCI.5775-11.2012

Guo, X., Colon, A., Akanda, N., Spradling, S., Stancescu, M., Martin, C., et al. (2017). Tissue engineering the mechanosensory circuit of the stretch reflex arc with human stem cells: sensory neuron innervation of intrafusal muscle fibers. *Biomaterials* 122, 179–187. doi: 10.1016/j.biomaterials.2017.01.005

Guo, X., Gonzalez, M., Stancescu, M., Vandenburgh, H. H., and Hickman, J. J. (2011). Neuromuscular junction formation between human stem cell-derived motoneurons and human skeletal muscle in a defined system. *Biomaterials* 32, 9602–9611. doi: 10.1016/j.biomaterials.2011.09.014

Hallfors, N., Khan, A., Dickey, M. D., and Taylor, A. M. (2013). Integration of pre-aligned liquid metal electrodes for neural stimulation within a user-friendly microfluidic platform. *Lab Chip* 13, 522–526. doi: 10.1039/C2LC40954B

Happe, C. L., Tenerelli, K. P., Gromova, A. K., Kolb, F., and Engler, A. J. (2017). Mechanically patterned neuromuscular junctions-in-a-dish have improved functional maturation. *Mol. Biol. Cell* 28, 1950–1958. doi: 10.1091/mbc.e17-01-0046

Hoffman-Kim, D., Mitchel, J. A., and Bellamkonda, R. V. (2010). Topography, cell response, and nerve regeneration. *Annu. Rev. Biomed. Eng.* 12, 203–231. doi: 10.1146/annurev-bioeng-070909-105351

Hosmane, S., Fournier, A., Wright, R., Rajbhandari, L., Siddique, R., Yang, I. H., et al. (2011). Valve-based microfluidic compression platform: single axon injury and regrowth. *Lab Chip* 11, 3888–3895. doi: 10.1039/c1lc20549h

Hosmane, S., Yang, I. H., Ruffin, A., Thakor, N., and Venkatesan, A. (2010). Circular compartmentalized microfluidic platform: study of axon–glia interactions. *Lab Chip* 10, 741–747. doi: 10.1039/b918640a

Hume, S. L., Hoyt, S. M., Walker, J. S., Sridhar, B. V., Ashley, J. F., Bowman, C. N., et al. (2012). Alignment of multi-layered muscle cells within three-dimensional hydrogel macrochannels. *Acta Biomater.* 8, 2193–2202. doi: 10.1016/j.actbio.2012.02.001

Hunter, G., Powis, R. A., Jones, R. A., Groen, E. J., Shorrock, H. K., Lane, F. M., et al. (2016). Restoration of SMN in schwann cells reverses myelination defects and improves neuromuscular function in spinal muscular atrophy. *Hum. Mol. Genet.* 25, 2853–2861. doi: 10.1093/hmg/ddw141

Hur, E. M., Yang, I. H., Kim, D. H., Byun, J., Saijilafu, X.U. W. L., Nicovich P. R., et al. (2011). Engineering neuronal growth cones to promote axon regeneration over inhibitory molecules. *Proc. Natl. Acad. Sci.U.S.A.* 108, 5057–5062. doi: 10.1073/pnas.1011258108

Hyun Sung P., Su, L., McDonald, J., Thakor, N., and In Hong Y. (2013). "Neuromuscular junction in a microfluidic device," in *2013 35th Annual International Conference of the IEEE Engineering in Medicine and Biology Society (EMBC)* (IEEE), 2833–2835.

Ionescu, A., Zahavi, E. E., Gradus, T., Ben-Yaakov, K., and Perlson, E. (2016). Compartmental microfluidic system for studying muscle–neuron communication and neuromuscular junction maintenance. *Eur. J. Cell Biol.* 95, 69–88. doi: 10.1016/j.ejcb.2015.11.004

Jablonka, S., Karle, K., Sandner, B., Andreassi, C., von Au, K., and Sendtner, M. (2006). Distinct and overlapping alterations in motor and sensory neurons in a mouse model of spinal muscular atrophy. *Hum. Mol. Genet.* 15, 511–518. doi: 10.1093/hmg/ddi467

Jang, J. M., Lee, J., Kim, H., Jeon, N. L., and Jung, W. (2016). One-photon and two-photon stimulation of neurons in a microfluidic culture system. *Lab Chip* 16, 1684–1690. doi: 10.1039/C6LC00065G

Jenkins, R. W., Aref, A. R., Lizotte, P. H., Ivanova, E., Stinson, S., Zhou, C. W., et al. (2018). *Ex vivo* profiling of PD-1 blockade using organotypic tumor spheroids. *Cancer Discov.* 8, 196–215. doi: 10.1158/2159-8290.CD-17-0833

Jeong, S., Kim, S., Buonocore, J., Park, J., Welsh, C. J., Li, J., et al. (2018). A three-dimensional arrayed microfluidic blood–brain barrier model with integrated electrical sensor array. *IEEE Trans. Biomed. Eng.* 65, 431–439. doi: 10.1109/TBME.2017.2773463

Joanne Wang, C., Li, X., Lin, B., Shim, S., Ming, G., and Levchenko, A. (2008). A microfluidics-based turning assay reveals complex growth cone responses to integrated gradients of substrate-bound ECM molecules and diffusible guidance cues. *Lab Chip* 8, 227–237. doi: 10.1039/b713945d

Kamm, R. D., and Bashir, R. (2014). Creating living cellular machines. *Ann. Biomed. Eng.* 42, 445–459. doi: 10.1007/s10439-013-0902-7

Kandel, E. R., Schwartz, J. H., Jessel, T. M., Siegelbaum, S. A., and Hudspeth, A. J. (eds.). (2013). *Principles of Neural Science*, *5th Edn*. New York, NY: Mc Graw Hill Medical.

Kiehn, O., and Dougherty, K. (2013). "Locomotion: circuits and physiology," in *Neuroscience in the 21st Century*, eds D. W. Pfaff (New York, NY: Springer), 1209–1236. doi: 10.1007/978-1-4614-1997-6_42

LaPlaca, M. C., Vernekar, V. N., Shoemaker, J. T., and Cullen, D. K. (2010). "Three-Dimensional Neuronal Cultures," in *Methods in Bioengineering: 3D Tissue Engineering*, eds F. Berthiaume and J. R. Morgan (Norwood, OH: Artech House), 187–204.

Levin, E., Andreadaki, A., Gobrecht, P., Bosse, F., and Fischer, D. (2017). Nociceptive DRG neurons express muscle lim protein upon axonal injury. *Sci. Rep.* 7:643. doi: 10.1038/s41598-017-00590-1

Lobsiger, C. S., and Cleveland, D. W. (2007). Glial cells as intrinsic components of non-cell-autonomous neurodegenerative disease. *Nat. Neurosci.* 10, 1355–1360. doi: 10.1038/nn1988

Maffioletti, S. M., Sarcar, S., Henderson, A. B. H., Mannhardt, I., Pinton, L., Moyle, L. A., et al. (2018). Three-dimensional human iPSC-derived artificial skeletal muscles model muscular dystrophies and enable multilineage tissue engineering. *Cell Rep.* 23, 899–908. doi: 10.1016/j.celrep.2018.03.091

Magdesian, M. H., Lopez-Ayon, G. M., Mori, M., Boudreau, D., Goulet-Hanssens, A., Sanz, R., et al. (2016). Rapid mechanically controlled rewiring of neuronal circuits. *J. Neurosci.* 36, 979–987. doi: 10.1523/JNEUROSCI.1667-15.2016

Maimon, R., Ionescu, A., Bonnie, A., Sweetat, S., Wald-Altman, S., Inbar, S., et al. (2018). miR126-5p down-regulation facilitates axon degeneration and

NMJ disruption via a non-cell-autonomous mechanism in ALS. *J. Neurosci.* 38, 5478–5494. doi: 10.1523/JNEUROSCI.3037-17.2018

Maoz, B. M., Herland, A., FitzGerald, E. A., Grevesse, T., Vidoudez, C., Pacheco, A. R., et al. (2018). A linked organ-on-chip model of the human neurovascular unit reveals the metabolic coupling of endothelial and neuronal cells. *Nat. Biotechnol.* 36, 865–874. doi: 10.1038/nbt.4226

Marieb, E. N. (ed.). (2015). *Essentials of Human Anatomy & Physiology*, *11th Edn*. Harlow: Pearson Education.

Martin, N. R., Passey, S. L., Player, D. J., Mudera, V., Baar, K., Greensmith, L., et al. (2015). Neuromuscular junction formation in tissue-engineered skeletal muscle augments contractile function and improves cytoskeletal organization. *Tissue Eng. Part A* 21, 2595–2604. doi: 10.1089/ten.tea.2015.0146

Martínez-Hernández, R., Bernal, S., Alias, L., and Tizzano, E. F. (2014). Abnormalities in early markers of muscle involvement support a delay in myogenesis in spinal muscular atrophy. *J. Neuropathol. Exp. Neurol.* 73, 559–567. doi: 10.1097/NEN.0000000000000078

Mary, P., Servais, L., and Vialle, R. (2018). Neuromuscular diseases: diagnosis and management. *Orthop. Traumatol. Surg. Res.* 104, S89–S95. doi: 10.1016/j.otsr.2017.04.019

Maschmeyer, I., Lorenz, A. K., Schimek, K., Hasenberg, T., Ramme, A. P., Hübner, J., et al. (2015). A four-organ-chip for interconnected long-term co-culture of human intestine, liver, skin and kidney equivalents. *Lab Chip* 15, 2688–2699. doi: 10.1039/C5LC00392J

Matthews, P. B. (2015). Where anatomy led, physiology followed: a survey of our developing understanding of the muscle spindle, what it does and how it works. *J. Anat.* 227, 104–114. doi: 10.1111/joa.12345

McCrea, D. A. (2001). Spinal circuitry of sensorimotor control of locomotion. *J. Physiol.* 533, 41–50. doi: 10.1111/j.1469-7793.2001.0041b.x

Millet, L. J., Stewart, M. E., Sweedler, J. V., Nuzzo, R. G., and Gillette, M. U. (2007). Microfluidic devices for culturing primary mammalian neurons at low densities. *Lab Chip* 7, 987–994. doi: 10.1039/b705266a

Moreno, E. L., Hachi, S., Hemmer, K., Trietsch, S. J., Baumuratov, A. S., Hankemeier, T., et al. (2015). Differentiation of neuroepithelial stem cells into functional dopaminergic neurons in 3D microfluidic cell culture. *Lab Chip* 15, 2419–2428. doi: 10.1039/C5LC00180C

Morimoto, Y., Kato-Negishi, M., Onoe, H., and Takeuchi, S. (2013). Three-dimensional neuron–muscle constructs with neuromuscular junctions. *Biomaterials* 34, 9413–9419. doi: 10.1016/j.biomaterials.2013.08.062

Morrison, B. (2016). Neuromuscular diseases. *Semin. Neurol.* 36, 409–418. doi: 10.1055/s-0036-1586263

Osaki, T., Uzel, S. G. M., and Kamm, R. D. (2018). Microphysiological 3D model of amyotrophic lateral sclerosis (ALS) from human iPS-derived muscle cells and optogenetic motor neurons. *Sci. Adv.* 4:eaat5847. doi: 10.1126/sciadv.aat5847

Park, J., Koito, H., Li, J., and Han, A. (2009). Microfluidic compartmentalized co-culture platform for CNS axon myelination research. *Biomed. Microdev.* 11, 1145–1153. doi: 10.1007/s10544-009-9331-7

Park, J. W., Vahidi, B., Taylor, A. M., Rhee, S. W., and Jeon, N. L. (2006). Microfluidic culture platform for neuroscience research. *Nat. Protoc.* 1, 2128–2136. doi: 10.1038/nprot.2006.316

Peyrin, J. M., Deleglise, B., Saias, L., Vignes, M., Gougis, P., Magnifico, S., et al. (2011). Axon diodes for the reconstruction of oriented neuronal networks in microfluidic chambers. *Lab Chip* 11, 3663–3673. doi: 10.1039/c1lc20014c

Prabhakarpandian, B., Shen, M. C., Nichols, J. B., Mills, I. R., Sidoryk-Wegrzynowicz, M., Aschner, M., et al. (2013). SyM-BBB: a microfluidic blood brain barrier model. *Lab Chip* 13, 1093–1101. doi: 10.1039/c2lc41208j

Prpar Mihevc, S., Pavlin, M., Darovic, S., Živin, M., Podbregar, M., Rogelj, B., et al. (2017). Modelling FUS mislocalisation in an *in vitro* model of innervated human muscle. *J. Mol. Neurosci.* 62, 318–328. doi: 10.1007/s12031-017-0940-y

Purves, D., Augustine, G. J., Hall, W. C., LaMantia, A. S., McNamara, J. O., and Williams, S. M. (eds) (2004). *Neuroscience*, *3rd Edn*. Sunderland: Sinauer Associates, Inc.

Puttonen, K. A., Ruponen, M., Naumenko, N., Hovatta, O. H., Tavi, P., and Koistinaho, J. (2015). Generation of functional neuromuscular junctions from human pluripotent stem cell lines. *Front. Cell. Neurosci.* 9:473. doi: 10.3389/fncel.2015.00473

Renault, R., Durand, J. B., Viovy, J. L., and Villard, C. (2016). Asymmetric axonal edge guidance: a new paradigm for building oriented neuronal networks. *Lab Chip* 16, 2188–2191. doi: 10.1039/C6LC00479B

Renault, R., Sukenik, N., Descroix, S., Malaquin, L., Viovy, J. L., Peyrin, J. M., et al. (2015). Combining microfluidics, optogenetics and calcium imaging to study neuronal communication *in vitro*. *PLoS ONE* 10:e0120680. doi: 10.1371/journal.pone.0120680

Rindt, H., Feng, Z., Mazzasette, C., Glascock, J. J., Valdivia, D., Pyles, N., et al. (2015). Astrocytes influence the severity of spinal muscular atrophy. *Hum. Mol. Genet.* 24, 4094–4102. doi: 10.1093/hmg/ddv148

Rumsey, J. W., Das, M., Bhalkikar, A., Stancescu, M., and Hickman, J. J. (2010). Tissue engineering the mechanosensory circuit of the stretch reflex arc: sensory neuron innervation of intrafusal muscle fibers. *Biomaterials* 31, 8218–8227. doi: 10.1016/j.biomaterials.2010.07.027

Saal, L., Briese, M., Kneitz, S., Glinka, M., and Sendtner, M. (2014). Subcellular transcriptome alterations in a cell culture model of spinal muscular atrophy point to widespread defects in axonal growth and presynaptic differentiation. *RNA* 20, 1789–1802. doi: 10.1261/rna.047373.114

Santhanam, N., Kumanchik, L., Guo, X., Sommerhage, F., Cai, Y., Jackson, M., et al. (2018). Stem cell derived phenotypic human neuromuscular junction model for dose response evaluation of therapeutics. *Biomaterials* 166, 64–78. doi: 10.1016/j.biomaterials.2018.02.047

Santosa, K. B., Keane, A. M., Jablonka-Shariff, A., Vannucci, B., and Snyder-Warwick, A. K. (2018). Clinical relevance of terminal Schwann cells: an overlooked component of the neuromuscular junction. *J. Neurosci. Res.* 96, 1125–1135. doi: 10.1002/jnr.24231

Sargsyan, S. A., Monk, P. N., and Shaw, P. J. (2005). Microglia as potential contributors to motor neuron injury in amyotrophic lateral sclerosis. *Glia* 51, 241–253. doi: 10.1002/glia.20210

Schwab, A. J., and Ebert, A. D. (2014). Sensory neurons do not induce motor neuron loss in a human stem cell model of spinal muscular atrophy. *PLoS ONE* 9:e103112. doi: 10.1371/journal.pone.0103112

Selvaraj, S., and Perlingeiro, R. C. R. (2018). "Induced pluripotent stem cells for neuromuscular diseases: potential for disease modeling, drug screening, and regenerative medicine," in *Reference Module in Biomedical Sciences*, eds C. A. McQueen, W. F. Boron, E. L. Boulpaep, A. Bradshaw, Ralph, D. B. Bylund, S. J. Enna, et al. (Elsevier). doi: 10.1016/B978-0-12-801238-3.65504-6

Shen, N. Y., Liu, Z., Jacquot, B. C., Minch, B. A., and Kan, E. C. (2004). Integration of chemical sensing and electrowetting actuation on chemoreceptive neuron MOS (CνMOS) transistors. *Sens. Actuators B Chem.* 102, 35–43. doi: 10.1016/j.snb.2003.10.013

Shin, H. S. (2009). Shear stress effect on transfection of neurons cultured in microfluidic devices. *J. Nanosci. Nanotechnol.* 9, 7330–7335. doi: 10.1166/jnn.2009.1769

Smith, A. S., Passey, S. L., Martin, N. R. W., Player, D. J., Mudera, V., Greensmith, L., et al. (2016). Creating interactions between tissue-engineered skeletal muscle and the peripheral nervous system. *Cells. Tissues. Organs* 202, 143–158. doi: 10.1159/000443634

Smith, S. J., Wilson, M., Ward, J. H., Rahman, C. V., Peet, A. C., Macarthur, D. C., et al. (2012). Recapitulation of tumor heterogeneity and molecular signatures in a 3D brain cancer model with decreased sensitivity to histone deacetylase inhibition. *PLoS ONE* 7:e52335. doi: 10.1371/journal.pone.0052335

Southam, K. A., King, A. E., Blizzard, C. A., McCormack, G. H., and Dickson, T. C. (2013). Microfluidic primary culture model of the lower motor neuron–neuromuscular junction circuit. *J. Neurosci. Methods* 218, 164–169. doi: 10.1016/j.jneumeth.2013.06.002

Su, H., Wang, L., Cai, J., Yuan, Q., Yang, X., Yao, X., et al. (2013). Transplanted motoneurons derived from human induced pluripotent stem cells form functional connections with target muscle. *Stem Cell Res.* 11, 529–539. doi: 10.1016/j.scr.2013.02.007

Takahashi, K., and Yamanaka, S. (2006). Induction of pluripotent stem cells from mouse embryonic and adult fibroblast cultures by defined factors. *Cell* 126, 663–676. doi: 10.1016/j.cell.2006.07.024

Taylor, M. D., Holdeman, A. S., Weltmer, S. G., Ryals, J. M., and Wright, D. E. (2005). Modulation of muscle spindle innervation by neurotrophin-3 following nerve injury. *Exp. Neurol.* 191, 211–222. doi: 10.1016/j.expneurol.2004.09.015

Thomson, S. R., Wishart, T. M., Patani, R., Chandran, S., and Gillingwater, T. H. (2012). Using induced pluripotent stem cells (iPSC) to model human neuromuscular connectivity: promise or reality? *J. Anat.* 220, 122–130. doi: 10.1111/j.1469-7580.2011.01459.x

Tong, Z., Segura-Feliu, M., Seira, O., Homs-Corbera, A., Del Río, J. A., and Samitier, J. (2015). A microfluidic neuronal platform for neuron axotomy and controlled regenerative studies. *RSC Adv.* 5, 73457–73466. doi: 10.1039/C5RA11522A

Tong, Z., Seira, O., Casas, C., Reginensi, D., Homs-Corbera, A., Samitier, J., et al. (2014). Engineering a functional neuro-muscular junction model in a chip. *RSC Adv.* 4, 54788–54797. doi: 10.1039/C4RA10219C

Tortora, G. J., and Derrickson, B. (eds.). (2017). *Principles of Anatomy and Physiology*, *15th Edn.* Danvers, MA: John Wiley & Sons, Inc.

Tourovskaia, A., Li, N., and Folch, A. (2008). Localized acetylcholine receptor clustering dynamics in response to microfluidic focal stimulation with agrin. *Biophys. J.* 95, 3009–3016. doi: 10.1529/biophysj.107.128173

Uzel, S. G., Platt, R. J., Subramanian, V., Pearl, T. M., Rowlands, C. J., Chan, V., et al. (2016b). Microfluidic device for the formation of optically excitable, three-dimensional, compartmentalized motor units. *Sci. Adv.* 2:e1501429–e1501429. doi: 10.1126/sciadv.1501429

Uzel, S. G. M., Amadi, O. C., Pearl, T. M., Lee, R. T., So, P. T. C., and Kamm, R. D. (2016a). Simultaneous or sequential orthogonal gradient formation in a 3D cell culture microfluidic platform. *Small* 12, 612–622. doi: 10.1002/smll.201501905

Uzel, S. G. M., Pavesi, A., and Kamm, R. D. (2014). Microfabrication and microfluidics for muscle tissue models. *Prog. Biophys. Mol. Biol.* 115, 279–293. doi: 10.1016/j.pbiomolbio.2014.08.013

Vilmont, V., Cadot, B., Ouanounou, G., and Gomes, E. R. (2016). A system for studying mechanisms of neuromuscular junction development and maintenance. *Development* 143, 2464–2477. doi: 10.1242/dev.130278

Wevers, N. R., van Vught, R., Wilschut, K. J., Nicolas, A., Chiang, C., Lanz, H. L., et al. (2016). High-throughput compound evaluation on 3D networks of neurons and glia in a microfluidic platform. *Sci. Rep.* 6:38856. doi: 10.1038/srep38856

Williamson, A., Singh, S., Fernekorn, U., and Schober, A. (2013). The future of the patient-specific body-on-a-chip. *Lab Chip* 13, 3471–3480. doi: 10.1039/c3lc50237f

Yang, I. H., Siddique, R., Hosmane, S., Thakor, N., and Höke, A. (2009). Compartmentalized microfluidic culture platform to study mechanism of paclitaxel-induced axonal degeneration. *Exp. Neurol.* 218, 124–128. doi: 10.1016/j.expneurol.2009.04.017

Yoshida, M., Kitaoka, S., Egawa, N., Yamane, M., Ikeda, R., Tsukita, K., et al. (2015). Modeling the early phenotype at the neuromuscular junction of spinal muscular atrophy using patient-derived iPSCs. *Stem Cell Rep.* 4, 561–568. doi: 10.1016/j.stemcr.2015.02.010

Zahavi, E. E., Ionescu, A., Gluska, S., Gradus, T., Ben-Yaakov, K., and Perlson, E. (2015). A compartmentalized microfluidic neuromuscular co-culture system reveals spatial aspects of GDNF functions. *J. Cell Sci.* 128, 1241–1252. doi: 10.1242/jcs.167544

Zhang, B., and Radisic, M. (2017). Organ-on-a-chip devices advance to market. *Lab Chip* 17, 2395–2420. doi: 10.1039/C6LC01554A

Conflict of Interest Statement: The authors declare that the research was conducted in the absence of any commercial or financial relationships that could be construed as a potential conflict of interest.

frontiers
in Bioengineering and Biotechnology

GENERAL COMMENTARY
published: 04 October 2018
doi: 10.3389/fbioe.2018.00138

Commentary: Human brain organoid-on-a-chip to model prenatal nicotine exposure

Haowen Qiao [1,2], Yu Shrike Zhang [3] and Pu Chen [1,2]**

[1] Department of Biomedical Engineering, School of Basic Medical Sciences, Wuhan University, Wuhan, China, [2] Hubei Provincial Key Laboratory of Developmentally Originated Disorder, Wuhan, China, [3] Division of Engineering in Medicine, Department of Medicine, Brigham and Women's Hospital, Harvard Medical School, Cambridge, MA, United States

Keywords: brain, Organoid, organ-on-a-chip, prenatal neurological disorder, nicotine exposure

Edited by:
Massimo Alberti,
*Agency for Science, Technology and Research (A*STAR), Singapore*

Reviewed by:
Toshio Takahashi,
Suntory Foundation for Life Sciences, Japan
Antoni Homs-Corbera,
Cherry Biotech, France

***Correspondence:**
Yu Shrike Zhang
yszhang@research.bwh.harvard.edu
Pu Chen
puchen@whu.edu.cn

Specialty section:
This article was submitted to Tissue Engineering and Regenerative Medicine,
a section of the journal Frontiers in Bioengineering and Biotechnology

Received: *16 July 2018*
Accepted: *13 September 2018*
Published: *04 October 2018*

Citation:
Qiao H, Zhang YS and Chen P (2018) Commentary: Human brain organoid-on-a-chip to model prenatal nicotine exposure.
Front. Bioeng. Biotechnol. 6:138.
doi: 10.3389/fbioe.2018.00138

A Commentary on

Human brain organoid-on-a-chip to model prenatal nicotine exposure
by Wang, Y., Wang, L., Zhu, Y., and Qin, J. (2018). Lab Chip 18, 851–860. doi: 10.1039/C7LC01084B

BRAIN ORGANOID AND BRAIN-ON-A-CHIP TECHNOLOGIES

Advances in three-dimensional (3D) neural culture models derived from human stem cells are revolutionizing the paradigm of neuroscience research. These 3D model systems offer a more faithful recapitulation of pivotal functions and cytoarchitectures of *in-vivo* neural tissues than conventional two-dimensional (2D) culture models and animal models (Zhuang et al., 2018).

To establish these 3D neural models, brain organoids (Lee et al., 2017), and brain-on-a-chip systems (Haring et al., 2017) represent two typical approaches based on the strategies of developmental biology and bioengineering, respectively. Brain organoids are formed by sequential steps in neural development *in vitro*, including generation of embryoid bodies (EBs) from stem cells, induction of neuroectoderm in a dish, expansion of neuroepithelium in Matrigel, and organoid differentiation in suspension (Jo et al., 2016). Brain organoids explore the power of developmental biology to reproduce the early stages of fetal brain development, including polarized neuroepithelium, cell type heterogeneity and segregation of discrete brain regions (Luo et al., 2016). In contrast, brain-on-a-chip systems provide better capacity to reconstitute *in-vivo* neural microenvironments including intercellular interactions, extracellular matrix (ECM), and hemodynamics, in a deterministic manner. However, both of these approaches have their own limitations. For instance, the brain organoid culture systems usually have very limited controllability over biochemical and biophysical factors in the surrounding 3D microenvironment, while the brain-on-a-chip systems are unable to reconstitute the biological complexity existing during the brain development.

By combining the advantages of both organ-on-a-chip and organoid technologies through a synergistic strategy, the organoid-on-a-chip platform has emerged as a new model to recapitulate the essential structural and physiological features of the *in vivo* tissue and the corresponding 3D tissue microenvironment (Skardal et al., 2016; Takebe et al., 2017). Following this concept, a recent paper from the Qin Group (Wang et al., 2018) demonstrated a brain organoid-on-a-chip system, which displayed remarkable capacity for a better study of prenatal neurological disorders.

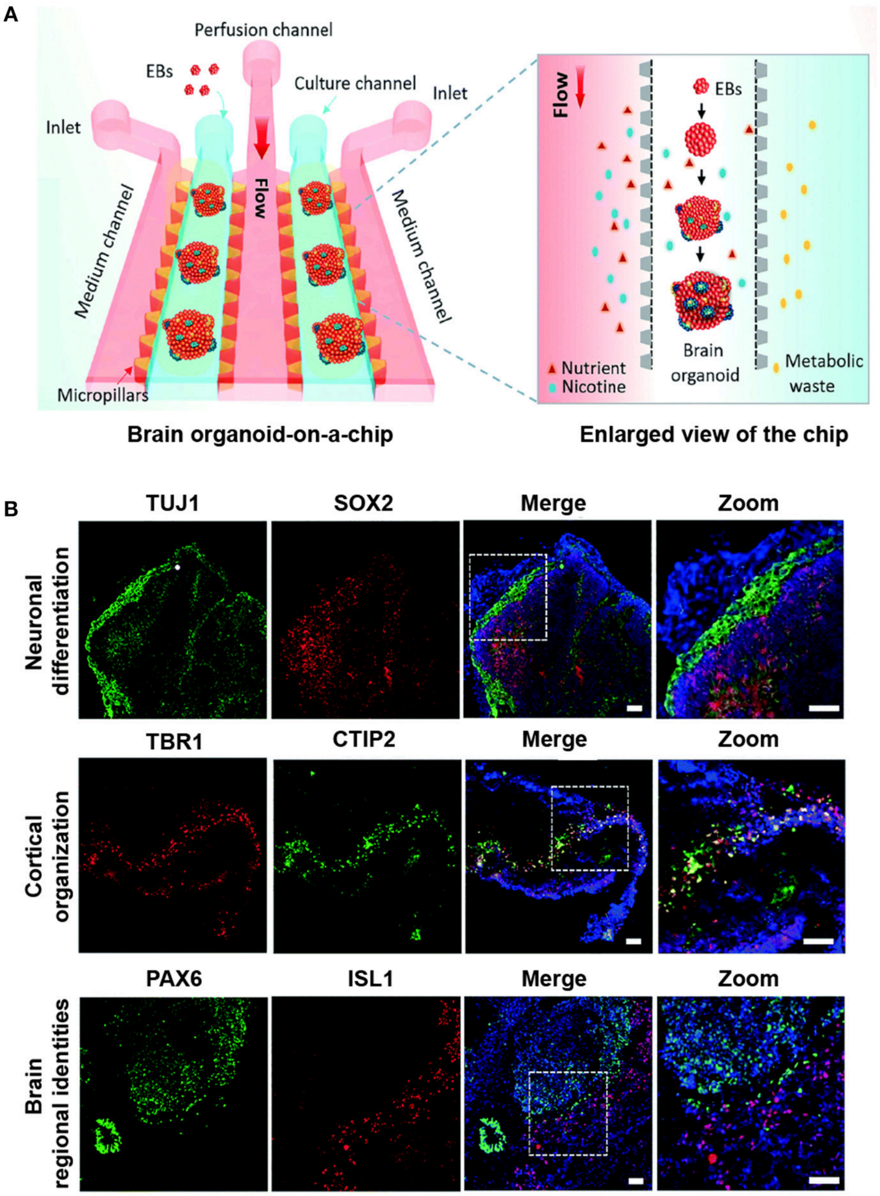

FIGURE 1 | Modeling prenatal nicotine exposure employing human brain organoid-on-a-chip. **(A)** The schematic diagram of the brain organoid-on-a-chip system for modeling prenatal nicotine exposure. The brain organoid-on-a-chip system was established by sequential steps including EBs culture, neural differentiation and formation of brain organoids by integrating 3D Matrigel and fluid flow. By using this system, the effects of nicotine exposure on brain development at early stages were explored at early stages. **(B)** Immunohistochemical staining was performed for the expression of neural progenitor marker SOX2(red), neuronal marker TUJ1 (green), cortical layer markers TBR1(red) and CTIP2 (green), specific forebrain marker PAX6 (green), and hindbrain marker ISL1(red) in brain organoids on day 33. Nuclei are stained with DAPI (blue). Scale bars = 50 μm. Adapted from Wang et al. (2018). (http://dx.doi.org/10.1039/C7LC01084B) with permission of The Royal Society of Chemistry.

BRAIN ORGANOID-ON-A-CHIP

Nicotine is recognized as a neurotoxin to trigger various neural dysfunctions and long-lasting deficit when exposing to the fetal brain (Pauly and Slotkin, 2008). Moreover, neurobehavioural disorders associated with maternal smoking during pregnancy are related to offspring intelligence (Breslau et al., 2005), anxiety behaviors (Moylan et al., 2015), cognitive ability (Batty et al., 2006), and neurodegenerative diseases of adulthood (Picciotto, 2008). However, the understanding of human neurological disorder under prenatal nicotine exposure (PNE) is an outstanding challenge due to the differences in histomorphology, physiology, and spatiotemporal patterns of neurodevelopment between humans and mice. The study by the Qin Group (Wang et al., 2018) established a brain organoid-on-a-chip system to model neurodevelopmental disorders for investigating PNE *in vitro*.

The brain organoid-on-a-chip consisted of two culture channels, one perfusion channel and two medium channels (**Figure 1A**). To generate the brain organoid, EBs mixed in Matrigel were pipetted into each culture channels for *in situ* 3D differentiation. The differentiation microenvironment on the chip recapitulated the *in vivo* fetal brain development by precisely controlling the biochemical and mechanical cues.

Consistent with the early stages of human brain organogenesis, this synergistically engineered model clearly revealed the feasibility of well-recognized neuronal differentiation, diverse brain regional identities, and cortical organization in the microfluidic chip (**Figure 1B**). In the areas mimicking neural differentiation, the organoids showed a high proportion of distinct neural identities, including markers for neural progenitor cells (SOX2) and neurons (TUJ1). Likewise, the different brain regional identities during brain organoid development were stained positive by the specific markers such as PAX6 and ISL1, suggesting the early developing forebrain and hindbrain. Furthermore, the layered cortical architecture could verify the initiation of the cortical plate layer formation, which was characterized by the deep-layer marker CTIP2 located adjacent and internal to the TBR1-positive pre-plate.

To investigate neurodevelopment under PNE, the authors focused on the effect of varying doses of nicotine on the development of brain organoids. During brain organogenesis on the chip, nicotine treatment led to premature neuronal differentiation and disruption of brain regionalization. Moreover, the authors utilized the brain organoids-on-a-chip model to examine nicotine-induced impaired cortical development from days 35 to 40, and the data might contribute to a better understanding of various postnatal cognitive dysfunctions under PNE. Intriguingly, these brain organoids exposed to nicotine showed the abnormal neurite outgrowth at a dose-dependent manner. The similar brain organoid-on-a-chip system has also been used to reveal the mechanism of the impaired neurogenesis under exposure to cadmium (Yin et al., 2018) and alcohol (Zhu et al., 2017).

Compared to the previous 3D neural culture models (Lancaster et al., 2013; Bouyer et al., 2016) which were based solely on the engineering approach or the developmental biology approach, the bioengineered brain organoids used in this study (Wang et al., 2018) more truthfully mimicked the brain development under PNE by integrating brain organoid in a microfluidic device. In addition, optically transparent property of the microfluidic device facilitated *in situ* real-time imaging of the neurodevelopmental process and the brain organoid responses to nicotine.

FUTURE PERSPECTIVE

A clear understanding of the early stages of human embryonic development is essential for a thorough investigation into the effects of PNE on human brain development. Despite that great efforts have been devoted to interrogating the effects of PNE on rodent models (Abreu-Villaça et al., 2004), the understanding of the human brain development under PNE remains elusive due to the significant difference between human and rodent physiology. Brain organoid-on-a-chip system utilized in the current work (Wang et al., 2018) could possibly serve as an alternative human-relevant neurodevelopmental model, eliminating ethical concerns regarding human clinical trials in smoking pregnant women.

For basic and translational neuroscience research, generation of standardized and homogenous brain organoid is critical but remain an unsolved issue in this system. Nevertheless, brain organoid-on-a-chip system opens a new avenue for modeling the human prenatal neurodevelopmental disorders. We expect that this commentary will stimulate motivation to expand the applications of organoid-on-a-chip systems and more complex multi-organoid-on-a-chip systems in screening of drug candidates, probing of disease mechanisms, as well as advancing novel therapies.

AUTHOR CONTRIBUTIONS

YZ and PC conceived the idea. HQ, YZ, and PC wrote the paper.

FUNDING

We gratefully acknowledge the financial support from National Natural Science Foundation of China (No. 31871018).

REFERENCES

Abreu-Villaça, Y., Seidler, F. J., and Slotkin, T. A. (2004). Does prenatal nicotine exposure sensitize the brain to nicotine-induced neurotoxicity in adolescence? *Neuropsychopharmacology* 29, 1440–1450. doi: 10.1038/sj.npp.1300443

Batty, G. D., Der, G., and Deary, I. J. (2006). Effect of maternal smoking during pregnancy on offspring's cognitive ability: empirical evidence for complete confounding in the us national longitudinal survey of youth. *Pediatrics* 118, 943–950. doi: 10.1542/peds.2006-0168

Bouyer, C., Chen, P., Güven, S., Demirtaş, T. T., Nieland, T. J., Padilla, F., et al. (2016). A bio-acoustic levitational (BAL) assembly method for engineering of multilayered, 3D brain-like constructs, using human embryonic stem cell derived neuro-progenitors. *Adv. Mater.* 28, 161–167. doi: 10.1002/adma.201503916

Breslau, N., Paneth, N., Lucia, V. C., and Paneth-Pollak, R. (2005). Maternal smoking during pregnancy and offspring IQ. *Int. J. Epidemiol.* 34, 1047–1053. doi: 10.1093/ije/dyi163

Haring, A. P., Sontheimer, H., and Johnson, B. N. (2017). Microphysiological human brain and neural systems-on-a-chip: potential alternatives to small animal models and emerging platforms for drug discovery and personalized medicine. *Stem Cell Rev.* 13, 381–406. doi: 10.1007/s12015-017-9738-0

Jo, J., Xiao, Y., Sun, A. X., Cukuroglu, E., Tran, H. D., Göke, J., et al. (2016). Midbrain-like organoids from human pluripotent stem cells contain functional dopaminergic and neuromelanin-producing neurons. *Cell Stem Cell* 19, 248–257. doi: 10.1016/j.stem.2016.07.005

Lancaster, M. A., Renner, M., Martin, C. A., Wenzel, D., Bicknell, L. S., Hurles, M. E., et al. (2013). Cerebral organoids model human brain development and microcephaly. *Nature* 501, 373–379. doi: 10.1038/nature12517

Lee, C. T., Bendriem, R. M., Wu, W. W., and Shen, R. F. (2017). 3D brain organoids derived from pluripotent stem cells: promising experimental models for brain development and neurodegenerative disorders. *J. Biomed. Sci.* 24:59. doi: 10.1186/s12929-017-0362-8

Luo, C., Lancaster, M. A., Castanon, R., Nery, J. R., Knoblich, J. A., and Ecker, J. R. (2016). Cerebral organoids recapitulate epigenomic signatures of the human fetal brain. *Cell Rep.* 17, 3369–3384. doi: 10.1016/j.celrep.2016.12.001

Moylan, S., Gustavson, K., Øverland, S., Karevold, E. B., Jacka, F. N., Pasco, J. A., et al. (2015). The impact of maternal smoking during pregnancy on depressive and anxiety behaviors in children: the norwegian mother and child cohort study. *BMC Med.* 13:24. doi: 10.1186/s12916-014-0257-4g

Pauly, J. R., and Slotkin, T. A. (2008). Maternal tobacco smoking, nicotine replacement and neurobehavioural development. *Acta Paediatr.* 97, 1331–1337. doi: 10.1111/j.1651-2227.2008.00852.x

Picciotto, M. R. (2008). Neuroprotection via nachrs: The role of nachrs in neurodegenerative disorders such as alzheimer's and parkinson's disease. *Front. Biosci.* 13:492–504. doi: 10.2741/2695

Skardal, A., Shupe, T., and Atala, A. (2016). Organoid-on-a-chip and body-on-a-chip systems for drug screening and disease modeling. *Drug Dis. Today* 21, 1399–1411. doi: 10.1016/j.drudis.2016.07.003

Takebe, T., Zhang, B., and Radisic, M. (2017). Synergistic engineering: organoids meet organs-on-a-chip. *Cell Stem Cell* 21, 297–300. doi: 10.1016/j.stem.2017.08.016

Wang, Y., Wang, L., Zhu, Y., and Qin, J. (2018). Human brain organoid-on-a-chip to model prenatal nicotine exposure. *Lab Chip* 18, 851–860. doi: 10.1039/C7LC01084B

Yin, F., Zhu, Y., Wang, Y., and Qin, J. (2018). Engineering brain organoids to probe impaired neurogenesis induced by cadmium. *ACS Biomater. Sci. Eng.* 4, 1908–1915. doi: 10.1021/acsbiomaterials.8b00160

Zhu, Y., Wang, L., Yu, H., Yin, F., Wang, Y., Liu, H., et al. (2017). *In situ* generation of human brain organoids on a micropillar array. *Lab Chip* 17, 2941–2950. doi: 10.1039/C7LC00682A

Zhuang, P., Sun, A. X., An, J., Chua, C. K., and Chew, S. Y. (2018). 3D neural tissue models: from spheroids to bioprinting. *Biomaterials* 154, 113–133. doi: 10.1016/j.biomaterials.2017.10.002

Conflict of Interest Statement: The authors declare that the research was conducted in the absence of any commercial or financial relationships that could be construed as a potential conflict of interest.

frontiers
in Bioengineering and Biotechnology

MINI REVIEW
published: 19 March 2019
doi: 10.3389/fbioe.2019.00039

Engineering Organoid Vascularization

Sergei Grebenyuk and Adrian Ranga*

Laboratory of Bioengineering and Morphogenesis, Department of Mechanical Engineering, KU Leuven, Leuven, Belgium

The development of increasingly biomimetic human tissue analogs has been a long-standing goal in two important biomedical applications: drug discovery and regenerative medicine. In seeking to understand the safety and effectiveness of newly developed pharmacological therapies and replacement tissues for severely injured non-regenerating tissues and organs, there remains a tremendous unmet need in generating tissues with both functional complexity and scale. Over the last decade, the advent of organoids has demonstrated that cells have the ability to reorganize into complex tissue-specific structures given minimal inductive factors. However, a major limitation in achieving truly *in vivo*-like functionality has been the lack of structured organization and reasonable tissue size. *In vivo*, developing tissues are interpenetrated by and interact with a complex network of vasculature which allows not only oxygen, nutrient and waste exchange, but also provide for inductive biochemical exchange and a structural template for growth. Conversely, *in vitro*, this aspect of organoid development has remained largely missing, suggesting that these may be the critical cues required for large-scale and more reproducible tissue organization. Here, we review recent technical progress in generating *in vitro* vasculature, and seek to provide a framework for understanding how such technologies, together with theoretical and developmentally inspired insights, can be harnessed to enhance next generation organoid development.

Keywords: organoid, vascularization, bioengineering, biofabrication, biomaterials

Edited by:
Massimo Alberti,
*Agency for Science, Technology and Research (A*STAR), Singapore*

Reviewed by:
Henrique de Amorim Almeida,
Polytechnic Institute of Leiria, Portugal
Nicolas Christoforou,
Pfizer, United States
Yilei Zhang,
Nanyang Technological University, Singapore

Correspondence:
Adrian Ranga
adrian.ranga@kuleuven.be

Specialty section:
This article was submitted to Tissue Engineering and Regenerative Medicine,
a section of the journal Frontiers in Bioengineering and Biotechnology

Received: *07 November 2018*
Accepted: *18 February 2019*
Published: *19 March 2019*

Citation:
Grebenyuk S and Ranga A (2019) Engineering Organoid Vascularization. Front. Bioeng. Biotechnol. 7:39. doi: 10.3389/fbioe.2019.00039

IN VITRO SELF-ORGANIZATION: TOWARD TISSUE-LEVEL COMPLEXITY

Organoids have been described as potentially transformational new model systems, which could create dramatic efficiencies in the drug discovery process and could become the building blocks for large-scale engineered tissues. Indeed, organoids bridge the gap between readily accessible and easily scalable traditional 2D *in vitro* cell culture and the complexity of animal models. Derived from pluripotent stem cells or self-renewing tissue progenitor stem cells, organoids have been generated for an increasing variety of organs, including intestine, kidney, brain, retina, liver and spinal cord. The self-organization process of organoids is uniquely manifested in three-dimensional culture systems, which resemble, to some extent, the *in vivo* organ or tissue from which they were derived, and which thereby allow for biologically relevant cell-cell and cell-matrix interactions (Clevers, 2016). In contrast to 2D cell culture, organoids provide a more realistic physiological response as they bear more physical and molecular similarity to their tissue of origin. Indeed, it has been observed that the signaling pathways governing organoid formation are similar to those utilized during *in vivo* organ development and homeostasis (Hynds and Giangreco, 2013; Camp et al., 2015). Another unique aspect of organoid models is the possibility to genetically manipulate human tissue, thereby opening unprecedented therapeutic perspectives for diseases characterized by genetic abnormalities. Indeed, the aberrant physiological effects of genetic disorders can be modeled by generating organoids from patient-derived induced pluripotent stem cells or by introducing known disease-specific mutations. Personalized medicine and cost-effective development of therapies for rare diseases is a recent example of the ongoing evolution of the field (Dekkers et al., 2013, 2016). Organoids are therefore extremely relevant to model human biology *in vitro*, and, as a consequence, are becoming cost-effective ways to develop therapies for human disease. The use of organoids is now increasingly being translated in areas of personalized medicine and drug discovery (Ranga et al., 2014a; Kelava and Lancaster, 2016), with initiatives already under way to turn organoid-based models into scalable and practical tools, including through institutional efforts to establish data banks of human cancer models in the form of organoids. For example, the molecular repertoire of gastric cancer organoids derived from 34 patients was recently characterized, and a subset of these were treated with a library of anti-cancer drugs, which enabled both the identification of effective new compounds for gastric cancer, as well as the demonstration of the possibility of repurposing a drug previously approved for breast cancer (Yan et al., 2018), all on the basis of specific effectiveness on molecular sub-categories of the disease. In addition to the three-dimensional cellular organization which is considered more relevant at the level of cellular identity and gene expression, the unique functional readouts emerging in organoid model systems are also beginning to be exploited for diagnostic applications. One striking recent example is in the establishment of forskolin-induced intestinal organoid swelling as a biomarker of cystic fibrosis transmembrane conductance regulator (CFTR) function (de Winter-de Groot et al., 2018). This novel functional *in vitro* assay was used to stratify patients and to tailor drug cocktails to individual patients based on the *in vitro* response of their organoid (Dekkers et al., 2016).

Although organoids have gained significant attention in the academic community and have now achieved increasing exposure in the pharmaceutical industry, there remain major challenges that prevent such models from achieving a broader deployment. One of the key limitations in using organoid-based approaches to generate functional tissue is that upon reaching a certain size, organoids cease to proliferate and develop a necrotic core. The process of growth arrest is thought to be linked to two phenomena: a switch from a proliferative, stem-like state to a non-proliferative, terminally differentiated one, as well as the loss of cell viability in the inner core of the organoid and subsequent necrosis upon reaching a limiting size beyond which diffusion alone can no longer allow for oxygen, nutrient and metabolite exchange. The rapid induction of terminal differentiation or aggregation of defined number of pre-differentiated cells are strategies used to limit the size of organoids, which are then more commonly referred to as spheroids. In order to maintain the complexity and scale of organoids it is therefore necessary to prevent the appearance of the necrotic inner core leading to the premature differentiation in the outer layers of the organoid. This phenomenon, in turn, can largely be ascribed to a lack of organoid vascularization and achieving such vascularization of organoids therefore remains a major challenge in the field. Strategies for enabling organoid vascularization can be analogous to the long-standing goal of generating vascularised tissue in the context of tissue engineering, however fundamental biological differences between engineered bulk tissues and complex organoid organization must be taken into account. Indeed, it long been realized that, with the exception of a few avascular tissues, any attempts at generating larger scale tissue constructs would be limited to a length scale of approximately 150 μm imposed by the natural diffusion limit of oxygen and nutrients in tissue. Recent reviews (Miller et al., 2012; Kim et al., 2016; Kinstlinger and Miller, 2016) have highlighted methods to overcome these limitations, which include approaches rooted in conventional microfluidics but which have also more recently evolved to include a variety of free-form 3D fabrication techniques. These include layer-by-layer deposition of materials, known as additive manufacturing, or selective removal of materials to form tubular voids connected to perfusion networks, as well as a range of hybrid approaches utilizing sacrificial materials. Here, we review the diversity of these approaches, focusing on techniques which have been proposed to recreate vasculature at various scales, and explore the potential and limitations of these platforms in interfacing with organoids.

BIOPRINTING

Layer-by-layer deposition of hydrogels incorporating cells of interest has generally been explored in studies aiming at generating large-scale tissue constructs, and has been most frequently performed by either filament deposition or droplet based approaches. Fused filament fabrication (FFF) or fused deposition modeling (FDM) involves the extrusion of a cell-containing gel in the form of a thin filament and its deposition in a pre-programmed, controlled manner to form a specific pattern (**Figures 1A**, **2A**). In the context of attempts to vascularise *in-vitro* tissue, FDM has been used to deposit endothelial cells (ECs) interleaved or combined with other cell types (Xu et al., 2012; Kinoshita et al., 2016; Roudsari et al., 2016; Zhang et al., 2016). Coaxial filaments have also been extruded, where the core of the filament incorporates endothelial cells while the external layer is composed of tissue-specific cells. As a proof-of-principle of this technique, functional adipose tissue pre-vascularized with an aligned endothelial vessel network was shown to anastomose with the host vasculature in a mouse model (Leong et al., 2013). A more versatile method consists in using composite materials which allow for sequential two-step crosslinking mechanisms. For example, a bioink consisting of gelatin methacryloyl (GelMA), sodium alginate, and 4-arm poly(-ethylene glycol)-tetra-acrylate (PEGTA) could first be ionically cross-linked by calcium ions to provide temporary structural stability during the bioprinting process, followed by covalent photo-crosslinking of GelMA and PEGTA to form stable

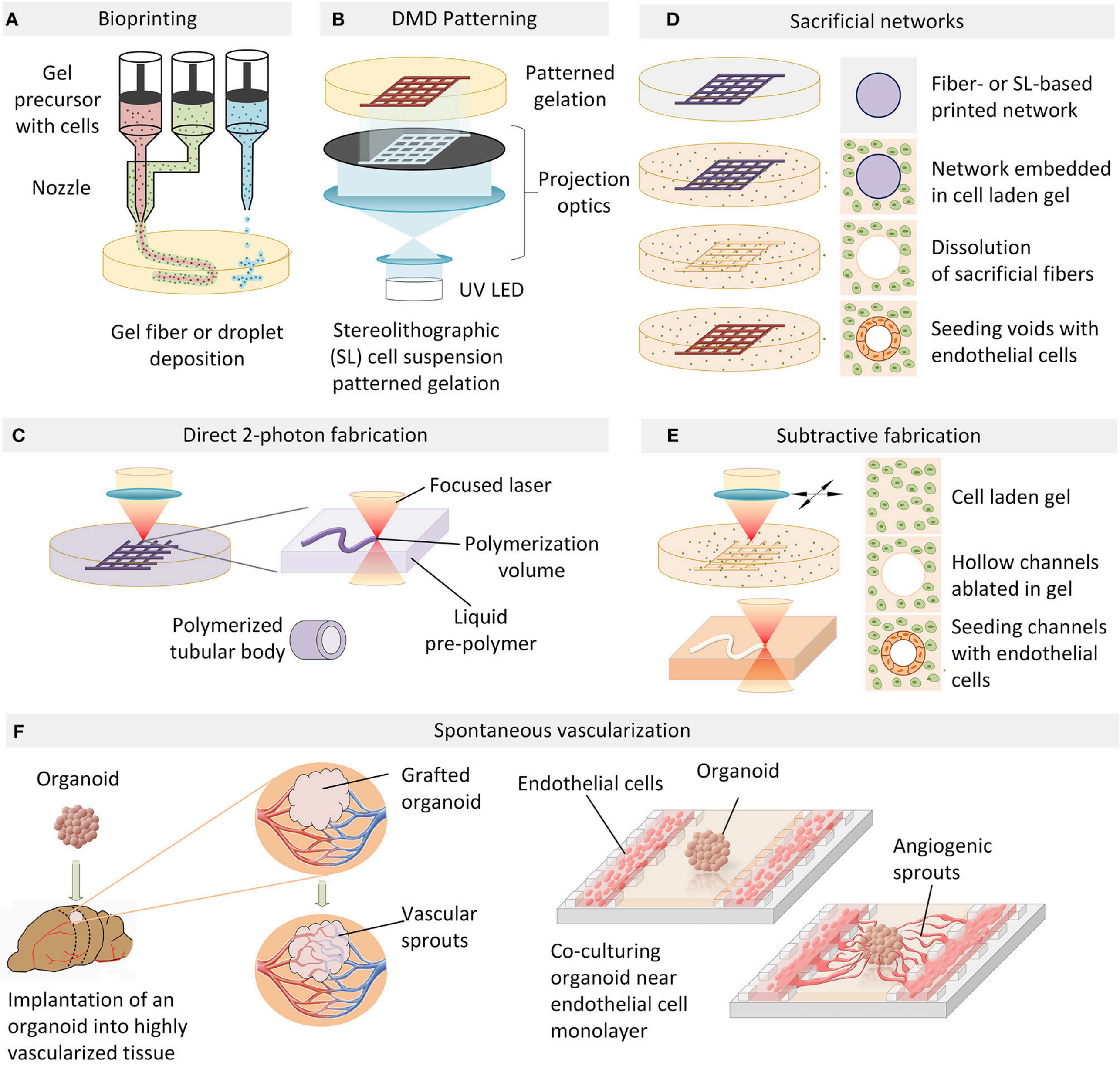

FIGURE 1 | An overview of vascularization techniques. **(A)** Vascular structures are bioprinted by extrusion or droplet deposition of cells suspended in biocompatible gel in a patterned manner. **(B)** Photo-induced gelation of cell-containing liquid precursors is performed in a layer-by-layer fashion with DMD patterning. **(C)** 2-photon photopolymerization is used to directly fabricate perfusable tubular networks of arbitrary geometry which can be embedded in a cell-containing hydrogel. **(D)** A cell-laden extracellular matrix is cast over a sacrificial filament lattice created by bioprinting or stereo-lithography. In an aqueous environment, the sacrificial filaments are dissolved and the resulting hollow perfusable network is perfused with endothelial cells which form a conformal layer around the inner diameter of the vessels. **(E)** Microchannels fabricated in a cell-laden hydrogel by laser ablation can be directly seeded with endothelial cells to generate functional blood vessels. **(F)** Organoid angiogenesis can be achieved by grafting in a highly vascularized animal tissue, with the host vasculature infiltrating the organoid. Alternatively, organoid vascularization is also achieved *in vitro* by endothelial cell co-culture in compartmentalized microfluidic chip. VEGF and hypoxia gradients established on-chip provide spatial guidance cues to direct angiogenic sprouting.

constructs (Jia et al., 2016). Combining the use of composite materials with a multilayered coaxial extrusion approach is a strategy which allows for direct one-step bioprinting of larger scale constructs (**Figure 1A**). Gel extrusion methods, despite their relative versatility, do not reproduce the intertwined and highly branched network topology occurring *in vivo* due to their continuous mode of filament deposition. Another limitation of the approach is that the minimal diameter of vessels achievable is determined by the diameter of the nozzle used for extrusion: the smaller the diameter, the higher the required extrusion pressure and therefore the more detrimental to cells.

Some of these limitations can be overcome by depositing cells and matrices in a contactless manner in the form of droplets, thereby allowing for a more precise spatial control of the resulting pattern. Methods to generate and eject droplets from nozzles include local thermally induced vaporization (Cui et al., 2012), electrostatic (Xie et al., 2018) or piezoelectric (Saunders et al., 2008; Kim et al., 2010) droplet formation, or micro-valve controlled pulsed ejection (Dababneh and Ozbolat, 2014; Gudapati et al., 2016). Alginate is a typical material used in these applications: it is ejected into a $CaCl_2$-containing solution which acts as both cross-linking agent and support material to provide buoyant force for the newly formed alginate gel. Well-defined vertical tubular structures with an inner diameter of $\sim 200\,\mu m$ (Nishiyama et al., 2008), as well as free-form fabrication of both horizontal and vertical vessel-like bifurcations has been demonstrated with this approach (Xu et al., 2014). Cell viability after bioprinting with most current methods, using alginate as well as a variety of other bioinks, is now well-established, with cell viabilities after printing on the order of 90% or more (Christensen et al., 2015). An additional advantage of these approaches is that a typical droplet has a volume in the picoliter range and contains only a few cells, thereby theoretically providing superior spatial resolution compared to filament-based deposition processes. In practice however, wetting and adhesion properties of the droplet-substrate interface significantly limit the effective achievable resolution (Nishiyama et al., 2008; Christensen et al., 2015). Conversely, discrete droplet based approaches are better suited to rapid and combinatorial switches in composition of several types of cells and matrices during the fabrication process, allowing for generation of cellular patterns of arbitrary complexity (Sala et al., 2011; Ranga et al., 2014b).

DIGITAL MICRO-MIRROR (DMD) PATTERNING

Stereolithography-based additive manufacturing based on light-mediated cross-linking of photosensitized polymers (photopolymerization) has gained widespread adoption in medical and biological applications due to its primary advantage of enabling truly arbitrary 3D geometries with unrivaled resolution. In order to create pre-vascularized tissues with more complex architecture at higher resolution, approaches based on photopolymerization of cell-laden gel liquid precursors by digital micro-mirror (DMD) devices have been explored. Polymerization is selectively induced in regions exposed to illumination in a 2D pattern generated by the projection of an image bitmap via a micro-fabricated mirror array (**Figure 1B**). Complex layer-by-layer 3D structures can be formed by repetitive illumination of serial projected patterns, interleaved by cycles of washing out of the unexposed, unpolymerized liquid gel precursor. In an example of this approach, a complex network of gelatin-methacrylate gel with human umbilical vein endothelial cells (HUVEC) was first subjected to patterned UV illumination and washed with medium, followed by over-casting and polymerization of another gel containing hepatocellular HepG2 and 10T1/2 support cells (Zhu et al., 2017). All cell types localized to the designated sections, and endothelial cells were shown to form lumen-like structures spontaneously *in vitro*. When implanted under the dorsal skin of a severe combined immunodeficiency (SCID) mouse, the tissue constructs demonstrated progressive formation of an endothelial network and anastomosis with the host circulation. In contrast, patterned constructs without HUVEC cells did not demonstrate any vascularization upon implantation, suggesting that *in vitro* endothelial pre-vascularization may be a necessary requirement for successful engraftment *in vivo*. Intriguingly, while the initially DMD-formed HUVEC-laden channels had diameters of 100–150 μm, the resulting vessels were as large as 1 mm in diameter, and no functional microvasculature was evidenced. Significantly smaller branched channels with capillary structures of 25–45 μm have been demonstrated with the same technology in a simplified biomimetic honeycomb scaffold using PEG-diacrylate as a photo-crosslinkable hydrogel (Huang et al., 2014), suggesting the potential of projection-based stereolithography as a high-resolution technique for the free-form fabrication of capillary networks.

DIRECT 2-PHOTON FABRICATION

Two-photon stereo-lithography, based on non-linear two-photon absorption, provides selective photopolymerization of sub-micron volumes and allows for the generation of complex three-dimensional microstructures in a single processing step (Ovsianikov et al., 2012; Raimondi et al., 2012). In one of the earliest studies showing the potential of this approach, the fabrication of micro-compartments for bacterial colonies by *in situ* two-photon cross-linking of gelatin demonstrated the possibility of creating arbitrary spatial arrangements at the micrometer scale to allow interactions between defined cell populations (Connell et al., 2013). Being a particularly dimensionally flexible and accurate technique, two-photon stereolithography has been increasingly used in cell biology and bioengineering applications (Ovsianikov et al., 2011; Connell et al., 2013; Sun et al., 2015), including in recent attempts to directly fabricate perfusable networks (**Figure 1C**). In pioneering work on direct 2-photon fabrication of tubular structures, branching vessels with internal diameters under 20 μm could be achieved (Meyer et al., 2012) (**Figure 2C**). While this study did not demonstrate the perfusability of the generated networks, it paved the way for similar approaches based on the flexible and versatile design-on-demand capabilities of this technique. In one strategy making use of these 3D design capabilities, micro-pores were created in the walls of a branched network of relatively large (circa 1 mm) polyacrylate vessels, thereby enabling the successful lining of the main vessels with human dermal microvascular endothelial cells (Huber et al., 2016), as well as the migration of cells and medium exchange across the vessel walls at

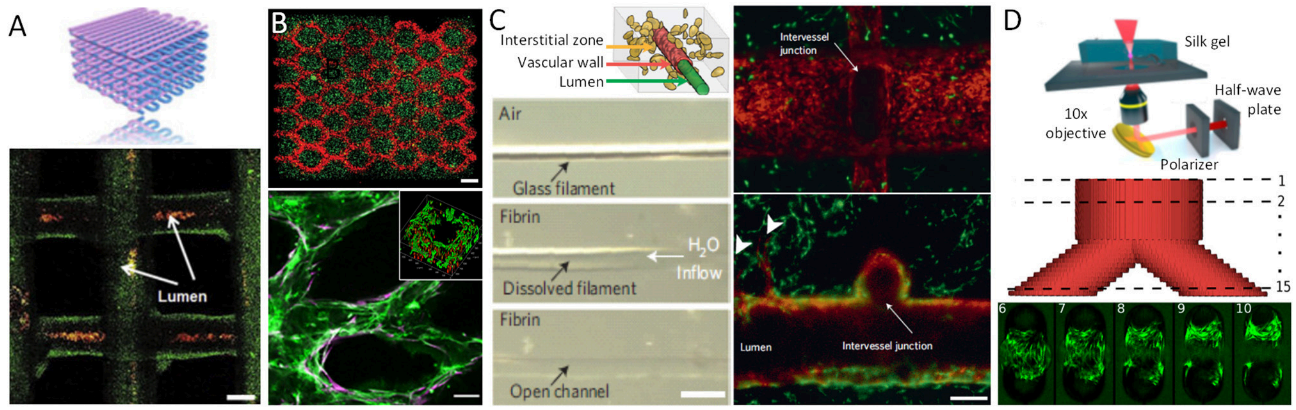

FIGURE 2 | Examples of vascularized constructs and tissues. **(A)** Schematic vascular network formed by bio-ink extrusion and confocal image of the bio-printed tubular constructs containing green fluorescent beads, perfused with red fluorescent micro-beads inside the lumens. **(B)** DMD-based bio-printing of cell-laden tissue constructs with HUVECs (red) encapsulated in the intended channels and HepG2 (green) cells encapsulated in the surrounding area (top). Scale bars, 250 µm. HUVECs (Green, CD31) and supportive 10T1/2 mesenchymal cells (Purple, α-SMA) aligned within the patterned channel regions after 1-week *in vitro* culture (bottom). Insert indicates cross-section of the channel, demonstrating a lumen formed by biodegradation of the gel. Scale bars: 100 µm. **(C)** Schematic of the vascular lumen, endothelial cells lining the vascular wall, and the interstitial zone containing matrix and encapsulated cells (top). A single sacrificial carbohydrate-glass fiber is encapsulated in a fibrin gel. After immersion in aqueous solution the fiber is dissolved (middle) yielding an open perfusable channel in the fibrin gel (bottom, scale bar, 500 µm). Representative vessel after 9 days in culture demonstrating endothelial monolayer (red) lining the vascular lumen, surrounded by 10T1/2 cells (green). Endothelial cells forming single and multicellular sprouts (arrowheads) from the patterned vasculature. Scale bars, 200 µm. **(D)** Multi-photon micromachining device generates hydrogel micro-channels allowing for fibroblast adhesion and growth within a Y-shaped feature 9 days after seeding. Scale bar, 100 µm.

precisely defined spatial locations. While 2-photon-based photopolymerization methods appear to achieve unprecedented resolution, their limited throughput (Ovsianikov et al., 2011; Connell et al., 2013; Sun et al., 2015), limited choice of biocompatible photoiniators (Wu et al., 2011; Li et al., 2016), and considerable infrastructural cost have precluded their wider adoption.

SACRIFICIAL NETWORKS

To create complex 3D networks, approaches based on removing, rather than adding material, have also been explored. Indeed a number of studies have been based on the idea that a sacrificial filament network can be embedded in a cell-containing matrix which, upon removal, leaves behind perfusable channels which can then be seeded with endothelial cells to form a vascular network with defined topology (**Figure 1D**). For example, a method for creating vascularized tissues which utilizes carbohydrate glass as a sacrificial material has been reported (Miller et al., 2012). An interconnected carbohydrate-glass lattice was printed (**Figure 2D**), encapsulated in ECM with live cells, and then dissolved within minutes in media without damage to nearby cells. In a similar approach, a sacrificial ink containing Pluronic and thrombin, and an cell-laden ink with gelatin and fibrinogen, was printed within a 3D perfusion chip (Kolesky et al., 2016). After printing, a matrix containing gelatin, fibrinogen, cells, thrombin, and transglutaminase was cast over the printed lattices. After thrombin-induced fibrinogen polymerization into fibrin and transglutaminase-induced cross-linking of the gelatin and fibrin, the fluidic chip was cooled and the sacrificial ink was solubilized and removed, leaving behind a vascular network coated with endothelial cells and connected to an external perfusion pump. Vascular networks obtained in this manner have been demonstrated to anastomose in a rat femoral artery graft model, with Doppler imaging confirming the vascular patency of the implants (Sooppan et al., 2016). A number of similar approaches involving sacrificial inks embedded in matrices have clearly established the possibility of creating thick vascularised tissue within perfusable fluidic chips with controlled composition and architecture, in some cases over several weeks (Golden and Tien, 2007; Wu et al., 2011; Bertassoni et al., 2014; Li et al., 2016). Droplet-based inkjet printing of gelatin has also been used to create sacrificial structures (Kolesky et al., 2016). However, the current limitations of most sacrificial network approaches have included the challenges of dimensional accuracy and precision, as well as of complete and homogenous removal of the sacrificial material, in particular for increasingly small and complex geometries. This may indeed account for the limits in achieved vessel dimensions of 150 µm (Miller et al., 2012), which are still an order of magnitude larger than the average capillary size.

In order to address some of these challenges, sacrificial perfusion networks have been generated using micro-stereolithographic processes with DMD-based instruments (**Figure 2B**). In one example, a custom DMD-based 3D printing device was used in a first step to polymerize a network of branching rods from a water-soluble photopolymer (Kang et al., 2016). The fabricated structure was coated with collagen and embedded in porous polycaprolactone (PCL) scaffold. The fabricated network was then dissolved in NaOH-containing solution and could be seeded with HUVECS, while the porous PCL scaffold was seeded with human lung fibroblasts to achieve a co-culture model system. This approach exemplifies what is expected to be an increasing trend toward deploying a mix of materials and fabrication technologies to achieve combinations of desired properties in complex co-culture platforms.

SUBTRACTIVE FABRICATION BY LASER ABLATION

Existing microfabrication techniques utilizing stereolithography are not limited to photo-patterning of biochemical cues, direct 3D printing or direct laser writing of photopolymerizable materials. Indeed, elegant optical approaches for generating free-form channels *in situ* within cellularized hydrogel materials have also been demonstrated based on laser photo-ablation (Applegate et al., 2015) (**Figures 1E**, **2C**). Induced by multiphoton absorption of light, photo-ablation allows for the generation of voids as small as 5 μm in diameter. Silk fibroin has been reported as an especially suitable material for this technique due to its large multi-photon cross-section which allows initiation of multiphoton absorption at low laser power thresholds, thereby reducing self-focusing of the laser beam and other non-linear optical effects (Applegate et al., 2015). As such, voids could be formed in within these gels nearly 1 cm below the gel surface, a significant enhancement over other materials tested (Oujja et al., 2009; Sarig-Nadir et al., 2009). These concepts were similarly applied in the context of preformed cellular aggregates of mesenchymal stem cells embedded in synthetic PEG-based matrices, into which perfusion channels were formed by ablating pulses of a picosecond infrared laser (Brandenberg and Lutolf, 2016). This technique has also been applied to other materials such as collagen type I, where perfused HUVECs within channels adhered to the walls of the newly created channels and formed a confluent EC layer. The idea of generating 3D structures within the bulk of a transparent cell-supporting hydrogel can be extended to selected other materials, with the clarity of the gels permitting the creation of patterns with features down to the micron scale and as deep as 1 cm within soft silk protein hydrogels (Applegate et al., 2015). In order to take full advantage of this method, the hydrogel material must have an appropriate multi-photon cross-section corresponding to the laser wavelength used for fabrication, which substantially limits the choice of available hydrogels. These material restrictions can be relaxed by introducing highly light-absorbing molecules into the fabrication volume. Indeed, when laser ablation of channels in a collagen scaffold was performed in the presence of fluorescein as a photo-absorption agent the laser exposure times were dramatically reduced and scanning velocities as high as 350–400 mm/s could be achieved, in a fluorescein concentration-dependent manner (Skylar-Scott et al., 2016). The obtained channels were perfused in a microfluidic device and their inner surface could be colonized by ECs. Remarkably, the diameter of the channels was approximately 50 μm, and there are seemingly no technical limitations to further reducing this dimension. Apart from thermal ablation, laser-induced photolysis has been suggested to generate tubular voids in hydrogels in presence of cells (Kloxin et al., 2010; Tibbitt et al., 2010), with one example using focused laser irradiation to induce localized dissociation of a PEG-based hydrogel (Tibbitt et al., 2010). While current studies have emphasized the potential of these materials for localized modulation of adhesion properties, these materials would likely be ideal substrates for on-demand free form generation of perfusion networks.

PRO-ANGIOGENIC MATRIX ENGINEERING FOR ORGANOID AND VASCULAR CELLS

For endothelial cells to be induced to migrate and form *de novo* vessels in conjunction with organoid development there is a need for an additional element in a constructed angiogenesis-promoting microenvironment: a three-dimensional extracellular matrix which can be co-permissive and supportive for both angiogenesis as well as organoid growth. This implies that angiogenesis must occur in a matrix used to support the growth of specific organoids. In almost all current protocols, the extracellular matrix which supports three-dimensional organoid development is Matrigel, a one-size-fits-all hydrogel whose components are highly uncontrolled and whose properties cannot be readily manipulated (Kleinman and Martin, 2005). The advent of highly modular and controllable artificial extracellular matrices has enabled the possibility to precisely tailor materials to specific biological applications (Langer and Tirrell, 2004; Griffith and Swartz, 2006; Lutolf et al., 2009). Such matrices are now being translated into the organoid field (Meinhardt et al., 2014), not only to enhance the reproducibility of organoid generation, but also allow for a better understanding of role of the biophysical cues in 3D morphogenesis (Gjorevski et al., 2016; Cruz-Acuña et al., 2017). For example, neural tube organoids generated in optimized synthetic matrices have been shown to have more homogeneous phenotypes than those in Matrigel, as well as enhanced morphogenetic features such as higher frequency of apico-basal and dorso-ventral patterning (Ranga et al., 2016). In addition to the tremendous variety of material compositions which can be tested, the combinations of soluble factors which provide critical inductive cues which drive differentiation and morphogenesis can also be varied. 3D artificial ECM microarrays, which allow for a wide variety of combinatorial conditions to be assayed simultaneously, can be used to quickly and systematically investigate the role of these matrix and soluble factor combinations (Ranga et al., 2014b). Combined with powerful image analysis, data visualization and statistical analysis tools, such approaches can help in rapidly generating a regulatory landscape of fate and morphogenesis (Ranga et al., 2016). While a number of matrices have been developed specifically to induce angiogenesis, including by the incorporation of increasingly sophisticated VEGF patterns and guidance cues (Ehrbar et al., 2008; Sacchi et al., 2014), it remains to be ascertained whether such matrices are also compatible with tissue-specific organoid growth, and an ongoing challenge will remain to develop matrices amenable to increasingly specialized co-cultures. Alternatively, it is possible that multi-matrix composites will be required to compartmentalize co-cultures.

INDUCED ANGIOGENESIS IN ENGINEERED TISSUES

The approaches described so far possess clear advantages such as full control over vascular network topology and immediate functionality. However, being predetermined by the fabrication process, such vascular structures cannot respond to dynamic changes in the environment, such as changes in oxygen consumption, tissue patterning, and growth. Thus, the presence of mechanisms of active vascular remodeling is a critical element of any tissue development model system. In addition to a direct fabrication of capillary networks or chemically guided cell patterning, novel approaches have recently been proposed to spontaneously vascularize engineered tissues (Gage and Fisher, 1991; Watson et al., 2014; Clevers, 2016; Pham et al., 2018) (**Figure 1F**). For example, the successful spontaneous vascularization of human lung fibroblast spheroids grown in microfluidic chip (Nashimoto et al., 2017) was recently demonstrated in a chip with three parallel fluidic channels separated by micro-posts allowing cell migration and proliferation between the channels (**Figure 1F**). Based on an earlier study standardizing spheroid cultures (Kunz-Schughart et al., 2006), human lung fibroblasts (hLF) and HUVECs were co-cultured to generate composite spheroids of approximately 600 μm in diameter. With the middle channel of the microfluidic chip seeded with spheroids and the adjacent side channels with HUVECs, the endothelial cells formed a network around and within which the spheroid and a fully perfusable vasculature was established. Interestingly, the hLFs and the HUVECs in the spheroid co-culture were shown to play different roles, with hLFs acting as a signaling source to stimulate network outgrowth toward the spheroid, and HUVECs promoting anastomosis of the sprouts from the side channels to the central spheroid-containing channel. Moreover, the most active form of angiogenesis was observed without exogenous VEGF present in medium, suggesting that interactions between hLFs and HUVECs were sufficient to drive the co-culture. This recent study is expected to be one of many which suggest that *in vitro*, as *in vivo*, interactions between vasculature and host/target tissue are bidirectional, with inductive roles for both.

ORGANOID VASCULARIZATION VIA *IN VIVO* ORGANOID TRANSPLANTATION

Despite recent advances with microfluidic or organ-on-chip approaches, fully functional organoid vascularization has thus far only been demonstrated by transplanting organoids into host animals, where native vasculature was seen to integrate into the ectopic implant. In most cases, initial *in vitro* co-culture with endothelial cells was required for vascularization and engraftment. In a first demonstration, human pluripotent stem cell (hiPSC)-derived liver buds were transplanted into immunodeficient mice (Takebe et al., 2013), with resulting formation of vascularized functional liver tissue capable of producing albumin starting from day 10 and up to day 45 post-transplantation. Remarkably, transplanted hIPSC-derived hepatocytes produced much less albumin, underscoring the importance of three-dimensional and vascularized tissue formation for functional use. Indeed, engraftment of immature organoids in vasculature-rich tissues such as kidney, lung or brain has been shown to result in invasion of the organoid by the host vascular network. Recently, a method for transplanting human brain organoids into the adult mouse brain has been developed (Mansour et al., 2018). Such organoid grafts progressively differentiated and matured, resulting in functional neuronal networks interconnected synaptically with host neuronal circuits, as demonstrated by extracellular recordings and optogenetic stimulation. Importantly, *in vivo* imaging revealed extensive infiltration of the host vasculature within a few days after transplantation.

STRATEGIES FOR *DE NOVO* DESIGN OF *IN VITRO* VASCULATURE

The *in vivo* vascularization of organoids clearly demonstrates that, given the right conditions and timing, organoids can be perfused throughout. It is therefore important to ask: what is missing in approaches focused on direct vascularization? One major limitation in most currently generated *in vitro* vascular constructs is that reported dimensions, ranging from 150–200 μm (Miller et al., 2012) to 1–2 mm (Huber et al., 2016), do not correspond to physiological length scales required, as the typical diameter of a capillary is about 10 μm. Indeed, the regulation of blood flow to achieve an oxygen supply matched to oxygen demand is controlled at the level of the local microcirculation (Pittman, 2013) and the balance in local oxygen pressure gradients results from interactions of local diffusion and consumption demands. As such, it is critical to generate the right dimensional structures at that scale, and it is here that additive micromanufacturing such as stereolithography based on two-photon polymerization may be particularly suitable to enable the level of 3D resolution required. Despite the fact that direct fabrication by photopolymerization is a maturing technology, some practical fabrication aspects remain to be resolved. For example, further development of biocompatible hydrogel materials composition will be required to limit swelling and deformation of printed structures in aqueous media after fabrication (Huber et al., 2016). Similar issues arise with photo-induced removal of material, where a gel block is subjected to a focused laser light. Since thicker samples must be processed to generate larger vascular networks, objectives with long working distance are required, which normally have low-numerical aperture and thus lead to low spatial resolutions. For both photo-ablation and photo-degradation techniques another limitation which will have to be overcome in order to increase throughput is the high power and/or long illumination times needed, rendering the technique less practical. It is possible that printing small-diameter capillary networks can be avoided altogether, and that organoid vascularization can be achieved instead by guiding angiogenesis from larger vessels to anastomose toward growing organoids. This idea has thus far been limited by the lack of easy and reliable connection to an *in vitro* perfusion system, however recent vascularization-on-chip work (Nashimoto et al., 2017) demonstrates that such systems may be optimized to achieve flow through an organoid. Notably, the successful proliferation of such vascular networks and connection to an organoid tissue still requires co-culture of target organoid cells with VEGF-secreting cells in order to provide the necessary chemo-attractive angiogenic cues, and it remains to be seen whether such neo-tissues can produce these signals independently.

REVISITING DESIGN PRINCIPLES FOR *DE NOVO* DESIGN OF *IN VITRO* VASCULATURE

Beyond the technical aspects of generating vasculature, one important question relates to the design of the network itself. With printing technologies at various scales now allowing for unprecedented versatility in creating three-dimensional structures, it is necessary to consider the network geometries relevant for organoid development. Indeed, the physical interaction between blood flow, vascular wall structure and branching architecture have all been shown to play an important role in optimizing and regulating the function of vascular systems, and the design principles that govern the organization of such systems have been extensively investigated both at the theoretical and experimental levels.

One of the first and most enduring theoretical frameworks has been Murray's law, which state that the laws governing branching in vascular networks are based on the optimization of the energy required to maintain blood volume and velocity. An important consequence of Murray's law is that the tangential shear stress at the wall remains constant throughout the vascular network, for symmetric bifurcating systems (Barber and Emerson, 2010). Murray's law has been experimentally validated for large arteries and arterioles, however, it does not provide a good description of the microcirculation. Additional features have been added to this framework over the years, notably adding the energy costs associated with maintaining smooth muscle contraction against the distending effects of wall shear stress, improving on the rheological representation of blood as well as including the geometric and material complexities of the vessel walls (Alarcón et al., 2005). These improved theoretical models have been applied to simulations of various types of microfluidic networks. For example, a generalized version of Murray's law was derived for the design of microfluidic manifolds and hierarchical fluid distribution systems (Emerson et al., 2006). More recently, these theoretical insights have been applied, in simulations and in practice, on applications-oriented microfluidic networks. For instance, simulation-driven procedures for optimal design of cell-seeded scaffolds have been proposed based on combining oxygen transport with design principles governing vascular trees (Kang et al., 2013), with experimentally validated results pointing to the role of branching points in ensuring optimal diffusion. Simulation tools have also been used to model increasingly complex 3D branched networks encompassing multiple length scales, with hemodynamic effects of design parameters calculated throughout the tree structure. Such simulations allow for systematic investigations of variations in geometrical parameters such as vessel diameter, vessel length, bifurcation angle and fractal dimensions of the tree, and their role in hemodynamics (Yang and Wang, 2013). Alternatively, data-driven models have focused on relating measured diffusion gradients of oxygen in *in vitro* cultured tissues to spatial distributions of cell number and viability (Radisic et al., 2005). These empirical models could then be used to conclude that oxygen concentration and cell viability decreased linearly with distance from the perfused surface, while live cell density decreased exponentially, with physiological levels only present within a thickness of approximately 130 μm. Interestingly, quantitative and analytical solutions to diffusion equations for different tissue geometries with a particular focus on organoids (McMurtrey, 2016) have shown that oxygen diffusion, rather than nutrient transport is generally the primary limiting factor at steady state in metabolically active constructs, and that cell density could be tuned such that enhanced growth could be achieved if metabolically active and proliferative cells were positioned closer to the source of oxygen.

GENERATING BIOMIMETIC VASCULATURE BASED ON DEVELOPMENTAL PRINCIPLES

While studies investigating the design principles of vascular beds have searched for overarching descriptions and mechanisms for explaining observed mature *in vivo* networks, these may need to be revised in the context of a dynamically developing system. In particular, iPSC-derived organoids recapitulate, at least in part, key steps of embryonic cell fate specification, patterning, morphogenesis, and growth. In this context, it becomes clear that the dynamic interplay between a growing, diversifying tissue and its interpenetrating vascular network could be a critical missing element in ensuring that development occurs in a temporally prescribed manner. Therefore, an important issue which has been overlooked in the emergent field of organoid vascularization is the question of appropriate design of the vascular network not only in space but also in time. While printing at various scales is now possible it remains to be determined what is the optimal vascular structure to print at a specific developmental time point, leading to the development of an optimized overall printing strategy. One approach could be based on principles of biomimetic *in vitro* generation of developing, anatomical, site-specific vasculature. Indeed, the formation of blood vessels during embryonic development is a highly choreographed process where bidirectional interactions between the developing tissue and its developing vasculature allow for stereotypical patterning of the vascular tree (Walls et al., 2008). The *de novo* formation of blood vessels is initiated by the assembly of precursor cells, a process known as vasculogenesis, followed by the sprouting of new vessels from pre-existing ones, termed angiogenesis. In humans, fetal vascularization is initiated early in the third week of gestation (approximately day 16), concurrently with axis formation and organogenesis; for comparison, these events occur at day 7 in the mouse. Vasculogenesis begins by the formation of blood islands from hemangioblasts of mesodermal origin, which then differentiate into two cell populations: angioblasts (vascular precursors), which form endothelial cells, and hemocytoblasts, which form blood cell precursors. Angioblasts migrate and coalesce into cords to form primitive lumens, thereby establishing the first fluidic networks. Growth factors such as vascular endothelial growth factor (VEGF) and placental growth factor (PlGF) secreted by adjacent tissues are critical in stimulating the growth and development of such primordial vascular networks. Vasculogenesis is the dominant process of vessel formation in early embryogenesis, from which the major large arteries such as the dorsal aorta are formed. As primitive plexi are established, smaller vessels are generated by angiogenesis. Sprouting from pre-existing vessels leads to mature vascularization of multiple organs such as the brain. Importantly, the vascular tree undergoes constant remodeling during embryonic development, driven both by genetically encoded information as well as by hemodynamic forces (Walls et al., 2008). While the earliest endothelial cells are molecularly distinguished by markers such as endoglin, von-Willebranf factor, CD31, VE-cadherin, Tie2, EphB4 and EphrinB2 (Augustin and Koh, 2017) and are not specified to a particular organ, vascular function becomes increasingly specialized in parallel with increasing organ specification. This molecular and cellular specialization is critical to achieve the required organ-specific function. For example, the endothelial cells in continuous capillaries are bound by tight junctions which ensure that most large molecules, drugs and pathogens do not cross the blood-brain barrier, whereas those in the sinusoidal capillaries of organs such as the liver, where freer exchange of large solutes is required, present completely different morphologies and large gaps. The early steps of pan-endothelial differentiation are generally well-understood, however the role of specific inductive cues for later specification and differentiation has only more recently been explored. Recent work analyzing and comparing transcriptomes, accessible chromatin, and DNA methylome signatures from mouse brain, liver, lung, and kidney endothelial cells (Sabbagh et al., 2018) is beginning to reveal the gene regulatory networks that control such specification, which is expected to lead to improved protocols for *in vitro* derivation of more organ-specific cells. The development of vasculature clearly does not involve endothelial cells alone: other cell types such as pericytes, smooth muscle cells and immune cells play varied roles in providing structural and functional support as well as signaling guidance, and will also be required to build more complete *in vitro* models. While current strategies of co-culture of endothelial cells with organoids are an important starting point, thus far, there has been no evidence of spontaneous vascularization in organoid systems (i.e., without exogenous addition of endothelial/support cells), most likely due to the fact that the vast majority of organoid models involve directed differentiation to specific organ systems, which presumably precludes the formation of alternative fates such as endothelium. Indeed adding the staged endothelial and support cells at the developmentally correct time point and in the appropriate geometrical relationship to the developing organoid will likely prove to be both necessary and highly challenging. The advent of increasingly detailed *in vivo* single cell transcriptomic and image-based spatial information (e.g., from lattice light-sheet microscopy) from early development to adult tissues provides a detailed roadmap for recreating these tissues *in vitro*, and will be particularly valuable for PSC-derived systems.

CONCLUSION

Today the advent of increasingly accurate and scalable 3D microfabrication technologies allows for unprecedented possibilities in generating free-form vascular structures. The deployment of these technologies in the context of organoid culture could help overcome the lack of vascularization in these model systems, which remains one of the major challenges in the field. Optimal approaches will involve finding a balance between the explicit structural patterning imposed by the printing process and the self-organizing nature of the organoid and the vascular network surrounding and interpenetrating it. We have shown in this review that constructing gel-based architectures can take many forms, with each being most appropriate depending on the desired dimensional and temporal scale. Depending on the methods used, the interaction between vasculature and organoid can be engineered to occur simultaneously or sequentially, and the spatial relationship can be designed to incorporate multi-material compartments and dimensions. Bioprinting in the form of filament or droplet deposition offers rapid layer-by-layer construction possibilities at the mesoscale (circa 1 mm) with a versatile material toolbox. Conversely, DMD and 2-photon fabrication offer unprecedented precision at the micro-scale, with limitations mainly in throughput and requirement for the use of photopolymerizable materials. With all such additive manufacturing options, a significant limitation is that the constructed structures are not readily modifiable after their initial creation, with, for example, the initial printing of a static vasculature followed by organoid seeding. A unique advantage of subtractive methods is that vessels or other structural guiding elements can be created at arbitrary points in time, conforming to organoid growth and development. While sacrificial networks must first be built up using additive manufacturing techniques, laser ablation allows for more flexibility in determining arbitrary structural configurations after organoid seeding. Laser ablation is limited however to the horizontal plane as the possibility to carve out space within a gel presupposes a clear optical path and precludes the creation of structures directly above or below the organoids. Additionally, these methods can only be used with polymers which have specific absorbing properties with the used wavelength, and local heat buildup may be unsuitable in regions close to organoids. Ultimately, leveraging the power of single or combinations of these 3D biofabrication technologies to create truly biomimetic, vascularized organoids will require integrating molecular and structural lessons from the embryonic development of both the target tissue as well as that of its specific microvasculature. Indeed, technological tools such as the ones we have described will allow for highly spatially and temporally defined interactions between organoids and their supporting vasculature, which will allow the exploration of minimal conditions for self-organization and larger-scale growth and maturation. Microvascular patterning and organ-on-a-chip microfluidic technology will increasingly allow for the incorporation of the right cells at the right place, such that perfusable organoids can serve as ever-more reliable model systems for basic and translational applications.

AUTHOR CONTRIBUTIONS

All authors have contributed to writing, editing and revising of the manuscript, and have approved it for publication.

FUNDING

This work was supported by FWO grant G087018N, Interreg BIOMAT-ON-CHIP, Vlaams-Brabant and Flemish Government co-financing, KU Leuven grants C14/17/111 and C32/17/027 and King Beadouin Foundation grant J1810950-207421.

REFERENCES

Alarcón, T., Byrne, H. M., and Maini, P. K. (2005). A design principle for vascular beds: the effects of complex blood rheology. *Microvasc. Res.* 69, 156–172. doi: 10.1016/j.mvr.2005.02.002

Applegate, M. B., Coburn, J., Partlow, B. P., Moreau, J. E., Mondia, J. P., Marelli, B., et al. (2015). Laser-based three-dimensional multiscale micropatterning of biocompatible hydrogels for customized tissue engineering scaffolds. *Proc. Natl. Acad. Sci. U.S.A.* 112, 12052–12057. doi: 10.1073/pnas.1509405112

Augustin, H. G., and Koh, G. Y. (2017). Organotypic vasculature: from descriptive heterogeneity to functional pathophysiology. *Science* 357:eaal2379. doi: 10.1126/science.aal2379

Barber, R. W., and Emerson, D. R. (2010). Biomimetic design of artificial micro-vasculatures for tissue engineering. *Altern. Lab. Anim.* 38(Suppl .1), 67–79.

Bertassoni, L. E., Cecconi, M., Manoharan, V., Nikkhah, M., Hjortnaes, J., Cristino, A. L., et al. (2014). Hydrogel bioprinted microchannel networks for vascularization of tissue engineering constructs. *Lab. Chip* 14, 2202–2211. doi: 10.1039/C4LC00030G

Brandenberg, N., and Lutolf, M. P. (2016). *In situ* patterning of microfluidic networks in 3D cell-laden hydrogels. *Adv. Mater.* 28, 7450–7456. doi: 10.1002/adma.201601099

Camp, J. G., Badsha, F., Florio, M., Kanton, S., Gerber, T., Wilsch-Bräuninger, M., et al. (2015). Human cerebral organoids recapitulate gene expression programs of fetal neocortex development. *Proc. Natl. Acad. Sci. U.S.A.* 112, 15672–15677. doi: 10.1073/pnas.1520760112

Christensen, K., Xu, C., Chai, W., Zhang, Z., Fu, J., and Huang, Y. (2015). Freeform inkjet printing of cellular structures with bifurcations. *Biotechnol. Bioeng.* 112, 1047–1055. doi: 10.1002/bit.25501

Clevers, H. (2016). Modeling development and disease with organoids. *Cell* 165, 1586–1597. doi: 10.1016/j.cell.2016.05.082

Connell, J. L., Ritschdorff, E. T., Whiteley, M., and Shear, J. B. (2013). 3D printing of microscopic bacterial communities. *Proc. Natl. Acad. Sci. U.S.A.* 110, 18380–18385. doi: 10.1073/pnas.1309729110

Cruz-Acuña, R., Quirós, M., Farkas, A. E., Dedhia, P. H., Huang, S., Siuda, D., et al. (2017). Synthetic hydrogels for human intestinal organoid generation and colonic wound repair. *Nat. Cell Biol.* 19, 1326–1335. doi: 10.1038/ncb3632

Cui, X., Boland, T., D'Lima, D. D., and Lotz, M. K. (2012). Thermal inkjet printing in tissue engineering and regenerative medicine. *Recent Pat. Drug Deliv. Formul.* 6, 149–155. doi: 10.2174/187221112800672949

Dababneh, A. B., and Ozbolat, I. T. (2014). Bioprinting technology: a current state-of-the-art review. *J. Manufact. Sci. Eng.* 136:061016. doi: 10.1115/1.4028512

de Winter-de Groot, K. M., Janssens, H. M., van Uum, R. T., Dekkers, J. F., Berkers, G., Vonk, A., et al. (2018). Stratifying infants with cystic fibrosis for disease severity using intestinal organoid swelling as a biomarker of CFTR function. *Eur. Respir. J.* 52, 02529–02017. doi: 10.1183/13993003.02529-2017

Dekkers, J. F., Berkers, G., Kruisselbrink, E., Vonk, A., de Jonge, H. R., Janssens, H. M., et al. (2016). Characterizing responses to CFTR-modulating drugs using rectal organoids derived from subjects with cystic fibrosis. *Sci. Transl. Med.* 8:344ra84. doi: 10.1126/scitranslmed.aad8278

Dekkers, J. F., Wiegerinck, C. L., de Jonge, H. R., Bronsveld, I., Janssens, H. M., de Winter-de Groot, K. M., et al. (2013). A functional CFTR assay using primary cystic fibrosis intestinal organoids. *Nat. Med.* 19, 939–945. doi: 10.1038/nm.3201

Ehrbar, M., Zeisberger, S. M., Raeber, G. P., Hubbell, J. A., Schnell, C., and Zisch, A. H. (2008). The role of actively released fibrin-conjugated VEGF for VEGF receptor 2 gene activation and the enhancement of angiogenesis. *Biomaterials* 29, 1720–1729. doi: 10.1016/j.biomaterials.2007.12.002

Emerson, D. R., Cieślicki, K., Gu, X., and Barber, R. W. (2006). Biomimetic design of microfluidic manifolds based on a generalised Murray's law. *Lab. Chip* 6, 447–454. doi: 10.1039/b516975e

Gage, F. H., and Fisher, L. J. (1991). Intracerebral grafting: a tool for the neurobiologist. *Neuron* 6, 1–12. doi: 10.1016/0896-6273(91)90116-H

Gjorevski, N., Sachs, N., Manfrin, A., Giger, S., Bragina, M. E., Ordóñez-Morán, P., et al. (2016). Designer matrices for intestinal stem cell and organoid culture. *Nature* 539, 560–564. doi: 10.1038/nature20168

Golden, A. P., and Tien, J. (2007). Fabrication of microfluidic hydrogels using molded gelatin as a sacrificial element. *Lab. Chip* 7, 720–725. doi: 10.1039/b618409j

Griffith, L. G., and Swartz, M. A. (2006). Capturing complex 3D tissue physiology *in vitro*. *Nat. Rev. Mol. Cell Biol.* 7, 211–224. doi: 10.1038/nrm1858

Gudapati, H., Dey, M., and Ozbolat, I. (2016).A comprehensive review on droplet-based bioprinting: Past, present and future. *Biomaterials* 102, 20–42. doi: 10.1016/j.biomaterials.2016.06.012

Huang, T. Q., Qu, X., Liu, J., and Chen, S. (2014). 3D printing of biomimetic microstructures for cancer cell migration. *Biomed. Microdevices* 16, 127–132. doi: 10.1007/s10544-013-9812-6

Huber, B., Engelhardt, S., Meyer, W., Krüger, H., Wenz, A., Schönhaar, V., et al. (2016). Blood-vessel mimicking structures by stereolithographic fabrication of small porous tubes using cytocompatible polyacrylate elastomers, biofunctionalization and endothelialization. *J. Funct. Biomater.* 7:11. doi: 10.3390/jfb7020011

Hynds, R. E., and Giangreco, A. (2013). Concise review: the relevance of human stem cell-derived organoid models for epithelial translational medicine. *Stem Cells* 31, 417–422. doi: 10.1002/stem.1290

Jia, W., Gungor-Ozkerim, P. S., Zhang, Y. S., Yue, K., Zhu, K., Liu, W., et al. (2016). Direct 3D bioprinting of perfusable vascular constructs using a blend bioink. *Biomaterials* 106, 58–68. doi: 10.1016/j.biomaterials.2016.07.038

Kang, T. Y., Hong, J. M., Jung, J. W., Kang, H. W., and Cho, D. W. (2016). Construction of large-volume tissue mimics with 3D functional vascular networks. *PLoS ONE* 11:e0156529. doi: 10.1371/journal.pone.0156529

Kang, T. Y., Hong, J. M., Jung, J. W., Yoo, J. J., and Cho, D. W. (2013). Design and assessment of a microfluidic network system for oxygen transport in engineered tissue. *Langmuir* 29, 701–709. doi: 10.1021/la303552m

Kelava, I., and Lancaster, M. A. (2016). Dishing out mini-brains: current progress and future prospects in brain organoid research. *Dev. Biol.* 420, 199–209. doi: 10.1016/j.ydbio.2016.06.037

Kim, J. D., Choi, J. S., Kim, B. S., Choi, Y. C., and Cho, Y. W. (2010). Piezoelectric inkjet printing of polymers: Stem cell patterning on polymer substrates. *Polymer* 51, 2147–2154. doi: 10.1016/j.polymer.2010.03.038

Kim, J. J., Hou, L., and Huang, N. F. (2016). Vascularization of three-dimensional engineered tissues for regenerative medicine applications. *Acta Biomater.* 41, 17–26. doi: 10.1016/j.actbio.2016.06.001

Kinoshita, K., Iwase, M., Yamada, M., Yajima, Y., and Seki, M. (2016). Fabrication of multilayered vascular tissues using microfluidic agarose hydrogel platforms. *Biotechnol. J.* 11, 1415–1423. doi: 10.1002/biot.201600083

Kinstlinger, I. S., and Miller, J. S. (2016). 3D-printed fluidic networks as vasculature for engineered tissue. *Lab. Chip* 16, 2025–2043. doi: 10.1039/C6LC00193A

Kleinman, H. K., and Martin, G. R. (2005). Matrigel: basement membrane matrix with biological activity. *Semin. Cancer Biol.* 15, 378–386. doi: 10.1016/j.semcancer.2005.05.004

Kloxin, A. M., Tibbitt, M. W., Kasko, A. M., Fairbairn, J. A., and Anseth, K. S. (2010). Tunable hydrogels for external manipulation of cellular microenvironments through controlled photodegradation. *Adv. Mater.* 22, 61–66. doi: 10.1002/adma.200900917

Kolesky, D. B., Homan, K. A., Skylar-Scott, M. A., and Lewis, J. A. (2016). Three-dimensional bioprinting of thick vascularized tissues. *Proc. Natl. Acad. Sci. U.S.A.* 113, 3179–3184. doi: 10.1073/pnas.1521342113

Kunz-Schughart, L. A., Schroeder, J. A., Wondrak, M., van Rey, F., Lehle, K., Hofstaedter, F., et al. (2006). Potential of fibroblasts to regulate the formation of three-dimensional vessel-like structures from endothelial cells *in vitro*. *Am. J. Physiol. Cell Physiol.* 290, C1385–C1398. doi: 10.1152/ajpcell.00248.2005

Langer, R., and Tirrell, D. A. (2004). Designing materials for biology and medicine. *Nature* 428, 487–492. doi: 10.1038/nature02388

Leong, M. F., Toh, J. K., Du, C., Narayanan, K., Lu, H. F., Lim, T. C., et al. (2013). Patterned prevascularised tissue constructs by assembly of polyelectrolyte hydrogel fibres. *Nat. Commun.* 4:2353. doi: 10.1038/ncomms3353

Li, S., Liu, Y. Y., Liu, L. J., and Hu, Q. X. (2016). Versatile method for fabricating tissue engineering scaffolds with a three-dimensional channel for prevasculature networks. *ACS Appl. Mater. Interfaces* 8, 25096–25103. doi: 10.1021/acsami.6b07725

Lutolf, M. P., Gilbert, P. M., and Blau, H. M. (2009). Designing materials to direct stem-cell fate. *Nature* 462, 433–441. doi: 10.1038/nature08602

Mansour, A. A., Gonçalves, J. T., Bloyd, C. W., Li, H., Fernandes, S., Quang, D., et al. (2018). An *in vivo* model of functional and vascularized human brain organoids. *Nat. Biotechnol.* 36, 432–441. doi: 10.1038/nbt.4127

McMurtrey, R. J. (2016). Analytic models of oxygen and nutrient diffusion, metabolism dynamics, and architecture optimization in three-dimensional tissue constructs with applications and insights in cerebral organoids. *Tissue Eng. Part C Methods* 22, 221–249. doi: 10.1089/ten.tec.2015.0375

Meinhardt, A., Eberle, D., Tazaki, A., Ranga, A., Niesche, M., Wilsch-Bräuninger, M., et al. (2014). 3D reconstitution of the patterned neural tube from embryonic stem cells. *Stem Cell Rep.* 3, 987–999. doi: 10.1016/j.stemcr.2014.09.020

Meyer, W., Engelhardt, S., Novosel, E., Elling, B., Wegener, M., and Krüger, H. (2012). Soft polymers for building up small and smallest blood supplying systems by stereolithography. *J. Funct. Biomater.* 3, 257–268. doi: 10.3390/jfb3020257

Miller, J. S., Stevens, K. R., Yang, M. T., Baker, B. M., Nguyen, D. H., Cohen, D. M., et al. (2012). Rapid casting of patterned vascular networks for perfusable engineered three-dimensional tissues. *Nat. Mater.* 11, 768–774. doi: 10.1038/nmat3357

Nashimoto, Y., Hayashi, T., Kunita, I., Nakamasu, A., Torisawa, Y. S., Nakayama, M., et al. (2017). Integrating perfusable vascular networks with a three-dimensional tissue in a microfluidic device. *Integr Biol* 9, 506–518. doi: 10.1039/C7IB00024C

Nishiyama, Y., Henmi, C., Iwanaga, S., Nakagawa, H., Yamaguchi, K., Akita, K., et al. (2018). Ink Jet Three-Dimensional Digital Fabrication for Biological Tissue Manufacturing: Analysis of Alginate Microgel Beads Produced by Ink Jet Droplets for Three Dimensional Tissue Fabrication. *J. Imaging Sci. Technol.* 52, 60201-1–60201-6(6). doi: 10.2352/J.ImagingSci.Technol.(2008)52:6(060201)

Oujja, M., Pérez, S., Fadeeva, E., Koch, J., Chichkov, B. N., and Castillejo, M. (2009). Three dimensional microstructuring of biopolymers by femtosecond laser irradiation. *Appl. Phys. Lett.* 95, 263703. doi: 10.1063/1.3274127

Ovsianikov, A., Deiwick, A., Van Vlierberghe, S., Pflaum, M., Wilhelmi, M., Dubruel, P., et al. (2011). Laser fabrication of 3D gelatin scaffolds for the generation of bioartificial tissues. *Materials* 4, 288–299. doi: 10.3390/ma4010288

Ovsianikov, A., Mironov, V., Stampf, J., and Liska, R. (2012). Engineering 3D cell-culture matrices: multiphoton processing technologies for biological and tissue engineering applications. *Expert Rev. Med. Devices* 9, 613–633. doi: 10.1586/erd.12.48

Pham, M. T., Pollock, K. M., Rose, M. D., Cary, W. A., Stewart, H. R., Zhou, P., et al. (2018). Generation of human vascularized brain organoids. *Neuroreport* 29, 588–593. doi: 10.1097/WNR.0000000000001014

Pittman, R. N. (2013). Oxygen transport in the microcirculation and its regulation. *Microcirculation* 20, 117–137. doi: 10.1111/micc.12017

Radisic, M., Deen, W., Langer, R., and Vunjak-Novakovic, G. (2005). Mathematical model of oxygen distribution in engineered cardiac tissue with parallel channel array perfused with culture medium containing oxygen carriers. *Am. J. Physiol. Heart Circ. Physiol.* 288, H1278–H1289. doi: 10.1152/ajpheart.00787.2004

Raimondi, M. T., Eaton, S. M., Nava, M. M., Laganà, M., Cerullo, G., and Osellame, R. (2012). Two-photon laser polymerization: from fundamentals to biomedical application in tissue engineering and regenerative medicine. *J. Appl. Biomater. Funct. Mater.* 10, 55–65. doi: 10.5301/JABFM.2012.9278

Ranga, A., Girgin, M., Meinhardt, A., Eberle, D., Caiazzo, M., Tanaka, E. M., et al. (2016). Neural tube morphogenesis in synthetic 3D microenvironments. *Proc. Natl. Acad. Sci. U.S.A.* 113, E6831–E6839. doi: 10.1073/pnas.1603529113

Ranga, A., Gjorevski, N., and Lutolf, M. P. (2014a). Drug discovery through stem cell-based organoid models. *Adv. Drug Deliv. Rev.* 70, 19–28. doi: 10.1016/j.addr.2014.02.006

Ranga, A., Gobaa, S., Okawa, Y., Mosiewicz, K., Negro, A., and Lutolf, M. P. (2014b). 3D niche microarrays for systems-level analyses of cell fate. *Nat. Commun.* 5:4324. doi: 10.1038/ncomms5324

Roudsari, L. C., Jeffs, S. E., Witt, A. S., Gill, B. J., and West, J. L. (2016). A 3D Poly(ethylene glycol)-based tumor angiogenesis model to study the influence of vascular cells on lung tumor cell behavior. *Sci. Rep.* 6:32726. doi: 10.1038/srep32726

Sabbagh, M. F., Heng, J. S., Luo, C., Castanon, R. G., Nery, J. R., Rattner, A., et al. (2018). Transcriptional and epigenomic landscapes of CNS and non-CNS vascular endothelial cells. *Elife* 6:36187. doi: 10.7554/eLife.36187

Sacchi, V., Mittermayr, R., Hartinger, J., Martino, M. M., Lorentz, K. M., Wolbank, S., et al. (2014). Long-lasting fibrin matrices ensure stable and functional angiogenesis by highly tunable, sustained delivery of recombinant VEGF164. *Proc. Natl. Acad. Sci. U.S.A.* 111, 6952–6957. doi: 10.1073/pnas.1404605111

Sala, A., Hänseler, P., Ranga, A., Lutolf, M. P., Vörös, J., Ehrbar, M., et al. (2011). Engineering 3D cell instructive microenvironments by rational assembly of artificial extracellular matrices and cell patterning. *Integr. Biol.* 3, 1102–1111. doi: 10.1039/c1ib00045d

Sarig-Nadir, O., Livnat, N., Zajdman, R., Shoham, S., and Seliktar, D. (2009). Laser photoablation of guidance microchannels into hydrogels directs cell growth in three dimensions. *Biophys. J.* 96, 4743–4752. doi: 10.1016/j.bpj.2009.03.019

Saunders, R. E., Gough, J. E., and Derby, B. (2008). Delivery of human fibroblast cells by piezoelectric drop-on-demand inkjet printing. *Biomaterials* 29, 193–203. doi: 10.1016/j.biomaterials.2007.09.032

Skylar-Scott, M. A., Liu, M.-C., Wu, Y., Dixit, A., and Yanik, M. F. (2016). Guided homing of cells in multi-photon microfabricated bioscaffolds. *Adv. Healthc. Mater.* 5, 1233–1243. doi: 10.1002/adhm.201600082

Sooppan, R., Paulsen, S. J., Han, J., Ta, A. H., Dinh, P., Gaffey, A. C., et al. (2016). In vivo anastomosis and perfusion of a three-dimensionally-printed construct containing microchannel networks. *Tissue Eng. Part C Methods* 22, 1–7. doi: 10.1089/ten.tec.2015.0239

Sun, Y. L., Li, Q., Sun, S. M., Huang, J. C., Zheng, B. Y., Chen, Q. D., et al. (2015). Aqueous multiphoton lithography with multifunctional silk-centred bio-resists. *Nat. Commun.* 6:8612. doi: 10.1038/ncomms9612

Takebe, T., Sekine, K., Enomura, M., Koike, H., Kimura, M., Ogaeri, T., et al. (2013). Vascularized and functional human liver from an iPSC-derived organ bud transplant. *Nature* 499, 481–484. doi: 10.1038/nature12271

Tibbitt, M. W., Kloxin, A. M., Dyamenahalli, K. U., and Anseth, K. S. (2010). Controlled two-photon photodegradation of PEG hydrogels to study and manipulate subcellular interactions on soft materials. *Soft Matter* 6, 5100–5108. doi: 10.1039/c0sm00174k

Walls, J. R., Coultas, L., Rossant, J., and Henkelman, R. M. (2008). Three-dimensional analysis of vascular development in the mouse embryo. *PLoS ONE* 3:0002853. doi: 10.1371/journal.pone.0002853

Watson, C. L., Mahe, M. M., Múnera, J., Howell, J. C., Sundaram, N., Poling, H. M., et al. (2014). An *in vivo* model of human small intestine using pluripotent stem cells. *Nat. Med.* 20, 1310–1314. doi: 10.1038/nm.3737

Wu, W., DeConinck, A., and Lewis, J. A. (2011). Omnidirectional printing of 3D microvascular networks. *Adv. Mater. Weinheim.* 23, H178–H83. doi: 10.1002/adma.201004625

Xie, M., Gao, Q., Zhao, H., Nie, J., Fu, Z., Wang, H., et al. (2018). Electro-assisted bioprinting of low-concentration GelMA microdroplets. *Small* 20, 201804216. doi: 10.1002/smll.201804216

Xu, C., Chai, W., Huang, Y., and Markwald, R. R. (2012). Scaffold-free inkjet printing of three-dimensional zigzag cellular tubes. *Biotechnol. Bioeng.* 109, 3152–3160. doi: 10.1002/bit.24591

Xu, C., Zhang, Z., Christensen, K., Huang, Y., Fu, J., and Markwald, R. R., et al. (2014). Freeform vertical and horizontal fabrication of alginate-based vascular-like tubular constructs using inkjetting. *J. Manufact. Sci. Eng.* 136:061020. doi: 10.1115/1.4028578

Yan, H. H. N., Siu, H. C., Law, S., Ho, S. L., Yue, S. S. K., Tsui, W. Y., et al. (2018). A comprehensive human gastric cancer organoid biobank captures tumor subtype heterogeneity and enables therapeutic screening. *Cell Stem Cell* 23, 882–897. doi: 10.1016/j.stem.2018.09.016

Yang, J., and Wang, Y. (2013). Design of vascular networks: a mathematical model approach. *Int. J. Numer. Method Biomed. Eng.* 29, 515–529. doi: 10.1002/cnm.2534

Zhang, Y. S., Arneri, A., Bersini, S., Shin, S. R., Zhu, K., Goli-Malekabadi, Z., et al. (2016). Bioprinting 3D microfibrous scaffolds for engineering endothelialized myocardium and heart-on-a-chip. *Biomaterials* 110, 45–59. doi: 10.1016/j.biomaterials.2016.09.003

Zhu, W., Qu, X., Zhu, J., Ma, X., Patel, S., Liu, J., et al. (2017). Direct 3D bioprinting of prevascularized tissue constructs with complex microarchitecture. *Biomaterials* 124, 106–115. doi: 10.1016/j.biomaterials.2017.01.042

Conflict of Interest Statement: The authors declare that the research was conducted in the absence of any commercial or financial relationships that could be construed as a potential conflict of interest.

frontiers
in Bioengineering and Biotechnology

ORIGINAL RESEARCH
published: 21 May 2019
doi: 10.3389/fbioe.2019.00109

Physical Vein Models to Quantify the Flow Performance of Sclerosing Foams

*Elisabetta Bottaro[1], Jemma Paterson[2], Xunli Zhang[1,3], Martyn Hill[1], Venisha A. Patel[4], Stephen A. Jones[4], Andrew L. Lewis[4], Timothy M. Millar[2] and Dario Carugo[1,3]**

[1] Faculty of Engineering and Physical Sciences, University of Southampton, Southampton, United Kingdom, [2] Faculty of Medicine, University of Southampton, Southampton, United Kingdom, [3] Institute for Life Sciences (IfLS), University of Southampton, Southampton, United Kingdom, [4] Biocompatibles UK Ltd. (a BTG group company), Camberley, United Kingdom

OPEN ACCESS

Edited by:
Martin Dufva,
Technical University of Denmark,
Denmark

Reviewed by:
Jerome Richard Duisit,
Catholic University of Louvain,
Belgium
Drago Sticker,
University of Copenhagen, Denmark

***Correspondence:**
Dario Carugo
d.carugo@soton.ac.uk

Specialty section:
This article was submitted to
Tissue Engineering and Regenerative Medicine,
a section of the journal
Frontiers in Bioengineering and Biotechnology

Received: *31 October 2018*
Accepted: *01 May 2019*
Published: *21 May 2019*

Citation:
Bottaro E, Paterson J, Zhang X, Hill M, Patel VA, Jones SA, Lewis AL, Millar TM and Carugo D (2019) Physical Vein Models to Quantify the Flow Performance of Sclerosing Foams.
Front. Bioeng. Biotechnol. 7:109.
doi: 10.3389/fbioe.2019.00109

Foam sclerotherapy is clinically employed to treat varicose veins. It involves intravenous injection of foamed surfactant agents causing endothelial wall damage and vessel shrinkage, leading to subsequent neovascularization. Foam production methods used clinically include manual techniques, such as the Double Syringe System (DSS) and Tessari (TSS) methods. Pre-clinical *in-vitro* studies are conducted to characterize the performance of sclerosing agents; however, the experimental models used often do not replicate physiologically relevant physical and biological conditions. In this study, physical vein models (PVMs) were developed and employed for the first time to characterize the flow behavior of sclerosing foams. PVMs were fabricated in polydimethylsiloxane (PDMS) by replica molding, and were designed to mimic qualitative geometrical characteristics of veins. Foam behavior was investigated as a function of different physical variables, namely (i) geometry of the vein model (i.e., physiological vs. varicose vein), (ii) foam production technique, and (iii) flow rate of a blood surrogate. The experimental set-up consisted of a PVM positioned on an inclined platform, a syringe pump to control the flow rate of a blood substitute, and a pressure transducer. The static pressure of the blood surrogate at the PVM inlet was measured upon foam administration. The recorded pressure-time curves were analyzed to quantify metrics of foam behavior, with a particular focus on foam expansion and degradation dynamics. Results showed that DSS and TSS foams had similar expansion rate in the physiological PVM, whilst DSS foam had lower expansion rate in the varicose PVM compared to TSS foam. The degradation rate of DSS foam was lower than TSS foam, in both model architectures. Moreover, the background flow rate had a significant effect on foam behavior, enhancing foam displacement rate in both types of PVM.

Keywords: physical vein model, varicose vein, microfluidic, foam, foam sclerotherapy, physician compounded foam

INTRODUCTION

Venous incompetence in the lower limbs is a common disease. Varicose veins have long been considered a cosmetic problem but—if left untreated—they may lead to more advanced form of chronic venous dysfunction, such as chronic venous insufficiency (CVI) (Spiridon and Corduneanu, 2017). Varicose veins are generally treated in order to prevent venous stasis, reflux, hypertension, and ulceration (Gloviczki et al., 2011). Sclerotherapy is a minimally invasive technique for treating varicose veins, and involves the intravenous injection of a sclerosing solution to cause endothelial damage, vessel shrinkage, and subsequent neovascularization (Goldman et al., 2017). Foam sclerotherapy is a development of liquid sclerotherapy, where the sclerosing solution is mixed with a gas in order to produce a "microfoam" (bubble diameter: 100–500 μm) (Eckmann, 2009). The use of foamed sclerosants offers significant benefits, particularly in the treatment of larger lower-extremity veins (Hamel-Desnos et al., 2003; Ouvry et al., 2008; Smith, 2009). Notably, a limitation of liquid sclerotherapy is that the sclerosing agent mixes rapidly with blood and is "consumed" or de-activated by blood cells and plasma proteins, respectively (Parsi et al., 2008; Connor et al., 2015). On the other hand, a cohesive foam displaces blood away from the diseased vein, reducing the extent of sclerosant's deactivation and leading to a greater contact time with the endothelial layer. As a result, sclerosing foams can be more effective in damaging the vessel wall, and this is achieved at lower concentrations of active molecule compared to their liquid counterparts (Goldman et al., 2017).

The flow behavior of sclerosing foams is therefore an important determinant of their ability to fully prime the target vein, and to provide sufficient contact time with the endothelial layer to result in effective therapeutic outcomes. The ideal foam should be sufficiently viscous and have low bubble size dispersity, to result in adequate handling stability and cohesiveness upon injection (Star et al., 2018). Increasing the quantity of surfactant agent may result in greater foam stability; however, this is undesirable as higher concentrations of sclerosant may lead to increased risk of side effects (Peterson and Goldman, 2012). Phlebologists often generate foams manually; these types of foam are referred to as physician-compounded foams (or PCFs). The two most common techniques utilized for producing PCFs are (i) the double syringe system (DSS) and (ii) the Tessari (TSS) methods (Tessari et al., 2001). Both techniques involve mixing of a liquid sclerosant solution with a gas or gas mixture, which is achieved by passing the liquid and gas between two syringes joined together via a connector (Jia et al., 2007). The gas phase most commonly used is room air (RA); its high nitrogen (N_2) content results in a foam that is more stable than N_2-free PCFs. However, the low solubility of nitrogen in blood may be responsible for increased risk of gas embolism and neurological events. Other gases employed are clinical grade carbon dioxide (CO_2), or CO_2 and oxygen (O_2) mixtures (Peterson and Goldman, 2011). Foams produced with these gases are reported to be less stable than RA-foams, due the high solubility of CO_2 in blood, but the risk of embolism is largely reduced (Cavezzi and Tessari, 2009; Peterson and Goldman, 2011). However, they may be less effective in displacing blood, which could limit their therapeutic efficacy. The characteristics of PCFs can depend on many variables, including (i) the type of gas (Larmignat et al., 2008; Peterson and Goldman, 2011), (ii) the liquid:gas volume ratio (typically in the range 1:3–1:7), (iii) the type of surfactant (polidocanol or sodium tetradecyl sulfate) and its volumetric concentration (typically in the range 0.5–3%) (Hanwright et al., 2005; Van Deurzen et al., 2011), (iv) the type of connector used (straight connector in DSS and a 3-way valve in TSS) (Rao and Goldman, 2005), and (v) the number of passes between syringes (in the range 5–10) (Peterson and Goldman, 2011). This large parametric space often limits the possibility of comparing results from different studies; thus, there is a growing need to establish standardized methodological approaches to evaluate physical stability of PCFs (Hamel-Desnos et al., 2007).

Foam stability is often evaluated *in-vitro* by measuring macroscopic or microscopic parameters, such as foam half time (FHT), foam drainage time (FDT), bubble size distribution, and foam dwell time (FDT) (Kruglyakov et al., 2008; Carugo et al., 2016; Critello et al., 2017). In a typical experiment, a defined volume of foam is produced and delivered into a vessel, where changes to its physical properties are monitored as a function of time. FHT is the time required for half of the volume of sclerosing solution to revert to liquid (Nastasa et al., 2015). FDT is instead the time at which visible liquid drainage begins (Kruglyakov et al., 2008). Both parameters can be measured by observing drainage in a standing column of foam, and quantifying the height (or volume) of the liquid phase over time. This can be determined by analyzing photographic images of the foam column at increasing time points, or it can be inferred from changes in back-scattering or transmission of an incident light beam. These indicators of foam stability are however strongly dependent on the type and size of vessel in which the foam is contained (Carugo et al., 2015). Foam bubble size distribution can be measured by optical microscopy or light scattering techniques (Osei-Bonsu et al., 2015; Watkins and Oliver, 2017). The measured bubble size may however be strongly influenced by the invasiveness of the method used, and the time elapsed between foam production and analysis. A technique commonly used involves the injection of a foam sample between two glass plates, where foam containment in a small environment reduces the drainage and coarsening rates to facilitate imaging (Carugo et al., 2016).

The characterization methods reported above have been largely employed in the literature as a means to evaluate stability of sclerosing foams, and have been particularly useful for comparing different foam formulations (McAree et al., 2012; Cameron et al., 2013; Bai et al., 2018). However, the experimental systems used (i.e., syringes or vials) do not reflect dynamic conditions that are relevant to the end-point usage of the foam. Recently, Carugo et al. developed a model for the analysis of sclerosing foam behavior under more clinically relevant conditions. The model consisted of a 4 or 10 mm inner diameter polytetrafluoroethylene tubing, placed onto a platform with an adjustable inclination angle. Foam was injected into the tube, which was initially primed using a blood substitute, and its expansion/degradation rates were quantified using computational-based image analysis software. The model allowed to measure the foam dwell time, which is the time taken for a foam plug to recede over a unit distance (Carugo et al., 2015). It was however designed for usage under static fluidic conditions, and it did not replicate the varicose vein architecture.

In order to address these limitations of previous test methods, the work in this study aims to develop physical models replicating qualitative architectural characteristics of varicose veins and to employ them as a screening platform for comparing the flow behavior of different foam formulation methods. The developed biomimetic-inspired vein model (referred to as physical vein model, or PVM) allows recapitulating features of physiological and varicose veins, including circular cross-section, tortuous and swollen vessel morphologies, and physiologically relevant flow conditions. PVMs were employed to compare the flow performance of polidocanol-based PCFs, as a function of vessel geometry (straight vs. curved centerline), foam production technique (PCF vs. TSS), and volumetric flow rate. Moreover, it was demonstrated that models can be coated with endothelial cells, enabling future investigations of both mechanical and biological performance of sclerosing agents.

MATERIALS AND METHODS

Physical Vein Models (PVM): Design and Manufacturing

PVMs were fabricated via replica molding. Firstly, the 3D vein architecture was designed in SolidWorks (Dassault Systemes, SolidWorks Corporation, USA). Two different designs were generated to model both physiological and varicose veins. The physiological vein model comprised of a straight channel, whilst the varicose vein model comprised of a serpentine-like channel that replicated qualitatively a varicose vein geometry. In both models, channel length and inner diameter were set to 70 and 4 mm, respectively (**Figure 1**). The inner diameter replicated the average diameter of veins treated with sclerotherapy (Sandri et al., 1999), while the length was selected so that the model could accommodate at least 1 mL of foam. The volume of foam injected clinically depends on the size of the vessel segment to be treated (Chwała et al., 2015).

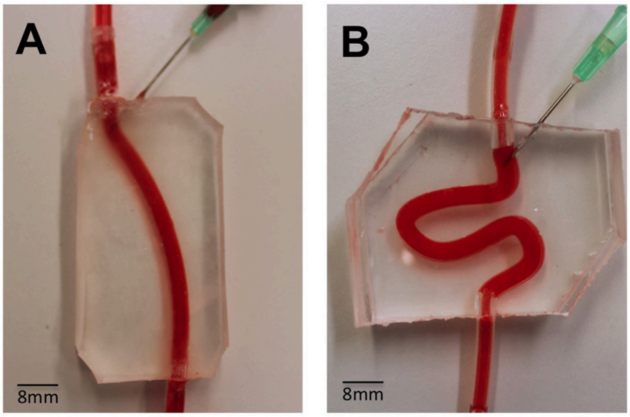

FIGURE 1 | Assembled PVMs representing simplified physiological **(A)** and varicose **(B)** vein models, and demonstration of perfusion using a red dye. These models were employed to test the flow behavior of foams. The main channel was punctured with a needle (16G), in order to mimic the clinical process of injection more closely.

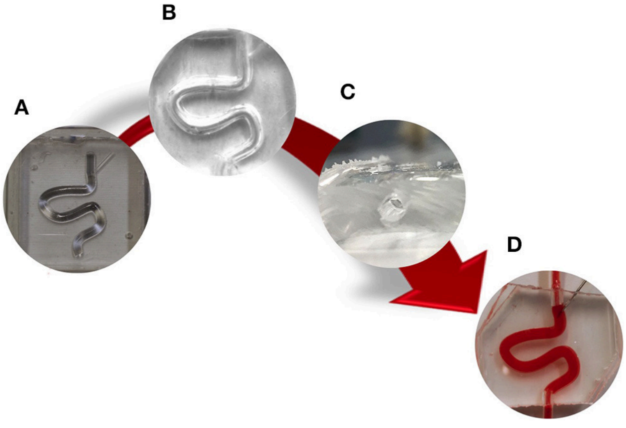

FIGURE 2 | Schematic of PVMs production via replica molding. Firstly, **(A)** a CAD design of positive molds was generated and 3D printed. Secondly, **(B)** two PDMS layers were produced from the molds, aligned together, and permanently bonded via oxygen plasma treatment to obtain a fully circular channel cross-section **(C)**. Finally, the main channel was punctured with a 16G needle **(D)**.

The PVM manufacturing process is illustrated in **Figure 2**. Firstly, positive molds of the design were 3D printed using an Objet350 Connex printer (Haycroft Works, Buckholt Drive, UK). Two specular molds were fabricated, each with a semi-circular channel cross-section, in order to obtain a model with a fully circular cross-section by combining the two molds. In addition, alignment pins were added to the mold design in order to facilitate the alignment process. Polydimethylsiloxane (PDMS) prepolymer and curing agent (Sylgard® 184, Dow Corning Corporation, USA) were mixed at a weight ratio of 10:1 (w/w), and then poured onto the 3D-printed molds. PDMS was then cured in an oven, at 65°C for 1 h, and allowed to solidify. The two specular PDMS layers were then aligned together and permanently bonded via treatment with oxygen plasma (Tepla 300 Plasma Asher, PVA TePla AG, Germany) (Bodas and Khan-Malek, 2007). The main channel was punctured with a 16G needle (BD Biosciences, UK) in order to replicate the clinical foam administration process (Goldman et al., 2017). Inlet/outlet ports were connected with silicone tubing (4 mm outer diameter, Cole-Palmer, UK).

Foam Production

PCFs were produced using polidocanol 1% (in buffered solution) and room air, at a liquid:gas volume ratio of 1:4. The foam production techniques employed were the double-syringe system (DSS) and Tessari (TSS) methods. In the

DSS method, two syringes (10 and 5 mL, BD Biosciences, USA) were interconnected using a Combidyn™ adapter (B. Braun Melsungen, Germany), whereas in the TSS method they were connected via a three-way stopcock (Baxter, USA) (Rao and Goldman, 2005; Critello et al., 2017). In both techniques, the foam was produced by passing the polidocanol solution (liquid phase) from one syringe, 10 times into and out of the other syringe initially containing room air.

Characterization of the Flow Behavior of Foams: Experimental Set-Up

The experimental set-up consisted of a PVM lodged onto a 3D printed inclined platform (inclination angle of 25°), to replicate patient's leg elevation as in the clinical procedure. The inlet tube was connected to the PVM using a three-way stopcock. A blood substitute (30% v/v glycerol in purified water) with a fluid dynamic viscosity, μ, of 0.003 Pa × sec and density, ρ, of 1,078 kg/m^3 (Pries et al., 1992) was conveyed through the vein model using a 10 mL syringe (BD Biosciences, USA). A steady flow of the blood substitute was imposed using a syringe pump (NE-1000 Programmable Single Syringe Pump, New Era Pump Systems, Inc., USA). A pressure transducer (Research Grade Blood Pressure Transducer, 230 VAC, 50 Hz, Harvard apparatus, UK) was positioned in line with the inlet tubing, and located 30 mm proximally to the PVM inlet (**Figure 3**). The pressure transducer was connected to a National Instruments I/O module (NI-DAQ, USB-6008, National Instrument, UK). The NI-DAQ system supports analog and digital inputs, and communicates with the NI-DAQ software (National Instrument, UK). A MATLAB® (The MathWorks Inc., USA) script was employed to store pressure data in an automated fashion.

Characterization of the Flow Behavior of Foams: Experimental Procedures

As described earlier, the 10 mL syringe was filled with a blood substitute, which was conveyed through the PVM at constant flow rates. A clinically relevant volume of foam (1 mL) (Eckmann, 2009) was injected manually into the PVM through a needle, using a silicon-free plastic syringe with capacity of 5 mL. The static pressure of the blood surrogate at the PVM inlet was measured before, during and after injection of foam, for a fixed time of 100 s. The static pressure was set to 0 mmHg before injecting the foam. Results were transferred to a personal computer and analyzed as described in the following paragraphs. The volumetric flow rates investigated were 62.5, 72.0, and 125.0 mL/h (**Figure 3**). The corresponding inlet Reynolds number was calculated using Equation 1, where ρ is the density of the blood surrogate (kg/m^3), v is the mean velocity of the blood surrogate (m/s), D is the hydraulic diameter of the vein model (m), and μ is the dynamic viscosity of the blood surrogate (Pa·s).

$$\mathrm{Re} = \frac{\rho v D}{\mu}. \tag{1}$$

The Reynolds number in these experiments ranged from 1.65 to 3.34, which is ∼100–200 times lower than physiological values (Raju et al., 2004), in order to replicate quasi-static or impaired flow conditions occurring in diseased veins.

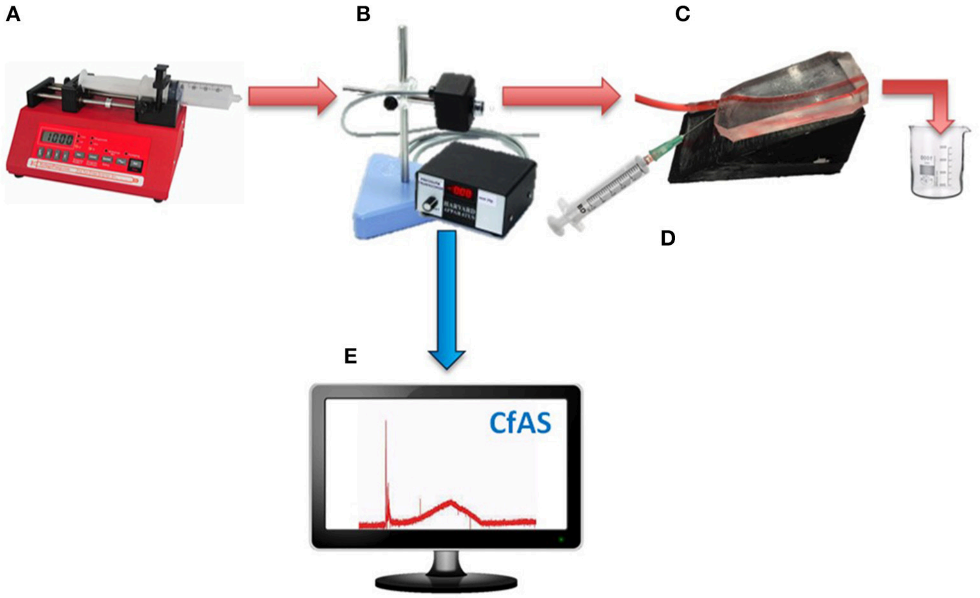

FIGURE 3 | Schematic illustrating the set-up for evaluating the flow behavior of foams in the PVM model. A steady flow is imposed using a syringe pump **(A)**, and a pressure transducer **(B)** is positioned in line with the inlet tubing and prior to the PVM **(C)**. The foam is injected through the 16G needle into the main channel **(D)**. The pressure transducer is connected to a National Instruments I/O module. The NI-DAQ system supports analog and digital inputs, and communicates with the NI-DAQ software. A Matlab code is employed to store pressure data in an automated fashion **(E)**.

Computational Foam Analysis System

A computational foam analysis system (CfAS) was developed with the aim of analyzing the pressure recordings upon foam injection. The analysis system was designed using MATLAB R2016a software (The MathWorks Inc., USA) with a flexible user-intended interface. The software read the experimental pressure measurements and performed a sequence of semi-automated operations, allowing extraction of relevant parameters from the pressure-time data. The pressure-time curve could be divided into three phases (**Figure 4**): (i) an initial spike due to the foam injection procedure, (ii) an almost linear increase in pressure due to the expansion of the foam within the PVM, and (iii) an almost linear decrease in pressure caused by foam degradation and "washing out." The CfAS calculated the slope of phases (ii) and (iii), which were referred to as expansion rate (ER) and degradation rate (DR), respectively. In addition, expansion time (ET) and degradation time (DT) were also quantified.

A representative pressure profile is illustrated in **Figure 4**, from which four different phases can be identified:

(i) *Foam injection*. This phase was associated with a rapid pressure spike, likely due to the insertion of the needle within the PVM or other mechanical perturbations associated with the injection procedure. Peak pressure values in this phase ranged from 10 to 50 mmHg.

(ii) *Foam plug expansion*. While the foam plug expanded within the PVM, the backpressure increased almost linearly. This is due to the significantly higher effective viscosity of foams compared to the blood surrogate, as reported in previous studies (Wong et al., 2015), leading to increased hydraulic resistance. The linear pressure increase is coherent with previous studies investigating foam behavior in a tube model, which revealed an almost linear increase in foam plug length during expansion (Carugo et al., 2015). The CfAS allowed quantifying the slope of the plug expansion phase, which was herein referred to as expansion rate (ER). It is hypothesized that more cohesive foams would fractionate more slowly and dilute less rapidly with the blood substitute, thus resulting in lower ER and higher peak pressures. The expansion time (ET) was also calculated from the pressure-time curve; higher ET corresponds to a longer contact time between the foam and the inner surface of the PVM.

(iii) *Foam plug degradation*. Once expansion was complete, the foam plug underwent degradation. This is due to a combination of processes, including foam drainage, coarsening, and the "washing out" action exerted by the background flow of a blood substitute. Foam degradation resulted in a reduction in hydraulic resistance, leading to an almost linear drop in PVM backpressure. As for the degradation phase, the shape of the pressure profile during degradation is consistent with prior studies (Carugo et al., 2015). The CfAS allowed quantifying the slope of the plug degradation phase, which was referred to as degradation rate (DR). It is hypothesized that more cohesive foams would destabilize more slowly, thus resulting in lower DR. The degradation time (DT) was also calculated from the pressure-time curve; higher DT corresponds to a longer contact time between the foam and the inner surface of the PVM.

(iv) *Residual pressure*. The pressure level at the end of the degradation phase could be equal or greater than the initial pressure (i.e., at the time of injection). Because of gravitational separation, bubbles accumulated at the top surface of the vein model. If sufficiently stable, they would remain in place for the duration of the pressure recording (up to 100 s), causing the residual pressure to be greater than the initial pressure.

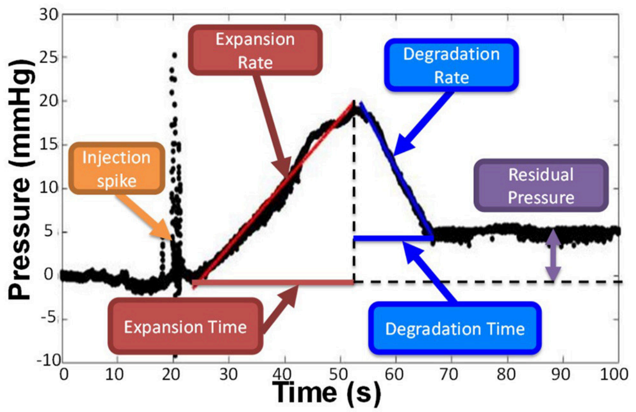

FIGURE 4 | Representative pressure vs. time curve obtained by the CfAS. The plots were divided into three phases: (i) an increase of the pressure due to the expansion of the foam inside the channel, (ii) a decrease of the pressure caused by the degradation of the foam, and (iii) an initial peak due to the injection.

Statistical Analysis

Comparisons between foam production methods were performed using an unpaired Student's *t*-test for two groups analysis, or one-way ANOVA in the case of more than two groups. Statistical significance was assumed for $p < 0.05$. All statistical tests were performed with Prism software (GraphPad Software Inc., USA). All data were reported as the mean ± SD of at least six independent repeats of the same experiment.

Cell Seeding

HUVECs (human umbilical venous endothelial cells) were seeded in the PVM models. HUVECs were extracted from umbilical cords, and this was carried out in accordance with the Human Tissue Act (2004) and the recommendations of Southampton & South West Hampshire Research Ethics Committee B with Governance provided by the University of Southampton Research Governance Office. Umbilical cords were collected from the Princess Anne Hospital (Southampton, UK) from non-complicated natural vaginal births following agreed ethical collection protocols [Local Research Ethical Committee

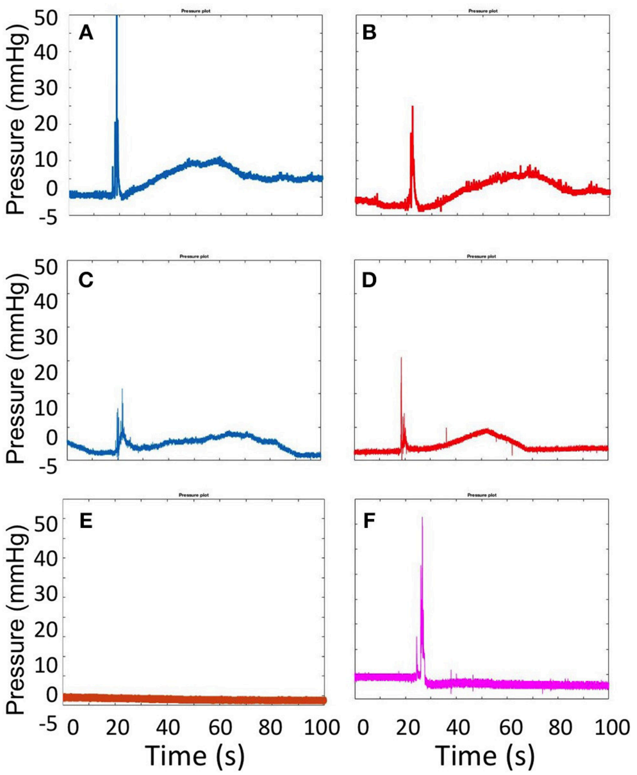

FIGURE 5 | Pressure plots obtained from the CfAS while injecting DSS **(A,C)** and TSS **(B,D)** foams. The upper panels show the recordings obtained using the straight channel geometry, whereas the lower panels show the recording obtained using the serpentine-like channel geometry. As a control test **(E)**, the pressure was measured without injecting foam, at a background constant flow rate (72 mL/h). The pressure inside the vein models was also measured while injecting the foam in the absence of a blood-surrogate flow **(F)**.

(LREC); Ref: 07/H0502/83]. Firstly, the PDMS devices were washed four times with 70% ethanol for sterilization. Then, HBSS (Hanks' Balanced Salt Solution, Thermo Fisher Scientific, USA) was conveyed through the channels to remove ethanol traces. Afterwards, the inner surfaces of the device were coated with 3 mL of different proteins: 50 µl/mL of rat type I collagen (100 µg/mL; Gibco^{TM}, UK) or (ii) 100 µl/mL of fibronectin (Sigma, UK). The device was subsequently placed at 37°C in a 5 % CO_2 incubator for 2 h, followed by rinsing with HM (HUVEC Medium, Thermo Fisher Scientific Inc., USA).

The HUVECs suspension was injected into the proteins-coated channels (at a concentration of 4–5 × 10^6 cells/mL), and the device was incubated for 2 h. In order to achieve complete coating, the device was then turned upside down, and primed with a fresh HUVEC suspension. The device was finally incubated overnight to promote cell attachment.

Image Acquisition

Bright field images of HUVECs within the PVM models were acquired with an optical microscope (Olympus, CKX41, Japan). Images were taken of live samples every 24–48 h.

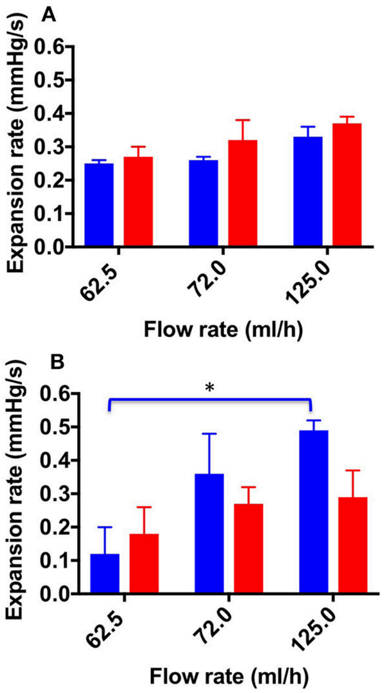

FIGURE 6 | Expansion rate values at the different flow rates investigated, and different foam production methods (TSS blue bars, DSS red bars). Measurements were obtained from the straight **(A)** and curved **(B)** channel geometry. Data represent the average of 6 measurements ± SD. An asterisk (*) indicates that differences between mean values are statistically significant ($p < 0.05$). The experiment was repeated six times, and results are reported as mean value ± standard deviation.

RESULTS

Characterization of the Flow Behavior of Foams in PVM Models

The PVM models developed in this study have been employed to characterize the flow behavior of sclerosing foams, by measuring static pressure of a blood surrogate at the PVM inlet.

Representative pressure-time curves obtained by CfAS, for both DSS (blue line) and TSS (red line) foams are shown in **Figure 5**. Both PVM geometries, i.e., straight (**Figures 5A,B**) and serpentine-like (**Figures 5C,D**), showed similar pressure profiles containing the four phases discussed earlier. As a control test, pressure was measured without injecting the foam, at a constant background flow rate of 72 mL/h (**Figure 5E**). As expected, no pressure variation was detected in these experiments for both PVM geometries. In addition, tests were also performed where foams were injected in the absence of background flow (**Figure 5F**). In this case, only the pressure spike corresponding to foam injection was present, due to the absence of a background pressure-driven flow.

Figure 6 shows the ER values determined for both TSS and DSS foams at all flow rates investigated, using both physiological (**Figure 6A**) and varicose (**Figure 6B**) PVMs. Lower ER is herein regarded as a therapeutically favorable property of foams, as it is

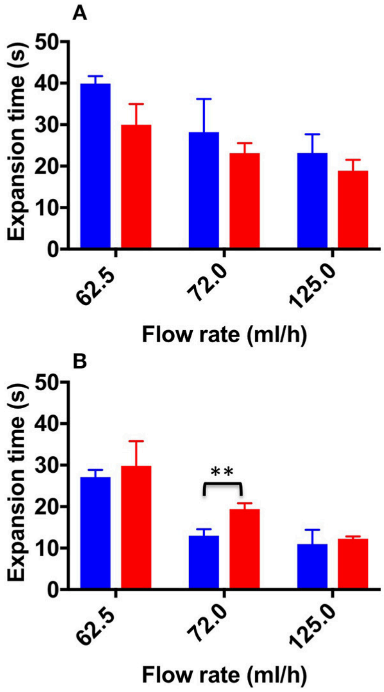

FIGURE 7 | Expansion time values at the different flow rates investigated, and different foam production methods (TSS blue bars, DSS red bars). Measurements were obtained from the straight **(A)** and curved **(B)** channel geometry. Two asterisks (**) indicate that differences between mean values are very statistically significant ($p < 0.01$). The experiment was repeated six times, and results are reported as mean value ± standard deviation.

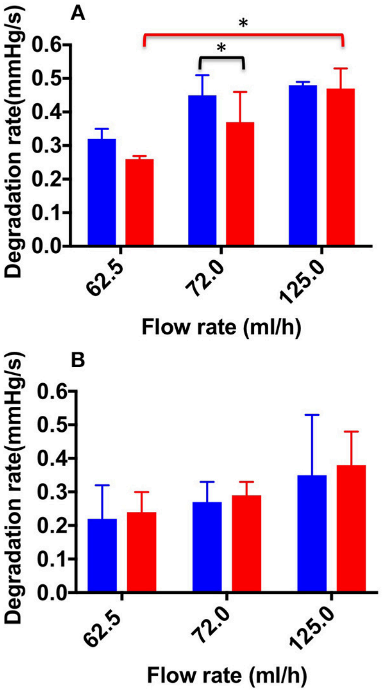

FIGURE 8 | Degradation rate values at the different flow rates investigated, and different foam production methods (TSS blue bars, DSS red bars). Measurements were obtained from the straight **(A)** and curved **(B)** channel geometry. An asterisk (*) indicates that differences between mean values are statistically significant ($p < 0.05$). The experiment was repeated six times, and results are reported as mean value ± standard deviation.

indicative of higher foam cohesion and longer persistence in the vein. In the physiological PVM, TSS and DSS had comparable ER at all flow rates investigated. Values were equal to 0.25 ± 0.01 mmHg/s (62.5 mL/h), 0.26 ± 0.01 mmHg/s (72.0 mL/h), and 0.33 ± 0.04 mmHg/s (125.0 mL/h) for TSS; and 0.27 ± 0.03 mmHg/s (62.5 mL/h), 0.32 ± 0.06 mmHg/s (72.0 mL/h), and 0.37 ± 0.02 mmHg/s (125.0 mL/h) for DSS. On the other hand, in the varicose PVM model, DSS foam had lower ER compared to TSS, particularly at the highest flow rate (0.49 ± 0.03 mmHg/s for TSS and 0.29 ± 0.08 mmHg/s for DSS). Differences in foam behavior may be attributed to their bubble size distribution and drainage kinetics (Carugo et al., 2015).

A one-way ANOVA was conducted to evaluate whether ER of both types of foam depended on the inlet flow rate. With respect to the TSS group, a significant difference was observed between all flow rates investigated; indeed, the average ER value increased with increasing the inlet flow rate.

Figure 7 shows the ET values determined for both TSS and DSS foams, at all flow rates investigated. As expected, the expansion time (ET) was slightly higher for TSS at 62.5 and 72.0 mL/h (39.9 ± 1.00 and 28 ± 8.00 s, respectively) compared to DSS (29.9 ± 5.00 and 23 ± 2.00 s, respectively). However, in the physiological PVM no statistical difference was determined between PCFs. In the varicose PVM, TSS foam had lower ET compared to DSS foam at all flow rates investigated, consistently with the expansion rate data reported previously. Statistical difference between TSS and DSS was found at 72.0 mL/h (12.98 ± 1.60 s and 19.35 ± 1.430 s for TSS and DSS, respectively) (**Figure 8B**). In both PVM models, increasing the background flow caused a reduction of ET, likely due to a "washing out" effect of the blood surrogate, as discussed earlier. In the varicose vein model, DSS foam demonstrated greater ability to oppose this effect, resulting in higher contact time with the vessel wall.

Figure 8 shows DR values determined for both TSS and DSS foams, at all flow rates investigated. In the physiological PVM, at the lowest flow rate (62.5 mL/h), DSS foam had a lower DR (0.26 ± 0.01 mmHg/s) compared to TSS foam (0.32 ± 0.03 mmHg/s). Significant difference in DR between TSS (0.45 ± 0.06 mmHg/s) and DSS (0.37 ± 0.09 mmHg/s) foams was found at 72.0 mL/h. At the highest flow rate (125.0 mL/h) both types of foam had similar DR (0.48 ± 0.03 mmHg/s for TSS and 0.47 ± 0.07 mmHg/s for DSS), suggesting that foam degradation performance is dominated by the background flow at these higher flow rates. A one-way ANOVA was performed to evaluate the effect of background flow rate on DR, for both types of PCF. With respect to the DSS group, a significant difference was observed with increasing the inlet flow rate; indeed, the average DR value increased with increasing the flow rate. With respect to the TSS group, no significant difference was found by varying the flow rate. Both foams had comparable degradation performance across the two PVM geometries, suggesting that once a foam plug

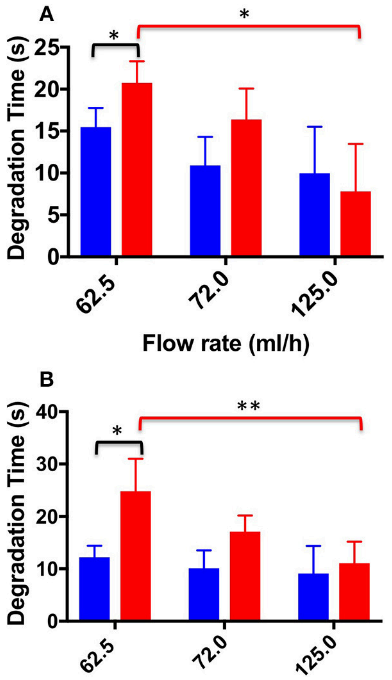

FIGURE 9 | Degradation time values at the different flow rates investigated, and different foam production methods (TSS blue bars, DSS red bars). Measurements were obtained from the straight **(A)** and curved **(B)** channel geometry. An asterisk (*) indicates that differences between mean values are statistically significant ($p < 0.05$) and two asterisks (**) indicate that differences between mean values are very statistically significant ($p < 0.01$). The experiment was repeated six times, and results are reported as mean value ± standard deviation.

has been established into the vein, its degradation dynamics is not significantly affected by the vessel architecture.

Figure 9 shows DT values determined for both TSS and DSS foams at all flow rates investigated. In the physiological PVM model, at the lower flow rate (62.5 mL/h), DSS foam had a statistically higher DT (20.73 ± 2.60 s) compared to TSS foam (15.46 ± 2.30 s). At the intermediate flow rate, the average DT value was still higher compared to TSS (16.38 ± 3.70 s and 10.90 ± 3.40 s, respectively). At the highest flow rate (125.0 mL/h) both PCFs had comparable DT (9.97 ± 5 s for TSS and 7.8 ± 5.6 s for DSS). As expected, foams with lower degradation rate had a longer degradation time. Similar observations were made using the varicose PVM model, where at the lowest flow rate (62.5 mL/h) DSS foam had statistically higher DT (24.8 ± 6.20 s) compared to TSS. Differences between foam types reduced with increasing the inlet flow rate. At 125.0 mL/h, both types of foam presented similar DT (9.1 ± 5.3 s for TSS and 11.07 ± 4.1 s for DSS). A one-way ANOVA was conducted to evaluate the effect of flow rate on DT for both types of foam. With respect to the DSS group, results show that there is a significant difference between DTs measured at increasing flow rates, for both types of geometry. Moreover, DT was not significantly influenced by the PVM geometry, as for the degradation rate. With respect to the TSS group, no significant difference was found by varying the background flow rate.

Cell Seeding and Channel Functionalization

With the aim of developing PVM models that can be coated with an endothelial monolayer, seeding of HUVECs over the inner PDMS surfaces of the device was investigated. PDMS has been extensively used for cell culture in microfluidic devices (Choi et al., 2013), because of its optical transparency, low cost, gas permeability, and biocompatibility. However, it is not an ideal substrate surface for cell attachment, due to its hydrophobicity. As shown in **Figure 10**, HUVECs attached and uniformly distributed over the surface of both lower and upper walls of the circular channels, upon coating with extracellular proteins. Particularly, fibronectin coating resulted in more effective seeding, with a larger surface area covered by HUVECs. It is important to highlight that PVM devices have a larger channel (4 mm in diameter) compared to microchannels typically used in vasculature-on-a-chip devices (10–400 µm) (Tien, 2014). This makes the cell coating process more challenging, given the larger surface area to be covered. However, despite channels were larger in this study, it was possible to obtain a relatively homogenous coating using a lower cell seeding concentration compared to previous studies (typically in the range 5×10^5−1.25×10^7 cells/mL) (Chung et al., 2009; Kim et al., 2013).

DISCUSSION

In this study, a novel experimental method to quantify and compare the flow behavior of sclerosing foams was developed. The method provided a quantitative determination of fluid pressure upon foam administration, within models of either physiological or varicose veins (referred to as physical vein model, or PVM).

When a cohesive foam is injected into the PVM, it forms a plug that displaces the blood substitute. The foam plug however degrades over time, due to its intrinsic instability and the "washing out" action of the background flow. Using our model system, we were able to characterize these phenomenological behaviors for the first time, by measuring the static pressure of a blood surrogate at the PVM inlet (**Figure 5**).

It is well-known that sclerosing foams produced using different techniques differ in their "static" physical properties. In this study, we evaluated for the first time the dynamic flow behavior of sclerosing foams, by analyzing their expansion and degradation within qualitative models of both physiological and varicose veins. In particular, the behavior of different PCFs was compared, at varying volumetric flow rates (in the range 62.5−125.0 mL/h).

Overall, the results reported in this study show that TSS and DSS foams had comparable expansion rate in the physiological vein model, whereas TSS had faster expansion rate in the varicose model (**Figures 6**, **7**). Therefore, DSS foam has the ability to expand more slowly within a varicose vein model

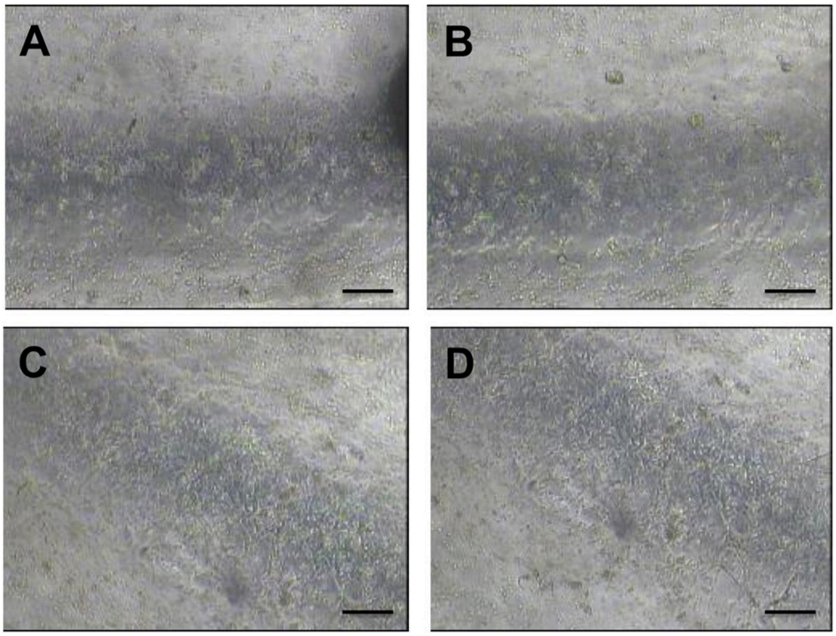

FIGURE 10 | Bright field microscope images of HUVECs cultured within the fully circular PVM channels. Images on the left show the lower channel wall coated with collagen **(A)** and fibronectin **(C)**, respectively. Images on the right show the upper channel wall coated with collagen **(B)** and fibronectin **(D)**, respectively. Images (4x magnification) were taken after 48 h from cell seeding. Scale bars are 200 μm long.

architecture, resulting in longer contact time (ET) with the vein wall upon injection. These results are consistent with prior studies showing that DSS foams are more cohesive than TSS foams in a tube model, in the absence of a background flow rate (Carugo et al., 2015).

Results also demonstrated that the flow field within the target vein can significantly influence the expansion dynamics of sclerosing foams. DSS foam was slightly less sensitive to changes in the background flow rate, suggesting that more cohesive foams may offer higher resistance to the "washing out" effect of the blood flow during expansion. Reducing blood flow rate during administration (i.e., via vein compression) may thus be preferable to enhance therapeutic efficacy.

With respect to the degradation dynamics of PCFs (**Figures 8**, **9**), at the lowest flow rate investigated DSS foam had lower degradation rate compared to TSS foam. This was likely due to the slower coarsening and drainage rate of DSS foams, coherently with previous studies (Carugo et al., 2015). Increasing the inlet flow rate resulted in PCFs having comparable degradation rate, suggesting that foam degradation performance is dominated by the background flow in these conditions. Interestingly, there was no significant difference in the degradation dynamics between the two PVM geometries investigated; suggesting that once a foam plug has been established into the vein, its degradation dynamics is not significantly affected by the vessel architecture.

It is important to highlight that expansion and degradation dynamics taken at the lowest flow rate are likely to be more representative of the flow conditions in a diseased (i.e., varicose) vein. In these conditions, DSS presented a slightly superior performance compared to TSS.

Finally, it was demonstrated that PVM models can be lined with endothelial cells in order to recreate the endothelial layer (**Figure 10**). The degree of endothelial damage upon treatment with foam can be employed as an indicator of therapeutic efficacy. In future work, we will employ these cell-coated PVM models to investigate the biological effects of sclerosing foams and correlate them with foam mechanical behavior.

CONCLUSION

In this study, we described the development of physical vein models replicating the qualitative architecture of physiological and varicose veins, and their utility as model platforms to screen the flow behavior of sclerosing foams, upon different formulation and administration conditions.

A simple method to manufacture vein models was developed, which aimed at generating channels with circular section and with a geometry that recapitulates some characteristics of the varicose vein. An experimental protocol was also established to investigate the flow performance of foams at conditions relevant to their clinical administration. Notably, the experimental set-up replicated some aspects of the clinical process of foam injection, including the use of a needle, patient's leg elevation, and the presence of a background blood flow.

Fluid pressure at the PVM inlet was measured during foam administration, which revealed different phases of the foam expansion and degradation dynamics. Particular emphasis was given to expansion and degradation of the foam plug, as indicators of its therapeutic efficacy.

As reported in previous studies (Carugo et al., 2015), the cohesiveness of foams is highly dependent on their rheological properties, which in turn are influenced by the bubble size distribution and foam drainage kinetics. Previous results showed that foam produced using the DSS method were more stable and presented longer dwell time compared to TSS foams (Carugo et al., 2015). Consistently with these previous observations, in our dynamic study DSS foam had longer degradation time and slower degradation rate than TSS foam. With respect to the expansion dynamics, no significant difference between the two foam formulations was found in the physiological vein model, whereas DSS had slower expansion in the varicose model. Differences in foam behavior across different model geometries could be attributed to the broader bubble size distribution of TSS foam compared to DSS foam; although these aspects merit further investigation.

In conclusion, the physical vein models and experimental methods developed in this study provide a novel technology platform to measure the behavior of different formulations of sclerosing foams, at physical conditions that resemble their clinical administration. They could therefore be employed as an additional test method in the pre-clinical pipeline, to innovate foam formulation and administration procedures. Moreover, we demonstrated that PVM models are suitable for coating with endothelial cells, which enables future investigations to correlate flow performance of sclerosing agents with their biological effects.

It should be noted that the PVM models reported in this study do not replicate the presence of venous valves, branching structures, or the mechanical properties of the vein wall, which may affect the flow behavior of foams. Ongoing research is focusing on the incorporation of these additional architectural and functional characteristics. Moreover, a more faithful replication of the physiological boundary conditions (including changes due to clinical practices; i.e., vein compression) will be considered in the future.

AUTHOR CONTRIBUTIONS

EB conducted all experiments and data analyses, designed all experimental procedures, and wrote the manuscript. DC co-designed all experimental procedures, wrote the Matlab code, co-wrote the manuscript and supervised the project. AL, SJ, and VP contributed to the design and implementation of the research and to the analysis of the results. All the other authors helped supervise the project.

FUNDING

This research was supported by Doctoral Training Partnership funded from EPSRC and Biocompatibles UK Ltd, a BTG International group company. The funding was awarded by the Faculty of Engineering and Environment (University of Southampton).

REFERENCES

Bai, T., Chen, Y., Jiang, W., Yan, F., and Fan, Y. (2018). Studies on foam decay trend and influence of temperature jump on foam stability in sclerotherapy. *Vasc. Endovascular Surg.* 52, 98–106. doi: 10.1177/1538574417741786

Bodas, D., and Khan-Malek, C. (2007). Hydrophilization and hydrophobic recovery of PDMS by oxygen plasma and chemical treatment—An SEM investigation. Sens. *Actuat. B Chem.* 123, 368–373. doi: 10.1016/j.snb.2006.08.037

Cameron, E., Chen, T., Connor, D. E., Behnia, M., and Parsi, K. (2013). Sclerosant foam structure and stability is strongly influenced by liquid air fraction. *Eur. J. Vasc. Endovasc. Surg.* 46, 488–494. doi: 10.1016/j.ejvs.2013.07.013

Carugo, D., Ankrett, D. N., O'Byrne, V., Wright, D. D. I., Lewis, A. L., Hill, M., et al. (2015). The role of clinically-relevant parameters on the cohesiveness of sclerosing foams in a biomimetic vein model. *J. Mater. Sci. Mater. Med.* 26:258. doi: 10.1007/s10856-015-5587-z

Carugo, D., Ankrett, D. N., Zhao, X., Zhang, X., Hill, M., O'Byrne, V., et al. (2016). Benefits of polidocanol endovenous microfoam (Varithena®) compared with physician-compounded foams. *Phlebology* 31, 283–295. doi: 10.1177/0268355515589063

Cavezzi, A., and Tessari, L. (2009). Foam sclerotherapy techniques: different gases and methods of preparation, catheter versus direct injection. *Phlebol. J. Venous Dis.* 24, 247–251. doi: 10.1258/phleb.2009.009061

Choi, J. S., Piao, Y., and Seo, T. S. (2013). Fabrication of a circular PDMS microchannel for constructing a three-dimensional endothelial cell layer. *Bioprocess Biosyst. Eng.* 36, 1871–1878. doi: 10.1007/s00449-013-0961-z

Chung, S., Sudo, R., Mack, P. J., Wan, C.-R., Vickerman, V., and Kamm, R. D. (2009). Cell migration into scaffolds under co-culture conditions in a microfluidic platform. *Lab Chip* 9, 269–275. doi: 10.1039/B807585A

Chwała, M., Szczeklik, W., Szczeklik, M., Aleksiejew - Kleszczynski, T., and Jagielska - Chwała, M. (2015). Varicose veins of lower extremities, hemodynamics and treatment methods. *Adv. Clin. Exp. Med.* 24, 5–14. doi: 10.17219/acem/31880

Connor, D. E., Cooley-Andrade, O., Goh, W. X., Ma, D. D. F., and Parsi, K. (2015). Detergent sclerosants are deactivated and consumed by circulating blood cells. *Eur. J. Vasc. Endovasc. Surg.* 49, 426–431. doi: 10.1016/j.ejvs.2014.12.029

Critello, C. D., Fiorillo, A. S., and Matula, T. J. (2017). Size of sclerosing foams prepared by ultrasound, mechanical agitation, and the handmade tessari method for treatment of varicose veins: sclerosing foams for treatment of varicose veins. *J. Ultrasound Med.* 36, 649–658. doi: 10.7863/ultra.16.02052

Eckmann, D. M. (2009). Polidocanol for endovenous microfoam sclerosant therapy. *Exp. Opin. Investig. Drugs* 18, 1919–1927. doi: 10.1517/13543780903376163

Gloviczki, P., Comerota, A. J., Dalsing, M. C., Eklof, B. G., Gillespie, D. L., Gloviczki, M. L., et al. (2011). The care of patients with varicose veins and associated chronic venous diseases: clinical practice guidelines of the society for vascular surgery and the American venous forum. *J. Vasc. Surg.* 53, 2S—48S. doi: 10.1016/j.jvs.2011.01.079

Goldman, M. P., Weiss, R. A., and Guex, J.-J. (2017). *Sclerotherapy: Treatment of Varicose and Telangiectatic Leg Veins*. Amsterdam: Elsevier.

Hamel-Desnos, C., Desnos, P., Wollmann, J.-C., Ouvry, P., Mako, S., and Allaert, F.-A. (2003). Evaluation of the efficacy of polidocanol in the form of foam compared with liquid form in sclerotherapy of the greater saphenous vein: initial results. *Dermatol. Surg.* 29, 1170–1175. doi: 10.1111/j.1524-4725.2003.29398.x

Hamel-Desnos, C., Ouvry, P., Benigni, J.-P., Boitelle, G., Schadeck, M., Desnos, P., et al. (2007). Comparison of 1% and 3% polidocanol foam in ultrasound guided sclerotherapy of the great saphenous vein: a randomised, double-blind trial with 2 year-follow-up. "The 3/1 Study." *Eur. J. Vasc. Endovasc. Surg.* 34, 723–729. doi: 10.1016/j.ejvs.2007.07.014

Hanwright, J., Zhou, J., Evans, G. M., and Galvin, K. P. (2005). Influence of surfactant on gas bubble stability. *Langmuir* 21, 4912–4920. doi: 10.1021/la0502894

Jia, X., Mowatt, G., Burr, J. M., Cassar, K., Cook, J., and Fraser, C. (2007). Systematic review of foam sclerotherapy for varicose veins. *Br. J. Surg*. 94, 925–936. doi: 10.1002/bjs.5891

Kim, S., Lee, H., Chung, M., and Jeon, N. L. (2013). Engineering of functional, perfusable 3D microvascular networks on a chip. *Lab. Chip* 13:1489. doi: 10.1039/c3lc41320a

Kruglyakov, P., Karakashev, S., Nguyen, A., and Vilkova, N. (2008). Foam drainage. *Curr. Opin. Colloid Interface Sci*. 13, 163–170. doi: 10.1016/j.cocis.2007.11.003

Larmignat, S., Vanderpool, D., Lai, H. K., and Pilon, L. (2008). Rheology of colloidal gas aphrons (microfoams). *Colloids Surf. Physicochem. Eng. Asp*. 322, 199–210. doi: 10.1016/j.colsurfa.2008.03.010

McAree, B., Ikponmwosa, A., Brockbank, K., Abbott, C., Homer-Vanniasinkam, S., and Gough, M. J. (2012). Comparative stability of sodium tetradecyl sulphate (std) and polidocanol foam: impact on vein damage in an *in-vitro* model. *Eur. J. Vasc. Endovasc. Surg*. 43, 721–725. doi: 10.1016/j.ejvs.2012.02.026

Nastasa, V., Samaras, K., Ampatzidis, C., Karapantsios, T. D., Trelles, M. A., Moreno-Moraga, J., et al. (2015). Properties of polidocanol foam in view of its use in sclerotherapy. *Int. J. Pharm*. 478, 588–596. doi: 10.1016/j.ijpharm.2014.11.056

Osei-Bonsu, K., Shokri, N., and Grassia, P. (2015). Foam stability in the presence and absence of hydrocarbons: From bubble- to bulk-scale. *Colloids Surf. Physicochem. Eng. Asp*. 481, 514–526. doi: 10.1016/j.colsurfa.2015.06.023

Ouvry, P., Allaert, F.-A., Desnos, P., and Hamel-Desnos, C. (2008). Efficacy of polidocanol foam versus liquid in sclerotherapy of the great saphenous vein: a multicentre randomised controlled trial with a 2-year follow-up. *Eur. J. Vasc. Endovasc. Surg*. 36, 366–370. doi: 10.1016/j.ejvs.2008.04.010

Parsi, K., Exner, T., Connor, D. E., Herbert, A., Ma, D. D. F., and Joseph, J. E. (2008). The lytic effects of detergent sclerosants on erythrocytes, platelets, endothelial cells and microparticles are attenuated by albumin and other plasma components *in vitro*. *Eur. J. Vasc. Endovasc. Surg*. 36, 216–223. doi: 10.1016/j.ejvs.2008.03.001

Peterson, J. D., and Goldman, M. P. (2011). An investigation into the influence of various gases and concentrations of sclerosants on foam stability. *Dermatol. Surg*. 37, 12–17. doi: 10.1111/j.1524-4725.2010.01832.x

Peterson, J. D., and Goldman, M. P. (2012). An investigation of side-effects and efficacy of foam-based sclerotherapy with carbon dioxide or room air in the treatment of reticular leg veins: a pilot study. *Phlebol. J. Venous Dis*. 27, 73–76. doi: 10.1258/phleb.2011.010073

Pries, A. R., Neuhaus, D., and Gaehtgens, P. (1992). Blood viscosity in tube flow: dependence on diameter and hematocrit. *Am. J. Physiol.-Heart Circ. Physiol*. 263, H1770–H1778. doi: 10.1152/ajpheart.1992.263.6.H1770

Raju, S., Cruse, G., Berry, M., Owen, S., Meydrech, E., and Neglen, P. (2004). Venous flow restriction: the role of vein wall motion in venous admixture. *Eur. J. Vasc. Endovasc. Surg*. 28, 182–192. doi: 10.1016/j.ejvs.2004.04.002

Rao, J., and Goldman, M. P. (2005). Stability of foam in sclerotherapy: differences between sodium tetradecyl sulfate and polidocanol and the type of connector used in the double-syringe system technique. *Dermatol. Surg*. 31, 19–22. doi: 10.1097/00042728-200501000-00004

Sandri, J. L., Barros, F. S., Pontes, S., Jacques, C., and Salles-Cunha, S. X. (1999). Diameter-reflux relationship in perforating veins of patients with varicose veins. *J. Vasc. Surg*. 30, 867–874.

Smith, P. C. (2009). Foam and liquid sclerotherapy for varicose veins. *Phlebology* 24, 62–72. doi: 10.1258/phleb.2009.09s007

Spiridon, M., and Corduneanu, D. (2017). Chronic venous insufficiency: a frequently underdiagnosed and undertreated pathology. *Ma Edica* 12, 59.

Star, P., Connor, D. E., and Parsi, K. (2018). Novel developments in foam sclerotherapy: Focus on Varithena® (polidocanol endovenous microfoam) in the management of varicose veins. *Phlebol. J. Venous Dis*. 33, 150–162. doi: 10.1177/0268355516687864

Tessari, L., Cavezzi, A., and Frullini, A. (2001). Preliminary experience with a new sclerosing foam in the treatment of varicose veins. *Dermatol. Surg*. 27, 58–60. doi: 10.1046/j.1524-4725.2001.00192.x

Tien, J. (2014). Microfluidic approaches for engineering vasculature. *Curr. Opin. Chem. Eng*. 3, 36–41. doi: 10.1016/j.coche.2013.10.006

Van Deurzen, B., Ceulen, R. P., Tellings, S. S., Van Der Geld, C., and Nijsten, T. (2011). Polidocanol concentration and time affect the properties of foam used for sclerotherapy. *Dermatol. Surg*. 37, 1448–1455. doi: 10.1111/j.1524-4725.2011.02095.x

Watkins, M. R., and Oliver, R. J. (2017). Physiochemical properties and reproducibility of air-based sodium tetradecyl sulphate foam using the Tessari method. *Phlebol. J. Venous Dis*. 32, 390–396. doi: 10.1177/0268355516655078

Wong, K., Chen, T., Connor, D. E., Behnia, M., and Parsi, K. (2015). Basic physiochemical and rheological properties of detergent sclerosants. *Phlebol. J. Venous Dis*. 30, 339–349. doi: 10.1177/0268355514529271

Conflict of Interest Statement: EB is in receipt of a Doctoral Training Partnership funded from EPSRC and Biocompatibles UK Ltd, a BTG International group company. AL, SJ, and VP are paid employees of Biocompatible UK Ltd.

The remaining authors declare that the research was conducted in the absence of any commercial or financial relationships that could be construed as a potential conflict of interest.

frontiers
in Bioengineering and Biotechnology

MINI REVIEW
published: 18 December 2018
doi: 10.3389/fbioe.2018.00197

Mimicking Epithelial Tissues in Three-Dimensional Cell Culture Models

Núria Torras [1†], María García-Díaz [1†], Vanesa Fernández-Majada [1*‡] and Elena Martínez [1,2,3*‡]

[1] Biomimetic Systems for Cell Engineering, Institute for Bioengineering of Catalonia, Barcelona Institute of Science and Technology, Barcelona, Spain, [2] Centro de Investigación Biomédica en Red, Madrid, Spain, [3] Department of Electronics and Biomedical Engineering, University of Barcelona, Barcelona, Spain

Edited by:
Massimo Alberti,
Agency for Science, Technology and Research (A*STAR), Singapore

Reviewed by:
Gopu Sriram,
Faculty of Dentistry, National University of Singapore, Singapore
Hyun Jung Kim,
University of Texas at Austin, United States

***Correspondence:**
Vanesa Fernández-Majada
vfernandez@ibecbarcelona.eu
Elena Martínez
emartinez@ibecbarcelona.eu

† These authors have contributed equally to this work and shared first authorship

‡ These authors have contributed equally to this work and shared corresponding authorship

Specialty section:
This article was submitted to Tissue Engineering and Regenerative Medicine,
a section of the journal Frontiers in Bioengineering and Biotechnology

Received: 28 September 2018
Accepted: 30 November 2018
Published: 18 December 2018

Citation:
Torras N, García-Díaz M, Fernández-Majada V and Martínez E (2018) Mimicking Epithelial Tissues in Three-Dimensional Cell Culture Models.
Front. Bioeng. Biotechnol. 6:197.
doi: 10.3389/fbioe.2018.00197

Epithelial tissues are composed of layers of tightly connected cells shaped into complex three-dimensional (3D) structures such as cysts, tubules, or invaginations. These complex 3D structures are important for organ-specific functions and often create biochemical gradients that guide cell positioning and compartmentalization within the organ. One of the main functions of epithelia is to act as physical barriers that protect the underlying tissues from external insults. *In vitro*, epithelial barriers are usually mimicked by oversimplified models based on cell lines grown as monolayers on flat surfaces. While useful to answer certain questions, these models cannot fully capture the *in vivo* organ physiology and often yield poor predictions. In order to progress further in basic and translational research, disease modeling, drug discovery, and regenerative medicine, it is essential to advance the development of new *in vitro* predictive models of epithelial tissues that are capable of representing the *in vivo*-like structures and organ functionality more accurately. Here, we review current strategies for obtaining biomimetic systems in the form of advanced *in vitro* models that allow for more reliable and safer preclinical tests. The current state of the art and potential applications of self-organized cell-based systems, organ-on-a-chip devices that incorporate sensors and monitoring capabilities, as well as microfabrication techniques including bioprinting and photolithography, are discussed. These techniques could be combined to help provide highly predictive drug tests for patient-specific conditions in the near future.

Keywords: epithelial barriers, 3D cell culture models, organoids, organ-on-a-chip, microengineered tissues, biofabrication, drug screening, disease modeling

INTRODUCTION

Epithelial tissues are composed of cells laid out in sheets with strong intercellular bonds that form physical barriers that line the cavities of major organs (lung, skin, intestine, etc.) and protect them from external physical, chemical, and microbial insults. Epithelial cells are polarized, i.e., their apical side, facing the lumen of the organ, differs in shape and composition from the basolateral side. Epithelial cells rest on a basement membrane that acts as a growth support and as a selectively permeable layer. Besides protection, the main functions of epithelial cells include secretion, selective absorption, transcellular transport, and detection of sensation. Epithelia are actively and rapidly renewing tissues due to the presence of fast dividing adult stem cells (Crosnier et al., 2006; Vrana et al., 2013). In addition, they are a major site for carcinogenesis (Beyer et al., 2013).

Many epithelial tissues have three-dimensional (3D) spatial features such as tissue widens, compact folds, invaginations, evaginations, and wavy morphologies. Such complex structures might generate biochemical factor gradients that drive the compartmentalization of the different cell types and are key determinants for organ-specific functions. Some examples are acini in the mammary gland, alveoli in the lung, Vogt palisades in the cornea, rete ridges in the skin, and crypt-villus structures in the small intestine (**Figure 1**). The latter are triggered by mechanical forces during morphogenesis and generate gradients of biochemical signals that spatially segregate the various tissue-forming cell types (Bollenbach and Heisenberg, 2015; Shyer et al., 2015).

Functional *in vitro* models of epithelial layers are key elements to basic research, disease modeling, drug discovery, and tissue replacement (Stange and Clevers, 2013). There is an increasing demand for *in vitro* models that are capable of capturing the complex epithelial architecture of tissues *in vivo*. Conventional preclinical models are typically two-dimensional (2D) or rely on animal models. While 2D models can provide useful information on early biological responses and are suitable for high-throughput drug screening, they have poor predictive capabilities. And while existing animal models can capture the complex physiology and interactions of *in vivo* tissues, they often fail to predict human responses due to species-specific differences. In addition, their use is often restricted due to ethical concerns. In an effort to overcome these limitations and as a kind of paradigm shift, 3D human models have emerged that are capable of capturing complex physiological responses *in vitro* (Griffith and Swartz, 2006). These new models rely on advances in cell biology, micro-engineering, biomaterials, and biofabrication.

In this study, we review the main technological strategies currently used to create 3D complex models of epithelial tissues: self-organized cell cultures, lab-on-chip devices, engineered microtissues, and various combinations of these. As the focus is typically placed on mimicking the epithelial tissue barrier properties *in vitro*, the studies reviewed here all focused on the epithelial compartment and the underlying matrix. We found that depending on the application, these engineered approaches can be extended to provide the 3D models with immunocompetent properties, microbiome, or vascularity.

SELF-ORGANIZED 3D CELL CULTURES

In contrast to 2D cell culture models where cells usually grow as monolayers on flat substrates, cells in 3D culture systems self-organize as 3D aggregates, either employing a matrix as a physical support or in a scaffold-free manner. Commonly used matrices include both biologically- and synthetically-derived hydrogels such as Matrigel®, polyethylene glycol, or poly(vinyl alcohol) (Tibbitt and Anseth, 2009; Rimann and Graf-Hausner, 2012; Fang and Eglen, 2017). Based on the type of cells and their cellular organization, there are currently two types of 3D self-organized cell culture models: spheroid and organoid models. Spheroids do not need a supportive matrix to grow and are more irregularly arranged cell aggregates with a rather poor organization of relevant tissue. Organoids, on the other hand, originate from stem cells, which give rise to different organ-specific cell types and ensure the culture's high self-renewal capabilities. Organoids require a matrix to grow and possess a more ordered assembly that typically recapitulates the 3D complex tissue structures. Both 3D models have gained recent popularity as new *in vitro* tools for drug testing, disease modeling, and tissue engineering (Fang and Eglen, 2017).

Essentially, spheroids are clumps of poorly organized cells that have become a popular model in oncology research. Due to their solid spherical morphology, both oxygen and nutrients decrease toward the center, decreasing cell viability from the outer cell layers to their hypoxic and necrotic cores (Lin and Chang, 2008) (**Figure 1**). This feature very closely recapitulates the biochemical and cellular conditions found in most solid tumors. Tumor-derived spheroids, or tumor-spheres, have been generated from primary cancer cells (including cancer stem cells) derived from various sources such as glioma, breast, colon, ovary, and prostate tumors (Ishiguro et al., 2017). In addition to their 3D nature, the methods for generating spheroids are simple, cost-effective, highly reproducible, and adaptable, which has favored their use as *in vitro* models in the drug discovery industry in a semi-high throughput format (Youn et al., 2006; Tung et al., 2011; Vinci et al., 2012). Despite these benefits, spheroids are only poor *in vitro* models of healthy epithelial tissues, mainly due to their lack of self-renewal and differentiation properties as well as their inability to organize in tissue-like structures.

Organoids are highly organized 3D cell cultures that originated from organ specific or pluripotent stem cells with self-renewal and differentiation capabilities. When embedded in a suitable matrix and cultured with specific biochemical factors that mimic the *in vivo* stem cell niche, stem cells possess an intrinsic ability to differentiate and self-organize into 3D structures that resemble the *in vivo* organ. The culture conditions needed to generate organoids derived from intestine, skin, lung, liver, and pancreas, among others organs, employing a wealth of different cells sources from different species, are known (Rossi et al., 2018). Due to their *in vivo* resemblance in cell composition, structure and function, organoids have become the gold standard *in vitro* culture method in basic and translational epithelia research, when modeling patient-specific diseases, or as a source of autologous tissue transplantation (Yui et al., 2012; Dekkers et al., 2013; Middendorp et al., 2014).

While organoid technology undoubtedly represents a scientific breakthrough in epithelial tissue research, organoids still do not fully recapitulate all characteristics of *in vivo* epithelia. A major drawback is their 3D closed geometry, which complicates access to specific organoid compartments. For instance, the inaccessibility of the organoid-analog lumen in intestinal organoids hampers the use of conventional assays and instrumentation designed for high throughput screening studies on nutrient transport, drug absorption and delivery, or microbe-epithelium interactions (Wilson et al., 2015). In addition, the use of conventional microscopy for experimental data collection is complicated by the fact that organoids are cultured while embedded in a 3D hydrogel matrix. New strategies have been

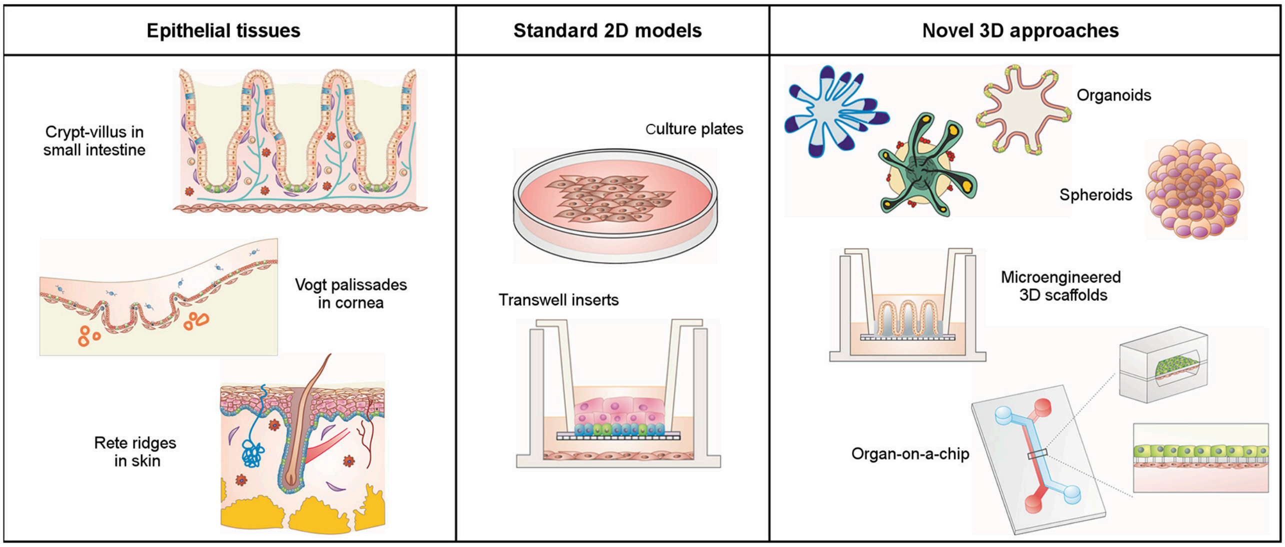

FIGURE 1 | Schematic representation of epithelial tissues with their native 3D architecture, conventional 2D cell cultures, and novel 3D cell culture approaches.

proposed to overcome these difficulties, with organoids "opened up" into flat epithelial monolayers that provide unhindered access to the luminal and basolateral compartments (Moon et al., 2014). In addition, this culture configuration has the potential to control the spatio-temporal delivery of biochemical factors through porous materials mimicking the basement membrane. When combined with 3D structures mimicking the epithelial architecture, this strategy could guide epithelial cell organization in an *in vivo*-like manner, leading to advanced organotypic 3D models (Wang et al., 2017). This will be aided by the continuing progress being made in microfluidics, biomaterials, and microfabrication techniques toward advanced 3D models.

LAB-ON-A-CHIP DEVICES MIMICKING EPITHELIAL TISSUES

Conventional approaches for differentiated epithelial cell culture are based on Transwell® systems (Rodriguez-Boulan et al., 2005) where cells form polarized monolayers on porous membranes creating independent apical and basolateral compartments, thus mimicking some basic properties of *in vivo* epithelial tissues (**Figure 1**). However, the highly dynamic *in vivo* environments are not represented by these static approaches (Mammoto et al., 2013). The organ-on-a-chip technology facilitates physiologically more relevant conditions and provides cells with physical and chemical stimuli by perfusing media in a laminar flow (Gayer and Basson, 2009; Cimetta et al., 2010; Thuenauer and Rodriguez-boulan, 2015). To promote cell polarization, organ-on-a-chip devices (also called microphysiological systems) usually include a porous membrane to separate two microfluidic channels. Different cells can be co-cultured on the opposite sides of this membrane, which provides a tissue-tissue interface with independent access to the cell culture chambers (**Figure 1**). Monitoring of the dynamic cellular responses can be achieved by incorporating biosensors and electrodes into the microfluidic device (Henry et al., 2017; Skardal et al., 2017), while its optical transparency enables direct visualization by conventional microscopy.

Several lab-on-a-chip devices, capable of representing the majority of epithelial barriers in the human body, have been designed, and kept alive and functional for several weeks. These devices can range from simple micrometer-sized chambers that simulate a specific tissue function to sophisticated "human-on-a-chip" or multi-organ microfluidic frameworks that recapitulate even complex tissue-tissue interactions (Rogal et al., 2017). One of the pioneering systems capable of fully reproducing the complex physiological functionality was the lung-on-a-chip device (Huh et al., 2010). This chip contained two apposed microchannels separated by a thin and flexible porous membrane where pulmonary epithelial cells and capillary endothelial cells were co-cultured. Cells were mechanically stimulated by the cyclic strain of breathing movements. This lung-on-a-chip system has been used for modeling respiratory diseases such as chronic obstructive pulmonary disease (Benam et al., 2016) or lung cancer (Hassell et al., 2017). Using a similar design, intestinal peristaltic movements could be mimicked with a gut-on-a-chip platform (Kim et al., 2012, 2015; Kim and Ingber, 2013). In this case, intestinal cells were exposed to fluid flow and peristaltic motion that induced villi formation and cell differentiation. This gut-on-a-chip device, along with other intestinal chips such as HuMiX, has been used to recapitulate the interplay between intestinal microbes and the epithelium (Kim et al., 2015; Shah et al., 2016). Innovative perfusable vascularized skin-on-a-chip models (Wufuer et al., 2016; Mori et al., 2017) or immune-competent models (Ramadan and Ting, 2016) have been proposed, both aiming to create more physiologically relevant skin equivalents for drug screening and disease modeling

(Abaci et al., 2015; Alberti et al., 2017; van den Broek et al., 2017; Sriram et al., 2018).

A unique advantage of the organ-on-a-chip technology is its inherent ability to integrate multiple organ functions into a closed microfluidic system, which facilitates a better recapitulation *in vitro* of the human metabolism and physiology. For example, the first-pass metabolism of oral drugs can be reproduced on a gut-liver chip (Choe et al., 2017; Lee et al., 2017). "Multi-organ-on-a-chip" devices have been developed that consist of several interconnected chambers, each representing different organs of the body. These sophisticated models aim to improve predictive capabilities with regard to the spatial distribution and temporal evolution of compounds, addressing issues such as targeting, safety, and toxicity in a single device (Abaci et al., 2015; Maschmeyer et al., 2015; Skardal et al., 2017).

Although organ-on-chip devices represent a huge leap toward the generation of improved *in vitro* epithelia models, challenges such as the functional scaling or the interaction with stromal components remain (Ronaldson-Bouchard and Vunjak-Novakovic, 2018). In addition, the epithelial basement membrane is usually mimicked by a porous membrane that neither possesses the physicochemical nor mechanical properties of the native tissue matrix. Current developments try to address these limitations by exploiting advances in biomaterials and microfabrication techniques. As recent examples, full-thickness skin-on-a-chip devices used dermal matrices to represent the 3D complexity of the skin (Schimek et al., 2018; Sriram et al., 2018) and gut-on-a-chip designs included a porous scaffold that mimicked the 3D villus architecture of the small intestine (Costello et al., 2017; Shim et al., 2017). On the other hand, the combination of microfluidics with organoids from human induced pluripotent stem cells (iPSCs) or patient biopsies would likely have major implications for personalized medicine, as already exemplified by intestinal chips (Kasendra et al., 2018; Workman et al., 2018).

ENGINEERED EPITHELIAL TISSUES AND MICROTISSUES

Organoid technology has revealed the key role played by the matrix in guiding a cell's intrinsic self-organizing ability when forming functional tissues. However, epithelial cells are cultured on flat porous membranes of hard polymers on both Transwell® and lab-on-a-chip devices. Advances in soft biomaterials and microfabrication techniques provide new alternatives to achieve a better representation of the complex basement membrane in native epithelial tissues (Abbott, 2003; Lutolf et al., 2009; Murphy and Atala, 2014).

3D bioprinting is a relatively recent and versatile manufacturing technique that builds tissues and microtissues layer by layer using bioinks from cell-laden materials (Derby, 2012; Vijayavenkataraman et al., 2018). Bioprinted tissue constructs that faithfully recapitulate the architecture of native tissues such as skin and cornea epithelia can be fabricated in a highly reproducible manner (He et al., 2018; Sorkio et al., 2018). This approach can also be used to generate complex tubular structures such as renal proximal tubules and trachea implants (Homan et al., 2016; Bae et al., 2018). Despite its advantages, 3D bioprinting is a complex procedure that still faces many challenges such as improving cell viability and density, decreasing printing times, and increasing the printed tissue dimensions (Chang et al., 2011; Murphy and Atala, 2014). Recent advances led to the development of new bioinks, e.g., cell-derived and decellularized extracellular matrices (Fitzpatrick and McDevitt, 2015; Gopinathan and Noh, 2018) or spheroids used as individual printed units to promote *in vitro* assembly (Mironov et al., 2009; Moroni et al., 2018). Bioprinting has also evolved into a 4D technique that aims at the fabrication of time-evolving tissues by employing programmable biomaterials (Qi et al., 2013).

Lithography-based microfabrication techniques, including replica molding and photolithography, have become the standard in microelectronics to manufacture structures at cellular and subcellular scales (Whitesides, 2003). Nowadays, their application has been extended to include soft materials and to mimic 3D geometries in epithelial tissues. For instance, replica molding has been used to generate 3D microstructures that mimic the villus protrusions of the small intestine on poly(lactic-co-glycol acid) and collagen (Sung et al., 2011; Yu et al., 2012; Wang et al., 2017). Drug permeability assays have demonstrated the benefits of including the 3D tissue architecture for better predictions of the permeability found *in vivo* (Yu et al., 2012). However, replica molding of hydrogels involves a sequence of molding and demolding steps that renders this process not very amenable for mass production (Nelson et al., 2006; Sung et al., 2011; Pan et al., 2013; Cerchiari et al., 2015). In contrast, light-based polymerization approaches such as mask-based photolithography and stereolithography (SLA) can produce 3D microstructures on soft polymers in a fast, robust, and moldless manner (Tsang et al., 2007; Moroni et al., 2018). When combined with cells, the use of photoinitiator molecules and UV light might compromise cell viability, which has led to the development of new photoinitiators that are sensitive to visible light. 3D microengineered tissues generated by these techniques have been introduced into microfluidic devices or Transwell® inserts to be used as *in vitro* testing platforms (Yu et al., 2012; Costello et al., 2017; García Castaño, 2017). Recent publications also emphasized the potential of interfacing light-based microfabrication techniques with organoids to create enhanced organomimetic tissues (Schneeberger et al., 2017).

SUMMARY AND FUTURE PERSPECTIVES

New cell culture platforms that incorporate the unique and complex 3D architectures of epithelial tissues promise *in vitro* models with unprecedented tissue functionality. This review has highlighted recent advances in biology, biomaterials, and microfabrication techniques that could prove pivotal for the creation of these organotypic models. Advances in stem cell biology have led to the generation of organoids that recapitulate the *in vivo* 3D tissue-structure and functionality, which in itself represents a giant step toward potential applications of *in vitro* assays in the medical field (Rossi et al., 2018). For example, forskolin-induced swelling in intestinal organoids is now used as an *in vitro* test for assessing drug response in cystic fibrosis patients (Dekkers et al., 2013). In addition, current developments to establish organoids from human iPSCs in combination with novel technologies for gene editing could pave the way to personalized medicine applications. iPSC-derived organoids are used to model human organ development and disease, to test therapeutic compounds, and in cell transplantation (Shi et al., 2017). Furthermore, the 3D tissue-like cell organization provided by organoids can also be exploited to improve the functionality of organ-on-a-chip devices. By increasing the complexity of the cellular models, organ-on-a-chip approaches offer controlled and relatively simple microenvironments of sufficient biological complexity to gain greater insight into the biological mechanisms that drive disease (Bhatia and Ingber, 2014). They possess a great potential to transform drug discovery (Miranda et al., 2018) by providing human cell-based models that are capable of predicting drug delivery through epithelial barriers. In fact, pharmaceutical and biotechnological companies have already begun to incorporate these systems into their preclinical assays in an effort to improve their predictive capabilities (Ahadian et al., 2018; Cirit and Stokes, 2018). However, a better standardization and more user-friendly setups with high-throughput capabilities are needed for a broader acceptance by both industry and regulatory authorities. In this context, the development of new biofabrication techniques together with advances in biological and biomaterial research should soon allow for the development of engineered tissues and microtissues. The advantages of these structures as *in vitro* models of epithelial tissues are 2-fold: (1) they would allow the integration of non-epithelial elements that are essential for tissue function such as the immune, mesenchymal, and vascular systems (Kirkpatrick and Fuchs, 2011; Vrana et al., 2013; Battiston et al., 2014), and (2) microtissues can be easily interfaced with well plate culture formats that promise high-throughput capabilities which should promote their acceptance in the pharmaceutical and medical industries. Finally, although the key technologies reviewed here seem capable of jointly generating a set of new tools that are capable of a more accurate representation of epithelia physiological functions, the targeted applications should maintain a manageable level of complexity to provide real and meaningful impact in the biomedical and biotechnological arena.

AUTHOR CONTRIBUTIONS

MG-D and NT wrote the manuscript and contributed equally to this work. VF-M and EM wrote and edited the manuscript and share corresponding authorship.

FUNDING

This work was supported by European Union's Horizon 2020 ERC grant agreement No 647863 (COMIET), the CERCA Program/Generalitat de Catalunya (2017-SGR-1079), and the Spanish Ministry of Economy and Competitiveness (TEC2014-51940-C2-2-R, TEC2017-83716-C2-1-R and the Severo Ochoa Program for Centers of Excellence in R&D 2016-2019). MG-D thanks the BEST Postdoctoral Program, funded by the European Commission under Horizon 2020's Marie Skłodowska-Curie Actions COFUND scheme (Grant Agreement no. 712754) and by the Severo Ochoa program of the Spanish Ministry of Science and Competitiveness [Grant SEV-2014-0425 (2015-2019)]. The results presented here reflect only the views of the authors; the European Commission is not responsible for any use that may be made of the information it contains.

ACKNOWLEDGMENTS

The authors thank Aina Abad Lazaro for proofreading the manuscript.

REFERENCES

Abaci, H. E., Gledhill, K., Guo, Z., Christiano, A. M., and Shuler, M. L. (2015). Pumpless microfluidic platform for drug testing on human skin equivalents. *Lab Chip* 15, 882–888. doi: 10.1039/C4LC00999A

Abbott, A. (2003). Biology' s new dimension. *Nature* 424, 870–872. doi: 10.1038/424870a

Ahadian, S., Civitarese, R., Bannerman, D., Mohammadi, M. H., Lu, R., Wang, E., et al. (2018). Organ-on-a-chip platforms: a convergence of advanced materials, cells, and microscale technologies. *Adv. Healthc. Mater.* 7, 1–53. doi: 10.1002/adhm.201700506

Alberti, M., Dancik, Y., Sriram, G., Wu, B., Teo, Y. L., Feng, Z., et al. (2017). Multi-chamber microfluidic platform for high-precision skin permeation testing. *Lab Chip* 17, 1625–1634. doi: 10.1039/C6LC01574C

Bae, S. W., Lee, K. W., Park, J. H., Lee, J. H., Jung, C. R., Yu, J. J., et al. (2018). 3D bioprinted artificial trachea with epithelial cells and chondrogenic-differentiated bone marrow-derived mesenchymal stem cells. *Int. J. Mol. Sci.* 19, 1–14. doi: 10.3390/ijms19061624

Battiston, K. G., Cheung, J. W., Jain, D., and Santerre, J. P. (2014). Biomaterials in co-culture systems: towards optimizing tissue integration and cell signaling within scaffolds. *Biomaterials* 35, 4465–4476. doi: 10.1016/j.biomaterials.2014.02.023

Benam, K. H., Villenave, R., Lucchesi, C., Varone, A., Hubeau, C., Lee, H. H., et al. (2016). Small airway-on-a-chip enables analysis of human lung inflammation and drug responses *in vitro*. *Nat. Methods* 13, 151–157. doi: 10.1038/nmeth.3697

Beyer, I., van Rensburg, R., and Lieber, A. (2013). Overcoming physical barriers in cancer therapy. *Tissue Barriers.* 1, 1–6. doi: 10.4161/tisb.23647

Bhatia, S. N., and Ingber, D. E. (2014). Microfluidic organs-on-chips. *Nat. Biotechnol.* 32, 760–772. doi: 10.1038/nbt.2989

Bollenbach, T., and Heisenberg, C. P. (2015). Gradients are shaping up. *Cell* 161, 431–432. doi: 10.1016/j.cell.2015.04.009

Cerchiari, A., Garbe, J. C., Todhunter, M. E., Jee, N. Y., Pinney, J. R., LaBarge, M. A., et al. (2015). Formation of spatially and geometrically controlled three-dimensional tissues in soft gels by sacrificial micromolding. *Tissue Eng. Part C Methods* 21, 541–547. doi: 10.1089/ten.tec.2014.0450

Chang, C. C., Boland, E. D., Williams, S. K., and Hoying, J. B. (2011). Direct-write bioprinting three-dimensional biohybrid systems for future regenerative therapies. *J. Biomed. Mater. Res. B* 98, 160–170. doi: 10.1002/jbm.b.31831

Choe, A., Ha, S. K., Choi, I., Choi, N., and Sung, J. H. (2017). Microfluidic Gut-liver chip for reproducing the first pass metabolism. *Biomed. Microdev.* 19, 1–11. doi: 10.1007/s10544-016-0143-2

Cimetta, E., Cannizzaro, C., James, R., Biechele, T., Moon, R. T., Elvassore, N., et al. (2010). Microfluidic device generating stable concentration gradients for long term cell culture: Application to Wnt3a regulation of β-catenin signaling. *Lab Chip* 10, 3277–3283. doi: 10.1039/c0lc00033g

Cirit, M., and Stokes, C. L. (2018). Maximizing the impact of microphysiological systems with: *in vitro - In vivo* translation. *Lab Chip* 18, 1831–1837. doi: 10.1039/C8LC00039E

Costello, C. M., Phillipsen, M. B., Hartmanis, L. M., Kwasnica, M. A., Chen, V., Hackam, D., et al. (2017). Microscale Bioreactors for *in situ* characterization of GI epithelial cell physiology. *Sci. Rep.* 7:12515. doi: 10.1038/s41598-017-12984-2

Crosnier, C., Stamataki, D., and Lewis, J. (2006). Organizing cell renewal in the intestine: stem cells, signals and combinatorial control. *Nat. Rev. Genet.* 7, 349–359. doi: 10.1038/nrg1840

Dekkers, J. F., Wiegerinck, C. L., De Jonge, H. R., Bronsveld, I., Janssens, H. M., de Winter-de Groot, K. M., et al. (2013). A functional CFTR assay using primary cystic fibrosis intestinal organoids. *Nat. Med.* 19, 939–945. doi: 10.1038/nm.3201

Derby, B. (2012). Printing and prototyping of tissues and scaffolds. *Science (80-.).* 338, 921–927. doi: 10.1126/science.1226340

Fang, Y., and Eglen, R. M. (2017). Three-dimensional cell cultures in drug discovery and development. *SLAS Discov.* 22, 456–472. doi: 10.1177/1087057117696795

Fitzpatrick, L. E., and McDevitt, T. C. (2015). Cell-derived matrices for tissue engineering and regenerative medicine applications. *Biomater. Sci.* 3, 12–24. doi: 10.1039/C4BM00246F

García Castaño, A. (2017). *Engineering Poly (Ethylene Glycol) Diacrylate-Based Microstructures to Develop an in vitro Model of Small Intestintal Epithelium*. Thesis, Universitat de Barcelona.

Gayer, C. P., and Basson, M. D. (2009). The effects of mechanical forces on intestinal physiology and pathology. *Cell Signal.* 21, 1237–1244. doi: 10.1016/j.cellsig.2009.02.011

Gopinathan, J., and Noh, I. (2018). Recent trends in bioinks for 3D printing. *Biomater. Res.* 22, 1–15. doi: 10.1186/s40824-018-0122-1

Griffith, L. G., and Swartz, M. A. (2006). Capturing complex 3D tissue physiology *in vitro*. *Nat. Rev. Mol. Cell Biol.* 7, 211–224. doi: 10.1038/nrm1858

Hassell, B. A., Goyal, G., Lee, E., Sontheimer-phelps, A., Levy, O., Chen, C. S., et al. (2017). Human organ chip models recapitulate orthotopic lung cancer growth, therapeutic responses, and tumor dormancy *in vitro* human organ chip models recapitulate orthotopic lung cancer growth, therapeutic responses, and tumor dormancy *in vitro*. *Cell Rep.* 21, 508–516. doi: 10.1016/j.celrep.2017.09.043

He, P., Zhao, J., Zhang, J., Li, B., Gou, Z., Gou, M., et al. (2018). Bioprinting of skin constructs for wound healing. *Burn. Trauma* 6, 5. doi: 10.1186/s41038-017-0104-x

Henry, O., Villenave, R., Cronce, M., Leineweber, W., Benz, M., and Ingber, D. (2017). Organs-on-chips with integrated electrodes for Trans-Epithelial Electrical Resistance (TEER) measurements of human epithelial barrier function. *Lab Chip* 17, 2264–2271. doi: 10.1039/C7LC00155J

Homan, K. A., Kolesky, D. B., Skylar-Scott, M. A., Herrmann, J., Obuobi, H., Moisan, A., et al. (2016). Bioprinting of 3D Convoluted renal proximal tubules on perfusable chips. *Sci. Rep.* 6:34845. doi: 10.1038/srep34845

Huh, D., Matthews, B. D., Mammoto, A., Montoya-Zavala, M., Hsin, H. Y., and Ingber, D. E. (2010). Reconstituting organ-level lung functions on a chip. *Science* 328, 1662–1668 doi: 10.1126/science.1188302

Ishiguro, T., Ohata, H., Sato, A., Yamawaki, K., Enomoto, T., and Okamoto, K. (2017). Tumor-derived spheroids: relevance to cancer stem cells and clinical applications. *Cancer Sci.* 108, 283–289. doi: 10.1111/cas.13155

Kasendra, M., Tovaglieri, A., Sontheimer-Phelps, A., Jalili-Firoozinezhad, S., Bein, A., Chalkiadaki, A., et al. (2018). Development of a primary human Small Intestine-on-a-Chip using biopsy-derived organoids. *Sci. Rep.* 8, 1–14. doi: 10.1038/s41598-018-21201-7

Kim, H. J., Huh, D., Hamilton, G., and Ingber, D. E. (2012). Human gut-on-a-chip inhabited by microbial flora that experiences intestinal peristalsis-like motions and flow. *Lab Chip* 12, 2165–2174. doi: 10.1039/c2lc40074j

Kim, H. J., and Ingber, D. E. (2013). Gut-on-a-Chip microenvironment induces human intestinal cells to undergovillus differentiation. *Integr. Biol.* 5, 1130–1140. doi: 10.1039/c3ib40126j

Kim, H. J., Li, H., Collins, J. J., and Ingber, D. E. (2015). Contributions of microbiome and mechanical deformation to intestinal bacterial overgrowth and inflammation in a human gut-on-a-chip. *Proc. Natl. Acad. Sci. U.S.A.* 113: 201522193. doi: 10.1073/pnas.1522193112

Kirkpatrick, C. J., and Fuchs, S. U. (2011). Co-culture systems for vascularization - Learning from nature. *Adv. Drug Deliv. Rev.* 63, 291–299. doi: 10.1016/j.addr.2011.01.009

Lee, D. W., Ha, S. K., Choi, I., and Sung, J. H. (2017). 3D gut-liver chip with a PK model for prediction of first-pass metabolism. *Biomed. Microdevices* 19:100. doi: 10.1007/s10544-017-0242-8

Lin, R. Z., and Chang, H. Y. (2008). Recent advances in three-dimensional multicellular spheroid culture for biomedical research. *Biotechnol. J.* 3, 1172–1184. doi: 10.1002/biot.200700228

Lutolf, M. P., Gilbert, P. M., and Blau, H. M. (2009). Designing materials to direct stem-cell fate. *Nature* 462, 433–441. doi: 10.1038/nature08602

Mammoto, T., Mammoto, A., and Ingber, D. E. (2013). Mechanobiology and developmental control. *Annu. Rev. Cell Dev. Biol.* 29, 27–61. doi: 10.1146/annurev-cellbio-101512-122340

Maschmeyer, I., Lorenz, A. K., Schimek, K., Hasenberg, T., Ramme, A. P., Hübner, J., et al. (2015). A four-organ-chip for interconnected long-term co-culture of human intestine, liver, skin and kidney equivalents. *Lab Chip* 15, 2688–2699. doi: 10.1039/C5LC00392J

Middendorp, S., Schneeberger, K., Wiegerinck, C. L., Mokry, M., Akkerman, R. D. L., Van Wijngaarden, S., et al. (2014). Adult stem cells in the small intestine are intrinsically programmed with their location-specific function. *Stem Cells* 32, 1083–1091. doi: 10.1002/stem.1655

Miranda, C. C., Fernandes, T., Diogo, M., and Cabral, J. (2018). Towards multi-organoid systems for drug screening applications. *Bioengineering* 5:49. doi: 10.3390/bioengineering5030049

Mironov, V., Visconti, R. P., Kasyanov, V., Forgacs, G., Drake, C. J., and Markwald, R. R. (2009). Biomaterials Organ printing : tissue spheroids as building blocks q. *Biomaterials* 30, 2164–2174. doi: 10.1016/j.biomaterials.2008.12.084

Moon, C., Vandussen, K. L., Miyoshi, H., and Stappenbeck, T. S. (2014). Development of a primary mouse intestinal epithelial cell monolayer culture system to evaluate factors that modulate IgA transcytosis. *Mucosal Immunol.* 7, 818–828. doi: 10.1038/mi.2013.98

Mori, N., Morimoto, Y., and Takeuchi, S. (2017). Skin integrated with perfusable vascular channels on a chip. *Biomaterials* 116, 48–56. doi: 10.1016/j.biomaterials.2016.11.031

Moroni, L., Burdick, J. A., Highley, C., Lee, S. J., Morimoto, Y., Takeuchi, S., et al. (2018). Biofabrication strategies for 3D *in vitro* models and regenerative medicine. *Nat. Rev. Mater.* 3, 21–37. doi: 10.1038/s41578-018-0006-y

Murphy, S. V., and Atala, A. (2014). 3D bioprinting of tissues and organs. *Nat. Biotechnol.* 32, 773–785. doi: 10.1038/nbt.2958

Nelson, C. M., Vanduijn, M. M., Inman, J. L., Fletcher, D. A., and Bissell, M. J. (2006). Tissue geometry determines sites of mammary branching morphogenesis in organotypic cultures. *Science* 314, 298–301. doi: 10.1126/science.1131000

Pan, J., Yung Chan, S., Common, J. E., Amini, S., Miserez, A., Birgitte Lane, E., et al. (2013). Fabrication of a 3D hair follicle-like hydrogel by soft lithography. *J. Biomed. Mater. Res. Part A* 101, 3159–3169. doi: 10.1002/jbm.a.34628

Qi, H., Ghodousi, M., Du, Y., Grun, C., Bae, H., Yin, P., et al. (2013). DNA-directed self-assembly of shape-controlled hydrogels. *Nat. Commun.* 4, 1–10. doi: 10.1038/ncomms3275

Ramadan, Q., and Ting, F. C. (2016). *In vitro* micro-physiological immune-competent model of the human skin. *Lab Chip* 16, 1899–1908. doi: 10.1039/C6LC00229C

Rimann, M., and Graf-Hausner, U. (2012). Synthetic 3D multicellular systems for drug development. *Curr. Opin. Biotechnol.* 23, 803–809. doi: 10.1016/j.copbio.2012.01.011

Rodriguez-Boulan, E., Kreitzer, G., and Müsch, A. (2005). Organization of vesicular trafficking in epithelia. *Nat. Rev. Mol. Cell Biol.* 6, 233–247. doi: 10.1038/nrm1593

Rogal, J., Probst, C., and Loskill, P. (2017). Integration concepts for multi-organ chips: how to maintain flexibility?! *Future Sci. OA* 3: FSO180. doi: 10.4155/fsoa-2016-0092

Ronaldson-Bouchard, K., and Vunjak-Novakovic, G. (2018). Organs-on-a-Chip: a fast track for engineered human tissues in drug development. *Cell Stem Cell* 22, 310–324. doi: 10.1016/j.stem.2018.02.011

Rossi, G., Manfrin, A., and Lutolf, M. P. (2018). Progress and potential in organoid research. *Nat. Rev. Genet.* 19, 671–687. doi: 10.1038/s41576-018-0051-9

Schimek, K., Hsu, H. H., Boehme, M., Kornet, J., Marx, U., Lauster, R., et al. (2018). Bioengineering of a full-thickness skin equivalent in a 96-well insert format for substance permeation studies and organ-on-a-chip applications. *Bioengineering* 5:43. doi: 10.3390/bioengineering5020043

Schneeberger, K., Spee, B., Costa, P., Sachs, N., Clevers, H., and Malda, J. (2017). Converging biofabrication and organoid technologies: The next frontier in hepatic and intestinal tissue engineering? *Biofabrication* 9:013001. doi: 10.1088/1758-5090/aa6121

Shah, P., Fritz, J. V., Glaab, E., Desai, M. S., Greenhalgh, K., Frachet, A., et al. (2016). A microfluidics-based *in vitro* model of the gastrointestinal human-microbe interface. *Nat. Commun.* 7: 11535. doi: 10.1038/ncomms 11535

Shi, Y., Inoue, H., Wu, J. C., and Yamanaka, S. (2017). Induced pluripotent stem cell technology: a decade of progress. *Nat. Rev. Drug Discov.* 16, 115–130. doi: 10.1038/nrd.2016.245

Shim, K. Y., Lee, D., Han, J., Nguyen, N. T., Park, S., and Sung, J. H. (2017). Microfluidic gut-on-a-chip with three-dimensional villi structure. *Biomed. Microdevices* 19:37. doi: 10.1007/s10544-017-0179-y

Shyer, A. E., Huycke, T. R., Lee, C., Mahadevan, L., and Tabin, C. J. (2015). Bending gradients: how the intestinal stem cell gets its home. *Cell* 161, 569–580. doi: 10.1016/j.cell.2015.03.041

Skardal, A., Murphy, S. V., Devarasetty, M., Mead, I., Kang, H. W., Seol, Y. J., et al. (2017). Multi-tissue interactions in an integrated three-tissue organ-on-a-chip platform. *Sci. Rep.* 7, 1–16. doi: 10.1038/s41598-017-08879-x

Sorkio, A., Koch, L., Koivusalo, L., Deiwick, A., Miettinen, S., Chichkov, B., et al. (2018). Human stem cell based corneal tissue mimicking structures using laser-assisted 3D bioprinting and functional bioinks. *Biomaterials* 171, 57–71. doi: 10.1016/j.biomaterials.2018.04.034

Sriram, G., Alberti, M., Dancik, Y., Wu, B., Wu, R., Feng, Z., et al. (2018). Full-thickness human skin-on-chip with enhanced epidermal morphogenesis and barrier function. *Mater. Today* 21, 326–340. doi: 10.1016/j.mattod.2017.11.002

Stange, D. E., and Clevers, H. (2013). Concise review: the Yin and Yang of intestinal (Cancer) stem cells and their progenitors. *Stem Cells* 31, 2287–2295. doi: 10.1002/stem.1475

Sung, J. H., Yu, J., Luo, D., Shuler, M. L., and March, J. C. (2011). Microscale 3-D hydrogel scaffold for biomimetic gastrointestinal (GI) tract model. *Lab Chip* 11, 389–392. doi: 10.1039/C0LC00273A

Thuenauer, R., and Rodriguez-boulan, E. (2015). Microfluidic approaches for epithelial cell layer culture and characterisation. *Analyst* 139, 3206–3218. doi: 10.1039/C4AN00056K

Tibbitt, M. W., and Anseth, K. S. (2009). Hydrogels as extracellular matrix mimics for 3D cell culture. *Biotechnol. Bioeng.* 103, 655–663. doi: 10.1002/bit. 22361

Tsang, V. L., Chen, A. A., Cho, L. M., Jadin, K. D., Sah, R. L., DeLong, S., et al. (2007). Fabrication of 3D hepatic tissues by additive photopatterning of cellular hydrogels. *FASEB J.* 21, 790–801. doi: 10.1096/fj.06-7117com

Tung, Y. C., Hsiao, A. Y., Allen, S. G., Torisawa, Y. S., Ho, M., and Takayama, S. (2011). High-throughput 3D spheroid culture and drug testing using a 384 hanging drop array. *Analyst* 136, 473–478. doi: 10.1039/C0AN00609B

van den Broek, L. J., Bergers, L. I. J. C., Reijnders, C. M. A., and Gibbs, S. (2017). Progress and future prospectives in skin-on-chip development with emphasis on the use of different cell types and technical challenges. *Stem Cell Rev. Rep.*13, 418–429. doi: 10.1007/s12015-017-9737-1

Vijayavenkataraman, S., Yan, W., Feng, W., Wang, C., Ying, J., and Fuh, H. (2018). 3D bioprinting of tissues and organs for regenerative medicine. *Adv. Drug Deliv. Rev.* 132, 296–332. doi: 10.1016/j.addr.2018.07.004

Vinci, M., Gowan, S., Boxall, F., Patterson, L., Zimmermann, M., Court, W., et al. (2012). Advances in establishment and analysis of three-dimensional tumor spheroid-based functional assays for target validation and drug evaluation. *BMC Biol.* 10:29. doi: 10.1186/1741-7007-10-29

Vrana, N. E., Lavalle, P., Dokmeci, M. R., Dehghani, F., Ghaemmaghami, A. M., and Khademhosseini, A. (2013). Engineering functional epithelium for regenerative medicine and *in vitro* organ models: a review. *Tissue Eng. Part B Rev.* 19, 529–543. doi: 10.1089/ten.teb.2012.0603

Wang, Y., Gunasekara, D. B., Reed, M. I., DiSalvo, M., Bultman, S. J., Sims, C. E., et al. (2017). A microengineered collagen scaffold for generating a polarized crypt-villus architecture of human small intestinal epithelium. *Biomaterials* 128, 44–55. doi: 10.1016/j.biomaterials.2017.03.005

Whitesides, G. M. (2003). The "right" size in nanobiotechnology. *Nat. Biotechnol.* 21, 1161–1165. doi: 10.1038/nbt872

Wilson, S. S., Tocchi, A., Holly, M. K., Parks, W. C., and Smith, J. G. (2015). A small intestinal organoid model of non-invasive enteric pathogen-epithelial cell interactions. *Mucosal Immunol.* 8, 352–361. doi: 10.1038/mi.2014.72

Workman, M. J., Gleeson, J. P., Troisi, E. J., Estrada, H. Q., Kerns, S. J., Hinojosa, C. D., et al. (2018). Enhanced utilization of induced pluripotent stem cell–derived human intestinal organoids using microengineered chips. *Cell. Mol. Gastroenterol. Hepatol.* 5, 669–677.e2. doi: 10.1016/j.jcmgh.2017.12.008

Wufuer, M., Lee, G. H., Hur, W., Jeon, B., Kim, B. J., Choi, T. H., et al. (2016). Skin-on-a-chip model simulating inflammation, edema and drug-based treatment. *Sci. Rep.* 6:37471. doi: 10.1038/srep37471

Youn, B. S., Sen, A., Behie, L. A., Girgis-Gabardo, A., and Hassell, J. A. (2006). Scale-up of breast cancer stem cell aggregate cultures to suspension bioreactors. *Biotechnol. Prog.* 22, 801–810. doi: 10.1021/bp050430z

Yu, J., Peng, S., Luo, D., and March, J. C. (2012). In vitro 3D human small intestinal villous model for drug permeability determination. *Biotechnol. Bioeng.* 109, 2173–2178. doi: 10.1002/bit.24518

Yui, S., Nakamura, T., Sato, T., Nemoto, Y., Mizutani, T., Zheng, X., et al. (2012). Functional engraftment of colon epithelium expanded *in vitro* from a single adult Lgr5 + stem cell. *Nat. Med.* 18, 618–623. doi: 10.1038/nm.2695

Conflict of Interest Statement: The authors declare that the research was conducted in the absence of any commercial or financial relationships that could be construed as a potential conflict of interest.

frontiers
in Bioengineering and Biotechnology

ORIGINAL RESEARCH
published: 22 January 2019
doi: 10.3389/fbioe.2019.00003

Impaired Wound Healing of Alveolar Lung Epithelial Cells in a Breathing Lung-On-A-Chip

Marcel Felder [1†], Bettina Trueeb [1†], Andreas Oliver Stucki [1†], Sarah Borcard [1,2], Janick Daniel Stucki [1,3], Bruno Schnyder [2], Thomas Geiser [4] and Olivier Thierry Guenat [1,3,4,5*]

[1] ARTORG Center, Medical Faculty, University of Bern, Bern, Switzerland, [2] HES-SO, Institute of Life Technologies, Sion, Switzerland, [3] AlveoliX, Bern, Switzerland, [4] Pulmonary Medicine Department, University Hospital of Bern, Bern, Switzerland, [5] Thoracic Surgery Department, University Hospital of Bern, Bern, Switzerland

The lung alveolar region experiences remodeling during several acute and chronic lung diseases, as for instance idiopathic pulmonary fibrosis (IPF), a fatal disease, whose onset is correlated with repetitive microinjuries to the lung alveolar epithelium and abnormal alveolar wound repair. Although a high degree of mechanical stress (>20% linear strain) is thought to potentially induce IPF, the effect of lower, physiological levels of strain (5–12% linear strain) on IPF pathophysiology remains unknown. In this study, we examined the influence of mechanical strain on alveolar epithelial wound healing. For this purpose, we adopted the "organ-on-a-chip" approach, which provides the possibility of reproducing unique aspects of the *in vivo* cellular microenvironment, in particular its dynamic nature. Our results provide the first demonstration that a wound healing assay can be performed on a breathing lung-on-a-chip equipped with an ultra-thin elastic membrane. We cultured lung alveolar epithelial cells to confluence, the cells were starved for 24 h, and then wounded by scratching with a standard micropipette tip. Wound healing was assessed after 24 h under different concentrations of recombinant human hepatic growth factor (rhHGF) and the application of cyclic mechanical stretch. Physiological cyclic mechanical stretch (10% linear strain, 0.2 Hz) significantly impaired the alveolar epithelial wound healing process relative to culture in static conditions. This impairment could be partially ameliorated by administration of rhHGF. This proof-of-concept study provides a way to study of more complex interactions, such as a co-culture with fibroblasts, endothelial cells, or immune cells, as well as the study of wound healing at an air–liquid interface.

Keywords: wound healing, organ-on-a-chip, air–blood barrier, cyclic stretch, idiopathic pulmonary fibrosis

Edited by:
Qasem Ramadan,
Agency for Science, Technology and Research (A*STAR), Singapore

Reviewed by:
Andrea Peloso,
Policlinico San Matteo Fondazione (IRCCS), Italy
Samy Gobaa,
Institut Pasteur, France

***Correspondence:**
Olivier Thierry Guenat
olivier.guenat@artorg.unibe.ch

† These authors have contributed equally to this work

Specialty section:
This article was submitted to Tissue Engineering and Regenerative Medicine, a section of the journal Frontiers in Bioengineering and Biotechnology

Received: 27 September 2018
Accepted: 03 January 2019
Published: 22 January 2019

Citation:
Felder M, Trueeb B, Stucki AO, Borcard S, Stucki JD, Schnyder B, Geiser T and Guenat OT (2019) Impaired Wound Healing of Alveolar Lung Epithelial Cells in a Breathing Lung-On-A-Chip. Front. Bioeng. Biotechnol. 7:3. doi: 10.3389/fbioe.2019.00003

INTRODUCTION

An organ-on-a-chip (OOC) is an advanced *in vitro* system that provides cells with an environment that closely resembles their *in vivo* milieu (Benam et al., 2015). In such environments, cells maintain their original functions and respond to external stimuli, such as mechanical forces or therapeutic compounds, as if they were within the tissues of the body. OOCs also recapitulate aspects of healthy and diseased cellular environments, allowing investigation of fundamental biological questions. In contrast to *in vivo* studies, OOCs make it possible to individually assess the effects of specific parameters of the microenvironment. Thus, OOCs are promising tools for improving and accelerating drug development, as well as obtaining deeper insights into pathophysiological processes (Chan et al., 2013; Sackmann et al., 2014; Esch et al., 2015).

Idiopathic pulmonary fibrosis (IPF) is a chronic, fatal lung disease characterized by an abnormal wound healing and remodeling process of alveolar epithelial cells (King et al., 2011). The various aspects of the disease and the lack of predictive *in vivo* and *in vitro* models make IPF difficult to study. It is generally accepted that IPF is initiated by repetitive microinjuries to the alveolar epithelium. Aberrant repair of those injuries is followed by a fibro-proliferative response that induces progressive scarring of the lung parenchyma, ultimately leading to respiratory failure. Although the cause of these microinjuries, as well as the cause of aberrant wound healing, remains unknown, it is thought that mechanical forces play important roles in the development and progression of IPF (Selman and Pardo, 2014). In particular, scarring of the lungs occurs with higher probability at the base and periphery, where mechanical forces due to breathing are greatest. Under physiologic conditions, alveolar regions of the lungs are exposed to a linear strain of up to 12% (Waters et al., 2012). However, scarred areas are less elastic than the healthy elastic regions and must compensate for the strain, resulting in higher mechanical stretch in those areas. High mechanical stretch causes apoptosis and slows wound repair in rat alveolar epithelial cells and decreases cell migration in bronchial 16HBE-14o-cells (Desai et al., 2008; Crosby et al., 2011). In addition, wound repair of primary human alveolar epithelial cells is delayed under physiologic (10%) linear strain (Ito et al., 2014). Thus far, the *in vitro* systems used to investigate wound healing have been based on stiff, Petri dish–based systems or stretchable systems assembled on thick silicone substrates (Guenat and Berthiaume, 2018). We recently demonstrated that microfluidics platforms enable investigation of alveolar epithelial microinjuries more reproducibly and at a smaller scale (Felder et al., 2012, 2014). The hypothesis that gastro-esophageal reflux is a source of repetitive microinjuries was also investigated on a chip (Felder et al., 2014).

Here, we report the use of a microengineered lung-on-a-chip (Stucki et al., 2015, 2018) with a "breathing" ultra-thin membrane to investigate the effects of cyclic mechanical stress induced by respiratory motions on alveolar wound repair. The open design of the lung-on-a-chip enabled the use of a scratch assay to create microinjuries in the intact alveolar epithelium. The epithelium was further exposed to hepatic growth factor, which promotes alveolar epithelial wound healing (Felder et al., 2012). The results confirmed that physiological mechanical stress affects alveolar wound closure. These results are a first step toward recapitulating the complex interplay of wound repair in the alveolar epithelium.

METHODS

Fabrication of the Lung-On-A-Chip

The working principle and fabrication of the lung-on-a-chip were described previously (Stucki et al., 2015, 2018). Briefly, the bioinspired lung-on-a-chip consists of an ultra-thin alveolar membrane that is deflected by the action of a microdiaphragm to mimic the mechanical strain of breathing (**Figures 1A–C**). The alveolar membrane, on which cells can be cultured on both sides, consists of a 3.5 μm–thick elastic membrane (with or without 3 μm pores, 800,000 pores/cm^2) made of polydimethylsiloxane (PDMS, Sylgard 184, Dow Corning). The membrane is sandwiched between an apical and a basal cell culture chamber. The microdiaphragm is a 40 μm–thick membrane located at the bottom of the basal chamber and actuated by an external electro-pneumatic system.

Cell Culture

A549 lung alveolar epithelial-like cells (ATCC cat#: CCL-185, RRID:CVCL_0023) were cultured on fibronectin-coated PDMS membranes (2.5 μg/cm^2, Corning) in RPMI 1640 culture medium with GlutaMAX™ (Gibco/Life Technologies, cat#: 61870-010) supplemented with 10% fetal bovine serum (FBS, Gibco/Life Technologies, cat#: 10270-1 06) and 1% penicillin–streptomycin (Gibco Life Technologies, cat#: 15140-122) at 37°C and 5% CO_2. The cells were seeded at 50,000 cells/cm^2 on the apical side of the alveolar membrane. Cell culture medium was exchanged daily. When the cells reached confluence after 48 h, they were cultured in starvation medium (RPMI 1640 without FBS) for an additional 24 h.

Wound-Healing Assay

The epithelial cell monolayer was scratched by dragging a 10 μl pipette tip across the thin membrane (**Figures 2A–C**). The cells were washed once with starvation medium to remove cell debris. The wounded monolayers were cultured for 24 h in starvation medium with or without recombinant human hepatic growth factor (rhHGF, 1, 10, or 100 ng/ml, R&D Systems, cat#: 294-HG-05). In addition, cells were cultured either under static (no stretch) or dynamic conditions (with three-dimensional stretch corresponding to 10% linear strain at 0.2 Hz).

Wound-Healing Analysis

Microscopic images of the entire wounded area were taken immediately after wounding and 24 h later. Images taken before wounding served as proof of confluence. The MosaicJ (National Center for Microscopy and Imaging Research: ImageJ Mosaic Plug-ins, RRID:SCR_001935) plug-in for Fiji (RRID:SCR_002285) was used to stitch images together. The wounded area was manually outlined based on images acquired immediately after wounding and 24 h later. Only wounds with areas between 1.2 and 2.5 mm^2 were analyzed to ensure that data would be comparable. Areas larger than 2.5 mm^2 (one third of the growth area) were excluded to ensure that sufficient cells were present to repopulate the wounded area. Areas smaller than 1.2 mm^2 were excluded to ensure that the wound was not completely closed after 24 h.

Immunofluorescence Microscopy

Cells were immunostained for tight junctions using goat anti–ZO-1 antibody (Abcam, cat#: ab99462) after fixation with 4% paraformaldehyde (PFA, Sigma-Aldrich) and blocking with 2% FBS in PBS. Hoechst-33342 (Molecular Probes, cat#: H3570) was used to stain nuclei. Microscopic images were acquired using a Zeiss Axioplan microscope with a 20× objective.

Scanning Electron Microscopy

Cells were fixed for 24 h in 2.5% glutaraldehyde (Sigma-Aldrich) in 10 mM HEPES buffer (Sigma-Aldrich). The cells

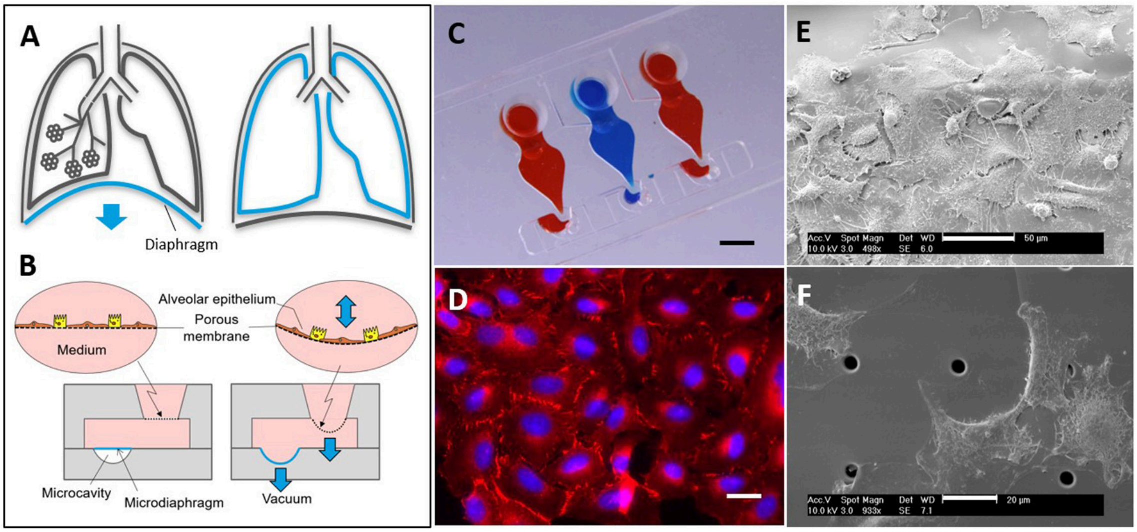

FIGURE 1 | (A) Breathing concept *in vivo*. When the diaphragm contracts, negative thoracic pressure is generated and the lungs and lung alveoli expand. **(B)** Breathing concept *in vitro*. A microdiaphragm deflects in a defined microcavity. Due to the negative pressure generated, the alveolar membrane, where the cells are cultured, deflects downward. Schematic adapted from (Guenat and Berthiaume, 2018). **(C)** Image of the lung-on-a-chip with three culture chambers. Scale bar: 3 mm. **(D)** Immunofluorescence image of A549 cells cultured on the membrane. Cell nuclei are stained in blue, and ZO-1 (a marker of tight junctions) is stained in red. Scale bar: 20 µm. **(E,F)** Scanning electron micrograph of A549 on non-porous (top) and porous (bottom) membranes. Scale bars: 50 µm (top), 20 µm (bottom).

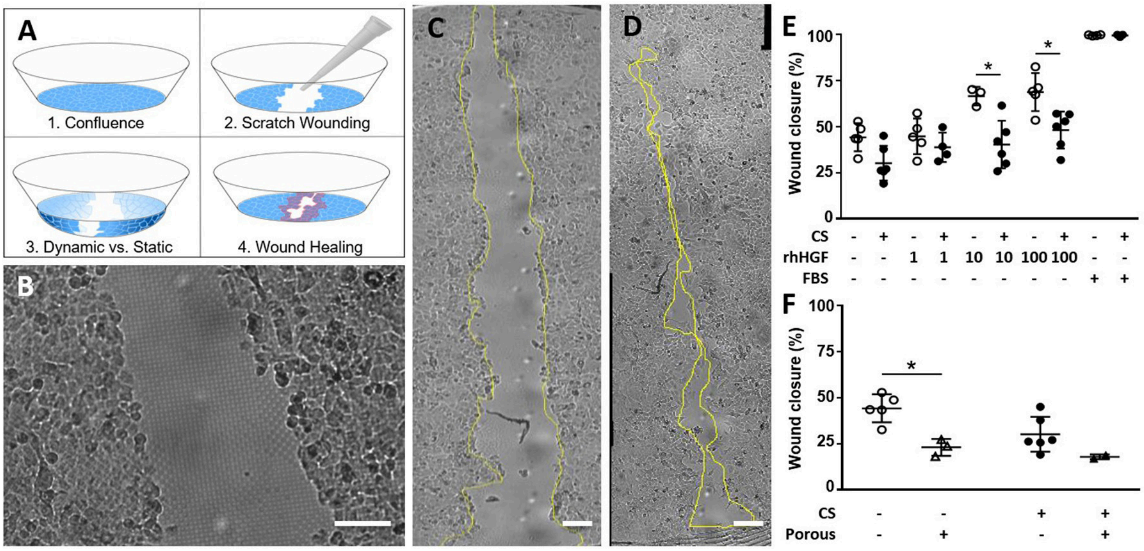

FIGURE 2 | (A) Scheme of the scratch wound assay. The wound is created by scratching the cell-covered surface with a standard pipette tip. **(B)** Micrograph of wounded A549 cells on a porous membrane. **(C,D)** Mosaic image of an entire wound immediately after wounding **(C)** and 24 h later **(D)**. **(E)** Wound closure on non-porous membranes, with or without cyclic stretch (CS, 10% linear, 0.2 Hz), recombinant human hepatic growth factor (rhHGF, in ng/mL), or 10% fetal bovine serum (FBS). Wound closure is promoted in a dose-dependent fashion by rhHGF, and impaired when CS is applied. **(F)** Wound closure is impaired when cells are cultured under CS or on a porous membrane. Scale bars: 100 µm.

were dehydrated using a sequence of ethanol concentrations (50–100%). Before images were acquired, the samples were dried using a critical point dryer (Baltec) and sputtered with gold.

Statistical Analysis

GraphPad prism (RRID:SCR_002798) was used for statistical analyses. All data are shown as means ± standard deviation (SD). A two-way ANOVA with Tukey correction for multiple comparison was used to determine statistical significance.

RESULTS

Lung alveolar epithelial cells were successfully cultured on the ultra-thin PDMS membrane. **Figure 1D** shows a confluent layer of cells stained with DAPI (nuclei) and anti–ZO-1 antibody (tight junctions). Cells adhered to the membrane with their filopodia spreading on the porous (**Figure 1F**) or non-porous silicone membrane (**Figure 1E**). The elastic membrane resisted the wound creation, where the cell layer was scratched with a pipette tip, and did not tear, despite being only 3.5 μm thick (**Figures 2A–C**). In medium containing 10% FBS, wound closure was complete after 24 h under both static (99.7%, $n = 4$) and dynamic (99.9%, $n = 3$) conditions (**Figure 2E**). Because FBS contains a plethora of growth factors, a starvation medium without FBS was used to slow down the wound closure and to measure the effect of HGF alone. In starvation medium, alveolar epithelial wound closure was faster under static than dynamic conditions (44.2 ± 7.6% with no stretching, 30.1 ± 9.5% with cyclic stretching, $n = 5$ and $n = 6$). rhHGF exerted a dose-dependent positive effect on wound closure, irrespective of culture conditions (static or dynamic). In 10 ng/ml rhHGF, wound healing was markedly accelerated under static conditions (44.2 to 66.6%, $n = 3$), and 100 ng/ml rhHGF further increased the wound-healing rate, albeit only slightly ($n = 5$). Under cyclic stress, a similar trend could be observed at 1 ng/ml rhHGF ($n = 4$). At 100 ng/ml rhHGF, wound closure improved from 30.1 to 38.8% ($n = 6$), almost reaching the degree of initial wound closure observed under static conditions.

When the cells were cultured on a porous membrane, wound healing was also significantly slowed relative to a non-porous membrane under static conditions (**Figure 2F**). With the addition of cyclic stretching, wound healing was delayed further, but not significantly compared to a non-porous membrane ($n = 3$ without stretch, $n = 2$ with stretch).

DISCUSSION

Wound-healing assays are widely used in drug discovery and in fundamental investigation of the pathogenesis of wound healing and of scar formation. Several organs, including the skin and lung, are affected by diseases whose onset is related to wounding. In the lung, IPF and acute lung injuries are severe diseases for which the wound-healing mechanisms are crucial in the development of the disease, but the cellular and molecular mechanisms are not completely understood. Unfortunately, *in vivo* models are of limited utility for investigating wound repair in the lung, in part because it is not possible to induce single small wounds and observe their repair over time. However, standard *in vitro* techniques are also limited because they poorly reproduce the *in vivo* milieu; instead, such systems often consist of a monolayer of cells cultured on a hard substrate and submerged in a static medium. The microenvironment of the lung, by contrast, undergoes constant mechanical stimulus induced by breathing motions. In addition, in a healthy lung, epithelial cells are exposed to air, and the tissue contains many other cell types. Recent advances in microengineering and cell biology have made it possible to develop advanced systems that mimic these properties (Huh et al., 2010; Stucki et al., 2015, 2018). We therefore assume that this *in vitro* model of epithelial wound repair including mechanical forces represents the *in vivo* situation at a higher level than conventional *in vitro* model systems.

Here, we performed a proof-of-concept study of a wound-healing assay on a lung-on-a-chip. Applying cyclic mechanical stretch reduced the wound-healing capabilities of alveolar cells over 24 h, consistent with studies of human bronchial cells and alveolar epithelial cells in rodents and humans (Desai et al., 2010; Crosby et al., 2011; Ito et al., 2014). The impaired wound closure was partially restored by the addition of rhHGF. This effect was concentration-dependent in all conditions, confirming earlier results (Felder et al., 2012, 2014; Ito et al., 2014). The mechanism underlying the impaired wound repair upon stretch is not completely understood. Desai et al. showed that cyclic stretch corresponding to 20% linear strain at 0.5 Hz inhibited phosphatidylinositol 3-kinase (PI3K) in bronchial epithelial cells (Desai et al., 2010). PI3K is typically activated in wound healing. However, Ito et al. did not observe the same downregulation in PI3K when alveolar cells were subjected to only 10% linear strain at 0.1 Hz (Ito et al., 2014). These discrepancies suggest that different pathways may be involved in wound healing depending on the stretch magnitude and frequency. However, other players, such as stiffness, which can importantly affect the strain level, are involved in IPF remodeling (Selman and Pardo, 2014). In the present lung-on-a-chip, the stiffness of the membrane may be modified in the future to mimic this aspect.

Furthermore, we observed reduced wound healing on a porous membrane (3 μm pores, 800,000 pores/cm^2) relative to a non-porous membrane, regardless of cyclic stretch. This can be partially explained by the fact that, on porous membranes, there is no continuous cell support. The interaction between cells and the extracellular matrix (ECM) plays an important role during growth, development and repair (Rosso et al., 2004). The absence of this ECM–cell interaction where the pores are located may slow down cell migration. Furthermore, A549 cells are capable of transmigrating through the 3 μm pores to the other side of the membrane and are thus not involved in the wound closure.

The semi-open design of the lung-on-a-chip provides an easy access to the apical cell culture well. Consequently, the cell layer can simply be wounded with a pipette tip, and wound healing can be observed during cyclic mechanical stretching. To the best of our knowledge this is the first report of a wound-healing assay performed on an ultra-thin, porous, and stretchable membrane. This system enables the development of more complex assays that can so far not be reproduced.

Preliminary results culturing epithelial cells with fibroblasts (see **Supplementary Materials**) show that wound-healing of a co-culture model can be investigated with this device. This is of great importance to study the pathophysiology of interstitial lung diseases. By further adding immune cells and/or endothelial cells, other biological questions may be investigated. In addition to the cyclic stress, other aspects of the unique lung alveolar environment can be emulated. Notably, the air-liquid interface, which all healthy pulmonary epithelial cells are exposed to.

In such configuration, the epithelial layer receives its nutrients via the basolateral side of the membrane (through endothelial cells) while being exposed to air on the apical side. The reproduction of these key environmental aspects may help to fully elucidate the complex interplay between mechanical strain and deficient alveolar wound repair that underlies IPF and other diseases. By culturing diseased cells from patients, our hope is to be able to develop cell-based assays for precision medicine.

AUTHOR CONTRIBUTIONS

OG and TG had the original idea to investigate microinjuries on a chip exposed to mechanical stimulation. MF, BS, and OG planned the microinjury study. BT, MF, and SB carried out the experiments involving the microinjuries. AS performed the immunostaining. JS prepared the samples for the SEM experiments and SEM imaging. AS, OG, MF, and BT wrote the manuscript. All authors reviewed the manuscript.

ACKNOWLEDGMENTS

We greatly appreciate the financial support of the Swiss National Science Foundation (project no. 141127) and the Innosuisse (project no. 27813.1 PFLS-LS). Images were acquired on a device supported by the Microscopy Imaging Center (MIC) of the University of Bern. We thank Beat Haenni for assistance with the SEM images.

SUPPLEMENTARY MATERIAL

The Supplementary Material for this article can be found online at: https://www.frontiersin.org/articles/10.3389/fbioe.2019.00003/full#supplementary-material

REFERENCES

Benam, K. H., Dauth, S., Hassell, B., Herland, A., Jain, A., Jang, K.-J., et al. (2015). Engineered *in vitro* disease models. *Annu. Rev. Pathol. Mech. Dis.* 10, 195–262. doi: 10.1146/annurev-pathol-012414-040418

Chan, C. Y., Huang, P. H., Guo, F., Ding, X., Kapur, V., Mai, J. D., et al. (2013). Accelerating drug discovery via organs-on-chips. *Lab Chip* 13, 4697–4710. doi: 10.1039/c3lc90115g

Crosby, L. M., Luellen, C., Zhang, Z., Tague, L. L., Sinclair, S. E., and Waters, C. M. (2011). Balance of life and death in alveolar epithelial type II cells: proliferation, apoptosis, and the effects of cyclic stretch on wound healing. *Am. J. Physiol.* 301, L536–L546. doi: 10.1152/ajplung.00371.2010

Desai, L. P., Chapman, K. E., and Waters, C. M. (2008). Mechanical stretch decreases migration of alveolar epithelial cells through mechanisms involving Rac1 and Tiam1. *AJP Lung Cell. Mol. Physiol.* 295, L958–L965. doi: 10.1152/ajplung.90218.2008

Desai, L. P., White, S. R., and Waters, C. M. (2010). Cyclic mechanical stretch decreases cell migration by inhibiting phosphatidylinositol 3-kinase- and focal adhesion kinase-mediated JNK1 activation. *J. Biol. Chem.* 285, 4511–4519. doi: 10.1074/jbc.M109.084335

Esch, E. W., Bahinski, A., and Huh, D. (2015). Organs-on-chips at the frontiers of drug discovery. *Nat. Rev. Drug Discov.* 14, 248–260. doi: 10.1038/nrd4539

Felder, M., Sallin, P., Barbe, L., Haenni, B., Gazdhar, A., Geiser, T., et al. (2012). Microfluidic wound-healing assay to assess the regenerative effect of HGF on wounded alveolar epithelium. *Lab Chip* 12, 640–646. doi: 10.1039/c1lc20879a

Felder, M., Stucki, A. O., Stucki, J. D., Geiser, T., and Guenat, O. T. (2014). The potential of microfluidic lung epithelial wounding: towards *in vivo*-like alveolar microinjuries. *Integr. Biol.* 6, 1132–1140. doi: 10.1039/c4ib00149d

Guenat, O. T., and Berthiaume, F. (2018). Incorporating mechanical strain in organs-on-a-chip: lung and skin. *Biomicrofluidics* 12:4. doi: 10.1063/1.5024895

Huh, D., Matthews, B. D., Mammoto, A., Montoya-Zavala, M., Hsin, H. Y., and Ingber, D. E. (2010). Reconstituting organ-level lung functions on a chip. *Science* 328, 1662–1668. doi: 10.1126/science.1188302

Ito, Y., Correll, K., Schiel, J. A., Finigan, J. H., Prekeris, R., and Mason, R. J. (2014). Lung fibroblasts accelerate wound closure in human alveolar epithelial cells through hepatocyte growth factor/c-Met signaling. *Am. J. Physiol. Lung Cell. Mol. Physiol.* 307, L94–L105. doi: 10.1152/ajplung.00233.2013

King, T. E., Pardo, A., and Selman, M. (2011). Idiopathic pulmonary fibrosis. *Lancet* 378, 1949–1961. doi: 10.1016/S0140-6736(11)60052-4

Rosso, F., Giordano, A., Barbarisi, M., and Barbarisi, A. (2004). From cell-ECM interactions to tissue engineering. *J. Cell. Physiol.* 199, 174–180. doi: 10.1002/jcp.10471

Sackmann, E. K., Fulton, A. L., and Beebe, D. J. (2014). The present and future role of microfluidics in biomedical research. *Nature* 507, 181–189. doi: 10.1038/nature13118

Selman, M., and Pardo, A. (2014). Revealing the pathogenic and aging-related mechanisms of the enigmatic idiopathic pulmonary fibrosis. An integral model. *Am. J. Respir. Critic. Care Med.* 189, 1161–1172. doi: 10.1164/rccm.201312-2221PP

Stucki, A. O., Stucki, J. D., Hall, S. R., Felder, M., Mermoud, Y., Schmid, R. A., et al. (2015). A lung-on-a-chip array with an integrated bio-inspired respiration mechanism. *Lab Chip* 15, 1302–1310. doi: 10.1039/c4lc01252f

Stucki, J. D., Hobi, N., Galimov, A., Stucki, A. O., Schneider-Daum, N., Lehr, C.-M., et al. (2018). Medium throughput breathing human primary cell alveolus-on-chip model. *Sci. Rep.* 8:14359. doi: 10.1038/s41598-018-32523-x

Waters, C. M., Roan, E., and Navajas, D. (2012). Mechanobiology in lung epithelial cells: measurements, perturbations, and responses. *Compr. Physiol.* 2, 1–29. doi: 10.1002/cphy.c100090

Conflict of Interest Statement: OG, TG, and JS are shareholders of the start-up AlveoliX AG, which aims at bringing to market a lung-on-a-chip system based on the model described in this article.

The remaining authors declare that the research was conducted in the absence of any commercial or financial relationships that could be construed as a potential conflict of interest.

frontiers
in Bioengineering and Biotechnology

ORIGINAL RESEARCH
published: 07 February 2019
doi: 10.3389/fbioe.2019.00013

A Robust Longitudinal Co-culture of Obligate Anaerobic Gut Microbiome With Human Intestinal Epithelium in an Anoxic-Oxic Interface-on-a-Chip

Woojung Shin[1†], Alexander Wu[1†], Miles W. Massidda[1†], Charles Foster[1], Newin Thomas[1], Dong-Woo Lee[2], Hong Koh[3], Youngwon Ju[4], Joohoon Kim[4,5] and Hyun Jung Kim[1,6]*

[1] Department of Biomedical Engineering, The University of Texas at Austin, Austin, TX, United States, [2] Department of Biotechnology, College of Life Science and Technology, Yonsei University, Seoul, South Korea, [3] Department of Pediatrics, Severance Fecal Microbiota Transplantation Center, Yonsei University College of Medicine, Seoul, South Korea, [4] Department of Chemistry, Research Institute for Basic Sciences, Kyung Hee University, Seoul, South Korea, [5] KHU-KIST Department of Converging Science and Technology, Kyung Hee University, Seoul, South Korea, [6] Department of Medical Engineering, Yonsei University College of Medicine, Seoul, South Korea

Edited by:
Qasem Ramadan,
*Agency for Science, Technology and Research (A*STAR), Singapore*

Reviewed by:
Arul Jayaraman,
Texas A&M University, United States
Alexander S. Mosig,
Universitätsklinikum Jena, Germany

***Correspondence:**
Hyun Jung Kim
hyunjung.kim@utexas.edu

† These authors have contributed equally to this work

Specialty section:
This article was submitted to Tissue Engineering and Regenerative Medicine, a section of the journal Frontiers in Bioengineering and Biotechnology

***Received:** 05 October 2018*
***Accepted:** 18 January 2019*
***Published:** 07 February 2019*

Citation:
Shin W, Wu A, Massidda MW, Foster C, Thomas N, Lee D-W, Koh H, Ju Y, Kim J and Kim HJ (2019) A Robust Longitudinal Co-culture of Obligate Anaerobic Gut Microbiome With Human Intestinal Epithelium in an Anoxic-Oxic Interface-on-a-Chip. Front. Bioeng. Biotechnol. 7:13. doi: 10.3389/fbioe.2019.00013

The majority of human gut microbiome is comprised of obligate anaerobic bacteria that exert essential metabolic functions in the human colon. These anaerobic gut bacteria constantly crosstalk with the colonic epithelium in a mucosal anoxic-oxic interface (AOI). However, *in vitro* recreation of the metabolically mismatched colonic AOI has been technically challenging. Furthermore, stable co-culture of the obligate anaerobic commensal microbiome and epithelial cells in a mechanically dynamic condition is essential for demonstrating the host-gut microbiome crosstalk. Here, we developed an anoxic-oxic interface-on-a-chip (AOI Chip) by leveraging a modified human gut-on-a-chip to demonstrate a controlled oxygen gradient in the lumen-capillary transepithelial interface by flowing anoxic and oxic culture medium at various physiological milieus. Computational simulation and experimental results revealed that the presence of the epithelial cell layer and the flow-dependent conditioning in the lumen microchannel is necessary and sufficient to create the steady-state vertical oxygen gradient in the AOI Chip. We confirmed that the created AOI does not compromise the viability, barrier function, mucin production, and the expression and localization of tight junction proteins in the 3D intestinal epithelial layer. Two obligate anaerobic commensal gut microbiome, *Bifidobacterium adolescentis* and *Eubacterium hallii*, that exert metabolic cross-feeding *in vivo*, were independently co-cultured with epithelial cells in the AOI Chip for up to a week without compromising any cell viability. Our new protocol for creating an AOI in a microfluidic gut-on-a-chip may enable to demonstrate the key physiological interactions of obligate anaerobic gut microbiome with the host cells associated with intestinal metabolism, homeostasis, and immune regulation.

Keywords: co-culture, gut microbiome, gut-on-a-chip, anoxic-oxic interface, host-microbiome interaction, microfluidics

INTRODUCTION

In the human colon, obligate anaerobic bacteria outnumber aerobic and facultative anaerobic bacteria by 2–3 orders of magnitude (Walsh et al., 2014). This commensal anaerobic microbiome constantly interacts with host cells and performs physiologically important functions including epithelial barrier function (Leslie et al., 2015; Chu, 2017), nutrient absorption (Krajmalnik-Brown et al., 2012), immune regulation (Luca et al., 2018), and the production of essential metabolic compounds such as short-chain fatty acids (SCFA) (Swanson, 2015). Interestingly, the host-gut microbiome ecosystem has been established in an anoxic-oxic interface (AOI) that is naturally created and maintained in the human colon. It has been known that the aerobic bacteria first colonize the luminal surface of the intestinal epithelium. Bacterial oxygen consumption is responsible for the creation of the oxygen gradient, eventually allowing the obligate anaerobes to colonize in the luminal microenvironment (Espey, 2013). The colonic microbiome has a complex spectrum from the oxygen-tolerant bacteria such as microaerophiles and obligate aerobes to the different types of anaerobic bacteria (i.e., facultative anaerobes, aerotolerant anaerobes, and obligate anaerobes; Albenberg et al., 2014). Since these colonic commensal bacteria substantially contribute to performing homeostatic and metabolic functions (Zhernakova et al., 2016), the establishment of the AOI with a defined transepithelial oxygen gradient is necessary to keep the microbial populations viable and functional.

It has been extremely challenging to recreate the human intestinal AOI *in vitro* and perform the host-gut microbiome co-culture because conventional aerobic *in vitro* cell culture models have failed to stably grow obligate anaerobic gut bacteria (Walker et al., 2014). For instance, a Transwell-based design was leveraged to co-culture the obligate anaerobic strain *Faecalibacterium prausnitzii* with intestinal epithelial Caco-2 cells, in which anaerobic and aerobic culture medium was applied to the apical and the basolateral compartment, respectively, to recreate a local AOI (Ulluwishewa et al., 2014). However, limited co-culture period (<8 h) and a lack of physiological flow and mechanical deformations substantially limited the longitudinal host-microbiome crosstalk (von Martels et al., 2017). A conical tube-based co-culture model was suggested to provide the AOI, where a solid agar compartment containing *F. prausnitzii* cells was incubated with a porous membrane lined by a monolayer of Caco-2 cells (Sadaghian Sadabad et al., 2015). However, in addition to the aforementioned restrictions of a static co-culture, the closed system in the design considerably hampered the necessary ventilation of the gases generated during the co-culture, which causes undesirable cracks in the agar.

Microfluidic models have also been proposed to recreate the AOI on-chip (Marzorati et al., 2014; Shah et al., 2016). However, these models separate the obligate or facultative anaerobic bacteria from the epithelial cell layer, preventing the direct host-microbiome interactions germane to the homeostatic functions of mucosal microbiome (Bäckhed et al., 2012). Furthermore, the lack of peristalsis-like mechanical movement, dynamic luminal flow, and fully differentiated 3-dimensional (3D) epithelial microarchitecture hamper the physiological legitimacy in modeling the human intestine. We previously developed a microengineered human gut-on-a-chip that permits robust co-culture of the living gut microbiome such as *Lactobacillus rhamnosus* GG (Kim et al., 2012), VSL#3 (Kim et al., 2016a,b; Shin and Kim, 2018b), and pathogenic enteroinvasive (Kim et al., 2016b) or non-pathogenic *Escherichia coli* (Bein et al., 2018; Shin and Kim, 2018a,b) in the 3D intestinal epithelium. However, it has not been fully verified if the longitudinal co-culture with obligate anaerobic gut bacteria is feasible in the gut-on-a-chip microphysiological system.

In this study, we modified the original design of the gut-on-a-chip with an increased height of the lumen microchannel to demonstrate the co-culture of obligate anaerobic bacteria with the intestinal epithelium by creating an anoxic-oxic interface-on-a-chip (AOI Chip). To validate the functionality of our *in vitro* AOI Chip, we chose two commensal obligate anaerobic bacteria, *Bifidobacterium adolescentis* and *Eubacterium hallii,* that have been known to syntrophically cross-feed and produce SCFAs (Belenguer et al., 2006). We also computationally and experimentally simulated the oxygen gradient microenvironment in the AOI Chip. Thus, we verified the feasibility of the AOI Chip by demonstrating the technically challenging co-culture of the human gut epithelium with obligate anaerobic gut microbiome.

MATERIALS AND METHODS

Computational Simulation

A finite element method was used in COMSOL Multiphysics 5.3 (COMSOL Inc.). Two studies, the laminar flow fluid dynamics and the transport of diluted species, were coupled to compute the profile of oxygen concentration inside the microchannels in the presence or the absence of intestinal epithelium. To model fluid dynamics, the Navier-Stokes equation assuming incompressible fluid was applied, and convection of the fluid was also included (Mattei et al., 2014). As a boundary condition, the interfaces between the cell microchannels and the silicone polydimethylsiloxane (PDMS) layer were set as no slip conditions. The linear flow rate (m/s) was derived from a volumetric unit (μL/h) by reflecting the unit cross-sectional area of the cell microchannel. To simulate the transport of oxygen molecules, Fick's 2nd law was applied (Mehta and Linderman, 2006; Buchwald, 2009). The oxygen consumption rate was calculated based on the known oxygen consumption rate per intestinal epithelial cell (mol/s·cell) (Lin et al., 2018). The total number of epithelial cells in the AOI Chip was experimentally determined. The flux of oxygen through a PDMS layer was calculated by reflecting the thickness of the upper and the lower PDMS layers (Giulitti et al., 2013; Mattei et al., 2014). A PDMS porous membrane was simplified to consider as a thin diffusion barrier (thickness, 20 μm) by applying the diffusion coefficient of dissolved oxygen in the PDMS (Cox and Dunn, 1986). The standard mesh size was applied, and all simulations were performed with the assumption that the system is at 37°C. Parameters used in the simulation are provided in **Table 1**.

TABLE 1 | Parameters used in COMSOL computational simulation.

Parameter	Description	Quantity	References
D_{medium}	The diffusion coefficient of oxygen in medium	3.0×10^{-9} m^2/s	Buchwald, 2009
D_{cell}	The diffusion coefficient of oxygen in intestinal epithelium	2.0×10^{-9} m^2/s	Buchwald, 2009
D_{PDMS}	Diffusion coefficient of oxygen in PDMS	5.0×10^{-9} m^2/s	Cox and Dunn, 1986
Cell density*	Epithelial cell number per unit volume	2.77×10^{14} cells/m^3	
$Q_{O2\ \mathrm{cell}}$	The oxygen consumption rate of intestinal epithelium	8.64×10^{-3} mol/m^3·s	Lin et al., 2018
$N_{O_2}^{ext}$, *top*	Oxygen flux from the top PDMS layer	1.22×10^{-7} mol/m^3	Giulitti et al., 2013
$N_{O_2}^{ext}$, *bottom*	Oxygen flux from the bottom PDMS layer	6.10×10^{-7} mol/m^3	Giulitti et al., 2013

**Cell density was experimentally determined in this study.*

Device Design and Microfabrication

An AOI Chip was fabricated using the soft lithography method as previously described (Kim et al., 2012; Huh et al., 2013). Cured PDMS (15:1, w/w; a mix ratio of the polymer base:curing agent; Dow Corning) was used to prepare the upper and lower microchannel layers demolded from a 3D printed cast made of MicroFine Green MR (Proto Labs). A microporous PDMS membrane was fabricated with PDMS (15:1, w/w) using a silicon wafer that conveys an array of micro-pillars (10 μm in diameter, 20 μm in height, 25 μm in spacing). After the uncured PDMS was poured onto the silicon wafer, covered with a thin fluoropolymer-coated polyester film (3M Scotchpak Release Liners), pressed with a 3 kg weight, then cured in an 80°C dry oven for at least 12 h. The upper PDMS layer was bonded to the PDMS membrane via plasma treatment (Femto Science) and subsequently bonded to the lower layer after corona treatment (Electro-Technic) after alignment under a stereoscope (Leica). The device setup was incubated at 80°C for the permanent bonding for longer than 12 h. Finally, a bent connector (hub-free stainless-steel blunt needle, 18G; Kimble Chase) linked to silicone tubing (Tygon 3350, ID 1/32′′, OD, 3/32′′, Beaverton) was inserted into each microchannel to supply oxic or anoxic cell culture medium or apply vacuum suction. A fabricated AOI chip was sterilized with 70% ethanol (v/v) and completely dried in a 60°C dry oven upon use.

Microfluidic Culture

After the surface activation by UV and ozone treatment (UVO, Jelight Company, Inc.) for 40 min, microchannels were coated with an extracellular matrix mix (collagen I, 30 μg/mL, Sigma; Matrigel, 300 μg/mL, Corning) at 37°C for 1 h. Human intestinal epithelial Caco-2BBE cells (Harvard Digestive Disease Center) resuspended in Dulbecco's Modified Eagle Medium (DMEM, Gibco) containing 20% (v/v) heat-inactivated fetal bovine serum (FBS, Gibco) and antibiotics (100 U/mL penicillin and 100 μg/mL streptomycin, Gibco) were seeded into the upper microchannel (final cell density, 1×10^7 cells/mL) and incubated for the cell attachment at 37°C in a humidified CO_2 incubator for 1 h. The attached cells were further cultured under constant flow (at 50 μL/h, 0.02 dyne/cm^2; Braintree Scientific) and mechanical deformations (10% in cell strain, 0.15 Hz in frequency; Flexcell International Corporation). For the microbial co-culture, the culture medium was replaced with the antibiotic-free medium 24 h before the bacterial cell seeding (final cell density, 1.0×10^7 CFU/mL; CFU, colony forming unit). To create the AOI on-chip, anoxic medium pre-incubated in a glove box overnight was infused into the upper microchannel for 24 h prior to the microbial seeding. After microbial cell attachment on the apical epithelial surface without perfusion for 1 h, microfluidic co-culture culture was resumed under peristalsis-like flow and motions.

Microbial Culture

Two obligate anaerobic bacteria, *Bifidobacterium adolescentis* (DSM 20083) and *Eubacterium hallii* (DSM 17630), were cultivated in the autoclaved tryptic soy broth (Difco) supplemented with 20% (v/v) FBS in an anaerobic glove box conditioned with the anaerobic gas mixture (5% O_2, 5% H_2, and 90% N_2) without shaking at 37°C for 16 h. Bacterial culture broth of each strain was centrifuged at 10,000 × *g* for 1 min; then the cell pellet was resuspended with anoxic and antibiotics-free cell culture medium (final cell density, 1×10^7 CFU/mL) for the seeding into the AOI Chip.

Assessment of Epithelial Barrier Function

Epithelial barrier function was quantified by measuring transepithelial electrical resistance (TEER) using Ag/AgCl electrodes (A-M Systems) connected to an Ohm meter (Fluke Corporation). TEER value was calculated based on the equation, TEER $(\Omega \cdot \mathrm{cm}^2) = (\Omega_t - \Omega_{\mathrm{blank}}) \times A$, where Ω_t is resistance at each time point, Ω_{blank} is a resistance of a cell-free blank chip, and A is a surface area (cm^2) of the microchannel lined by Caco-2 cells.

Real-Time Microfluorimetric Detection of Oxygen

For the detection of oxygen *in situ* in the AOI Chip, platinum dendrimer-encapsulated nanoparticles (Pt-DENs) were used as an alternative to a peroxidase to catalyze the 10-acetyl-3,7-dihydroxyphenoxazine (Amplex Red reagent) into the resorufin in the presence of molecular oxygen. The Pt-DENs synthesized using the dendrimer-templating method (Crooks et al., 2001; Kim and Kim, 2014; Cho et al., 2018) were provided as a gift from Dr. Joohoon Kim. To detect the dissolved oxygen in the microfluidic channel, the cell culture medium pre-conditioned in either oxic or anoxic condition was mixed with Pt-DENs (3 μM) and Amplex Red reagent (500 μM), then added into the microchannel lined by the intestinal villous epithelium in the AOI chip. To create an AOI, the anoxic and oxic media were infused into the upper and lower microchannels, respectively, at 50 μL/h for 1 h. The device was imaged in a confocal microscope (DMi8, Leica) at an excitation and emission wavelength of 563 and 590 nm, respectively. An XZ-vertical scanning was performed in real-time to quantify the fluorescent intensity of the upper and lower channels at three different locations (inlet, middle, and outlet) across the microchannel in the device (**Supplementary Figure 2**). The oxygen tension as a function of fluorescent intensity detected by the confocal microscopy was determined by a calibration curve (**Supplementary Figure 3B**). Briefly, the absolute anoxic medium was prepared in a culture medium containing sodium sulfide (final concentration, 6.5 mM) and the reaction mixture (3 μM Pt DENs and 500 μM Amplex Red reagent; final concentration), then used to estimate the 0% oxygen tension. The saturated oxic medium in the given room temperature and pressure (1 atm) was prepared by mixing a conventional culture medium with the aforementioned reaction mixture to evaluate the 100% oxygen tension. The absolute anoxic medium was also used to obtain an initial kinetic profile of the oxygen dissolution from air into the culture medium in a 96 well plate (**Supplementary Figure 3A**). Finally, these anoxic and oxic media were independently introduced into the upper and lower microchannels in the AOI Chip, then placed in a confocal microscope to obtain micrographs that visualize the XZ scanning at different locations in the AOI Chip. The calibration curve (**Supplementary Figure 3B**) was used to quantitatively estimate oxygen tension in the upper and lower channels (**Figure 3**).

Image Analysis

Immunofluorescence staining of the Caco-2 cells grown in the device was performed to characterize the epithelium of the AOI chip. When Caco-2 epithelium was fully grown under standard oxic culture conditions for a week, the anoxic and oxic media were perfused in the upper and the lower microchannels, respectively. After the AOI cultures for 3 days, cells were fixed (paraformaldehyde, 4%, w/v; Electron Microscopy Science), permeabilized (Triton X-100, 0.3%, v/v; Spectrum Chemical), and blocked [bovine serum albumin (BSA), 2%, w/v; HyClone] by sequentially flowing each reagent at 20 μL/h at room temperature for 15, 30, and 60 min, respectively. The primary antibodies for visualizing ZO-1 (Invitrogen; 50 μg/mL final concentration) and Mucin 2 (Santa Cruz Biotechnology; 40 μg/mL final concentration) were dissolved in the 2% BSA solution, then applied into the microchannel at room temperature for 1.5 h or at 4°C overnight. The secondary antibodies of anti-mouse 488 (50 μg/mL; Abcam) and anti-rabbit 650 (50 μg/mL; Abcam) dissolved in 2% BSA were introduced into the microchannel at room temperature in the dark for 1 h. After washing the microchannels with phosphate buffered saline (PBS; Ca^{2+} and Mg^{2+} free; Gibco), imaging analysis was performed with the confocal microscope (DMi8, Leica).

To perform Live/Dead cell viability assay to the epithelium, a mixture of Calcein AM (4 μM) and ethidium homodimer (EH)-1 (8 μM; ThermoScientific) was used. After villous epithelium was cultured in the AOI Chip for 7 days, the assay solution was perfused into the upper microchannel at 30 μL/h, 37°C for 30 min, then washed with PBS (Ca^{2+}- and Mg^{2+}-free). Images were taken under the confocal microscope (DMi8, Leica). Bacterial microcolonies were visualized by introducing the mixture of live (SYTO 9, 6 μM) and dead reagent (propidium iodide, 30 μM; Thermo Scientific) pre-incubated in the anaerobic glove box for 12 h prior to use. After Live/Dead assay, fluorescent

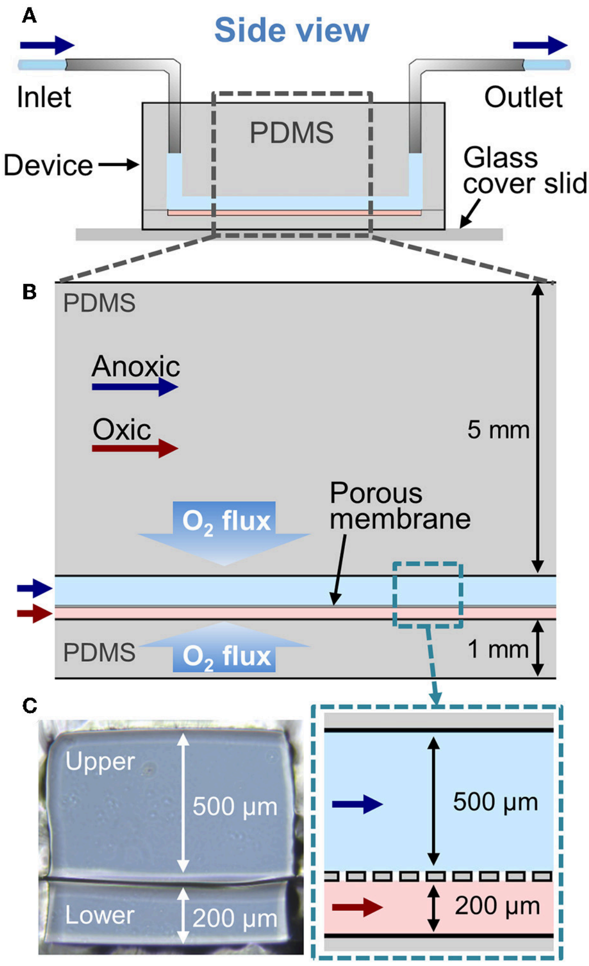

FIGURE 1 | A configuration of the Anoxic-Oxic Interface-on-a-Chip. **(A)** A schematic of the side view of a microfluidic AOI Chip. The upper and the lower microchannel are indicated in light blue and pink, respectively. Arrows indicate the direction of culture medium in the microfluidic channels. **(B)** A zoom-in schematic of the AOI Chip shown in **(A)**. The upper and the lower cell microchannels are separated by a porous PDMS membrane (20 μm in thickness). Blue and red arrows represent the flow of anoxic and oxic culture media, respectively. **(C)** Cross-cut views of the microchannel area in the AOI Chip. A photographic (left) and a schematic (right) zoomed in from the dashed blue box in **(B)**.

images were immediately taken within 10 min to avoid epithelial staining. All the fluorescence imaging was performed using the TCS SPE confocal microscopy (DMi8, Leica) equipped with solid state excitation laser sources of 405, 488, 532, and 635 nm and a PMT. A 25× objective (NA 0.95, Leica) was used for the differential interference contrast (DIC) and fluorescence imaging. The acquisition of an image was performed in the LAS X software (Leica). Bacterial cell viability was quantified based on the integrative intensity of the live and dead signal, read by the ImageJ. The following equation was used to calculate the viability; Viability (%) $= Int_L/(Int_L+Int_D)$, where Int_L indicates the integrative intensity of live cells and Int_D denotes the intensity of dead cells. Epithelial cell viability was quantified based on the live and dead cell number which was counted in ImageJ using the multipoint tool. The viability percentage was then calculated using the following formula; Viability (%) $= Cell_L/(Cell_L+Cell_D)$, where $Cell_L$ stands for the number of live cells counted and $Cell_D$ indicates the number of dead cells counted.

Statistical Analysis

Two-tailed unpaired *t*-test was performed for statistical analysis between the experimental groups. One-way ANOVA with multiple comparison test was used to compare the means among three experimental groups in **Figures 5D** and **6D**. All the statistical analysis was performed using GraphPad Prism 8 (GraphPad Software Inc.). All the plots and error bars were represented as mean ± standard error of the mean (SEM). Differences between experimental groups were considered as statistically significant when $p < 0.05$.

RESULTS

Parameters for Computational Simulation of the AOI On-Chip

To evaluate the feasibility of the AOI Chip model to create an oxygen gradient, we performed a simple 2D computational simulation to model the oxygen flux in the microfluidic device by varying experimental parameters such as the flow rate of culture medium, the diffusion of dissolved oxygen, and the presence or absence of an epithelial layer. Our microfluidic device made of PDMS has two microchannels separated by a thin PDMS porous membrane, in which the inlet and the outlet of each microchannel are connected to the silicone tubing (**Figure 1A**). The upper and the lower microchannels represent the lumen and the capillary side vasculature in the gut, respectively (Kim et al., 2016a). We constantly flowed the culture medium to both microchannels at the same flow rate (range, 50–200 μL/h, equivalent shear stress in the upper microchannel with 500 μm in height is 0.003–0.01 dyne/cm^2). To create the AOI in the device, we perfused the anoxic cell culture medium to the upper microchannel (**Figure 1B**, light blue), whereas the oxic culture medium was flowed into the lower microchannel (**Figure 1B**, light pink). Since PDMS is gas permeable (Merkel et al., 2000), we applied the oxygen flux applied from the upper and the lower PDMS layers as 1.22×10^{-7} and 6.10×10^{-7} mol/m^3, respectively. The different height of each microchannel (e.g., $H_{upper} = 500\,\mu m$ vs. $H_{lower} = 200\,\mu m$) contributed to recreate controllable shear stress to the cells grown on the upper microchannel (**Figure 1C**). The geometry of the 2D microchannel, temperature (37°C), atmospheric pressure (1 atm), and the diffusion coefficient of dissolved oxygen in PDMS and medium were set constant in the simulation. The concentration of dissolved oxygen and the linear flow rate of culture medium in both microchannels were set as the key variables contributing to the formation of transepithelial oxygen gradient in the chip. Oxygen concentration applied in the upper and the lower microchannel was ranged from 0 (i.e., no oxygen) and 0.2 mol/m^3 (i.e., oxygen saturated), respectively. The linear flow rate of culture medium was varied in a range of 27.8–111.2 μm/s (upper) and 69.5–278 μm/s (lower microchannel) as the cross-sectional area is different. Parameters used in the simulation are provided in **Table 1**.

Theoretical Profile of Oxygen Gradient in the Cell-Free AOI Chip

First, we tested the effect of luminal and vascular flow rates on the recreation of AOI in the absence of an epithelial layer. The 2D simulation, in which we flowed the oxic medium through both upper and the lower microchannels at 50 μL/h (equivalent linear flow rate is 27.8 and 69.5 μm/s to the upper and the lower microchannels, respectively), demonstrates a steady influx of oxygen to both the upper and lower channels, and a steady-state aerobic condition is achieved in the AOI Chip (**Figure 2A**). When the anoxic and oxic medium was independently perfused to the upper and the lower microchannel at 50 μL/h, the AOI was partially created approximately 1/3 of the upstream of the microchannels (**Figure 2B**). We found that the oxygen supplied from the lower microchannel progressively diffused through the porous membrane toward the upper microchannel, so parabolic pattern of the convection of dissolved oxygen was observed predominantly in the upper microchannel. This parabolic oxygen gradient was further propagated from the upstream to the downstream of the upper microchannel when the flow rate was increased from 50 to 100 (**Figure 2C**) and 200 μL/h (**Figure 2D**) for both the upper and the lower microchannels (139, and 278 μm/s at the lower microchannel). However, in the absence of the colonic epithelial cell layer, the system failed to create the AOI in the given microenvironmental milieu.

Profile of the Oxygen Gradient in the Epithelium-Containing AOI Chip

Next, we performed an additional computational simulation to see the effect of 3D epithelial microarchitecture that constantly consumes the oxygen in the colonic microenvironment (**Supplementary Figure 1**). When we adopted the same boundary conditions applied to the cell-free simulations in **Figure 2B** (e.g., linear flow rates are 27.8 and 69.5 μm/s at the upper and lower microchannels, respectively) to the epithelium-containing AOI Chip, the oxygen profile in the upper microchannel was remarkably maintained the hypoxic condition in the mid-stream location of the microchannel, whereas the down-stream was nearly anoxic condition at steady-state (**Figure 3B**, upper). Individual line plots at the upper-, mid-, and down-stream regions showed that the anoxic gradient across the

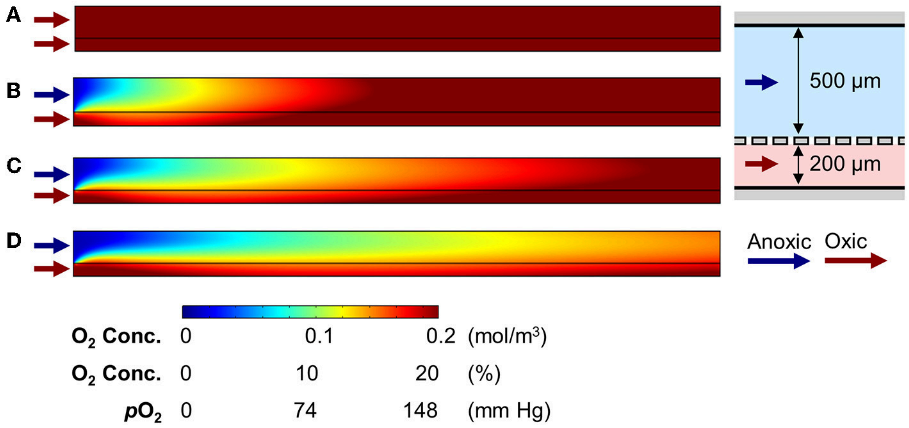

FIGURE 2 | Generation of oxygen gradient in the cell-free AOI Chip by changing the flow rate of anoxic and oxic culture medium. **(A)** A heat map of the computational simulation displays the oxygen concentration gradient established in the microchannels of the AOI Chip when the oxic medium was flowed to both the upper and lower microchannels at 50 µL/h. **(B–D)** Heat maps of the oxygen gradient generated in the AOI Chip by flowing the anoxic (upper) and oxic medium (lower microchannel) at the flow rate of 50 µL/h (27.8 and 69.5 µm/s for upper and lower) **(B)**, 100 µL/h (55.6 and 138 µm/s for upper and lower) **(C)**, and 200 µL/h (111.2 and 278 µm/s for upper and lower) **(D)**. Blue and red arrows represent the flow of anoxic and oxic culture medium, respectively. A side-view schematic of the microchannels is placed in the right inset. A color bar at the bottom shows the scaled gradient of oxygen concentration with various convertible units.

vertical crosscut of the microchannel was successfully recreated (**Figure 3B**, lower). In addition to the computational simulation, actual oxygen gradient generated in the epithelium-containing AOI Chip was visualized in real-time using a fluorescent oxygen indicating reagent (Amplex Red) in concert with the platinum (Pt) dendrimer-encapsulated nanoparticles (Pt-DENs) (Kim and Kim, 2014; Ju and Kim, 2015) in the microchannels (**Figure 3C** and **Supplementary Figure 2**). As a catalyst that converts the dissolved molecular oxygen to reactive oxygen species, we used the Pt-DENs that exhibit peroxidase-like activity comparable to a conventional horseradish peroxidase assay (**Supplementary Figure 3**). In the presence of reactive oxygen species, the Pt-DENs catalyze the oxidation of the Amplex Red reagent to produce fluorescent resorufin. By performing an XZ-vertical scanning of the AOI Chip via confocal microscopy, we quantitatively estimated the level of oxygen tension in the AOI Chip in a spatiotemporal manner (**Figure 3C** and **Supplementary Figure 3**). This result suggests that an AOI is stably formed across entire microchannel in the presence of 3D villous epithelium. However, the presence of an epithelial cell layer was not sufficient to consume the dissolved oxygen and generate the AOI on-chip when the oxic medium was perfused to both upper and lower microchannels (**Figure 3D**), suggesting that the infusion of anoxic culture medium into the lumen microchannel is a necessary approach to recreate the AOI on-chip.

Epithelial Functionality in the AOI Chip

Next, we verified the basic physiological functions of the intestinal epithelium in the AOI Chip by comparing to the epithelial cell functions grown in the oxic control. First, we conditioned the microfluidic device lined by the 3D villous epithelium by flowing the antibiotic-free anoxic and the oxic culture medium in the upper and the lower microchannel, respectively, for at least 12 h before seeding the microbial cells. It is noted that the device was incubated in a conventional humidified 5% CO_2 incubator. Thus, the experimental setup is exposed to the atmospheric oxygen. We verified that the microengineered villi grown in the AOI Chip do not show any compromised epithelial barrier function assessed by measuring the transepithelial electrical resistance (TEER) before and after AOI conditioning for 48 h (**Figure 4A**). We also confirmed that the incubation of an epithelial layer in the AOI for 72 h also does not induce any cell death (**Figure 4B**), compromised expression of tight junction protein (ZO-1) (**Figure 4C**), or decreased level of mucin (MUC) 2-positive epithelium (**Figure 4D**) compared to the oxic control.

Co-culture of Obligate Anaerobic Gut Microbiome in the AOI Chip

To demonstrate the stable co-culture of obligate anaerobic human gut microbiome with the human intestinal epithelial cells in the AOI Chip, we selected commensal *B. adolescentis* and *E. hallii* that have been known to synergistically produce SCFA in the human colon (Belenguer et al., 2006). More importantly, since these two strains are extremely sensitive to oxygen (Shimamura et al., 1992; Flint et al., 2007), it is substantially challenging to keep these microbial cells in the PDMS device lined by the gut epithelium that constantly requires oxygen (Zeitouni et al., 2015).

We performed the co-culture of *B. adolescentis* and *E. hallii*, respectively, in the AOI Chip lined by the villous epithelium and conditioned with the anoxic (lumen) and oxic (capillary) culture medium as optimized in **Figure 4**. After we seeded the *B. adolescentis* cells into the pre-conditioned anoxic upper microchannel, the co-culture setup underwent constant fluid shear stress (0.003 dyne/cm^2) and mechanical deformations (10%, 0.15 Hz) to maintain the steady-state of nutrient as well

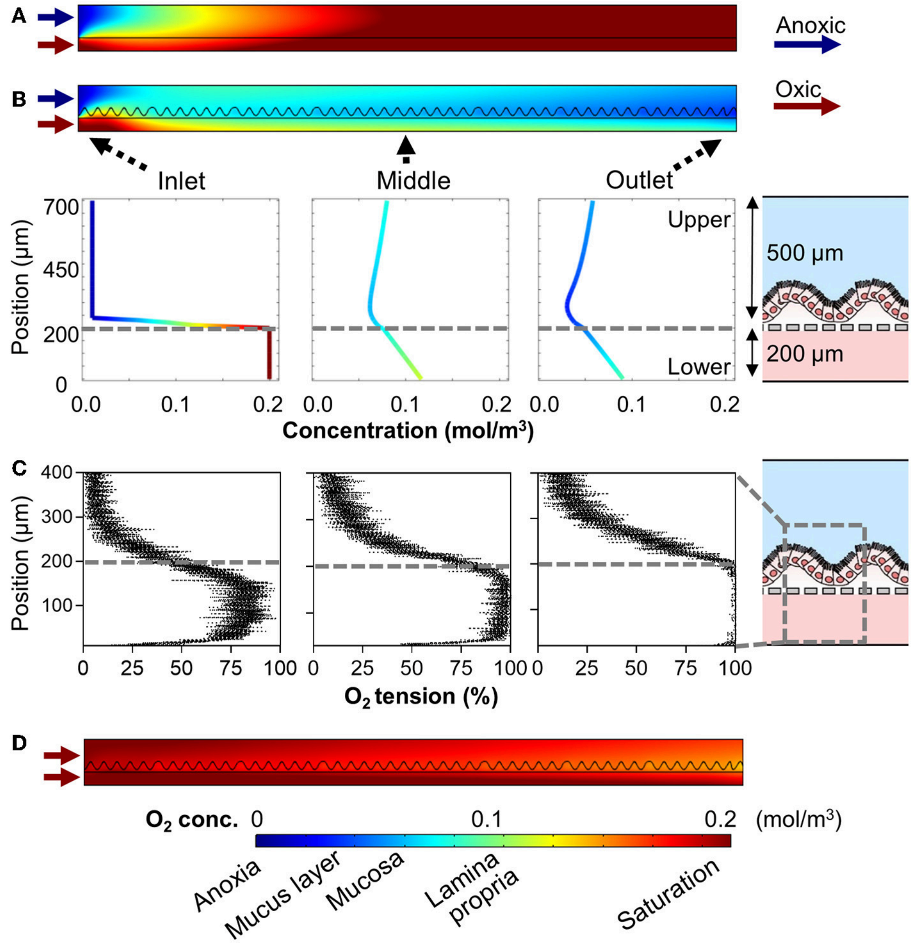

FIGURE 3 | Profiles of the oxygen gradient generated in the AOI Chip in the presence of the 3D intestinal epithelial layer. **(A)** A heat map that computationally simulates the anoxic and oxic flow at 50 μL/h in the upper and the lower microchannels in the absence of an epithelial layer. This heat map is a replica of **Figure 2B** as a reference. **(B)** A heat map of the same computational simulation performed in **(A)** in the presence of a 3D intestinal epithelial layer (an undulating line in the upper microchannel). Colored line plots of the cell channel show the vertical concentration profile of the dissolved oxygen at three representative positions (Inlet, Middle, and Outlet). A relative position of the microchannel is set as 0 and 700 μm to the bottom of the lower microchannel and the top of the upper microchannel, respectively, in the y-axis. Gray dashed lines indicate the position where the porous PDMS membrane exists. A schematic in the right inset shows the XZ-configuration of the AOI Chip lined by the 3D epithelial layer. **(C)** Profiles of actual oxygen concentration generated at the inlet, middle, and outlet of the microchannels in the AOI Chip established at steady state. XZ line scan plots are obtained by the real-time microfluorimetric method via confocal microscopy after flowing the preconditioned culture medium at anoxic (upper) or oxic (lower microchannel) that contains Amplex Red reagent and Pt-DENs catalyst in the AOI Chip lined by the 3D epithelium for 1 h. The volumetric flow rate was fixed at 50 μL/h ($N = 4$). Gray dashed lines indicate the position of a porous PDMS membrane. A gray dashed box in the right schematic shows the location where the microfluorimetry XZ scanning was performed in the AOI Chip. **(D)** A heat map reveals the oxygen gradient in the presence of the intestinal epithelium where the oxic culture medium was flowed to both upper and lower microchannel at 50 μL/h. A color bar at the bottom shows the scaled gradient of oxygen concentration and the corresponding physiological conditions in the intestinal microenvironment. Blue and red arrows represent the flow of anoxic and oxic culture media, respectively.

as oxygen level in the AOI Chip. After 48 and 72 h of the co-culture, we observed that the majority of *B. adolescentis* cells were dead when they are co-cultured in the oxic medium (**Figure 5A**, "Oxic"). On the contrary, *B. adolescentis* cells are progressively colonized and expanded the number of a live population in the AOI Chip (**Figure 5A**, "AOI"), which showed a significant difference in microbial viability compared to the "Oxic" control (**Figure 5B**). A high-power magnification image reveals that the viable population of *B. adolescentis* cells is found at the intervillus crevice (**Figure 5C** and **Supplementary Figure 4A**). We also evaluated the epithelial barrier function by measuring TEER, where the epithelial barrier in the AOI Chip did not show any significant difference from the Control (i.e., the AOI Chip without co-culture with *B. adolescentis* cells). However, the AOI Chip culture showed a significant difference in TEER values from the Oxic control (**Figure 5D**).

To validate the functionality of the AOI Chip, we repeated the same experimental strategy with another commensal gut microbiome, *E. hallii*. This strain is also an obligate anaerobe and the anoxic culture is always required for the colonization (Flint et al., 2007). We found that *E. hallii* cells did not maintain their viability in the microfluidic device under the oxic

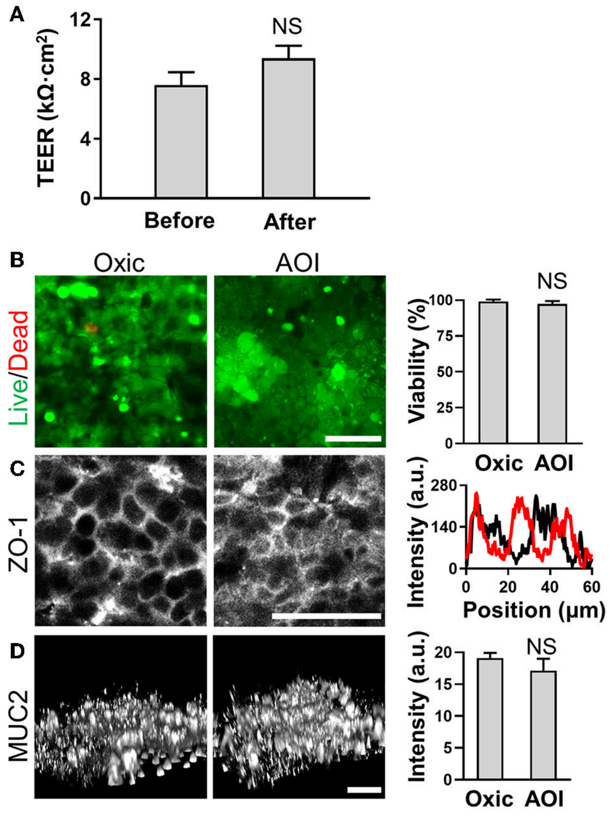

FIGURE 4 | Epithelial barrier function and cell viability in the steady-state AOI on-chip. **(A)** The profile of the epithelial barrier integrity measured by TEER before (Before) and after (After; additional AOI culture for 24 h) the onset of AOI culture in the microfluidic device ($N = 20$). **(B)** The viability of the intestinal epithelium cultured in the presence (Oxic) or the absence (AOI) of oxygen in the upper microchannel whereas the lower microchannel is perfused with oxic medium for 7 days before the assays. The live (green) and dead cells (red) are visualized using Calcein AM (4 μM) and ethidium homodimer-1 (8 μM) in the overlaid confocal micrographs. Representative images are provided, and the quantification of cell viability is provided in the right chart ($N = 6$). **(C)** Expression and localization of the tight junction protein, ZO-1 (left) and the line scan at an arbitrary position of each immunofluorescence image (right). Black and red lines represent the oxic and the AOI, respectively. **(D)** Angled views of the 3D reconstruction of the expressed mucin 2 (MUC2) protein on the 3D intestinal epithelium (left) and the quantitative analysis (right; $N = 3$). NS, not significant. Bars, 50 μm.

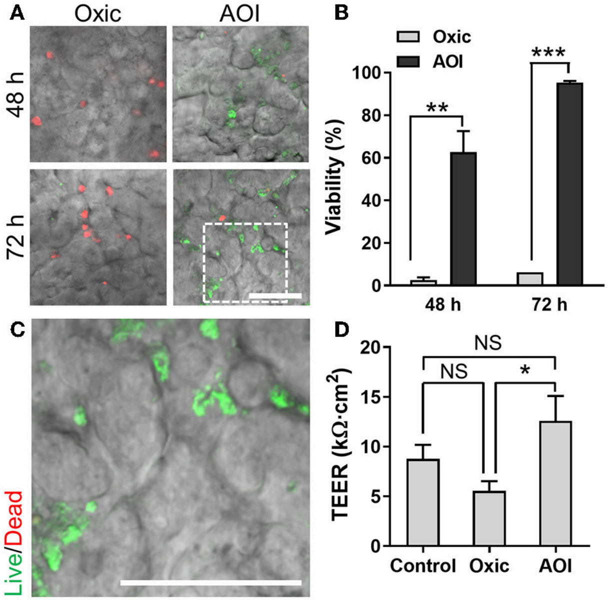

FIGURE 5 | Co-culture of *B. adolescentis* strain with the 3D intestinal epithelial cells in the AOI Chip. **(A)** The viability of *B. adolescentis* cells co-cultured with the epithelium in the AOI Chip visualized by the bacterial Live/Dead assay (live, green; dead, red) in the presence (Oxic) or the absence (AOI) of oxygen in the upper microchannel whereas the lower microchannel is perfused with the oxic medium. Overlaid images are presented by merging a DIC and fluorescence confocal images (red and green channels). For the Live/Dead assay, a mixture of SYTO9 (6 μM) and propidium iodide (30 μM) pre-conditioned in the dark anaerobic glove box was applied into the upper microchannel and assess the bacterial viability assay in a timely manner (<10 min). **(B)** Quantification of the viability of *B. adolescentis* cells by analyzing the Live/Dead assay results using ImageJ ($N = 7$). **(C)** A zoom-in image cropped from the white dashed square in **(A)** shows the live microcolonies of *B. adolescentis* cells. **(D)** Barrier integrity of the intestinal epithelium grown in the modified gut-on-a-chip at various culture conditions. Control, epithelial monoculture in the AOI Chip; Oxic, co-culture with *B. adolescentis* strain in the oxic chip; AOI, co-culture with *B. adolescentis* cells in the AOI Chip. TEER measurement was performed at 72 h of the co-culture ($N = 4$). NS, not significant. *$p < 0.05$, **$p < 0.001$, ***$p < 0.0001$. Bars, 50 μm.

condition (**Figure 6A**, "Oxic"), whereas they decently grow and maintained the viable microcolonies in the AOI Chip (**Figure 6A**, "AOI"). The quantification of cellular viability at 48 and 72 h of the co-culture showed strong evidence that the AOI Chip is necessary and sufficient to maintain the viable population of the obligate anaerobic commensal gut microbiome in the presence of the host epithelium with a statistical significance (**Figure 6B**). The crevicular growth of the viable *E. hallii* cells over 7 days also revealed the stable coexistence of the host cells and the gut microbiome in the AOI Chip (**Figure 6C** and **Supplementary Figure 4B**). We also confirmed that there is no significant difference in the TEER value between groups, indicating that the colonization of the commensal *E. hallii* cells does not compromise the epithelial barrier function (**Figure 6D**). Finally, we demonstrated that both strains were highly viable more than a week of the co-culture (**Figure 7**), suggesting that the AOI Chip provides a compelling transepithelial anoxic gradient that allows a robust maintenance of the anaerobic commensal microbial population in the presence of aerobic host epithelium, by which the longitudinal study of the host-microbiome crosstalk can be performed *in vitro*.

DISCUSSION AND CONCLUSION

In this study, we demonstrated an *in vitro* anoxic-oxic interface (AOI) to co-culture the obligate anaerobic gut microbiome with human intestinal epithelial cells in the modified human gut-on-a-chip microphysiological system and analyzed the oxygen gradient generated in the AOI chip by leveraging the computational simulation and experimental validation. The

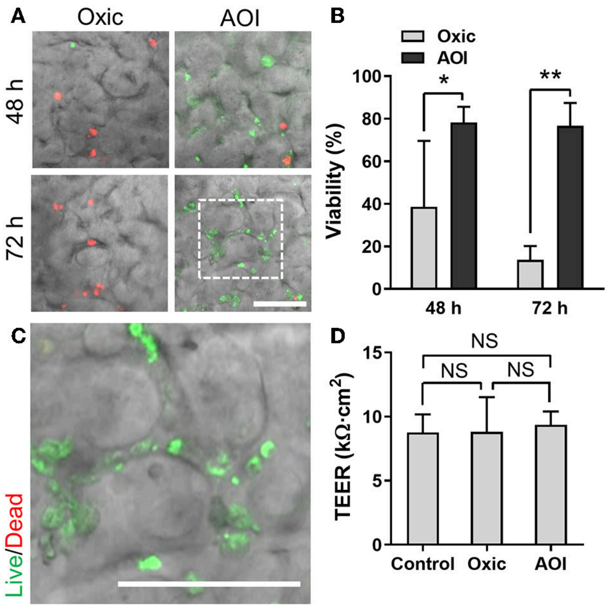

FIGURE 6 | Co-culture of *E. hallii* with the 3D intestinal epithelial cells in the AOI Chip. **(A)** The viability of *E. hallii* cells co-cultured with the epithelium in the AOI Chip visualized by the bacterial Live/Dead assay (live, green; dead, red) in the presence (Oxic) or the absence (AOI) of oxygen in the upper microchannel whereas the lower microchannel was perfused with the oxic medium. Overlaid images are presented by merging a DIC and fluorescence confocal images (red and green channels). For the Live/Dead assay, a mixture of SYTO9 (6 μM) and propidium iodide (30 μM) pre-conditioned in the dark anaerobic glove box was applied into the upper microchannel and assess the bacterial viability assay promptly (<10 min). **(B)** Quantification of the viability of *E. hallii* cells by analyzing the Live/Dead assay results using ImageJ ($N = 5$). **(C)** A zoom-in image cropped from the white dashed square in **(A)** shows the live microcolonies of *E. hallii* cells. **(D)** Barrier integrity of the intestinal epithelium grown in the modified gut-on-a-chip at various culture conditions. Control, epithelial monoculture in the AOI Chip; Oxic, co-culture with *E. hallii* strain in the oxic chip; AOI, co-culture with *E. hallii* cells in the AOI Chip. TEER measurement was performed at 72 h of the co-culture ($N = 4$). NS, not significant. $^*p < 0.05$, $^{**}p < 0.001$. Bars, 50 μm.

salient finding in this study is the experimental verification of an anaerobic-aerobic interface *in vitro* and the validation of its physiological functionality to support the robust and stable co-culture of obligate anaerobic bacteria with the aerobic host epithelium. We proved that this metabolically challenging co-culture was enabled simply by flowing the preconditioned culture medium without any complicated equipment or facility.

In the colonic microenvironment, anaerobic commensal microbiome colonizes the lumen while oxygen steadily diffuses from capillary vessels toward the lumen (Zheng et al., 2015). Thus, the recreation of this *in vivo* oxygen gradient is necessary to recapitulate the structural (e.g., a lumen-capillary interface) and the functional (e.g., a host-gut microbiome co-culture) configuration in the experimental human intestine model. Reconstituting the intestinal AOI is particularly crucial because stable maintenance of this oxygen gradient is linked to various physiological functions. For example, the homeostatic balance of the oxygen gradient and associated reactive oxygen species (ROS) may play an essential role in regulating the onset of digestive diseases (Espey, 2013). Additionally, the maintenance of an AOI can directly contribute to the stability of colonic host-microbiome crosstalk associated with the production of SCFA by the anaerobic commensal gut microbiome. It has been appreciated that the microbial SCFAs prodigiously orchestrate the metabolic homeostasis of the intestinal epithelium, intestinal barrier function, and regulation of immune functions (Smith et al., 2013; Kelly et al., 2015).

Current experimental models have attempted to recreate this microenvironment, but the metabolically-mismatched co-culture has been challenging to maintain *in vitro*. Conventional static cell culture models are extremely limited in generating an AOI because the culture setup must be incubated in a fixed atmospheric condition (e.g., in an anaerobic glove box or a CO_2 incubator), which cannot produce and maintain the AOI. For example, a Transwell culture system may temporarily create an oxygen gradient by introducing anoxic and oxic medium to the apical and basolateral side, respectively, but the culture condition in a 5% CO_2 incubator will rapidly jeopardize the AOI. Furthermore, incubation of the experimental setup in an anaerobic glove box is not appropriate because the introduction of anoxic culture medium substantially compromises cell viability (von Martels et al., 2017). Notably, static cell cultures are limited in demonstrating stable host-microbiome co-culture for an extended period (Kim et al., 2012; Park et al., 2017). Recent microfluidic cell culture models have demonstrated promising results regarding AOI formation *in vitro* (Marzorati et al., 2014; Shah et al., 2016). Introduction of the anoxic and oxic medium into the microbial and epithelial cell microchannels, respectively, established an AOI in both models. However, these models failed to produce a direct contact of the anaerobic microbiome and host epithelium, demonstrated a very short co-culture period (<24 h), and lacked the mechanical deformations that are critical to yield a physiologically accurate intestinal epithelium and sustain stable co-culture (Kim et al., 2016b). The physically segregated compartments in these models also hinder the study of metabolic or pathophysiological crosstalk between the mucosal gut microbiome and the epithelium.

To improve these challenges, we first leveraged the computational simulation to understand the resultant oxygen gradient in a given geometry of the AOI Chip as a function of the linear flow rate and the initial oxygen concentration in the inlet microchannel. We found that a higher linear flow rate may contribute to forming an anoxic or a hypoxic condition in the upper microchannel, suggesting that microfluidic manipulation of the luminal microenvironment may recreate the AOI in our device setup. However, this approach is limited because the flow rate regime in the simulation as well as in the device should accurately mimic the physiological fluidic microenvironment in the colon. The physiological range of the linear flow rate in the ascending colon is approximately 5–30 μm/s (Cremer et al., 2017), and the applied linear flow rate in our experimental model was 27.8 μm/s (equivalent to the volumetric flow rate at 50 μL/h in the microchannel with the height at 500 μm), proving an excellent physiological relevance. Thus, the simple

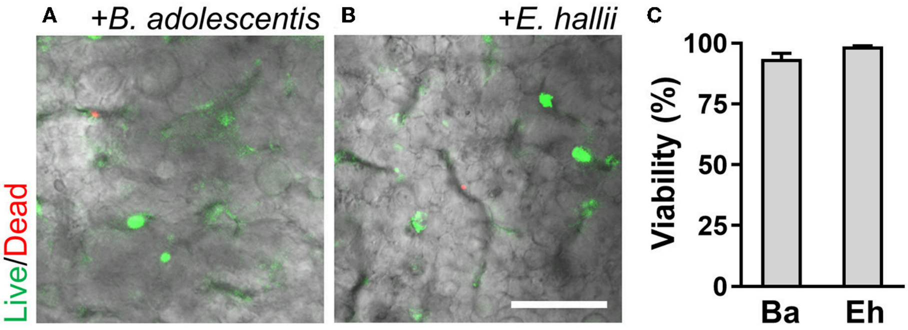

FIGURE 7 | A longitudinal co-culture of the obligate bacteria with 3D intestinal epithelium in the AOI Chip. Bacterial colonies of *B. adolescentis* **(A)** and *E. hallii* **(B)** grown in the intestinal epithelium are highlighted with the fluorescence signals at day 7 of the co-culture. Overlaid images are presented by merging a DIC and fluorescence confocal images (red and green channels). **(C)** Quantification of the viability of bacterial cells by analyzing the Live/Dead assay results using ImageJ ($N = 4$). Ba, *B. adolescentis*; Eh, *E. hallii*. Bar, 50 µm.

increase of the flow rate in a microfluidic device may not reflect the physiological conditions of the colon. Furthermore, in the absence of an epithelium, the generated AOI was only observed upstream of the microchannels even at a volumetric flow rate 200 µL/h, suggesting that the manipulation of the flow rate alone will not recreate a stable AOI across the entire microchannel. Interestingly, the presence of an epithelial cell layer remarkably changed the oxygen gradient in both the upper and lower microchannels even at a flow rate of 50 µL/h. This observation is mainly attributed to the consumption of oxygen by the epithelial cell layer compared to the simulation result in cell-free conditions. The simulation result also revealed that a steady-state AOI is rapidly established at the upstream edge of the AOI Chip and the mucosal hypoxic condition can be stably maintained across the entire channel in the presence of an epithelial cell layer. Notably, our experimental measurement of oxygen tension showed that the oxygen gradient generated vertically revealed a very sharp change across the epithelial barrier whereas we observed only a gradual change in the computational simulation. This result strongly supports that the biological (e.g., epithelial tight junction), structural (e.g., tall villous height), or physiological factors (e.g., a mucus layer, cytodifferentiation) substantially contribute to the formation of transepithelial AOI in the colon. However, the presence of an epithelial layer alone was also not sufficient to create the AOI in the experimental setup, suggesting that microengineered manipulations, including the flow of anoxic medium and the presence of epithelial cell barrier, are necessary and sufficient for building a stable AOI on-chip. Finally, we did not consider the impact of cyclic strains in the computational simulation. However, we routinely applied the cyclic mechanical deformations in the chip studies, where we did not find any evidence that the cyclic mechanical strain jeopardizes the formation of the anoxic-oxic gradient in the AOI Chip.

To experimentally verify the oxygen profile demonstrated in the computational simulation, we used a commercially available resorufin-based oxygen indicating reagent (Amplex Red) to detect the level of dissolved oxygen in the culture medium in an AOI Chip. As a catalyst, we used platinum-based nanoparticles (Pt-DENs) that performs a peroxidase-like activity. Peroxidases have been found to catalyze the oxidation of various compounds including Amplex Red in the presence of molecular oxygen although the catalyzed oxidation is more dramatic with the addition of hydrogen peroxide (Klapper and Hackett, 1963; Wang et al., 2017). The Pt-DENs have been proved to show a peroxidase-like catalytic activity (Ju and Kim, 2015; Lim et al., 2016), where the nanoscale size of this molecule enabled us to readily mix with the culture medium and introduce into the microchannel. More importantly, since the Pt-DENs are considered to be inert with epithelium without any cytotoxicity, we tested it in our experiments to estimate the *in situ* oxygen level with the Amplex Red. By performing an XZ-vertical real-time microfluorimetric scanning via confocal microscopy, we quantitatively evaluated the concentration of oxygen in the AOI Chip in a spatiotemporal manner. It is noted that we established the steady-state condition by flowing the oxic and anoxic medium independently into the lower and upper microchannels, respectively. Thus, our experimental setup also fully reflects the possible oxygen flux from the PDMS layer into the culture medium *in situ*. Importantly, we did not try to collect the effluent from the chip to measure the oxygen level to avoid inaccurate assessment of the oxygen profile inside the AOI Chip.

We modified the design of the upper (luminal) compartment with 500 µm in height for multiple reasons. First, by increasing the height of the upper microchannel, the intestinal epithelium was allowed to grow up to 300–400 µm (unpublished data). Second, as the cells grow higher, the void volume in the upper microchannel is rapidly reduced, causing a substantial increase in fluid shear stress that is applied to the apical brush border of the epithelium. This high shear stress may cause unintended loss of microbial cells that are adherent on the apical brush border of an epithelial cell layer and also can cause undesired epithelial damage. The original gut-on-a-chip microdevice with an upper microchannel height of 150 µm was designed to emulate 0.02 dyne/cm^2 of fluid shear stress when the cells form a monolayer (Kim et al., 2012). To compensate for the effects of the high shear stress after the villi formation, we increased the height of the upper microchannel up to 500 µm, which can decrease the shear stress approximately 10 folds. Finally, the increased height of the upper microchannel allowed determining an appropriate volumetric flow rate that is efficiently recreating the physiological transepithelial anoxic gradient. Through the computational simulation, we found that 50 μL/h of volumetric flow rate (equivalent to 27.8 μm/s of linear flow rate in the microchannel at 500 μm in height) was sufficient to form the anoxic gradient in the presence of the epithelial cells. Furthermore, a higher volumetric flow rate generates a sharper anoxic gradient in the AOI chip. As described before, our current experimental setup with 27.8 μm/s of the linear flow rate also well fits within the range of the physiological condition. On the contrary, the upper microchannel with the 150 μm height in the original gut-on-a-chip results in much higher linear flow rate (92.67 μm/s at 50 μL/h) to form the similar profile of the anoxic gradient, which significantly exceeds the physiological linear flow rate.

The live/dead staining of the intestinal epithelium in the AOI Chip strongly suggested that the influx of dissolved oxygen from the lower microchannel is necessary to maintain epithelial cell viability. This biomimetic oxygen manipulation is analogous to the anatomical configuration of the *in vivo* colonic mucosal microenvironments, in which oxygen is perpetually supplied by the underlying capillary vessels (Zheng et al., 2015). Furthermore, no significant difference of MUC2 and ZO-1 expression and localization was found in the villi grown in the AOI Chip, compared to the oxic control, indicating that epithelial barrier functions are well maintained in this transepithelial anoxic gradient. Additionally, epithelial height ($p = 0.0562$; $N = 3$) and the total number of cells ($p = 0.5019$; $N = 2$) are not significantly different between groups in oxic and AOI. In this microengineered colonic microenvironment, we successfully demonstrated the co-culture of the obligate anaerobic gut microbiome with 3D intestinal epithelial cells for up to a week without any loss of epithelial barrier function. Notably, *B. adolescentis* and *E. hallii* strains are known to be extremely sensitive to oxic conditions, and their sustained viability for up to a week-long co-culture demonstrates the efficacy of our AOI chip (Shimamura et al., 1992; Flint et al., 2007). High-resolution confocal imaging analyses also confirmed that the viable population of either *B. adolescentis* or *E. hallii* was colonized between the 3D microarchitecture of epithelial cells. It is noted that the Live/Dead bacterial cell viability assay assessed in a controlled temporal incubation (<10 min) of the assay solution could demonstrate the stochastic spatial colonization of each strain, without any non-specific staining of the epithelium.

In the human gastrointestinal tract, it is believed that the hypoxic gradient is created due to the initial culture of the intestinal mucosa by oxygen-consuming aerobic bacteria, thus allowing subsequent colonization by obligate anaerobes (Espey, 2013). This phenomenon occurs because the oxygen-tolerant microorganisms reduce oxygen tension and oxygen-reduction potential to levels that support the growth of obligate anaerobic bacteria (Savage, 1978). In our study, instead of copying and pasting the whole complexity of intestinal development, we engineered our device to replicate the anoxic gradient in the gut by simplifying the intestinal complexity in a physiologically relevant epithelial tissue interface. We successfully demonstrated the crucial microenvironmental components that are necessary to recreate the AOI in the living human gut such as 3D epithelial microarchitecture, tight junction barrier, and differentiation of MUC2-positive epithelium that contributes to the mucus production. This physiological gut microenvironment enables the formation of an AOI in the microfluidic device after perfusing anoxic and oxic culture media into the upper (luminal) and the lower (abluminal) microchannels, respectively. Although we omitted the colonization of aerobic microbial species, we verified that the microengineered AOI on-chip is necessary and sufficient to manipulate the oxygen gradient accurately. A transepithelial anoxic gradient established with a spatial resolution of ∼500 μm around the villous epithelial layer enabled a stable co-culture of obligate anaerobic human gut microbiomes such as *B. adolescentis* and *E. hallii*. By applying the central concept of reverse microengineering, we minimized the biological complexity while still demonstrating the critical elements of a symbiotic ecosystem in the human gut. We believe that our current study shows how to build and validate this physiologically functional circuit to emulate biological complexity.

We selected *B. adolescentis* and *E. hallii* as the representative anaerobic commensal gut microbiome because of their unique contributions to human colon homeostasis. *B. adolescentis* strain predominantly degrades the prebiotic fibers (e.g., inulin or fructooligosaccharides) and produces acetate during the process of fermentation in the colon (Macfarlane and Macfarlane, 2003). *E. hallii* strain utilizes this acetate and produces the SCFA butyrate (Engels et al., 2016). To quantify the potential probiotic effect of these co-cultured bacteria on the viability and the functionality of the epithelial cells, we measured TEER values and determined the epithelial barrier function. Interestingly, the epithelial barrier integrity was significantly increased in the co-culture of *B. adolescentis* in the AOI condition compared to its control culture in the oxic medium (**Figure 5D**), whereas co-culture with *E. hallii* did not cause any significant difference in the barrier integrity (**Figure 6D**). This observation is possibly due to the production of SCFA, such as acetate, by *B. adolescentis*, whereas *E. hallii* requires precursor molecules such as acetate to produce other SCFA such as butyrate. Thus, a lack of intermediate metabolic compounds may limit the functionality of the *E. hallii* strain in this experimental format. A future study investigating the co-culture of both species in the AOI Chip may demonstrate the syntrophic cross-feeding between these two strains and exhibit the unique microbial crosstalk that occurs in the gut.

In conclusion, we experimentally and computationally demonstrated that the transepithelial anoxic gradient in the AOI Chip is necessary and sufficient to co-culture the metabolically mismatched obligate anaerobic gut microbiome with the aerobic host epithelial cells. We showed that the oxygen gradient could be successfully recreated and sustained without needing a complicated, resource-intensive apparatus to maintain the anoxic conditions necessary for creating the AOI. Additionally, all experiments were performed in conventional aerobic lab equipment (e.g., a humidified CO_2

incubator). Thus, our experimental setup does not require the anaerobic glove box to perform AOI-related experiments. The successful co-culture of obligate gut anaerobes in the AOI Chip can potentially lead to studies involving the host-microbiome crosstalk germane to the homeostasis of gastrointestinal functions, regulation of tissue-specific resident immune cells, or the pathophysiology of the intestinal disease. Furthermore, testing the chyme, or indigestible carbohydrates (i.e., prebiotics) with the gut microbiome in our AOI Chip will more closely mimic the chemical microenvironment of the human colon, which can be potential future directions of our study.

AUTHOR CONTRIBUTIONS

WS, AW, MM, CF, NT, D-WL, HK, and HJK designed the study. WS, AW, MM, CF, NT, and HJK performed experiments and analyzed data. YJ and JK provided an experimental resource. WS, AW, MM, CF, NT, and HJK wrote and revised the manuscript.

FUNDING

This work was supported in part by the Alternatives in Scientific Research of The International Foundation for Ethical Research Graduate Fellowship (UTA15-001318 to WS), the Bio & Medical Technology Development Program of the National Research Foundation (NRF) funded by the Ministry of Science and ICT (2018M3A9H3025030 to WS, D-WL, HK, and HJK), Cancer Research Institute (UTA18-000889 to HJK), Alternative Research and Development Foundation (UTA18-001198 to HJK), and the National Research Foundation of Korea funded by the Ministry of Science, ICT and Future Planning (NRF-2017R1A2B4004285 to YJ and JK).

SUPPLEMENTARY MATERIAL

The Supplementary Material for this article can be found online at: https://www.frontiersin.org/articles/10.3389/fbioe.2019.00013/full#supplementary-material

REFERENCES

Albenberg, L., Esipova, T. V., Judge, C. P., Bittinger, K., Chen, J., Laughlin, A., et al. (2014). Correlation between intraluminal oxygen gradient and radial partitioning of intestinal microbiota in humans and mice. *Gastroenterology* 147, 1055–1063.e1058. doi: 10.1053/j.gastro.2014.07.020

Bäckhed, F., Fraser, C. M., Ringel, Y., Sanders, M. E., Sartor, R. B., Sherman, P. M., et al. (2012). Defining a healthy human gut microbiome: current concepts, future directions, and clinical applications. *Cell Host Microbe* 12, 611–622. doi: 10.1016/j.chom.2012.10.012

Bein, A., Shin, W., Jalili-Firoozinezhad, S., Park, M. H., Sontheimer-Phelps, A., Tovaglieri, A., et al. (2018). Microfluidic organ-on-a-chip models of human intestine. *Cell Mol. Gastroenterol. Hepatol.* 5, 659–668. doi: 10.1016/j.jcmgh.2017.12.010

Belenguer, A., Duncan, S. H., Calder, A. G., Holtrop, G., Louis, P., Lobley, G. E., et al. (2006). Two routes of metabolic cross-feeding between bifidobacterium adolescentis and butyrate-producing anaerobes from the human gut *Appl. Environ. Microbiol.* 72, 3593–3599. doi: 10.1128/AEM.72.5.3593-3599.2006

Buchwald, P. (2009). FEM-based oxygen consumption and cell viability models for avascular pancreatic islets. *Theoret. Biol. Med. Model.* 6:5. doi: 10.1186/1742-4682-6-5

Cho, T., Yoon, C. W., and Kim, J. (2018). Repetitively coupled chemical reduction and galvanic exchange as a synthesis strategy for expanding applicable number of Pt atoms in dendrimer-encapsulated Pt nanoparticles. *Langmuir* 34, 7436–7444. doi: 10.1021/acs.langmuir.8b01169

Chu, H. (2017). Host gene–microbiome interactions: molecular mechanisms in inflammatory bowel disease. *Gen. Med.* 9:69. doi: 10.1186/s13073-017-0459-4

Cox, M., and Dunn, B. (1986). Oxygen diffusion in poly (dimethyl siloxane) using fluorescence quenching. I. Measurement technique and analysis. *J. Polymer Sci. Part A Polymer Chem.* 24, 621–636. doi: 10.1002/pola.1986.080240405

Cremer, J., Arnoldini, M., and Hwa, T. (2017). Effect of water flow and chemical environment on microbiota growth and composition in the human colon. *Proc. Natl. Acad. Sci. U. S. A.* 114, 6438–6443. doi: 10.1073/pnas.1619598114

Crooks, R. M., Zhao, M., Sun, L., Chechik, V., and Yeung, L. K. (2001). Dendrimer-encapsulated metal nanoparticles: synthesis, characterization, and applications to catalysis. *Acc. Chem. Res.* 34, 181–190. doi: 10.1021/ar000110a

Engels, C., Ruscheweyh, H. J., Beerenwinkel, N., Lacroix, C., and Schwab, C. (2016). The common gut microbe *Eubacterium hallii* also contributes to intestinal propionate formation. *Front. Microbiol.* 7:713. doi: 10.3389/fmicb.2016.00713

Espey, M. G. (2013). Role of oxygen gradients in shaping redox relationships between the human intestine and its microbiota. *Free Rad. Biol. Med.* 55, 130–140. doi: 10.1016/j.freeradbiomed.2012.10.554

Flint, H. J., Duncan, S. H., Scott, K. P., and Louis, P. (2007). Interactions and competition within the microbial community of the human colon: links between diet and health. *Environ. Microbiol.* 9, 1101–1111. doi: 10.1111/j.1462-2920.2007.01281.x

Giulitti, S., Magrofuoco, E., Prevedello, L., and Elvassore, N. (2013). Optimal periodic perfusion strategy for robust long-term microfluidic cell culture. *Lab. Chip* 13, 4430–4441. doi: 10.1039/c3lc50643f

Huh, D., Kim, H. J., Fraser, J. P., Shea, D. E., Khan, M., Bahinski, A., et al. (2013). Microfabrication of human organs-on-chips. *Nat. Prot.* 8:2135. doi: 10.1038/nprot.2013.137

Ju, Y., and Kim, J. (2015). Dendrimer-encapsulated Pt nanoparticles with peroxidase-mimetic activity as biocatalytic labels for sensitive colorimetric analyses. *Chem. Commun.* 51, 13752–13755. doi: 10.1039/C5CC06055A

Kelly, C. J., Zheng, L., Campbell, E. L., Saeedi, B., Scholz, C. C., Bayless, A. J., et al. (2015). Crosstalk between microbiota-derived short-chain fatty acids and intestinal epithelial HIF augments tissue barrier function. *Cell Host Microbe* 17, 662–671. doi: 10.1016/j.chom.2015.03.005

Kim, H. J., Huh, D., Hamilton, G., and Ingber, D. E. (2012). Human gut-on-a-chip inhabited by microbial flora that experiences intestinal peristalsis-like motions and flow. *Lab Chip* 12, 2165–2174. doi: 10.1039/c2lc40074j

Kim, H. J., Lee, J., Choi, J. H., Bahinski, A., and Ingber, D. E. (2016a). Co-culture of living microbiome with microengineered human intestinal villi in a gut-on-a-chip microfluidic device. *J. Vis. Exp.* 114:54344. doi: 10.3791/54344

Kim, H. J., Li, H., Collins, J. J., and Ingber, D. E. (2016b). Contributions of microbiome and mechanical deformation to intestinal bacterial overgrowth and inflammation in a human gut-on-a-chip. *Proc. Natl. Acad. Sci. U. S. A.* 113, E7–E15. doi: 10.1073/pnas.1522193112

Kim, Y., and Kim, J. (2014). Modification of indium tin oxide with dendrimer-encapsulated nanoparticles to provide enhanced stable electrochemiluminescence of Ru (bpy) 32+/tripropylamine while preserving optical transparency of indium tin oxide for sensitive electrochemiluminescence-based analyses. *Anal. Chem.* 86, 1654–1660. doi: 10.1021/ac403415m

Klapper, M. H., and Hackett, D. P. (1963). The oxidatic activity of horseradish peroxidase I. Oxidation of hydro-and naphthohydroquinones. *J. Biol. Chem.* 238, 3736–3742.

Krajmalnik-Brown, R., Ilhan, Z. E., Kang, D. W., and DiBaise, J. K. (2012). Effects of gut microbes on nutrient absorption and energy regulation. *Nutr. Clin. Pract.* 27, 201–214. doi: 10.1177/0884533611436116

Leslie, J. L., Huang, S., Opp, J. S., Nagy, M. S., Kobayashi, M., Young, V. B., et al. (2015). Persistence and toxin production by clostridium difficile within human intestinal organoids result in disruption of epithelial paracellular barrier function. *Infect. Immun.* 83, 138–145. doi: 10.1128/IAI.02561-14

Lim, H., Ju, Y., and Kim, J. (2016). Tailoring catalytic activity of Pt nanoparticles encapsulated inside dendrimers by tuning nanoparticle sizes with subnanometer accuracy for sensitive chemiluminescence-based analyses. *Anal. Chem.* 88, 4751–4758. doi: 10.1021/acs.analchem.6b00073

Lin, C. S., Liu, L. T., Ou, L. H., Pan, S. C., Lin, C. I., and Wei, Y.-H. (2018). Role of mitochondrial function in the invasiveness of human colon cancer cells. *Oncol. Rep.* 39, 316–330. doi: 10.3892/or.2017.6087

Luca, F., Kupfer, S. S., Knights, D., Khoruts, A., and Blekhman, R. (2018). Functional genomics of host–microbiome interactions in humans. *Trends Genet.* 34, 30–40. doi: 10.1016/j.tig.2017.10.001

Macfarlane, S., and Macfarlane, G. T. (2003). Regulation of short-chain fatty acid production. *Proc. Nutr. Soc.* 62, 67–72. doi: 10.1079/PNS2002207

Marzorati, M., Vanhoecke, B., De Ryck, T., Sadaghian Sadabad, M., Pinheiro, I., Possemiers, S., et al. (2014). The HMI$^{\mathrm{TM}}$ module: a new tool to study the Host-Microbiota Interaction in the human gastrointestinal tract *in vitro*. *BMC Microbiol.* 14, 133–133. doi: 10.1186/1471-2180-14-133

Mattei, G., Giusti, S., and Ahluwalia, A. (2014). Design criteria for generating physiologically relevant *in vitro* models in bioreactors. *Processes* 2, 548–569. doi: 10.3390/pr2030548

Mehta, K., and Linderman, J. J. (2006). Model-based analysis and design of a microchannel reactor for tissue engineering. *Biotechnol. Bioengin.* 94, 596–609. doi: 10.1002/bit.20857

Merkel, T., Bondar, V., Nagai, K., Freeman, B., and Pinnau, I. (2000). Gas sorption, diffusion, and permeation in poly (dimethylsiloxane). *J. Polymer Sci. Part B Polymer Phys.* 38, 415–434. doi: 10.1002/(SICI)1099-0488(20000201)38:3<415::AID-POLB8>3.0.CO;2-Z

Park, G. S., Park, M. H., Shin, W., Zhao, C., Sheikh, S., Oh, S. J., et al. (2017). Emulating host-microbiome ecosystem of human gastrointestinal tract *in vitro*. *Stem Cell Rev. Rep.* 13, 321–334. doi: 10.1007/s12015-017-9739-z

Sadaghian Sadabad, M., von Martels, J. Z., Khan, M. T., Blokzijl, T., Paglia, G., Dijkstra, G., et al. (2015). A simple coculture system shows mutualism between anaerobic faecalibacteria and epithelial Caco-2 cells. *Sci. Rep.* 5:17906. doi: 10.1038/srep17906

Savage, D. C. (1978). Factors involved in colonization of the gut epithelial surface. *Am. J. Clin. Nutr.* 31, S131–S135. doi: 10.1093/ajcn/31.10.S131

Shah, P., Fritz, J. V., Glaab, E., Desai, M. S., Greenhalgh, K., Frachet, A., et al. (2016). A microfluidics-based *in vitro* model of the gastrointestinal human–microbe interface. *Nat. Commun.* 7:11535. doi: 10.1038/ncomms 11535

Shimamura, S., Abe, F., Ishibashi, N., Miyakawa, H., Yaeshima, T., Araya, T., et al. (1992). Relationship between oxygen sensitivity and oxygen metabolism of bifidobacterium species. *J. Dairy Sci.* 75, 3296–3306. doi: 10.3168/jds.S0022-0302(92)78105-3

Shin, W., and Kim, H. J. (2018a). "Chapter 7 - Pathomimetic modeling of human intestinal diseases and underlying host-gut microbiome interactions in a gut-on-a-chip," in *Methods in Cell Biology*, eds. J. Doh, D. Fletcher and M. Piel (Cambridge, MA: Academic Press), 135–148.

Shin, W., and Kim, H. J. (2018b). Intestinal barrier dysfunction orchestrates the onset of inflammatory host–microbiome cross-talk in a human gut inflammation-on-a-chip. *Proc. Natl. Acad. Sci. U. S. A.* 115, E10539–E10547. doi: 10.1073/pnas.1810819115

Smith, P. M., Howitt, M. R., Panikov, N., Michaud, M., Gallini, C. A., Bohlooly,-Y., et al. (2013). The microbial metabolites, short-chain fatty acids, regulate colonic treg cell homeostasis. *Sciencec* 341, 569–573. doi: 10.1126/science.1241165

Swanson, H. I. (2015). Drug metabolism by the host and gut microbiota: a partnership or rivalry? *Drug Metabol. Dispos.* 43, 1499–1504. doi: 10.1124/dmd.115.065714

Ulluwishewa, D., Anderson, R. C., Young, W., McNabb, W. C., van Baarlen, P., Moughan, P. J., et al. (2014). Live Faecalibacterium prausnitzii in an apical anaerobic model of the intestinal epithelial barrier. *Cell. Microbiol.* 17, 226–240. doi: 10.1111/cmi.12360

von Martels, J. Z. H., Sadaghian Sadabad, M., Bourgonje, A. R., Blokzijl, T., Dijkstra, G., Faber, K. N., et al. (2017). The role of gut microbiota in health and disease*: in vitro* modeling of host-microbe interactions at the aerobe-anaerobe interphase of the human gut. *Anaerobe* 44, 3–12. doi: 10.1016/j.anaerobe.2017.01.001

Walker, A. W., Duncan, S. H., Louis, P., and Flint, H. J. (2014). Phylogeny, culturing, and metagenomics of the human gut microbiota. *Trends Microbiol.* 22, 267–274. doi: 10.1016/j.tim.2014.03.001

Walsh, C. J., Guinane, C. M., O'Toole, P. W., and Cotter, P. D. (2014). Beneficial modulation of the gut microbiota. *FEBS Lett.* 588, 4120–4130. doi: 10.1016/j.febslet.2014.03.035

Wang, T., Xiang, Y., Liu, X., Chen, W., and Hu, Y. (2017). A novel fluorimetric method for laccase activities measurement using Amplex Red as substrate. *Talanta* 162, 143–150. doi: 10.1016/j.talanta.2016.10.006

Zeitouni, N. E., Fandrey, J., Naim, H. Y., and von Köckritz-Blickwede, M. (2015). Measuring oxygen levels in Caco-2 cultures. *Hypoxia* 3:53. doi: 10.2147/HP.S85625

Zheng, L., Kelly, C. J., and Colgan, S. P. (2015). Physiologic hypoxia and oxygen homeostasis in the healthy intestine. A review in the theme: cellular responses to Hypoxia. *Am. J. Physiol. Cell Physiol.* 309, C350–C360. doi: 10.1152/ajpcell.00191.2015

Zhernakova, A., Kurilshikov, A., Bonder, M. J., Tigchelaar, E. F., Schirmer, M., Vatanen, T., et al. (2016). Population-based metagenomics analysis reveals markers for gut microbiome composition and diversity. *Science* 352, 565–569. doi: 10.1126/science.aad3369

Conflict of Interest Statement: The authors declare that the research was conducted in the absence of any commercial or financial relationships that could be construed as a potential conflict of interest.

frontiers in Bioengineering and Biotechnology

ORIGINAL RESEARCH
published: 18 February 2019
doi: 10.3389/fbioe.2019.00017

In vitro Liver Zonation of Primary Rat Hepatocytes

Lauren Tomlinson[1], Lauren Hyndman[2], James W. Firman[1,3], Robert Bentley[1], Jonathan A. Kyffin[4], Steven D. Webb[4,5], Sean McGinty[2] and Parveen Sharma[1]*

[1] MRC Centre for Drug Safety Science, Department of Clinical and Molecular Pharmacology, University of Liverpool, Liverpool, United Kingdom, [2] Division of Biomedical Engineering, University of Glasgow, Glasgow, United Kingdom, [3] Department of Pharmacy and Biomolecular Science, Liverpool John Moores University, Liverpool, United Kingdom, [4] Department of Applied Mathematics, Liverpool John Moores University, Liverpool, United Kingdom, [5] EPSRC Liverpool Centre for Mathematics in Healthcare, Department of Mathematical Sciences, University of Liverpool, Liverpool, United Kingdom

The ability of the liver to simultaneously carry out multiple functions is dependent on the metabolic heterogeneity of hepatocytes spatially located within a liver lobule spanning from the portal triad to the central vein. This complex zonal architecture of the liver, however, makes accurate *in vitro* modeling a challenge and often standard culture systems assume a homogenous model which may lead to inaccurate translatability of results. Here, we use a combination of mathematical modeling and experimental data to demonstrate a readily constructible *in vitro* flow system capable of liver zonation in primary rat hepatocytes. We show the differential expression of zonation markers, enhanced functionality when compared to standard static cultures and zone-specific metabolism and cell damage in the presence of paracetamol, a known zone-specific toxin. This type of advanced system provides a more in-depth and essential understanding of liver physiology and pathophysiology as well as the accurate evaluation of pharmacological interventions at a zone-specific level.

Keywords: liver zonation, mathematical modeling, flow system, drug-induced liver injury, *in vitro* model

Edited by:
Massimo Alberti,
*Agency for Science, Technology and Research (A*STAR), Singapore*

Reviewed by:
Ciprian Iliescu,
National University of Singapore, Singapore
Giovanni Vozzi,
University of Pisa, Italy

***Correspondence:**
Parveen Sharma
parveen.sharma@liverpool.ac.uk

Specialty section:
This article was submitted to Tissue Engineering and Regenerative Medicine, a section of the journal Frontiers in Bioengineering and Biotechnology

***Received:** 30 August 2018*
***Accepted:** 23 January 2019*
***Published:** 18 February 2019*

Citation:
Tomlinson L, Hyndman L, Firman JW, Bentley R, Kyffin JA, Webb SD, McGinty S and Sharma P (2019) In vitro Liver Zonation of Primary Rat Hepatocytes. Front. Bioeng. Biotechnol. 7:17. doi: 10.3389/fbioe.2019.00017

INTRODUCTION

Drug-induced liver injury (DILI) represents a major global human health concern and is one of the most common side effects of many therapeutic compounds, leading to a high incidence of patient morbidity and mortality (Gaskell et al., 2016). Exposure to hepatotoxic compounds can result in liver failure, a life threatening condition usually requiring a liver transplant (Reuben et al., 2010). DILI carries a mortality rate of around 10% (Singh et al., 2016) which can be attributed to a poor understanding of the mechanisms underlying the toxic response and to a lack of appropriate tools for the prediction of toxic outcome. Current *in vitro* test systems include simple liver-derived 2 dimensional (2D) cell-based models that are poorly predictive of toxicity (Williams et al., 2013). Further complexity arises since it has previously been determined that hepatocytes in the liver are a heterogeneous population and, that in order to cope with an immense spectrum of functions which are performed simultaneously, liver cells show a considerable heterogeneity and functional plasticity known as metabolic zonation (Colnot and Perret, 2011). Hepatocytes within the liver sinusoid are exposed to varying gradients of oxygen, nutrients, hormones, and metabolites giving rise to zonation whereby cells along the sinusoid have vastly different levels of gene expression and metabolic competence (Kietzmann, 2017). The 3 main zones (**Figure 1**) along a sinusoidal unit, namely periportal (PP), central lobular (CL) and perivenous (PV), are functionally and biochemically different affecting key functions such as ammonia detoxification, glucose/energy metabolism (PP), and xenobiotic metabolism (PV) (Colnot and Perret, 2011). Hepatocytes located in the periportal region surround the portal triad, in close proximity to the blood, which is associated with zone 1. Perivenous hepatocytes associated with zone 3 are situated near the efferent centrilobular vein. Zone 2 consists of hepatocytes which are positioned in the midlobular region (Birchmeier, 2016; Kietzmann, 2017). Therefore, standard cell culture techniques that assume a homogeneous population may not provide the best biological test model to emulate DILI. It is well-established that an oxygen gradient exists throughout the three liver zones (Colnot and Perret, 2011; Birchmeier, 2016; Kietzmann, 2017) and that this gradient may contribute in part to the differential metabolic functions along the liver sinusoid (Allen and Bhatia, 2003). The liver receives highly oxygenated blood from the hepatic artery, whereas oxygen depleted blood is associated with the hepatic portal vein. In contrast, hepatocytes cultured under standard conditions in an *in vitro* environment receive a uniform oxygen supply thereby not accurately emulating an *in vivo* environment.

Using a combination of mathematical modeling and experimental data, we have designed and developed a zonated *in vitro* liver model using 3 chambers in the Quasi Vivo system[1]. By varying the elevation of cells within the system, the oxygen tension that the cells are exposed to also varies. The resulting model is therefore more representative of an *in vivo* system in which cells are exposed to multiple solute gradients, shear stress, circulating nutrients and mechanical compression. By using primary rat hepatocytes (PRH), we have shown that the cells exhibit differential protein expression and toxicity profiles when exposed to known hepatotoxins, mimicking a response more like that seen *in vivo*.

METHODS

Primary Rat Hepatocyte Sandwich Culture

Hepatocytes were isolated from Wistar rats. This study was carried out in accordance with the principles of the Basel Declaration and recommendations of ARRIVE guidelines issued by the NC3Rs, with approval from the University of Liverpool's AWERB committee (Animal Welfare and Ethical Review Body). The University is a signatory on the concordat on openness in animal research and all work was authorized by the Home Office under the Animals (Scientific Procedures) act 1986 and the EU Directive. Primary rat hepatocytes were cultured using Williams' E media, supplemented with 10% heat inactivated FBS, 1% transferrin, 1% L-glutamine, 1% penicillin streptomycin, and 100 nM dexamethasone. Glass cover slips (13 mm) were collagen-coated 1:60 with rat tail collagen 1 and acetic acid prior to cell seeding. Cells were seeded at a density of 1×10^6 per well in a 24-well plate. Following 3 h post seeding, cover slips were coated with 1:80 dilution of Matrigel (Corning) in Williams' E media, prior to overnight incubation at 37°C with a humidified atmosphere of 5% CO_2.

Kirkstall Quasi Vivo Flow System

The Kirkstall QV-900 is a millifluidic media perfusion system that enables cells to be cultured in a slow-flow environment (**Figure 2A**). The QV-900 was washed in 20 ml of 70% IPA followed by two washes with Hanks solution. The glass cover slips containing the PRH sandwich cultures were placed in to each chamber on three different levels determined by the mathematical modeling to represent the perivenous, central, and periportal zones (**Figure 2B**). Each QV-900 circuit consisted of a total of 20 ml of Williams' E media flowing through the cells chamber, tubes and reservoir bottle. The system was set up at a flow rate of 150 μl/min and incubated at 37°C with a humidified atmosphere of 5% CO_2 for 72 h. Comparisons were made to static cultures in which cells were grown in identical conditions but placed in a standard 6-well cell culture plate (Corning) without flow.

Mathematical Modeling of Zonated Liver

We developed a mathematical model of fluid flow, oxygen transport and consumption of oxygen by the cells within the QV-900 chambers. The fluid flow was described by the steady Navier-Stokes equations, with the transport of oxygen described by a convection-diffusion equation. Consumption of oxygen by the cells was modeled via Michaelis-Menten kinetics and implemented through a flux boundary condition. For full details of the model equations, boundary conditions, solution method and parameters, the reader is referred to the **Supplementary Material**.

The mathematical model was employed to estimate the oxygen concentration at the cell surface for a variety of chamber depths, with the aim of generating a physiologically relevant oxygen gradient across 3 chambers, representing the periportal, central, and perivenous zones. The chamber depths were chosen such that the oxygen concentration ranged from approximately 4–15% (Mazzei et al., 2010) across the 3 chambers. In order to alter the depth at which cells were cultured in the chambers, inserts were produced with the heights determined from the mathematical modeling.

Adenosine Triphosphate (ATP) Cell Viability Assay

ATP cell viability assay was performed using CellTiter-Glo Luminescent Cell Viability Assay (Promega) following manufacturer's instructions.

Bradford Assay

Total protein concentration was calculated using Bradford Reagent (Sigma) using manufacturer's instructions. Briefly, a standard curve was generated using known concentrations of bovine serum albumin (Sigma) and used to calculate sample concentrations using a Varioskan Flash plate reader (Thermo Scientific).

Lactate Dehydrogenase (LDH) Release

LDH release was measured using Cytotoxicity detection kit (Sigma) following manufacturer's instructions. Briefly, total LDH was calculated by the summation of the LDH measured in the cell

---

[1] Available online at: http://www.kirkstall.com/about-kirkstall/

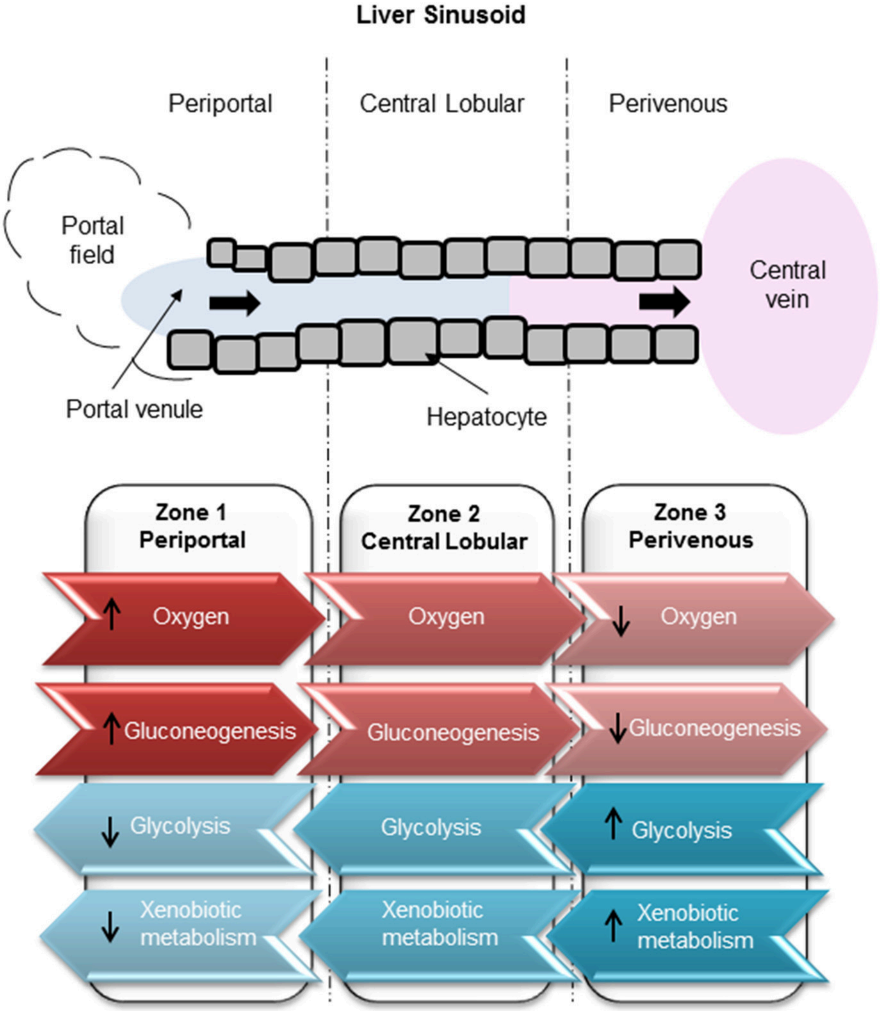

FIGURE 1 | Zonation of liver metabolism. High oxygen exposure of hepatocytes in the periportal region compared to low exposure in the perivenous zone. Glucose production carried out through gluconeogenesis in the periportal zone. Glucose utilization carried out by glycolysis in the perivenous zone.

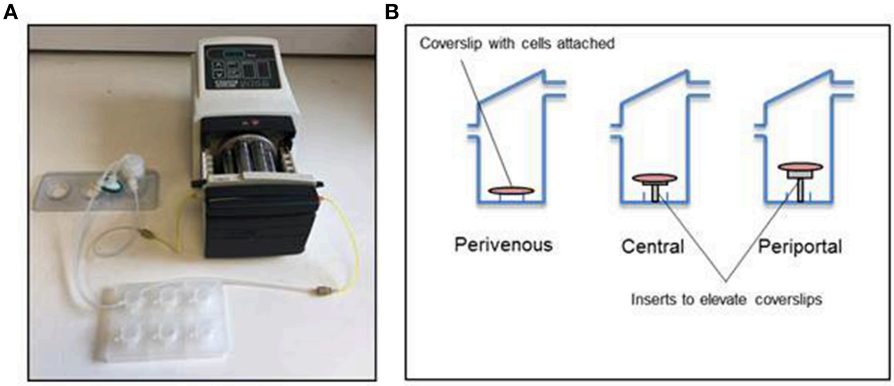

FIGURE 2 | Kirkstall QV-900 setup. **(A)** Kirkstall QV-900 plates are connected using Tygon silicone tubing to reservoir bottle (Kirkstall) and then connected to a multi-channel cassette pump (Watson-Marlow) using manifold tubing (Watson-Marlow). **(B)** Schematic of setup on the inside of the QV-900 wells.

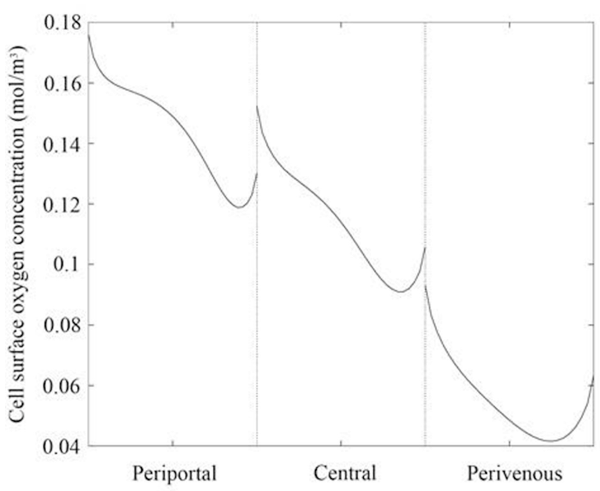

FIGURE 3 | Oxygen concentration profile across the center of the cell surface for each liver zone. Periportal (cells raised by 7 mm), central (cells raised by 4 mm), and perivenous (cells raised by 0 mm i.e., cultured at the base of the chamber).

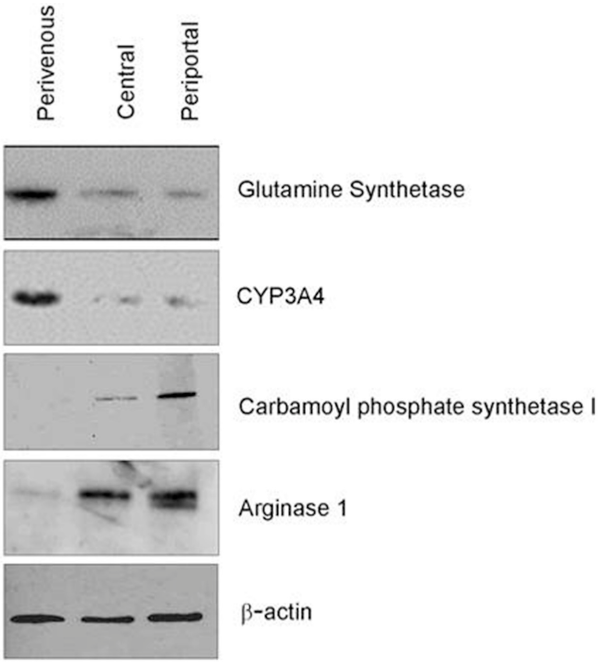

FIGURE 4 | Verification of zonation. Western blot analysis of zone specific protein markers.

TABLE 1 | Mean oxygen concentration and magnitude of shear stress at the cell surface for each liver zone, periportal (cells raised by 7 mm), central (cells raised by 4 mm), and perivenous (cells raised by 0 mm i.e., cultured at the base of the chamber).

Liver zone	Mean oxygen concentration at the cell surface (mol/m^3) (O$_2$%)	Mean magnitude of shear stress at cell surface (Pa)
Periportal	0.15 (15%)	1.69×10^{-6}
Central	0.12 (12%)	4.32×10^{-7}
Perivenous	0.06 (6%)	2.50×10^{-8}

lysate and media and LDH released then calculated in the media as a proportion of the total.

Albumin Secretion

Media from static and flow conditions were centrifuged at 3,000 g for 10 min, with the supernatant collected for analysis. A series of albumin standards were prepared, alongside the media samples and each subsequent step was carried out at room temperature. A total volume of 50 μL for each standard and sample was placed in to a 96-well plate for 1 h. Standards and samples were washed five times in 1 × wash buffer. A total volume of 50 μL of 1 × Biotinylated Albumin antibody was added to each well for 1 h, prior to a series of washes as previously described. A total volume of 50 μL of 1 × SP Conjugate (100 × Streptavidin-Peroxidase Conjugate diluted 1:100 with 1 × Diluent N) was added to each well for 30 min, prior to the wash step. A total volume of 50 μL of Chromogen Substrate was added to each well for 10 min. In order to inhibit the reaction, a final volume of 50 μL of Stop solution was added to each well. The absorbance was recorded at 450 nm on a microplate reader.

Western Blot

Samples were suspended in lysis buffer (250 mM Sucrose, 50 mM Tris pH 7.4, 1 MgCl, and 0.2 % (v/v) Triton X-100). The cell lysates were then centrifuged at 5,000 g at 4°C for 15 min. A total of 20 μg of protein was analyzed using standard immunoblotting analysis. Membranes were blocked overnight in 5% milk in blocking buffer (0.2% Triton X-100 in PBS) at 4°C. The primary antibodies used were; Glutamine synthetase (GS, Abcam) 1:1,000, CYP3A4 (Abcam) 1:1,000, carbamoyl-phosphate synthase 1 (CPS1, Abcam) 1:1,000, Arginase 1 (Arg1, Abcam) 1:1,000, β-actin (Abcam) 1:1,000.

Zone Specific Toxicity

Cells were incubated under flow for 24 h, after which they were dosed with 50 mM paracetamol, a zone specific toxin, dissolved in the circulating Williams' E media for 48 h.

RESULTS

Mathematical Modeling of an *in vitro* Liver

Firstly, simulations were performed assuming that the cells were cultured at the base of the chamber to obtain a baseline for the cell surface oxygen concentration. The minimum cell surface oxygen concentration for this configuration was found to be approximately 4% (see **Supplementary Material**), whereas the mean value was approximately 6% (**Table 1**). Therefore, cells cultured at the base of the chamber were assumed to be representative of the perivenous zone. The height at which the cells were assumed to be cultured was subsequently raised by increments of 1 mm (see **Supplementary Material**) until a mean

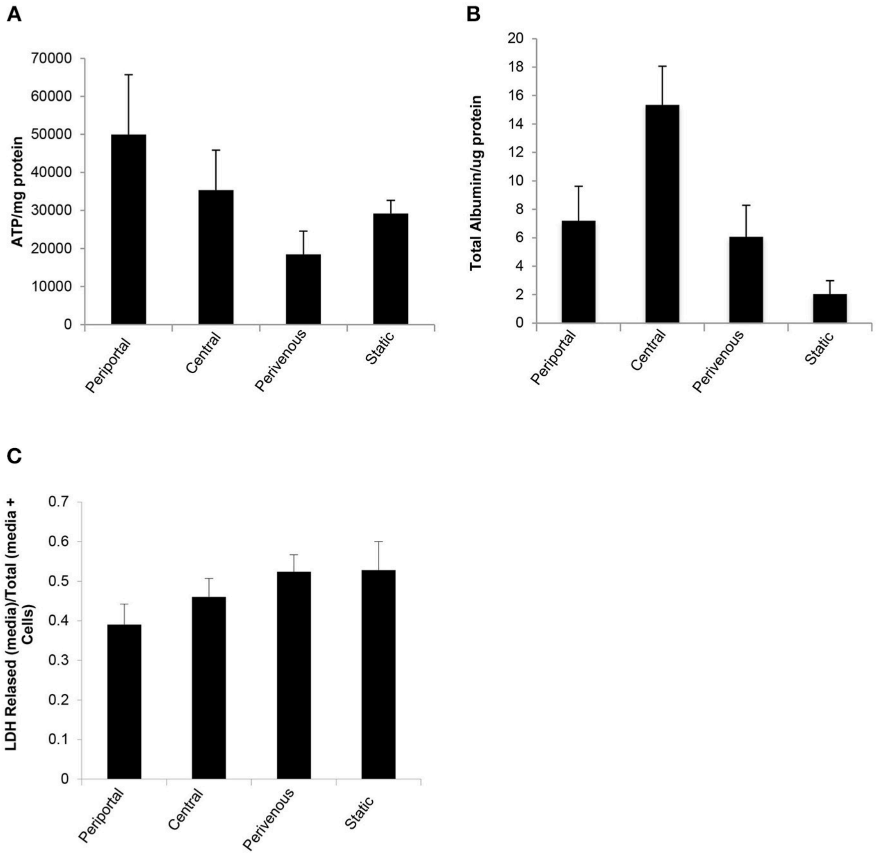

FIGURE 5 | Functional analysis of PRH in each zone compared to standard 2D static conditions. After 48 h under flow conditions or static conditions functional parameters were assessed **(A)** ATP ($n = 4$), **(B)** Albumin secretion ($n = 4$). Both were normalized to protein concentration calculated using a Bradford assay, and **(C)** Cytotoxicity of shear stress analyzed by LDH assay. Data shown as LDH released (in media)/Total LDH (present in cells + media).

cell surface oxygen concentration of approximately 15% was obtained. This corresponded to raising the cells by 7 mm and so this height was selected for the chamber representing the periportal zone. Finally, an intermediate height of 4 mm was selected for the chamber representing the central zone. Therefore, inserts with heights 4 mm and 7 mm were created for use in the experiments. The results of all preliminary simulations are provided in the **Supplementary Material**.

Whilst raising the cells within the chambers enables exposure to higher oxygen concentrations, a potential drawback is that the fluid environment also varies with height, leading to higher cell surface shear stress which has the potential to damage the cells. We therefore also calculated the variation in shear stress with height. For each liver zone, **Table 1** displays the simulated mean oxygen concentration and magnitude of shear stress at the cell surface and **Figure 3** shows the oxygen concentration profile across the center of the cell surface.

Verification of Zonation

Confirmation of zonation by immunoblotting showed differential expression of specific zonation markers in each chamber (**Figure 4**). Glutamine synthetase (GS) converts ammonia into glutamine in the perivenous hepatocytes and drug detoxification enzymes CYP 3A4 were shown to be expressed highest in the perivenous chamber whereas carbamoyl phosphate synthetase 1 (CPS1) and arginase 1 (Arg1), two enzymes within the urea cycle, were found predominantly in the periportal zone.

The *in vitro* system was maintained in full nutritional state and in keeping with the fact that glycolysis is accelerated in a fed state and gluconeogenesis is diminished (Phillips et al., 2002) we found a significantly greater release of ATP in the periportal zone, where gluconeogenesis is predominate (**Figure 1**) when compared to the perivenous zone ($p < 0.05$, students t-test) (**Figure 5A**). The low shear stress felt by the cells ensures that cells are not lost in the flow system and retain functionality as evident by ATP levels (**Figure 5A**) however, to account for any loss values were normalized to protein content carried out using a standard Bradford assay (see methods). As a measure of cell health we next analyzed albumin production and found a 3 fold increase in the perivenous region, 3.5 fold increase in the periportal region and a 7.5 fold increase in the central region when compared to cells grown under standard static conditions (**Figure 5B**). In order to ascertain if the application of shear stress damaged the cells we next determined levels of

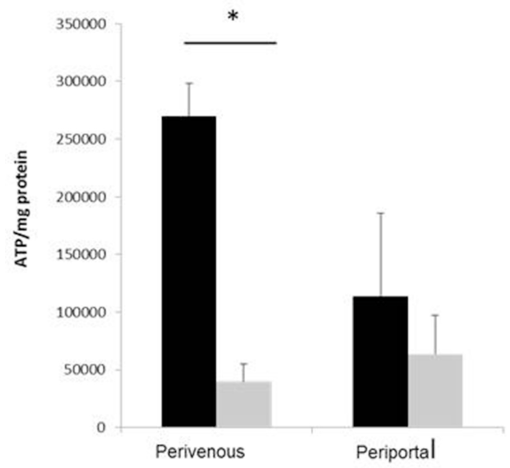

FIGURE 6 | Confirmation of zone specific metabolism. Cells were dosed with 50 mM paracetamol for 48 h. Viability (calculated using ATP assay) was normalized to protein concentration calculated using a Bradford assay. $n = 3$, student's test used for statistical analysis. $^*p < 0.05$.

lactate dehydrogenase (LDH) as an established biomarker of liver damage. **Figure 5C** shows that no additional LDH was released in the cells under the flow systems when compared to those grown under standard static conditions.

Zone Specific Metabolism

Paracetamol is metabolized in the liver predominantly by CYP enzymes where it is metabolized to the cytotoxic intermediate NAPQI, which in turn depletes glutathione, leading to cell death after an overdose (McCarty et al., 2016). We next incubated the cells with paracetamol for 48 h and showed that significantly greater cell death occurred at the perivenous zone when compared to the periportal confirming that our system has zone specific drug metabolism (**Figure 6**).

DISCUSSION

Accurate *in vitro* modeling is essential to data translatability *in vivo*. Despite the distinct metabolic zonation signature of the *in vivo* liver, many standard 2D and 3D culture systems overlook the metabolic heterogeneity of the 3 distinct zones largely due to the complexity of the generation of an *in vitro* zonated model (Dash et al., 2009). To facilitate this process and to make a zonated *in vitro* liver model more widely available, we have modeled fluid flow and oxygen transport within the chambers of a Quasi-vivo 900 system[1]. We chose the QV-900 for two main reasons. Firstly, it allows one to expose cells to flow (as we would have along the hepatic sinusoid) at relatively low shear stress levels which assures the conservation of cell numbers in our system. Secondly, it is straightforward to customize the cell culture depth within the chambers. Our experimental and mathematical modeling efforts allow for the simulation of flow patterns, shear stress and physiological oxygen levels similarly experienced by the *in vivo* cells within the distinct zones of the liver sinusoid. We demonstrate differential expression of established zone specific markers and metabolic cell health functions such as ATP and albumin production that supersede those seen in standard 2D culture systems. To further evaluate cell death or damage we used the LDH analysis which is a standard method of evaluating dead or dying cells (Smith et al., 2011; Zahedifard et al., 2015; Kumar et al., 2018). As we show in **Figure 5C** there is no additional LDH release in any of the zones when compared to the static cells indicating that the low shear stress applied in this system does not damage the cells.

A major concern in using primary hepatocytes for drug safety analysis is their rapid dedifferentiation in static culture resulting in a loss of hepatic phenotype and functionality within hours of the isolation procedure (Yixin et al., 2012; Lauschke et al., 2016; Lauschkek et al., 2016). However, research has suggested that the addition of fluid flow maintains the expression of genes involved in xenobiotic and drug metabolism and transport over a sustained culture period (Vinci et al., 2011; Lauschkek et al., 2016). Here we show a zonated drug toxicity response after exposure to paracetamol 48 h after initial isolation of cells. Paracetamol toxicity was seen predominantly in the perivenous zone where hepatocytes are known to have a high zonal expression of the CYP450 enzymes responsible for the generation of the toxic metabolite NAPQI (Henderson et al., 2000; Mazer and Perrone, 2008).

Research into factors driving liver zonation have reported several mechanisms by which the different metabolic zones arise (Kietzmann, 2017). These include gradients of morphogens such as Wnt, hedgehog, hormones or growth factors as well as oxygen (Colnot and Perret, 2011; Kietzmann, 2017). Although it was previously deemed insufficient for oxygen alone to drive zonation (McCarty et al., 2016), more recent thinking has implicated that oxygen level variations may drive Wnt/β-catenin pathway which is considered to be a master driver of hepatic zonation (Kietzmann, 2017). The low oxygen content in the perivenous zone has been implicated to activate β-catenin which acts as a positive regulator of perivenous genes including glutamine synthetase (GS) and in turn negatively regulates arginase 1 (Arg1). Within the perivenous zone of our system we observe an upregulation of GS, an essential enzyme in nitrogen metabolism, and down regulation of Arg1, a key enzyme in the urea cycle supporting the concept of an oxygen-controlled element in the mechanism of the Wnt/β-catenin pathway.

We would like to emphasize that a number of assumptions have been made in our mathematical model (see **Supplementary Material**). In particular, in common with mathematical modeling of most biological systems, it is a challenge to obtain a reliable and consistent set of parameter values. In this work, we utilized Michaelis-Menten parameter values reported in the literature (Mazzei et al., 2010) in a study which conducted computational modeling of a bioreactor system similar to the one modeled here. Although variations in these parameters will have an influence on the magnitude of oxygen gradient simulated, the trends should be the same. Our goal was not to accurately *predict* concentration gradients. Rather, the focus of our work was to demonstrate the feasibility of creating oxygen gradients that result in differential expression of zonation markers and enhanced functionality of hepatocytes, and we have achieved this in the current study. A useful next step would be to obtain accurate measurement of the Michaelis-Menten parameters associated with hepatocytes and to validate the resulting oxygen gradients predicted in our model. This would enable us to confirm the predictive nature of the model and in turn would allow us to assess the effect of varying future experimental conditions.

Over the past decade, several organ-on-a-chip systems have been developed (Huh et al., 2013; David et al., 2017) with microfluidic flow systems in order to emulate a more *in vivo* like system. However, several limitations of these systems remain, including complex operational control, custom (non-commercial) chip design (Halldorsson et al., 2015; Kang et al., 2018) the presences of bubbles that may damage cells (Sbrana and Ahluwalia, 2012; Bhatia and Ingber, 2014), handling of small volume and ultimately having a limited sample size for downstream applications. However, our zonated system described here takes advantage of a commercially available system specifically designed to remove air bubbles (Sbrana and Ahluwalia, 2012) that allows the seeding and recovery of 1×10^6 zone-specific cells for all manner of downstream applications and its millifluidic nature further reduces technical complications. We provide here a user friendly operational system optimized to emulate a zonated liver that will allow a more *in vivo* like assessment of liver physiology and pathophysiology as well as evaluation of drug metabolism and safety.

AUTHOR CONTRIBUTIONS

LT, JWF, RB, JAK, and PS carried out the molecular lab work and participated in data analysis. LH, SM, and SDW carried out mathematical modeling. PS, SM, and SDW conceived and designed the study and helped draft the manuscript. All authors gave final approval for publication.

FUNDING

LT, RB, and PS are funded by the University of Liverpool. JWF was funded by NC3R CRACKIT challenge 5:VIVE. SM and LH gratefully acknowledge a financial donation from Kirkstall Ltd., funding provided by the EPSRC (EP/M506539/1 and EPM508056/1) and the award of an Alan & Kathie Stross Summer Fellowship to LH by the Dr. Hadwen Trust. JAK was supported by a BBSRC industrial CASE partnership award BB/M503435/1 supported by Syngenta Ltd. SDW acknowledges funding support from the Liverpool Centre for Mathematics in Healthcare (EPSRC grant: EP/N014499/1).

SUPPLEMENTARY MATERIAL

The Supplementary Material for this article can be found online at: https://www.frontiersin.org/articles/10.3389/fbioe.2019.00017/full#supplementary-material

REFERENCES

Allen, J. W., and Bhatia, S. N. (2003). Formation of steady-state oxygen gradients *in vitro*: application to liver zonation. *Biotechnol. Bioeng.* 82, 253–262. doi: 10.1002/bit.10569

Bhatia, S. N., and Ingber, D. E. (2014). Microfluidic organs-on-chips. *Nat. Biotechnol.* 32, 760–772. doi: 10.1038/nbt.2989

Birchmeier, W. (2016). Orchestrating Wnt signalling for metabolic liver zonation. *Nat. Cell Biol.* 18, 463–465. doi: 10.1038/ncb3349

Colnot, S., and Perret, C. (2011). "Liver zonation," in *Molecular Pathology of Liver Diseases*, ed S. P. S. Monga (Boston, MA: Springer), 7–16.

Dash, A., Inman, W., Hoffmaster, K., Sevidal, S., Kelly, J., Obach, R. S., et al. (2009). Liver tissue engineering in the evaluation of drug safety. *Expert Opin. Drug Metab. Toxicol.* 5, 1159–1174. doi: 10.1517/17425250903160664

David, B., Anita, I., Karsta, L., Julia, H., and Manuel, C. P. (2017). Organs-on-a-chip: a new paradigm for toxicological assessment and preclinical drug development. *Toxicol. Res. Appl.* 1, 1–16. doi: 10.1177/2397847317726351

Gaskell, H., Sharma, P., Colley, H., E., Murdoch, C., Williams, D., et al. (2016). Characterization of a functional C3A liver spheroid model. *Toxicol. Res.* 1053–1065. doi: 10.1039/C6TX00101G

Halldorsson, S., Lucumi, E., Gómez-Sjöberg, R., and Fleming, R. M. T. (2015). Advantages and challenges of microfluidic cell culture in polydimethylsiloxane devices. *Biosens. Bioelectron.* 63, 218–231. doi: 10.1016/j.bios.2014.07.029

Henderson, C. J., Wolf, C. R., Kitteringham, N., Powell, H., Otto, D., and Park, B. K. (2000). Increased resistance to acetaminophen hepatotoxicity in mice lacking glutathione S-transferase Pi. *Proc. Nat. Acad. Sci. U.S.A.* 97, 12741–12745. doi: 10.1073/pnas.220176997

Huh, D., Kim, H. J., Fraser, J. P., Shea, D. E., Khan, M., Bahinski, A., et al. (2013). Microfabrication of human organs-on-chips. *Nat. Protoc.* 8, 2135–2157. doi: 10.1038/nprot.2013.137

Kang, Y. B. A., Eo, J., Mert, S., Yarmush, M. L., and Usta, O. B. (2018). Metabolic patterning on a chip: towards *in vitro* liver zonation of primary rat and human hepatocytes. *Sci. Rep.* 8:8951. doi: 10.1038/s41598-018-27179-6

Kietzmann, T. (2017). Metabolic zonation of the liver: the oxygen gradient revisited. *Redox Biol.* 11, 622–630. doi: 10.1016/j.redox.2017.01.012

Kumar, P., Nagarajan, A., and Uchil, P. D. (2018). Analysis of cell viability by the lactate dehydrogenase assay. *Cold Spring Harbor Protocols* 2018:pdb.prot095497. doi: 10.1101/pdb.prot095497

Lauschke, V. M., Hendriks, D. F. G., Bell, C. C., Andersson, T. B., and Ingelman-Sundberg, M. (2016). Novel 3D culture systems for studies of human liver function and assessments of the hepatotoxicity of drugs and drug candidates. *Chem. Res. Toxicol.* 29, 1936–1955. doi: 10.1021/acs.chemrestox.6b00150

Lauschkek, V. M., Vorrink, S. U., Moro, S. M. L., Rezayee, F., Nordling, Å., Hendriks, D. F. G., et al. (2016). Massive rearrangements of cellular MicroRNA signatures are key drivers of hepatocyte dedifferentiation. *Hepatology* 64, 1743–1756. doi: 10.1002/hep.28780

Mazer, M., and Perrone, J. (2008). Acetaminophen-induced nephrotoxicity: pathophysiology, clinical manifestations, and management. *J. Med. Toxicol.* 4, 2–6. doi: 10.1007/bf03160941

Mazzei, D., Guzzardi, M. A., Giusti, S., and Ahluwalia, A. (2010). A low shear stress modular bioreactor for connected cell culture under high flow rates. *Biotechnol. Bioeng.* 106, 127–137. doi: 10.1002/bit.22671

McCarty, W. J., Usta, O. B., and Yarmush, M. L. (2016). A microfabricated platform for generating physiologically-relevant hepatocyte zonation. *Sci. Rep.* 6:26868. doi: 10.1038/srep26868

Phillips, J. W., Jones, M. E., and Berry, M. N. (2002). Implications of the simultaneous occurrence of hepatic glycolysis from glucose and gluconeogenesis from glycerol. *Eur. J. Biochem.* 269, 792–797. doi: 10.1046/j.0014-2956.2001.02687.x

Reuben, A., Koch, D. G., Lee, W. M., and the Acute Liver Failure Study, G. (2010). Drug-induced acute liver failure: results of a U.S. multicenter, prospective study. *Hepatology* 52, 2065–2076. doi: 10.1002/hep.23937

Sbrana, T., and Ahluwalia, A. (2012). "Engineering quasi-vivo® *in vitro* organ models," in *New Technologies for Toxicity Testing*, eds M. Balls, R. D. Combes, and N. Bhogal (New York, NY: Springer), 138–153.

Singh, D., Cho, W. C., and Upadhyay, G. (2016). Drug-induced liver toxicity and prevention by herbal antioxidants: an overview. *Front. Physiol.* 6:e363. doi: 10.3389/fphys.2015.00363

Smith, S. M., Wunder, M. B., Norris, D. A., and Shellman, Y. G. (2011). A simple protocol for using a LDH-based cytotoxicity assay to assess the effects of death and growth inhibition at the same time. *PLoS ONE* 6:e26908. doi: 10.1371/journal.pone.0026908

Vinci, B., Duret, C., Klieber, S., Gerbal-Chaloin, S., Sa-Cunha, A., Laporte, S., et al. (2011). Modular bioreactor for primary human hepatocyte culture: medium flow stimulates expression and activity of detoxification genes. *Biotechnol. J.* 6, 554–564. doi: 10.1002/biot.201000326

Williams, D. P., Shipley, R., Ellis, M. J., Webb, S., Ward, J., Gardner, I., et al. (2013). Novel *in vitro* and mathematical models for the prediction of chemical toxicity. *Toxicol. Res.* 2, 40–59. doi: 10.1039/c2tx20031g

Yixin, C., Wong, P. P., Sjeklocha, L., Steer, C. J., Behnan Sahin, M. (2012). Mature hepatocytes exhibit unexpected plasticity by direct dedifferentiation into liver progenitor cells in culture. *Hepatology* 55, 563–574. doi: 10.1002/hep.24712

Zahedifard, M., Lafta Faraj, F., Paydar, M., Yeng Looi, C., Hajrezaei, M., Hasanpourghadi, M., et al. (2015). Synthesis, characterization and apoptotic activity of quinazolinone Schiff base derivatives toward MCF-7 cells via intrinsic and extrinsic apoptosis pathways. *Sci. Rep.* 5:11544. doi: 10.1038/srep11544

Conflict of Interest Statement: The authors declare that the research was conducted in the absence of any commercial or financial relationships that could be construed as a potential conflict of interest.

frontiers in Bioengineering and Biotechnology

ORIGINAL RESEARCH
published: 02 April 2019
doi: 10.3389/fbioe.2019.00072

Tubing-Free Microfluidic Microtissue Culture System Featuring Gradual, *in vivo*-Like Substance Exposure Profiles

Christian Lohasz[1]*, **Olivier Frey**[2], **Flavio Bonanini**[1], **Kasper Renggli**[1] and **Andreas Hierlemann**[1]

[1] Bioengineering Laboratory, Department of Biosystems Science and Engineering, ETH Zürich, Zurich, Switzerland,
[2] InSphero AG, Schlieren, Switzerland

OPEN ACCESS

Edited by:
Qasem Ramadan,
Agency for Science, Technology and Research, Singapore

Reviewed by:
Mohammad Ameen Qasaimeh,
New York University Abu Dhabi, United Arab Emirates
Ngoc-Duy Dinh,
University of Cambridge, United Kingdom

***Correspondence:**
Christian Lohasz
christian.lohasz@bsse.ethz.ch

Specialty section:
This article was submitted to Tissue Engineering and Regenerative Medicine, a section of the journal Frontiers in Bioengineering and Biotechnology

Received: 26 September 2018
Accepted: 13 March 2019
Published: 02 April 2019

Citation:
Lohasz C, Frey O, Bonanini F, Renggli K and Hierlemann A (2019) Tubing-Free Microfluidic Microtissue Culture System Featuring Gradual, in vivo-Like Substance Exposure Profiles. Front. Bioeng. Biotechnol. 7:72. doi: 10.3389/fbioe.2019.00072

In vitro screening methods for compound efficacy and toxicity to date mostly include cell or tissue exposure to preset constant compound concentrations over a defined testing period. Such concentration profiles, however, do not represent realistic *in vivo* situations after substance uptake. Absorption, distribution, metabolism and excretion of administered substances in an organism or human body entail gradually changing pharmacokinetic concentration profiles. As concentration profile dynamics can influence drug effects on the target tissues, it is important to be able to reproduce realistic concentration profiles in *in vitro* systems. We present a novel design that can be integrated in tubing-free, microfluidic culture chips. These chips are actuated by tilting so that gravity-driven flow and perfusion of culture chambers can be established between reservoirs at both ends of a microfluidic channel. The design enables the realization of *in vivo*-like substance exposure scenarios. Compound gradients are generated through an asymmetric Y-junction of channels with different hydrodynamic resistances. Six microtissues (MTs) can be cultured and exposed in compartments along the channel. Changes of the chip design or operation parameters enable to alter the dosing profile over a large range. Modulation of, e.g., the tilting angle, changes the slope of the dosing curves, so that concentration curves can be attained that resemble the pharmacokinetic characteristics of common substances in a human body. Human colorectal cancer (HCT 116) MTs were exposed to both, gradually decreasing and constant concentrations of Staurosporine. Measurements of apoptosis induction and viability after 5 h and 24 h showed different short- and long-term responses of the MTs to dynamic and linear dosing regimes

Keywords: microfluidics, tilting chip, microtissues, pharmacokinetics, drug dosing

INTRODUCTION

In the last decades, microphysiological systems (MPSs) have been proven to better mimic human *in vivo* physiology in *in vitro* cell cultures. MPSs, often referred to as "organs on chips," are *in vitro* platforms designed to model the spatial, chemical, structural, and physiological elements of *in vivo* cellular environments. In most cases, they include a combination of advanced cell culture models and microfluidic technology. In the last couple of years, a plethora of new, specialized systems have been presented by both, academia and industry (Marx et al., 2016). The list of different systems ranges from single- to multi-organ platforms and include tissues in healthy or diseased states (Zhang et al., 2018). All these systems commonly include defined microchannel structures that enable fluidic interconnection. Perfusion enables to (i) precisely control the microenvironment directly at the cell culture site, (ii) constantly deliver nutrients, oxygen, and other substances, (iii) establish a communication route between individual modules, i.e., organs or microtissues, and (iv) wash away cellular waste products. A precise liquid-flow and temperature control, as well as the possibility to very closely mimic *in vivo* situations make these tools very promising candidates for efficacy and/or toxicity testing of substances for the pharmaceutical industry, in particular as they allow to investigate processes in a more systemic way (Marx et al., 2016; Wang et al., 2018). As those systems become better and better in reproducing *in vivo* situations in the human body, one of the remaining challenges that has been largely neglected in setting up an efficacy and toxicity screening pipeline is pharmacokinetics (PK).

PK describe the fate of a substance, once it enters the human body. Upon entering, there are four key processes that happen with the substance (**Figure 1**): (i) absorption into the body through an epithelial barrier, (ii) distribution of the substance within the body or certain tissues, (iii) metabolization of the substance, and (iv) excretion of the substance itself and/or its metabolites. These four processes are summarized by the acronym ADME, and their interplay results in distinct concentration profiles over time in the human body, which highly depend on the nature of the substance and its administration. The concentration dynamics of a substance can also impact its efficacy and/or toxicity, since those dynamics define the exposure duration above a specific effective/toxic threshold concentration (Saif et al., 2009; Sejoong et al., 2016). While *in vitro* model systems have been used to extract specific ADME parameters, only very few systems allow for exposure of target organ models to such dynamic concentration profiles of a substance of interest. On the contrary, *in vitro* studies routinely include dosage of constant substance concentrations over a defined time, which are not representative of the *in vivo* situation. **Figure 1** illustrates the differences between (left) *in vitro* substance concentration profiles, which are mostly linear, or, in some cases, more complex and then realized through precisely-timed, stepwise pipetting, and (right) dynamically and gradually changing *in vivo* concentration profiles. Studies showed that simplified protocols often lead to false positive results during toxicity and efficacy testing (Tsaioun et al., 2016).

To attain an improved representation of pharmacokinetics in *in vitro* systems, there are two major thrusts that are currently pursued and implemented. In a first thrust, a majority of the relevant organs that are involved in ADME are included and inter-linked in a single chip or microfluidic system (Sung et al., 2010; Maass et al., 2017; Edington et al., 2018). Substantial efforts are required for finding the appropriate organ ratio and for combining all organ surrogates so that they are functional at the same time in a common culture medium. This approach, therefore, entails very high biological complexity (Prantil-Baun et al., 2018), which may compromise experimental reproducibility and throughput. In a second approach, pharmacokinetic concentration profiles are generated through rather complex external devices, for example, by a combination of multiple precision pumps that enable a defined temporal modulation of the substance concentration for specific single organs of interest (Wikswo et al., 2018). There have been several attempts to use such systems and apply spatial and temporal gradients of substances on biological samples, such as Xenopus embryonic tissue (Kim et al., 2011), or lymphoid tissue explants (Ross et al., 2017). Further, Song et al. (2018) investigated exposure of single cells to pulsatile and gradually ramped concentration profiles of growth factors. Another solution to expose cancer cells to pulses of tumor necrosis factor (TNF) without the need for external pumps, has been presented by Lee et al. (2016). Perfusion in their chip was gravity-driven, and pulses of TNF were induced by manually elevating the dosing reservoir.

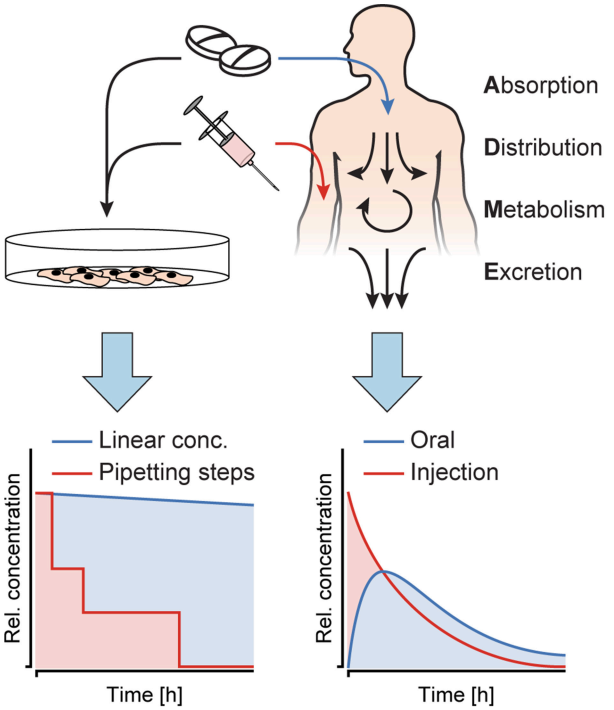

FIGURE 1 | Substance concentration profiles in *in vitro* experiments as opposed to *in vivo*. Cell culture models *in vitro* are exposed to constant concentrations or sudden substance concentration steps generated by pipetting, while in the human body, the interplay of absorption, distribution, metabolism and excretion (ADME) produces distinct, dynamic substance concentration profiles upon oral administration or injection of a substance.

Here, we developed a new approach to generate dynamic substance concentration profiles in microfluidic cell culture systems. The proposed design and working principle can be integrated into tubing-free microfluidic platforms, which feature gravity-driven flow perfusion upon platform tilting. The specific new design feature consists of an asymmetric Y-junction, connected to three medium reservoirs (Lohasz et al., 2017). Upon repeated tilting of the chip, the liquids from the reservoirs mix, which gradually changes the substance concentration at the cell culture sites. The slope of the concentration profile can be modulated by changing the channel dimensions, the initial volume of the substance solution, or the tilting angle.

As a proof on concept, we integrated the new design feature into a microfluidic microtissue culture chip with 6 compartments that was similar to a previously presented approach (Kim et al., 2015a; Lohasz et al., 2018). Human colorectal tumor microtissues (HCT 116) were loaded into the MT compartments of the chip and exposed to Staurosporine. Staurosporine features strong, promiscuous kinase inhibitor properties by competitive binding to the ATP-binding site of kinases (Karaman et al., 2008). Therefore, it is frequently used as an anti-cancer tool compound for *in vitro* studies. The tumor microtissues (TuMTs) were exposed to a physiologically relevant concentration profile, which resembled that after an injection of a substance in a human body. This profile could be recreated by the chip system. The results were compared to constant-concentration drug dosing schemes. We saw that the TuMTs responded differently to *in vivo*-like drug dosing with decreasing concentrations in comparison to traditionally applied, constant concentrations.

MATERIALS AND METHODS

Design Principle

A microfluidic channel design was developed, that enables a gradual change of substance concentrations over time at the cell or MT culturing site. Prerequisite for the integration of the proposed design feature is a chip system with medium reservoirs at both ends of a main channel and a flow actuation upon tilting of the system. Cell or MT models are cultured in compartments along the main channel and perfused upon tilting the chip back and forth. The specific new design feature consists of an asymmetric Y-junction, which is connected to three medium reservoirs, two reservoirs at one end of the main channel and a third reservoir at the other end of the channel (see **Figure 2**).

To produce a gradually changing concentration profile in the main channel, the two reservoirs left of the Y-junction in **Figure 2A** are filled with two different medium compositions, e.g., plain cell culture medium and medium containing a substance of interest. Upon tilting of the chip so that the 2 reservoirs left of the Y-junction are higher, the two liquids in the reservoirs start flowing and combine in the Y-junction to flow along the common main channel. The different cross-sections of the two left channels entail different hydrodynamic resistances and different flow rates through the two channels into the main channel. Upon tilting in the opposite direction so that the reservoir at the right side is higher, a flow backwards to the Y-junction is initiated. The liquid in the main channels then splits up at the Y-junction at the same volume ratio at which it entered the common channel before. Repeated tilting of the device with a defined tilting angle slowly mixes the media originating from the two reservoirs at the left side over time, until an equilibrium in the main channel is reached (**Figure 2B**). If, for example, a substance is added into the reservoir that is connected to the channel featuring the lower flow rate, and plain cell culture medium is applied to the other one, the substance concentration in the main channel is gradually enriched over time (**Figure 2B**).

The change in the substance concentration in the main channel depends on the different flow rates through the channels at the left side and the resulting total liquid volumes that are fed into the main channel per tilting interval (**Figure 3B**). Flow rates, in turn depend on the height difference or hydrostatic pressure difference between the upper and lower reservoirs of the tilting system. The tilting angle α and the distance L between the opposite ends of the channel define the height difference Δh between the two reservoirs, to which the height of the liquid column in the upper reservoir h_{up} is added and from which the liquid column height in the lower reservoir h_{low} is subtracted.

$$\Delta h = L \cdot sin\alpha + h_{up} - h_{low} \tag{1}$$

In a rectangular channel, the hydrodynamic resistance R_h is dependent on the liquid viscosity and the channel dimensions, as described by Bruus (2008):

$$R_h \approx \frac{12 \cdot \eta \cdot L}{w \cdot h^3 \cdot \left(1 - 0.63 \cdot \frac{h}{w}\right)} \tag{2}$$

with η denoting the liquid viscosity and L, w, and h ($w > h$) describing the length, width and height of the channel, respectively.

Using the tilting-dependent hydrostatic pressure difference

$$\Delta P = \rho \cdot g \cdot \Delta h \tag{3}$$

and the hydrodynamic resistance R_h (equation 2) of each section of the channel, the volumetric flow rates Q in each section of the channel can be calculated as:

$$Q = \frac{\Delta P}{R_h} \cdot \tag{4}$$

The flow rates in the three channels connected to the Y-junction then are determined by:

$$Q_1 + Q_2 = Q_3 \tag{5}$$

with Q_1 and Q_2 referring to the differently sized channels joining into the common channel featuring a flow rate Q_3 (**Figure 3B**).

To establish unequal flow rates in the two channels left of the Y-junction, their hydrodynamic resistances or geometric dimensions can be adjusted. Thus, a change of dimensions, such as the channel widths of the two channels, allows for simple adjustment of their specific hydrodynamic resistances. **Figure 2** shows a schematic view of the microfluidic-channel layout with an integrated, asymmetric Y-junction. To predict the substance concentration in the common channel, the dilution equation:

$$C_x \cdot V_x = C_y \cdot V_y \tag{6}$$

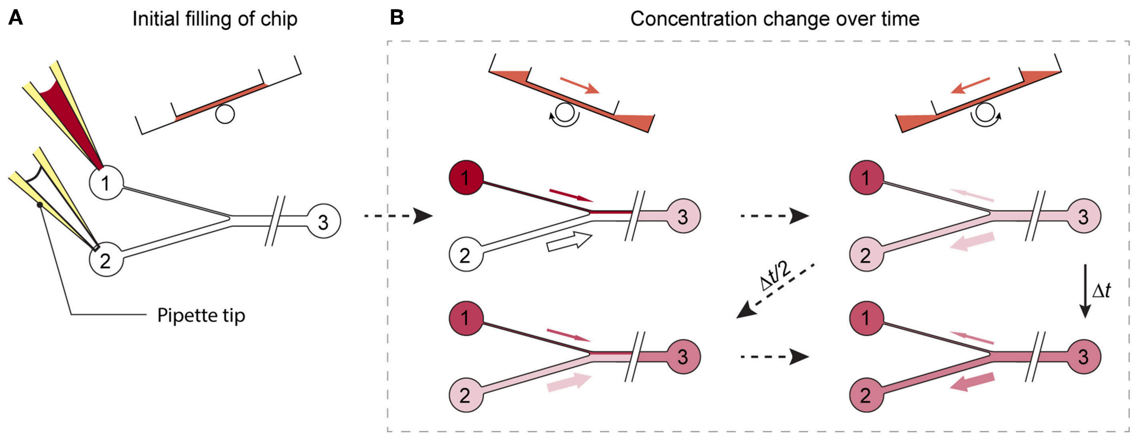

FIGURE 2 | Working principle of the design. **(A)** Reservoirs 1 and 2 are filled with substance-loaded and plain cell culture medium. **(B)** Upon tilting of the chip, unequal volumes of liquid flow through the differently sized channels. While the substance concentration is, with each tilting interval *Δt*, gradually enriched in reservoirs 2 and 3, the substance is diluted in reservoir 1, until a concentration equilibrium is reached.

was used and adjusted to calculate the concentration resulting from mixing three liquids:

$$C_3(t) = \frac{C_1 \cdot V_1(t) + C_2 \cdot V_2(t) + C_3(t_0) \cdot V_3(t_0)}{V_1(t) + V_2(t) + V_3(t_0)}. \tag{7}$$

C_3 refers to the concentration in the common channel and reservoir 3 at time point t after tilting of the chip. C_1 and C_2 represent the concentrations of the liquids in the differently sized channels upstream of the Y-junction, and V_1 and V_2 are the liquid volumes flowing into the main channel during time t. $C_3(t_0)$ and $V_3(t_0)$ denote the concentration and volume of the liquid phase already present in the main channel before initiation of the tilting cycle. The liquid volumes V_1 and V_2 can further be described by:

$$V_1(t) = Q_1 \cdot t, \textit{ and}$$

$$V_2(t) = Q_2 \cdot t \tag{8}$$

with t denoting the time, during which the flow rates Q_1 and Q_2 are present in the two differently sized channels and during which the liquid flows into the common channel.

Equation (7), combined with equations (4) and (8), was then used to derive the time-dependent recurrence relation for calculating the concentrations in the system, when the chip is tilted toward reservoir 3:

$$C_3\,(t+\Delta t) = \frac{C_1\,(t)\,\cdot Q_1 \cdot \Delta\, t + C_2\,(t)\,\cdot Q_2 \cdot \Delta\, t + C_3\,(t0)\,\cdot V_3\,(t)}{Q_1 \cdot \Delta\, t + Q_2 \cdot \Delta\, t + V_3\,(t)} \tag{9}$$

When tilting the chip into the opposite direction, the concentrations in reservoirs 1 and 2 can be calculated using:

$$C_1\left(t+\Delta\frac{t}{2}\right) = \frac{C_3\,(t)\,\cdot Q_3 \cdot \Delta t + C_1\,(t)\,\cdot Q_1 \cdot \Delta t}{Q_3 \cdot \Delta t + Q_1 \Delta t}\text{, } \textit{and} \tag{10}$$

$$C_2\left(t+\Delta\frac{t}{2}\right) = \frac{C_3\,(t)\,\cdot Q_3 \cdot \Delta t + C_2\,(t)\,\cdot Q_2 \cdot \Delta t}{Q_3 \cdot \Delta t + Q_2 \cdot \Delta t}. \tag{11}$$

Here, *Δt* denotes the interval between two successive tilting cycles into the same direction, and *Δt/2* between two tilting steps into the opposite direction (**Figure 2B**). $C_1(t)$, $C_2(t)$, and $C_3(t)$ are the time-dependent concentrations in reservoirs 1 to 3, and $V_3(t)$ is the time-dependent liquid volume within the main channel and in reservoir 3. At $t = 0$, all channels are assumed to be filled with plain cell culture medium. Equations (9–11) allow for simple calculations of the analyte concentration in the main channel and in the reservoirs at discrete times.

Chip Fabrication

The chip was fabricated using polydimethylsiloxane (PDMS) and conventional soft lithography methods. The bottom structures comprised the channel structures and were fabricated using a two-layer SU-8 master on a 4-inch silicon wafer (**Supplementary Figure 1**). For the first layer with the perfusion channel designs, SU-8 100 photoresist (Microchem Corp., Newtown, MA, USA) was spin-coated onto the wafer in a 100-µm thick layer and was exposed to UV through a transparency mask featuring the designed pattern. The second 25-µm-thick layer of SU-8 25 photoresist (Microchem Corp.) comprising the mixing structures was coated on top of the first layer and was exposed a second time to UV though a transparency mask.

For the top structures of the chip, a positive mold of the chip was designed and 3D-printed (Protolabs, Feldkirchen, Germany). The structures comprised the top part of the MT compartments and the reservoirs. The positive mold was then used to cast a flexible, negative mold out of PDMS (Dow Corning, Midland, MI, USA). A 7:1 ratio of polymer and curing agent were used for better stability, and the cast was cured at room temperature for 24 h to reduce heat-induced shrinking of PDMS as much as possible (Lee and Lee, 2008). The SU-8 bottom mold and the PDMS top mold were then placed in a desiccator and treated with trichloro(1H, 1H, 2H, 2H-perfluoroctyl)silane (Sigma-Aldrich Chemie GmbH, Buchs, Switzerland) to prevent fusion with the final chip and to enable multiple usage of both molds.

Designated alignment structures enabled the easy and fast alignment of the two molds, before PDMS was filled and cured in a vacuum oven at 80°C for 4 h. Subsequently, the casted PDMS devices were removed from the molds and cut into their final size of 23 mm × 73 mm. To close the channels at the bottom side, the PDMS devices were O_2-plasma-bonded to microscopy glass slides that were previously spin-coated with a thin layer of PDMS (30 s, 2,000 rpm). The PDMS layer on the glass slide was needed to achieve uniform coating properties of all four channel surfaces. The glass slides enabled easy device handling and use with standard inverted microscopy setups. After the assembly, all channels and surfaces to be exposed to liquids or cells were coated with Biolipidure 206 (NOF America Corporation, White Plains, NY, USA) to render them hydrophilic and to prevent MTs from attaching to the surfaces.

Device Operation

The devices were operated in a handling frame (Microfluidic ChipShop, Jena, Germany) holding four chips in parallel. To limit evaporation, a custom-cut adhesive polyester film with small holes for oxygen exchange was attached to cover the MT compartments and the medium reservoirs. Further, a lid (Microfluidic ChipShop), fitting to the handling frame, was used to close the chips and enabled stacking of multiple frames.

Channels and reservoirs were initially flooded with plain cell culture medium to a level that standing drops formed within the top rim of the MT compartments. Throughout the experiment, these standing drops remained stable at the top rim structure of the MT compartments. Surface tension stabilized the standing drops, which resulted in a constant volume in the compartment. Next, preformed spherical MTs were transferred into the corresponding compartments. They were harvested from a 96-well microtiter plate with a pipette. After sedimentation of the MTs to the opening of the pipette tip, the tip was brought into contact with the standing drop. The MT then sedimented down—driven by gravity—to the bottom of the designated compartment.

Before starting an experiment, the frame was tilted along its long axis with the branched side facing down while the upper reservoir on the other side was completely emptied of medium. The channels did not completely drain due to capillary forces at the connections to the reservoirs. The medium in the two lower reservoirs was then removed and replaced with the required volume of plain medium and medium containing a substance of interest at a predefined concentration. The reservoirs could hold a maximum volume of 100 μL. To achieve dosing curves with increasing concentration, the substance was administered into the reservoir connected to the narrow channel. For dosing curves featuring decreasing concentrations, the reservoir connected to the wide channel was loaded with the substance. After loading, repetitive tilting was started and the experiment began.

The assembled and loaded handling frame was operated on a programmable tilting stage (InSphero AG, Schlieren, Switzerland), as shown in **Supplementary Figure 2**. The stage allows for precise adjustment of positive and negative tilting angles, for defining resting times at tilted or horizontal positions and transition times between positive and negative angles. The entire experimental setup including the tilting stage and a stack of handling frames was operated in a standard cell-culture incubator at mammalian cell culture conditions (37°C, 5% CO_2, 95% humidity).

Measurements of Concentration Curves

To track concentration curves over time, cell culture medium containing amaranth red dye (Sigma-Aldrich, Buchs, Switzerland) was used to mimic a drug solution. 100 μL of the dye solution were loaded into one reservoir at the branched side of the channel and 100 μL of plain cell culture medium were added to the other one at the same side of the chip. While repeatedly tilting the chip, 1 μL of the mixed liquid was removed from the shared reservoir on the other side of the chip, and its absorbance at a wavelength of 520 nm was measured in reference to the initially loaded solution of amaranth red using a NanoDrop2000 (Life Technologies Europe B.V., Zug, Switzerland).

For the realization of concentration profiles that resembled *in vivo* concentrations after injection of a substance, cell culture medium containing 15 μM 5-fluorouracil (5-FU; Sigma-Aldrich) was used, along with plain cell culture medium in the chip. To measure the concentration profile, medium-filled chips with and without tumor microtissues (TuMTs) were used. 25 μL of drug-containing medium were loaded into the reservoir, connected to the wide channel, and 75 μL of plain medium were loaded into the reservoir with the narrow channel. The concentration profile was induced by tilting the chip at a tilting angle of 20° with waiting times of 2 min and 30 s at the tilted positions and transition times of 30 s. Samples of 10 μL were taken from the common reservoir after 3, 15, 33, 63, 123 min and after 24 h. For each time point, individual chips were used. The samples were diluted with 40 μL of plain medium and snap-frozen on dry ice. 5-FU was externally quantified by ultra-performance liquid chromatography, coupled to mass spectrometry UPLC-MS (Admescope Oy, Oulu, Finland).

Cell Culturing

HCT 116 colorectal tumor cells (ATCC®, LGC Standards GmbH, Wesel, Germany) were used for cell culture experiments. The cells were maintained in RPMI-1640 basal medium (Gibco, Fisher Scientific, Illkirch Cedex, France), supplemented with 10% fetal bovine serum (FBS, Sigma-Aldrich) and 1% penicillin/streptomycin (Life Technologies Europe B.V.). Cells were passaged at 80% confluency. To form MTs with a diameter of 200–250 μm, 70 μL of medium, containing 300 cells, were transferred into each well of an Akura™ 96-well plate (InSphero AG) and centrifuged for 2 min at 250 × g. The plate was then placed in a tilted position in an incubator to collect cells in one corner of the wells and to promote MT formation. Cells were used for further experiments after 96 h.

Dosing Experiments

For physiological dosing experiments, previously formed and equally sized MTs were transferred into the six MT

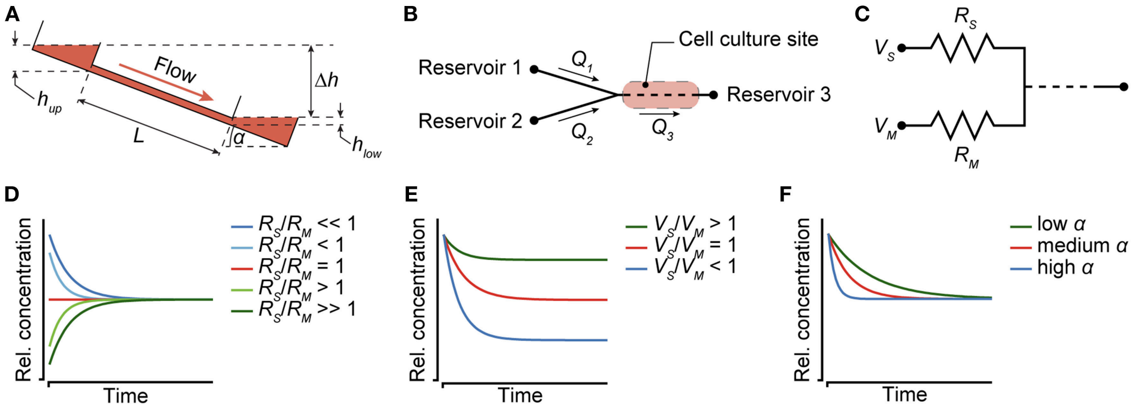

FIGURE 3 | Modulation of concentration profiles. **(A)** Flow in the chip is dependent on the tilting angle α and the resulting height difference Δh between the liquid levels in the reservoirs at the left and right side. **(B)** Two reservoirs that are connected to channels with unequal flow rates Q_1 and Q_2 feed into a Y-junction. The flow-rate difference can be generated by different channel widths or dimensions. A cell culture site is located between the Y-junction and a third reservoir, and can be subjected to dynamic substance concentration profiles. **(C)** The channel resistances R_S and R_M, the initially applied liquid volumes V_S and V_M, and the tilting angle α can be used to modulate the concentration profiles. **(D)** The ratio of resistances can be used to define the time, after which an equilibrium is reached (for constant V and α). **(E)** The ratio of input volumes in reservoirs 1 and 2 defines the concentration, at which an equilibrium is reached (for constant R and α). **(F)** The tilting angle α modulates the slope of the concentration profile (for constant R and V).

compartments of the microfluidic chip. Briefly, MTs were aspired together with 3 μL of cell culture medium using a standard micropipette. Upon sedimentation of the MT by gravity to the opening of the pipette tip, the MT was transferred into the MT compartment by contact transfer.

To produce gradually decreasing concentrations over time, which are representing concentration profiles, e.g., upon intravenous injection of a drug, 25 μL of the drug solution containing the maximum concentration ($C_{max} = 0.75\,\mu M$ Staurosporine) were loaded into the reservoir, connected to the wide channel, while 75 μL of plain cell culture medium were loaded into the reservoir connected to the thin channel. The unequal amounts of input liquids enabled to decrease the compound concentration to 25% of the initial concentration. Side by side to the gradually changing concentration profile, MTs were exposed to a constant concentration of 0.75 μM Staurosporine. Control groups were cultured without compound in the chip under identical perfusion conditions and under static conditions in 96-well microtiter plates. The tilting angle was set to 20°, tilting intervals to 2 min 30 s and transition times to 30 s. The chips were then repeatedly tilted. For imaging, the tilting was briefly interrupted, and the plate was transferred onto a microscope. Experiments were performed with at least six MTs per chip and 2–4 chips per condition.

Biochemical Assays

Intracellular adenosine triphosphate (ATP) was measured using the CellTiter-Glo® 3D Cell Viability Assay (Promega AG, Dübendorf, Switzerland) as a measure of MT viability. The Caspase 3/7-Glo® Assay Systems (Promega AG) was used to assess onset of apoptosis. For both assays, MTs were removed from the chip and transferred into Akura 96-well plates (InSphero AG). MTs were washed with PBS (Life Technologies Europe B.V.), before the assay was performed according to the manufacturer's protocol.

Imaging

Bright-field images of MTs were recorded using an inverted wide-field microscope (DMI-6000B; Leica Microsystems AG, Heerbrugg, Switzerland), equipped with a CCD camera (DFC-340-FX; Leica) and a stage-top cell culture incubator to maintain cell-culture conditions during the imaging process (Life Imaging Services GmbH, Basel, Switzerland). To focus on the elevated microfluidic chips in the handling frame, a distance ring (Thorlabs GmbH, Dachau, Germany) was used to increase the parfocal length of the objective. All images were analyzed using ImageJ/Fiji software.

RESULTS

Theoretical

Modulation of the Concentration Profile

The new microfluidic channel design is aimed at reproducing physiologically relevant drug dosing curves *in vitro*. Operation of the chip was intended to be simple and not to rely on additional equipment, such as tubing and pumps. Therefore, the concept of gravity-driven flow by tilting of the chip was applied. Nevertheless, the new design features great flexibility in producing a variety of substance concentration profiles.

Three parameters can be changed to modulate the shape of the produced dosing curve: (i) the dimensions of the channels, (ii) the liquid volumes in the reservoirs at the beginning of an experiment, and (iii) the tilting angle during an experiment. The influence of these three parameters is illustrated in **Figure 3A**. The hydrodynamic resistance R_S and the initial input volume V_S denote those of the channel containing medium with a compound, while R_M and V_M denote those of the channel with plain medium. The normalized concentration profile curves were calculated using equation (10) after each tilting interval. The initial concentrations were set to 0 in V_M and in the main channel, and 1 in V_S.

- Modulation of the channel dimensions (**Figure 3D**): Equation (4) defines how the flow rates through the channels depend on their hydrodynamic resistance R_h. The resistance, in turn, is determined by the channel dimensions, e.g., the channel width (equation 2). Thus, the flow rates through the two channels upstream or left of the Y-junction (**Figure 3B**) can be individually modulated by adjusting their hydrodynamic resistances R_S and R_M (**Figure 3C**). The R_S-to-R_M-ratio influences the mixing ratio of the two liquids originating from the two separate reservoirs. Very large or very small R_S-to-R_M-ratios result in slowly increasing/decreasing concentrations until an equilibrium is reached. The lower the difference of R_S and R_M, the shorter and steeper become the concentration curves. For $R_S/R_M < 1$, a curve with decreasing concentrations is produced, while $R_S/R_M > 1$ yields increasing concentrations. Equal flow resistances in both channels result in linear, stable concentrations over time.
- Varying the initial volumes in the reservoirs (**Figure 3E**): The initially applied liquid volumes V_S and V_M determine the equilibrium concentration at the end of the gradual concentration change, i.e., the dilution of the initial substance concentration. For equal volumes in both reservoirs at the beginning of an experiment, the equilibrium is reached at 50% of the initial substance concentration. For $V_S/V_M > 1$, the concentration profile covers only a small range, before equilibrium is reached at a concentration, which is higher than 50% of the initial substance concentration. For $V_S/V_M < 1$, the opposite holds true. Loading unequal amounts of liquid into the reservoirs also results in different Δh between the lower reservoir at the right side and the two upper reservoirs at the left upon first tilting. The different Δh has an effect on the respective flow through the two channels, which also needs to be taken into account for calculating the flow rates and the concentration profile.
- A variation of the tilting angle of the chip during an experiment can be used to modulate the slope of the dosing curve on demand. The higher the tilting angle, the higher are the flow rates in all channels and, consequently, the steeper becomes the slope of the dosing curve. **Figure 3F** shows concentration curves at low (~5–10°), medium (~10–30°) and high (~30–50°) tilting angles α, while hydrodynamic resistances and input volumes were kept constant.

The possibility to vary these three parameters leads to a large flexibility in dosing regimens. While the latter two parameters (reservoir filling volume and tilting angle) can be changed during operation, the channel dimensions have to be already defined while designing the microfluidic chip. Practically, the chip has been designed to cover a fairly wide range of dosing curve slopes, which can be fine-tuned by adjusting the input volume and tilting angle to obtain the intended dosing curve.

Experimental

Design Integration Into a Microfluidic Microtissue Culture Chip

To test the new design, we integrated it into a previously developed microfluidic microtissue culture chip. The original chip features two parallel channels, each with one reservoir at each side and 10 compartments in between, which can be used to culture spherical MTs under constant substance concentrations. The chip is operated by tilting (Lohasz et al., 2018). The basic channel and compartment structure of the chip was maintained. On one side, the left side in **Figure 4**, a second reservoir and the Y-junction (**Figure 4B**) were implemented and the number of MT compartments was reduced to six. Further, a mixing structure was added (**Figure 4A**). As turbulent mixing does not occur at the inherently low Reynolds numbers in microchannels, mixing structures are required to obtain a homogenous substance concentration (Lee et al., 2011). Therefore, we implemented a meander-shaped channel and so-called herring bone structures (Stroock et al., 2002) between the Y-junction and the six MT compartments (**Figure 4C**). The mixing structure smoothened the sharp spatial gradient originating from the two reservoirs across the channel width to expose all MTs to an almost uniform substance concentration (**Supplementary Figure 3** and **Supplementary Movie 1**). By connecting the chip to syringe pumps and by perfusing it with differently colored solutions, we could show that substance concentrations in all MT compartments change uniformly and in accordance with the concentrations inside the main channel. Furthermore, no differences could be observed between the first and the last MT comportment along the perfusion direction (**Supplementary Figure 4** and **Supplementary Movie 1**).

In addition to the dosing channel with the Y-junction, a control channel was included into each chip. This control channel is similar to the dosing channel, but lacks the Y-junction. Instead, it features a single channel, the design parameters of which were adjusted to obtain similar hydraulic resistances as in the dosing channel, and one reservoir (**Figure 4F**). The two differently sized channels leading into the Y-junction were 400 and 100 μm wide. The width of the first segment at the left in the control channel was 400 μm wide, and both main channels with MT compartments were 600 μm wide. All channels had a height of 100 μm. Having these two device architectures side by side on the same chip, the effects of a gradually changing concentration profile could be compared to those obtained by applying a linear concentration on the same chip. Twelve MTs were exposed to two different dosing conditions (6 per condition) in each device.

The MT compartments (**Figure 4D**) are open to the top to facilitate loading of externally produced MTs and their removal after an experiment to be able to individually analyze each MT. Surface tension of the medium generates a liquid-air-interface (*Standing Drop Port*, **Figure 4E**) defined by the hydrophobic rim structure of the MT compartment. During experimentation, barrier structures hold the MT in place, and protect them from shear stress as a consequence of the liquid flow (**Figure 4D**). The barrier structures, however, do not hinder mass transport of biomolecules to the MT culturing site, as confirmed by the streamlines in a flow simulation (**Supplementary Figure 2C**). The details of the MT compartment design and the flow through the compartment have been thoroughly described and characterized previously (Kim et al., 2015b; Lohasz et al., 2018). The MT compartments are 800 μm in diameter and are spaced at a pitch of 4.5 mm. Rectangular reservoirs at

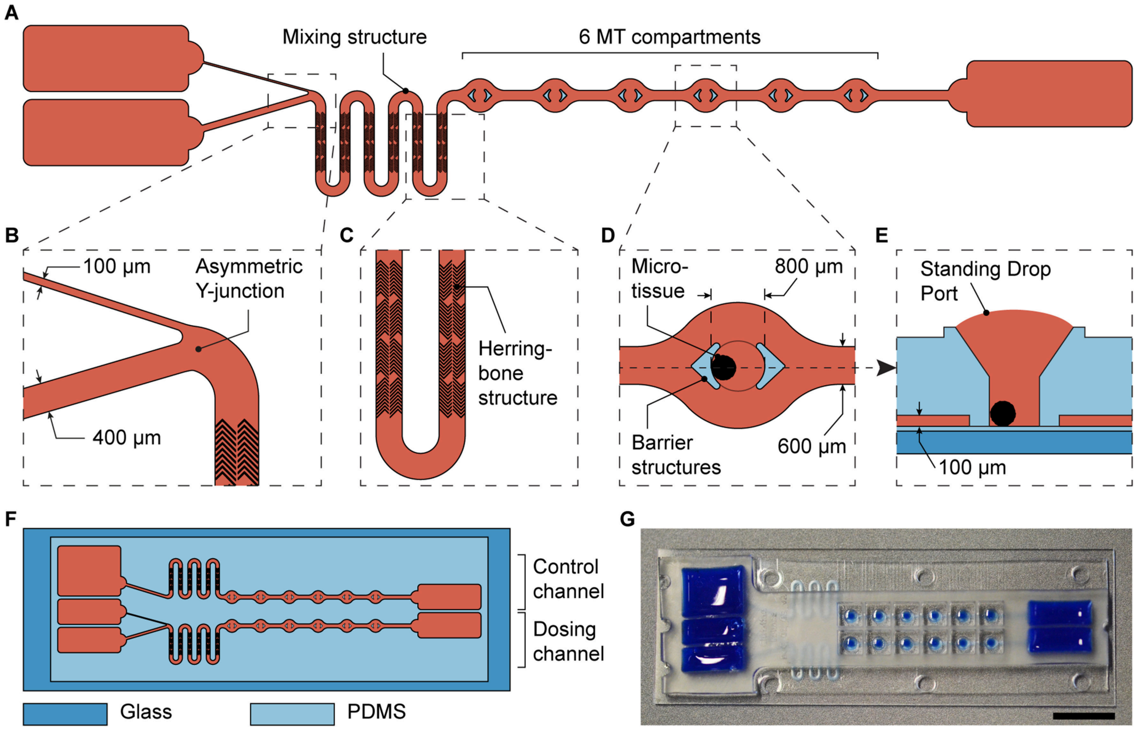

FIGURE 4 | Integration of the asymmetric design into a microfluidic microtissue-culture chip. **(A)** Microfluidic channel layout with the asymmetric Y-junction, followed by a mixing structure and six microtissue (MT) compartments. Details are shown in **(B)** the asymmetric Y-junction, **(C)** the micromixer including herringbone structures in a meander-shaped channel, and **(D)** the top view of a MT compartment with protective barrier structures and **(E)** a side view of a MT compartment. **(F)** Each microfluidic chip has the size of a microscopy slide and includes a dosing channel with a Y-junction, next to a control channel for linear exposure profiles. **(G)** Photograph of the microfluidic chip the channels and reservoirs of which have been filled with a colored liquid (scale bar: 10 mm).

the ends of the channels contain up to 150 µL per channel. The chip was fabricated using PDMS, and had a total size of 25 × 75 mm.

Concentration Profile Characterization

We designed a chip that could be used to deliver approximately typical, decreasing blood-plasma concentrations of substances that are administered to patients by injection (Kwon, 2001). Injection of compounds generally results in initially high-concentration peaks, followed by a decrease over time (**Figure 1**). For the two channels at the left or upstream of the Y-junction in the dosing device, we used 400 µm width and 100 µm width.

We demonstrated the flexible modulation of the concentration profile on demand upon changing the tilting angle α (**Figure 5A**) through concentration measurements of amaranth red dye in the shared reservoir at the right side. Dye solution was loaded into the reservoir connected to the narrow channel, while plain medium was loaded into the other one. Repeated tilting resulted in a gradual increase of the dye concentration within the main channel and the shared reservoir. **Figure 5A** shows the measured curves for tilting angles of 20 and 40° until a concentration equilibrium was reached (after 6.5 h at 20° and after 3.5 h at 40°). The curve was also compared to calculated curves for the respective chip dimensions and a V_S-to-V_M-ratio of 1. The measured concentrations matched the calculated values, however, with a small offset. Furthermore, the curve, obtained with a tilting angle of 20°, showed minor fluctuations between 2 and 4 h. Both features can be explained by medium evaporation due to opening of the chip system at 15-min intervals for sampling. The results show that the concentration increase to a steady state concentration is faster with a steeper slope at higher tilting angles. A modulation of the shape of the dosing curve by changing the tilting angle α was indeed possible.

For obtaining decreasing concentration profiles, the wide channel was used for the substance-containing medium, and the narrow channel for plain medium. By interchanging the two liquids in the reservoirs, as compared to the first characterization experiment, a R_S-to-R_M-ratio > 1 was achieved. Decreasing concentration profiles could be used to reproduce physiologically relevant conditions upon injection of a compound. For this second characterization experiment, 5-fluorouracil (5-FU) was used. 5-FU is a commonly used anti-cancer drug, which is administered by infusion or injection (Casale et al., 2004). Tilting was started with an angle of 20°, and samples were taken from the shared reservoir at the right side after 15, 33, 63, and 123 min, as well as after 24 h. 5-FU concentrations were measured by mass spectrometry (**Figure 5B**). The measured points were in good agreement with the calculated concentration profile and a steeply

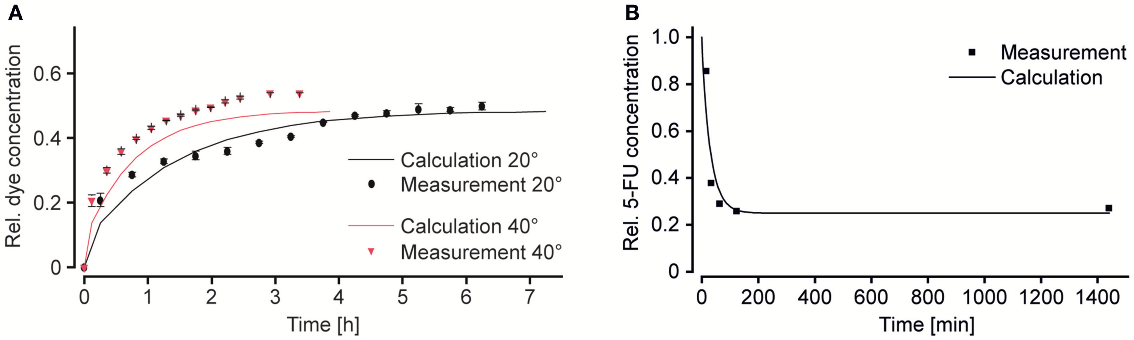

FIGURE 5 | Modulation of the substance concentration profile. **(A)** Amaranth red dye was used to simulate and track substance concentrations in the chip over time. Changing the tilting angle α modulates the slope of the concentration curve ($V_S/V_M = 1$; $R_S/R_M = 4$; $n = 3$ chips). **(B)** Decreasing concentration of 5-fluorouracil (5-FU) in the main channel over time. Peak area and concentration measurements were done by means of ultra-performance liquid chromatography, coupled to mass spectrometry UPLC-MS ($V_S/V_M = 0.66$; $R_S/R_M > 0.25$; $\alpha = 20°$; $n = 1$ chip).

decreasing dosing curve was produced. A steady state at 25% of the initially applied concentration could be reached by applying a V_S-to-V_M-ratio of 0.66. The steady state was reached after ∼2 h of continuous tilting of the chip.

The results of the two characterization experiments showed that concentration profiles can indeed be modulated by changing parameters, such as tilting angles (**Figure 5A**), resistances of the channels, or input volumes in the reservoirs (**Figure 5B**). One major difference between the concentration profiles produced with the device and the ones found *in vivo* is that the final equilibrium substance concentration obtained with the microfluidic chip is defined by the two initial concentrations and volumes in the reservoirs at the left and is always larger than 0, whereas the substance is eliminated completely in the human body in case of a single dosage. A possible solution to also reach a concentration of 0 with the microfluidic chip could include medium exchanges after the intended exposure time. Moreover, most substances are, to a certain amount, metabolized by the respective target tissue, which—depending on the initial substance concentration—might also contribute to decreasing the final concentration to physiological levels.

According to the MT compartment design, all MTs sit under a vertical liquid column of ∼1 µL, which is not fully subjected to active perfusion from the channels. Alterations of the exposure profile by diffusion effects originating from these liquid columns, however, were considered negligible. This assumption is based on the small volume of the liquid columns in comparison to the continuous active perfusion with flow rates of 10–25 µL min^{-1}, depending on the tilting angle.

All in all, the proposed chip features large flexibility to produce concentration profiles that resemble those of *in vivo* scenarios upon injection of a substance. Concentration curves in the chip system could reliably be predicted and reproduced.

Dosing Experiments

After the new system had been characterized, it was tested by exposing a tumor MT (TuMT) model to a gradually decreasing, PK-like dosing profile, and, for comparison, to a constant dose (**Figure 6A**). We used the human colorectal cancer-cell line HCT 116 as a suitable tumor model, based on (i) the possibility to reliably generate uniform TuMTs, and (ii) its sensitivity to Staurosporine. Staurosporine is an anti-cancer tool compound, commonly used for *in vitro* studies. It acts as a potent, promiscuous kinase inhibitor and induces apoptosis in proliferating cancer cells (Chae et al., 2000; Karaman et al., 2008). The dosing curve that was previously characterized with 5-fluorouracil (5-FU) was applied to the TuMTs over a duration of 24 h. The initial maximum concentration (C_{max}) of the PK-curve was chosen as constant concentration for comparison. A concentration of 0.75 µM was determined as C_{max} by a static titration prior to the dosing experiment (**Supplementary Figure 5**).

After 5 h and 24 h of incubation, caspase 3 and 7 activity was measured to assess the induction of apoptosis as a reaction to the different Staurosporine treatment strategies (**Figure 6B**). After 5 h of treatment, TuMTs under both treatment conditions showed increased caspase 3/7 activity, as compared to the untreated controls. Moreover, TuMTs treated constantly with the C_{max} concentration showed higher levels of apoptosis. Measurements of apoptosis after 24 h indicated slightly increased caspase activity for the C_{max} condition, while caspase levels were similar to those of the control groups for the PK-like dosing regimen. **Figure 6C** shows intracellular ATP concentrations of the TuMTs as a measure of viability after 5 h and 24 h. The increasing ATP concentrations for all conditions over time indicate proliferation of the cancer cells in the TuMTs. While ATP concentrations in the PK-treated and the control MTs increased to a similar extent, they remained almost constant for the C_{max}-treated MTs. Bright-field images of the conditions at the start of the experiment and after 24 h confirm the ATP findings, as they show slight MT growth for all conditions, except for the C_{max}-treated ones (**Figure 6D**). Furthermore, a constant high dose of Staurosporine led to a morphological change of the TuMTs, which appeared darker and denser after 24 h of treatment. Noteworthy, the switch from static to perfusion culture did not affect cell viability and health, as can be seen by comparing the perfusion control to the static control (**Figures 6B,C**). This observation

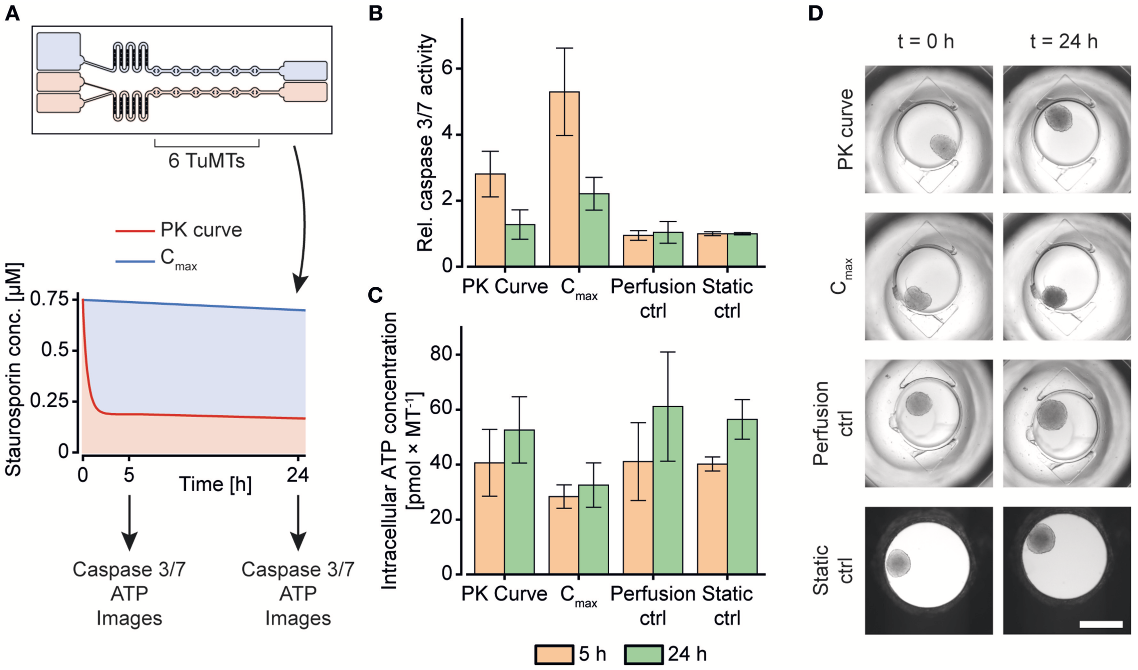

FIGURE 6 | Staurosporine treatment of human colorectal tumor (HCT 116) microtissues (TuMTs) in the microfluidic chip. **(A)** Experimental layout: A chip was used to expose six TuMTs per channel to a PK-like dosing profile or a constant dose. The initial maximum concentration (C_{max}) of the PK-like profile was chosen as the constant concentration for the second channel. The perfusion control and the static control MTs were cultured without any compound treatment in the chip and in a 96-well microtiter plate, respectively. Readouts were taken 5 and 24 h after treatment start. **(B)** Relative caspase 3/7 activity, normalized to those of the static control of the respective sampling time points (data represented as mean ± SD; $n = 6$–12 TuMTs). **(C)** Intracellular ATP concentration as a measure of viability (data represented as mean ± SD; $n = 6$–12 TuMTs). **(D)** Representative images of TuMTs on the chip and in the microtiter plate at 0 and 24 h (scale bar: 500 µm).

indicates that flow-induced shear stress on the TuMTs does not compromise their characteristics and behavior, and it evidences that the developed device is suitable for assessing effects of pharmacokinetic substance profiles on TuMTs.

The acquired data indicated, that the different treatment conditions with the same starting concentration may, indeed, yield different results. While the anti-cancer effect of Staurosporine lead to an early onset of apoptosis for the PK-profile, the mid-term and long-term effect was more prominent for the constant high dose. The experiments highlight that a certain threshold concentration of an active compound has to be maintained over the treatment duration in order to obtain the desired effect. Metabolization effects of administered compounds as they occur *in vivo*, however, may decrease the concentration even more rapidly so that it may be difficult to maintain the concentration within the therapeutic window. In any case, it is advantageous for an *in vitro* system that is intended to reproduce the *in vivo* situation as much as possible to have options to adapt the dosing profile to accommodate various effects and maintain critical concentrations.

DISCUSSION

We presented in this article a technical solution for the exposure of cellular models to temporal gradients of a substance of interest. The concentration profile was achieved by an asymmetrical Y-junction in a microfluidic microtissue culture chip that relied on perfusion by gravity-driven flow. We did not use external pumps and tubing, and we applied SBS Standard ANSI/SLAS 4-2004[1] for the MT compartments and Standard ANSI/SLAS 1-2004[2] for the chip handling frames, so that our platform meets all criteria for parallelization and automation of experiments.

Other systems featuring dynamic exposure profiles of cellular model systems have been presented in the last couple of years. Song et al. (2018) presented a system to expose HEK cells to short pulses and gradually ramped profiles of epidermal growth factor (EGF). Their pump-driven microfluidic chip enabled to optically monitor cellular responses at single-cell resolution. Differential pathway activation was detected in an exposure-profile-dependent manner. The application of such pump-driven systems, however, requires technically experienced operators, which limits their broad use, experimental throughput, and the transfer of such systems to non-expert labs.

Another approach for pulsatile substance exposure of cellular models, was realized by relying on passive, gravity-driven perfusion (Lee et al., 2016). The proposed microfluidic chip was connected to two inlet reservoirs at different heights, one filled with medium, and the other one filled with substance-containing medium. In their work, the authors cultured cancer cells in a microfluidic chip and exposed them to pulses of tumor necrosis factor (TNF). Pulses were initiated by manually elevating the reservoir containing the substance for the duration of the pulse. Interestingly, their results evidenced higher anticancer effects for

---

[1] ANSI/SLAS 1-2004: Microplates–Footprint Dimensions.
[2] ANSI/SLAS 4-2004: Microplates–Well Positions.

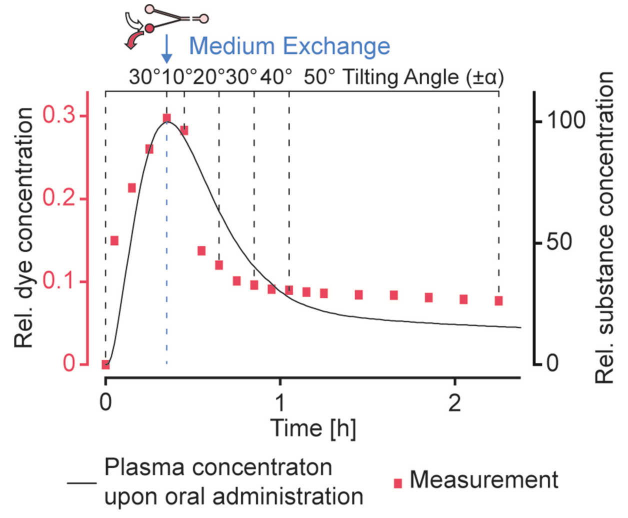

FIGURE 7 | Realization of more complex dosing profiles. A typical concentration profile (Kwon, 2001) upon oral administration of a substance could be approximated by using a sequence of different tilting angles. A medium exchange to replace the substance-loaded medium in the reservoir connected to the narrow channel with plain medium was performed after ∼20 min. Amaranth red dye was used as drug-surrogate.

using shorter pulses of TNF, which underline the importance of investigating dosage-dependent toxicity and efficacy. The system, however, was only used to generate pulses of TNF, and gradual concentration changes over time were not realized. The system presented here, on the other hand, can be used to produce gradual changes of substance concentrations without the need for manual actuation, while still fully relying on gravity-driven operation. It can be used with a minimum set of specialized equipment. Furthermore, in contrast to other systems, which were designed for culturing 2D monolayers of cells, our chip was devised to culture multiple 3D MTs.

Combining a controlled microfluidic environment with 3D cell culture techniques to enable the realization of PK profiles and modification of the respective parameters, we see great potential for our design for investigating concentration profile-dependent efficacy and/or toxicity of substances.

Future Perspective

As shown in the presented experiments, different concentration profiles could be produced in the microfluidic chip, and tumor MTs could be exposed to dynamically changing concentrations profiles. So far, the chip was used for experimentation with only one type of MTs. The chip, however, is not limited to a single organ surrogate, but also allows for combining several different MTs or organ types. The behavior of different organs upon substance exposure can be monitored simultaneously, which allows for a combined readout of efficacy on the primary target organ and toxicity on a secondary organ. For mimicking cancer treatment, tumor MTs and liver MTs could be combined to assess the side effects of tumor treatment on the liver. The developed device could help to experimentally modify the dosing curve in order to find a dosing strategy with an optimum trade-off between efficacy on the tumor and liver toxicity. Moreover, communication between the two tissues types through secreted molecules, which might further influence their drug and treatment response, could be included in *in vitro* testing.

In addition to the presented concentration profiles, more complex dosing profiles could be approximated by applying a sequence of different tilting angles and precisely timed medium changes in the reservoirs. We could produce a concentration profile that features the characteristics of a typical plasma concentration over time upon oral administration of a substance (Kwon, 2001), as we have demonstrated by using amaranth red dye as drug-surrogate (**Figure 7**). A sequence of precisely timed medium exchanges, or the implementation of capillary stop valves that burst when sufficient pressure is built up at high tilting angles (Olanrewaju et al., 2016, 2018) can be used over longer culturing periods to reproduce long-term substance fluctuations, e.g., repeated drug dosing or circadian hormone profiles. Alternating filling of the reservoir connected to the narrow channel with hormone-containing and plain medium could be used to gradually increase and decrease hormone concentrations in the MT compartments. Since circadian profiles modulate organ functions, they may play an important role in future substance testing and for translating of *in vitro* organ responses to *in vivo* conditions (Cyr et al., 2017).

CONCLUSION

In this article, we presented a novel microfluidic design for the generation of gradually changing substance concentration profiles for an easy-to-use microfluidic tilting system. The integration of the new design into cell culture chips enabled to run dynamically changing concentration profiles and to reproduce, e.g., the dosing curve upon injection of a substance without the need for a series tedious pipetting steps or expensive pumping equipment. By changing design and operation parameters, the dosing curves could be adjusted to experimenters needs, and the dosing curves could be modulated on demand as demonstrated by recreating an oral uptake profile. Experiments with colorectal tumor MTs and the cytotoxic substance Staurosporine showed the different short- and long-term responses of the MTs to dynamic and traditional, linear dosing regimes.

AUTHOR CONTRIBUTIONS

CL, OF, and KR conceived the approach and designed the experiments. CL and FB performed the experiments. CL analyzed the data. CL, OF, KR, and AH wrote the paper.

FUNDING

This work was financially supported by CTI grant 18024.1 PFLS-LS.

SUPPLEMENTARY MATERIAL

The Supplementary Material for this article can be found online at: https://www.frontiersin.org/articles/10.3389/fbioe.2019.00072/full#supplementary-material

REFERENCES

Bruus, H. (2008). *Theoretical Microfluidics*. Oxford: Oxford University Press.

Casale, F., Canaparo, R., Serpe, L., Muntoni, E., Pepa, C. D., Costa, M., et al. (2004). Plasma concentrations of 5-fluorouracil and its metabolites in colon cancer patients. *Pharmacol. Res.* 50, 173–179. doi: 10.1016/j.phrs.2004.01.006

Chae, H.-J., Kang, J.-S., Byun, J.-O., Han, K.-S., Kim, D.-U., Oh, S.-M., et al. (2000). Molecular mechanism of staurosporine-induced apoptosis in osteoblasts. *Pharmacol. Res.* 42, 373–381. doi: 10.1006/phrs.2000.0700

Cyr, K. J., Avaldi, O. M., and Wikswo, J. P. (2017). Circadian hormone control in a human-on-a-chip: *in vitro* biology's ignored component? *Exp. Biol. Med.* 242, 1714–1731. doi: 10.1177/1535370217732766

Edington, C. D., Chen, W. L. K., Geishecker, E., Kassis, T., Soenksen, L. R., Bhushan, B. M., et al. (2018). Interconnected microphysiological systems for quantitative biology and pharmacology studies. *Sci. Rep.* 8:4530. doi: 10.1038/s41598-018-22749-0

Karaman, M. W., Herrgard, S., Treiber, D. K., Gallant, P., Atteridge, C. E., Campbell, B. T., et al. (2008). A quantitative analysis of kinase inhibitor selectivity. *Nat. Biotechnol.* 26, 127–132. doi: 10.1038/nbt1358

Kim, J. Y., Fluri, D. A., Kelm, J. M., Hierlemann, A., and Frey, O. (2015a). 96-well format-based microfluidic platform for parallel interconnection of multiple multicellular spheroids. *J. Lab. Autom.* 20, 274–282. doi: 10.1177/2211068214564056

Kim, J. Y., Fluri, D. A., Marchan, R., Boonen, K., Mohanty, S., Singh, P., et al. (2015b). 3D spherical microtissues and microfluidic technology for multi-tissue experiments and analysis. *J. Biotechnol.* 205, 24–35. doi: 10.1016/j.jbiotec.2015.01.003

Kim, Y., Joshi, S. D., Messner, W. C., LeDuc, P. R., and Davidson, L. A. (2011). Detection of dynamic spatiotemporal response to periodic chemical stimulation in a xenopus embryonic tissue. *PLoS ONE.* 6:e14624. doi: 10.1371/journal.pone.0014624

Kwon, Y. (2001). *Handbook of Essential Pharmacokinetics, Pharmacodynamics and Drug Metabolism for Industrial Scientists*. New York, NY: Springer Science & Business Media.

Lee, C.-Y., Chang, C.-L., Wang, Y.-N., and Fu, L.-M. (2011). Microfluidic mixing: a review. *Int. J. Mol. Sci.* 12, 3263–3287. doi: 10.3390/ijms12053263

Lee, R. E. C., Qasaimeh, M. A., Xia, X., Juncker, D., and Gaudet, S. (2016). NF-κB signalling and cell fate decisions in response to a short pulse of tumour necrosis factor. *Sci. Rep.* 6:39519. doi: 10.1038/srep39519

Lee, S. W., and Lee, S. S. (2008). Shrinkage ratio of PDMS and its alignment method for the wafer level process. *Microsyst. Technol.* 14, 205–208. doi: 10.1007/s00542-007-0417-y

Lohasz, C., Frey, O., Renggli, K., and Hierlemann, A. (2017). A tubing-free, microfluidic platform for the realization of physiologically relevant dosing curves on cellular models. *Proceedings* 1:497. doi: 10.3390/proceedings1040497

Lohasz, C., Rousset, N., Renggli, K., Hierlemann, A., and Frey, O. (2018). Scalable microfluidic platform for flexible configuration of and experiments with microtissue multiorgan models. *SLAS Technol.* 24, 79–95. doi: 10.1177/2472630318802582

Maass, C., Stokes, C. L., Griffith, L. G., and Cirit, M. (2017). Multi-functional scaling methodology for translational pharmacokinetic and pharmacodynamic applications using integrated microphysiological systems (MPS). *Integr. Biol. (Camb).* 9, 290–302. doi: 10.1039/C6IB00243A

Marx, U., Andersson, T. B., Bahinski, A., Beilmann, M., Beken, S., Cassee, F. R., et al. (2016). Biology-inspired microphysiological system approaches to solve the prediction dilemma of substance testing. *ALTEX* 33, 272–321. doi: 10.14573/altex.1603161

Olanrewaju, A., Beaugrand, M., Yafia, M., and Juncker, D. (2018). Capillary microfluidics in microchannels: from microfluidic networks to capillaric circuits. *Lab Chip* 18, 2323–2347. doi: 10.1039/C8LC00458G

Olanrewaju, A. O., Robillard, A., Dagher, M., and Juncker, D. (2016). 3D-printed autonomous capillaric circuits. *bioRxiv*, 059238. doi: 10.1101/059238

Prantil-Baun, R., Novak, R., Das, D., Somayaji, M. R., Przekwas, A., and Ingber, D. E. (2018). Physiologically based pharmacokinetic and pharmacodynamic analysis enabled by microfluidically linked organs-on-chips. *Annu. Rev. Pharmacol. Toxicol.* 58, 37–64. doi: 10.1146/annurev-pharmtox-010716-104748

Ross, A. E., Belanger, M. C., Woodroof, J. F., and Pompano, R. R. (2017). Spatially resolved microfluidic stimulation of lymphoid tissue *ex vivo*. *Analyst* 142, 649–659. doi: 10.1039/C6AN02042A

Saif, M. W., Choma, A., Salamone, S. J., and Chu, E. (2009). Pharmacokinetically guided dose adjustment of 5-fluorouracil: a rational approach to improving therapeutic outcomes. *J. Natl. Cancer Inst.* 101, 1543–1552. doi: 10.1093/jnci/djp328

Sejoong, K., Sasha Cai, L., Byoung choul, C. K., Cameron, Y., Joseph, M. L., Brendan, L., et al. (2016). Pharmacokinetic profile that reduces nephrotoxicity of gentamicin in a perfused kidney-on-a-chip. *Biofabrication* 8:015021. doi: 10.1088/1758-5090/8/1/015021

Song, J., Ryu, H., Chung, M., Kim, Y., Blum, Y., Lee, S. S., et al. (2018). Microfluidic platform for single cell analysis under dynamic spatial and temporal stimulation. *Biosens. Bioelect.* 104, 58–64. doi: 10.1016/j.bios.2017.12.038

Stroock, A. D., Dertinger, S. K., Ajdari, A., Mezic, I., Stone, H. A., and Whitesides, G. M. (2002). Chaotic mixer for microchannels. *Science* 295, 647–651. doi: 10.1126/science.1066238

Sung, J. H., Kam, C., and Shuler, M. L. (2010). A microfluidic device for a pharmacokinetic-pharmacodynamic (PK-PD) model on a chip. *Lab Chip* 10, 446–455. doi: 10.1039/b917763a

Tsaioun, K., Blaauboer, B. J., and Hartung, T. (2016). Evidence-based absorption, distribution, metabolism, excretion (ADME) and its interplay with alternative toxicity methods. *ALTEX* 33, 343–358. doi: 10.14573/altex.1610101

Wang, Y. I., Carmona, C., Hickman, J. J., and Shuler, M. L. (2018). Multiorgan microphysiological systems for drug development: strategies, advances, and challenges. *Adv. Healthc. Mater.* 7. doi: 10.1002/adhm.201701000

Wikswo, J. P., Markov, D. A., Samson, P. C., Block, I. I. I., Frank, E., Schaffer, D. K., et al. (2018). *Interconnections of Multiple Perfused Engineered Tissue Constructs and Microbioreactors, Multi-Microformulators and Applications of the Same*. US20170081625A1 United States patent application.

Zhang, B., Korolj, A., Lai, B. F. L., and Radisic, M. (2018). Advances in organ-on-a-chip engineering. *Nat. Rev. Mater.* 3, 257–278. doi: 10.1038/s41578-018-0034-7

Conflict of Interest Statement: OF is part of the management team at InSphero AG commercializing microfluidic culturing devices.

The remaining authors declare that the research was conducted in the absence of any commercial or financial relationships that could be construed as a potential conflict of interest.

Advantages of publishing in Frontiers

OPEN ACCESS
Articles are free to read
for greatest visibility
and readership

FAST PUBLICATION
Around 90 days
from submission
to decision

HIGH QUALITY PEER-REVIEW
Rigorous, collaborative,
and constructive
peer-review

TRANSPARENT PEER-REVIEW
Editors and reviewers
acknowledged by name
on published articles

Frontiers
Avenue du Tribunal-Fédéral 34
1005 Lausanne | Switzerland

Visit us: www.frontiersin.org
Contact us: info@frontiersin.org | +41 21 510 17 00

REPRODUCIBILITY OF RESEARCH
Support open data
and methods to enhance
research reproducibility

DIGITAL PUBLISHING
Articles designed
for optimal readership
across devices

FOLLOW US
@frontiersin

IMPACT METRICS
Advanced article metrics
track visibility across
digital media

EXTENSIVE PROMOTION
Marketing
and promotion
of impactful research

LOOP RESEARCH NETWORK
Our network
increases your
article's readership